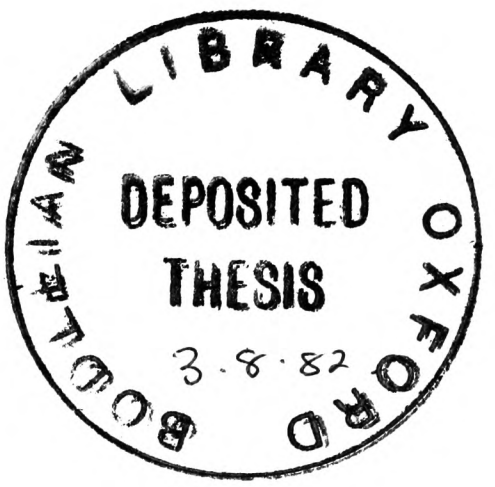
# "MAGNETIC AND STRUCTURAL STUDIES OF SOME MIXED METAL OXIDES"

A Thesis in part fulfilment of the requirements for the degree of Doctor of Philosophy of the University of Oxford.

by

D.A.C. Hope, B.A.,
St. John's College




Michaelmas Term 1981

CONTENTS


| | | PAGE |
|---|---|---|
| Abstract | | |
| Acknowledgements | | |
| | PART I : INTRODUCTION AND EXPERIMENTAL | |
| Chapter 1 | Aims of Research | 1 |
| Chapter 2 | Introduction | |
| | 2.1 Stability and Structure of the Iron Group Monoxides and their Solid Solutions | 2 |
| | 2.2 Magnetic Ordering in Transition Metal Oxides, MO($M^{2+}$ = $3d^5$ - $3d^8$) | 14 |
| | 2.3 Magnetic Properties of Disordered Ionic Antiferromagnets | 45 |
| Chapter 3 | Experimental Techniques | |
| | 3.1 Sample Preparation and Analysis | 52 |
| | 3.2 Neutron Diffraction | 56 |
| | 3.3 Mossbauer Effect Spectroscopy | 72 |
| | 3.4 Magnetic Susceptibility Measurements | 76 |
| | PART II : RESULTS AND DISCUSSION | |
| Chapter 4 | Magnetic Ordering in $Mn_xNi_{1-x}O$ | |
| | 4.1 Magnetic Phase Diagram | 78 |
| | 4.2 Magnetic Structure and Lattice Distortions at 5K | 80 |
| | 4.3 Summary | 88 |
| Chapter 5 | Magnetic Ordering in $Mn_xCo_{1-x}O$ | |
| | 5.1 Magnetic Phase Diagram | 90 |
| | 5.2 Lattice Distortions and Magnetic Structure | 93 |
| | 5.3 Summary | 114 |
| Chapter 6 | The Crystal and Magnetic Structures of $(Mn_xFe_{1-x})_zO$ and $(Co_xFe_{1-x})_zO$ | |
| | 6.1 Defect Structures of the Solid Solutions | 117 |
| | 6.2 Magnetic Ordering in $(Mn_xFe_{1-x})_zO$ and $(Co_xFe_{1-x})_zO$ | 135 |
| Chapter 7 | Conclusions and Future Developments | |
| | 7.1 Summary of Results and their Interpretation | 164 |

(Contents continued)


| | PAGE |
|---|---|
| 7.2 Suggestions for Future Work | 171 |
| References | 174 |
| Appendix 1 | 185 |
| Appendix 2 | 193 |

ABSTRACT

"MAGNETIC AND STRUCTURAL STUDIES OF SOME MIXED METAL OXIDES"

A thesis submitted for the degree of Doctor of Philosophy in Michaelmas Term 1981 by D.A.O. Hope B.A. (St. John's College).

Powder neutron diffraction and magnetic susceptibility measurements of the antiferromagnetic phases of $Mn_xNi_{1-x}O$, $Mn_xCo_{1-x}O$, $(Mn_xFe_{1-x})_zO$ and $(Co_xFe_{1-x})_zO$ reveal that the magnetic moments of unlike ions are always effectively collinear, despite the presence of competing anisotropies.

The magnetic moments of $Mn_xNi_{1-x}O$ (x = 0.24,0.48 and 0.77) at 5K are confined to (111) planes by dipole-dipole forces, and the small trigonal exchangestrictions are the products of opposed antiferromagnetic $Mn^{2+}$-$Mn^{2+}$ and ferromagnetic $Ni^{2+}$-$Mn^{2+}$ nearest neighbour interactions.

In $Mn_xCo_{1-x}O$ (x = 0.05, 0.10, 0.25,0.36) at 5K, the orbital degeneracy of $Co^{2+}$ is removed by both Jahn-Teller (J.T) and spin-orbit coupling (S.O) mechanisms, leading to orthorhombic or triclinic symmetries and partially quenched $Co^{2+}$ moments. Monoclinic symmetry is observed for $0.51<x<0.67$, and Jahn-Teller stabilisations and spin-only $Co^{2+}$ moments are evident. The cobalt concentration is too small to support a co-operative J.T stabilisation in $Mn_{0.83}Co_{0.17}O$, where a magnetostriction ($c/a < 1$) is observed (in agreement with previous AFMR results).

Previous results for $Co_xNi_{1-x}O$, and those for $Mn_xCo_{1-x}O$, $(Mn_xFe_{1-x})_zO$ (x = 0.05, 0.1, 0.12, 0.23, 0.36,0.56,0.66,0.89) and $(Co_xFe_{1-x})_zO$ (x = 0.04,0.12,0.50,0.63,0.81) at 5K indicate that the anisotropy order for the iron group monoxides is $CoO>MnO>>Fe_zO\approx NiO$. The weak trigonal anisotropy of $Fe^{2+}$ correlates with the near-cubic symmetries of $(Co_xFe_{1-x})_z$( (x = 0.04,0.12) and $(Mn_xFe_{1-x})_zO$ ($0.1<x<0.66$), and a tetragonal ($c/a>1$) magnetostriction of $Fe^{2+}$ is observed in $(Co_xFe_{1-x})_zO$ with $x > 0.5$.

Measurements of vacancy-ferric interstitial ratios for $(Mn_xFe_{1-x})_zO$ and $(Co_xFe_{1-x})_zO$ suggest that non-stoichiometry is accommodated by 6:2 or 8:3 defect clusters in the former, and by larger units in the latter. The observed magnetic moments of defective samples are normally larger than those calculated according to a previous model for $Fe_zO$, and require the postulation of partial antiferromagnetic order around the clusters.

The room temperature Mössbauer effect parameters of $(Mn_xFe_{1-x})_zO$ ($0<x<0.975$,$0.910<z<1.0$) indicate that while $Fe^{2+}$ and $Mn^{2+}$ ions are randomly distributed over octahedral sites, ferric ions are localised around defect clusters.

ACKNOWLEDGEMENTS

It would have been impossible to carry out this work without the help of very many people, and I am especially indebted to the following:

Dr A.K. Cheetham for his valuable advice and supervision;

Dr G.A. Gehring, who deputised in his absence;

Dr G.J. Long for instruction in Mossbauer spectroscopy and magnetic measurements, and (with his family and Messrs S. Tetrick, R. Jones and D.L. Bogart) for making my stay in Rolla so enjoyable;

Dr P.D. Battle, Prof. J.B. Goodenough and Dr C. Gleitzer for some rewarding discussions.

Drs A.R. Rae-Smith and A.J. Skarnulis, whose Powder system aided the neutron data reduction greatly;

Drs A.W. Hewat, C. Wilkinson, J.L. Buevoz and S. Heathman of the I.L.L, Grenoble;

Messrs D.H.C. Harris, W. Futcher, G. Proudfoot and N.S. Clarke of the University Support group at Harwell;

Mrs A.E. Stoker for electron microscope analyses;

The ICL staff for atomic absorption analyses;

Mr K. Waters for photography;

Mrs S. Parkinson for her excellent typing;

The many occupants of the Chemical Crystallography Laboratory for their companionship during my three year sojourn;

The S.R.C., St. John's College Oxford and the Chemical Crystallography Laboratory for financial support; and my parents, and wife, Pam, for their encouragement and tolerance.

# PART I

## INTRODUCTION AND EXPERIMENTAL

# CHAPTER ONE

## AIMS OF RESEARCH

The investigation of disordered systems covers a very broad area [1], and an important aspect of the field is the study of mixed magnets. In particular, the theoretical phase diagram of a random antiferromagnet having components with competing anisotropy energies has been vindicated by a range of experiments on two-dimensional systems. However, few investigations have been devoted to the mixed crystals of the isomorphous three-dimensional antiferromagnets MnO, $Fe_zO$, CoO and NiO which, again, have different magnetic easy axes.

Consequently, following a recent crystallographic and magnetic study of $Co_xNi_{1-x}O$ [2] at low temperatures, it was of interest to make a similar examination of other binary combinations of the iron group monoxides. Using magnetic susceptibility and powder neutron diffraction measurements, the main objectives were to (i) determine the Néel temperature-composition phase diagram of each system, (ii) reveal any changes in magnetic moment direction or magnetic structure across the solid solution series, and (iii) study the changes in crystallographic symmetry produced by doping. A comparison with the two-dimensional antiferromagnetic systems could then be obtained, and the relative sizes of the magnetic anisotropy energies of the ions involved and the exchange energies between like and unlike ions would, possibly, be revealed. These parameters are related to the electronic structures of $Mn^{2+}$, $Fe^{2+}$, $Co^{2+}$ and $Ni^{2+}$ as described by ligand field theory. To further these objectives, the low temperature phases of members of MnO-NiO, MnO-CoO, MnO-$Fe_zO$ and CoO-$Fe_zO$ were studied by powder neutron

diffraction, and magnetic susceptibility measurements were made for five samples of the $MnO-Fe_zO$ solid solution.

A second facet of the work was concerned with the use of Mössbauer spectroscopy and neutron diffraction to probe (i) any structural order associated with solid solution formation and (ii) the non-stoichiometry inherent in solid solutions incorporating ferrous oxide. Using the latter information, the effect of any defect clustering on the coherent magnetic neutron scattering could be assessed, as has been accomplished in ferrous oxide itself [3]. Data relating to the above questions were derived from all the neutron diffraction studies, particularly those of $MnO-Fe_zO$ and $CoO-Fe_zO$, and from an examination of the paramagnetic phase of $MnO-Fe_zO$ by means of Mössbauer effect spectroscopy.

# CHAPTER TWO

# INTRODUCTION

## 2.1 Stability and Structure of the Iron Group Monoxides and their Solid Solutions

### 2.1.1 Undoped Oxides

(a) Occurrence. The chemistry of the "divalent" oxides of manganese, iron, cobalt and nickel reflects the range of oxidation states generally available to elements of a transition series. The compounds tend to become non-stoichiometric[4] by the oxidation of metal ions and the creation of cation vacancies, and are normally represented as $M_zO$ ($z \leqslant 1$). Samples of manganous, cobaltous and nickelous oxides formed at low temperatures are known to be highly reactive and to contain large numbers of defects[5], but have received much less attention than those prepared at higher temperatures. These are normally considered to be close to stoichiometry, although large deviations from the 1:1 M:O ratio occur at very high temperatures[6,7,8]. Ferrous oxide disproportionates below 570°C, normally to iron and magnetite ($Fe_3O_4$), and is always markedly non-stoichiometric[9,10]. $Fe_{1.0}O$ is non-existent at ambient pressure, although the near-stoichiometric compound has been reported to result from the disproportionation of $Fe_zO$ below 570°C [11] and to be a product of the hydrogen reduction of $Fe_2O_3$ between 425 and 570°C [12]. Ferrous oxide also approaches stoichiometry if prepared under pressures greater than 36 Kbar [13,14].

Carel et al [15,16] have reviewed the current knowledge of the ferrous oxide phase diagram at atmospheric pressure, part of which is shown in Figure 2.1.

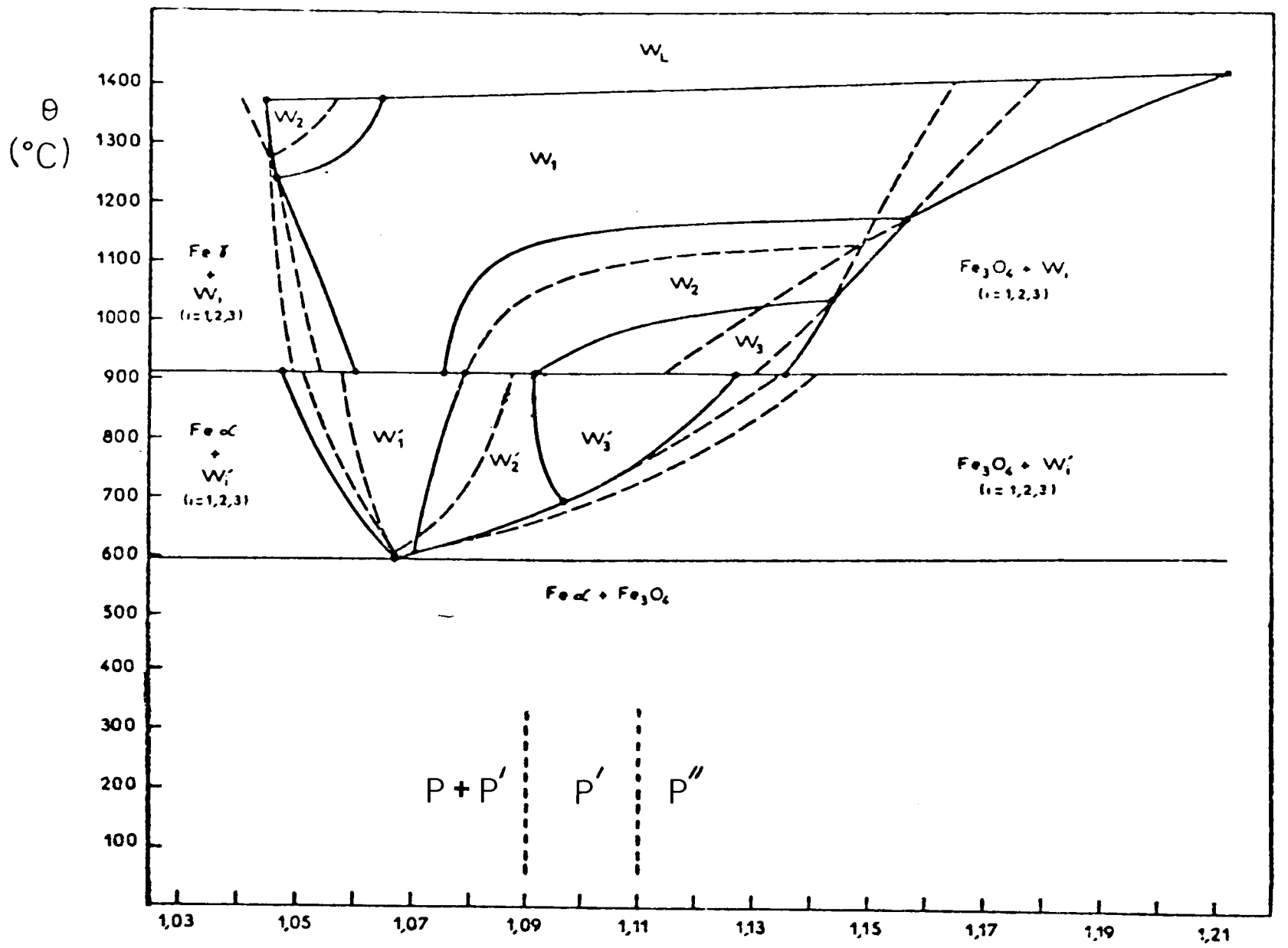



Figure 2.1 Temperature-composition phase diagram for $Fe_zO$, adapted from Vallet and Carel (Ref 17).

This is the result of a recent [17] statistical thermodynamic analysis of some previous experimental data [18] and is in broad agreement with other work [9,10]. An interesting feature is the existence of sub-phases both in the equilibrium and metastable regions, the latter (labelled P, P' and P'' in Figure 2.1) being attained by rapid quenching from high temperatures. The existence of the high temperature sub-phases has been disputed on the basis of lattice parameter measurements [19,20].

(b) Long Range Order. A magnetic phase transition occurs at temperatures ranging from 118 K (MnO) to 523 K (NiO), and in the paramagnetic phases these oxides have the rocksalt structure, consisting of

interlocking face-centred cubic cation and anion arrays (Figure 2.2).

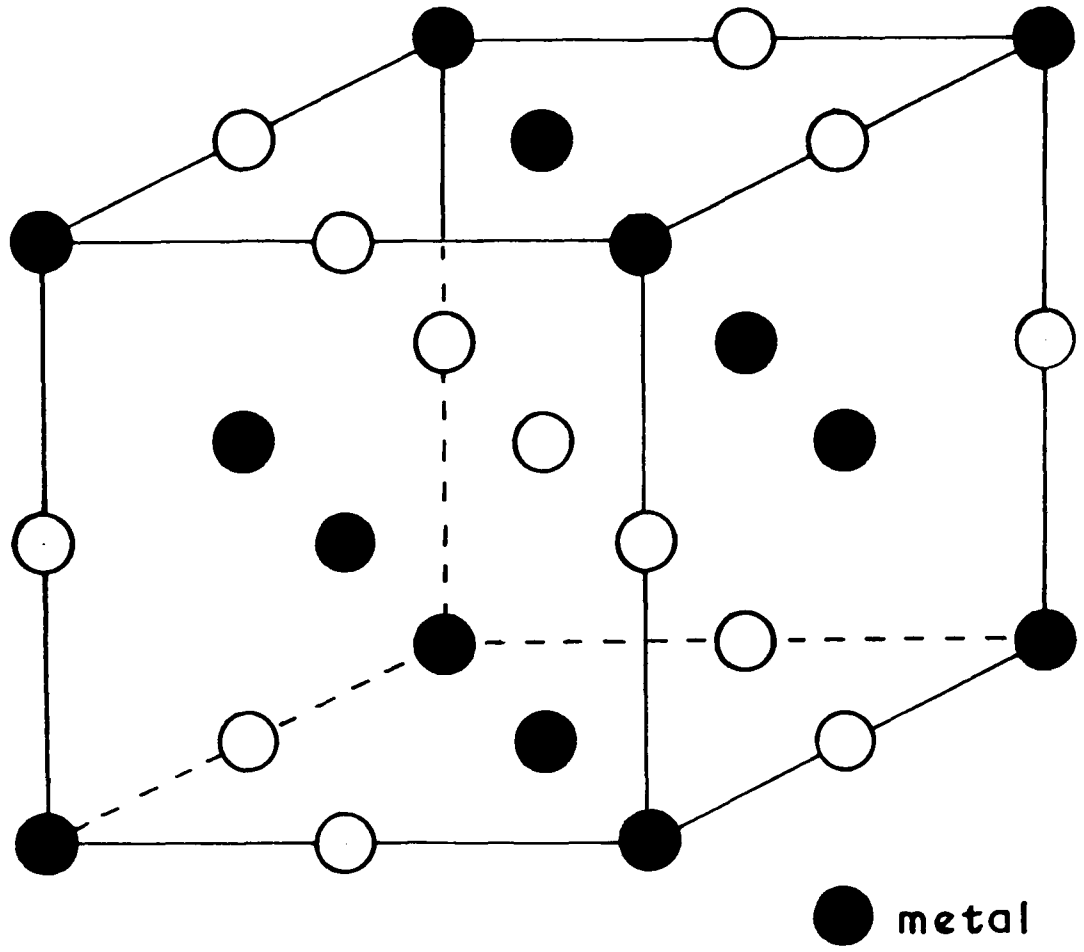



Figure 2.2 The f.c.c. rocksalt structure adopted by MnO, $Fe_zO$, CoO and NiO.

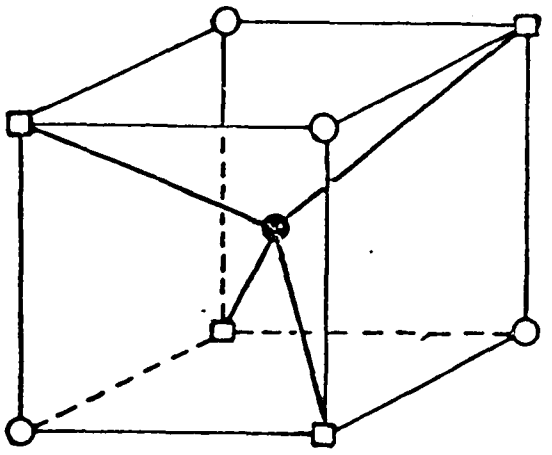
Distortions to lower symmetry are associated with the onset of antiferromagnetism; the behaviour in the magnetically ordered states will be discussed in section 2.2. No abrupt changes in electrical conductivity are associated with the magnetic phase change, the stoichiometric oxides being good insulators, but departure from stoichiometry introduces tripositive cations and p-type semiconduction. Ferrous oxide is a better conductor than the other compounds [21] and experiences a p-n transition at high temperatures and large defect concentrations [22]. Although a Mössbauer effect study [23] has suggested that a rapid electron exchange occurs between $Fe^{2+}$ and $Fe^{3+}$ ions at room temperature, it is now thought that the holes are localised on the Mössbauer timescale [24]. In all four compounds, conduction is believed to occur by an activated "hopping"

process involving small polarons [25,26], although large polarons and extended band-like states have been suggested in CoO and NiO [27].

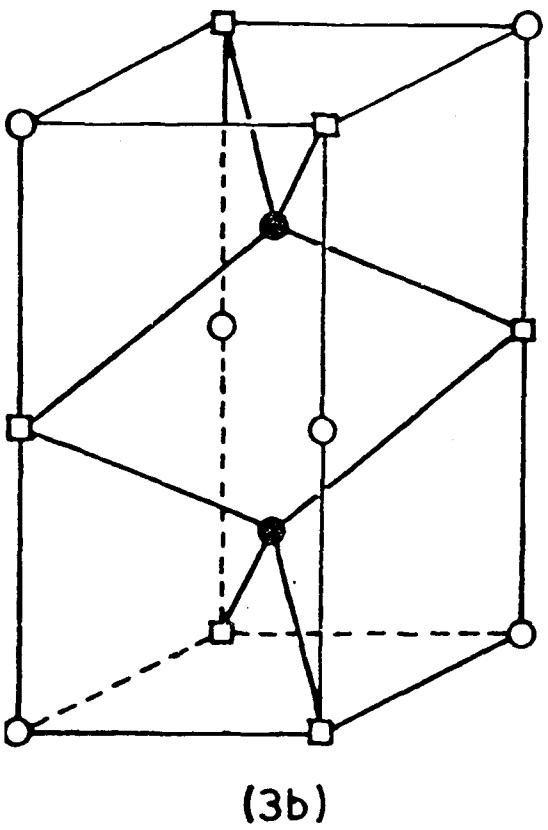
The powder and single crystal diffraction patterns of MnO, CoO and NiO only show the peaks expected of a face centred cubic cell, but quenched single crystals of $Fe_zO$ give rise to both X-ray [28] and neutron [29] superlattice reflections, apparently resulting from the long range order of defects. The nature of these defects will now be considered.

(c) Defects in $M_zO$. The characterisation of the defects in $Fe_zO$ has received much more attention than those in MnO, CoO and NiO, but recent calculations [30,31] suggest that similar defect units are present in all four oxides. Powder X-ray studies of $Fe_zO$ [32,33] suggest the presence of octahedral iron vacancies, with charge compensating ferric ions occupying octahedral sites so as to complex with the virtual negative charges of the vacant sites. However, the neutron diffraction study of a quenched sample by Roth [34] reveals a small proportion of $Fe^{3+}$ ions on tetrahedral interstices. The interstitial was thought to be associated with two octahedral vacancies, forming a 2:1 defect cluster, but more recent work suggests that the basic defect unit arises from the condensation of four vacancies and one interstitial (4:1 cluster). Further complexes may be formed by edge - or corner-sharing of the tetrahedral 4:1 clusters, and some possibilities are shown in Figure 2.3. Neither the edge-sharing clusters (Figures 3a to 3c) nor the Koch-Cohen cluster (Figure 3d) resemble the mode of aggregation of the 4:1 units in the spinel structure, where the tetrahedra share one corner only, and these defects cannot be regarded as micro-domains of $Fe_3O_4$.

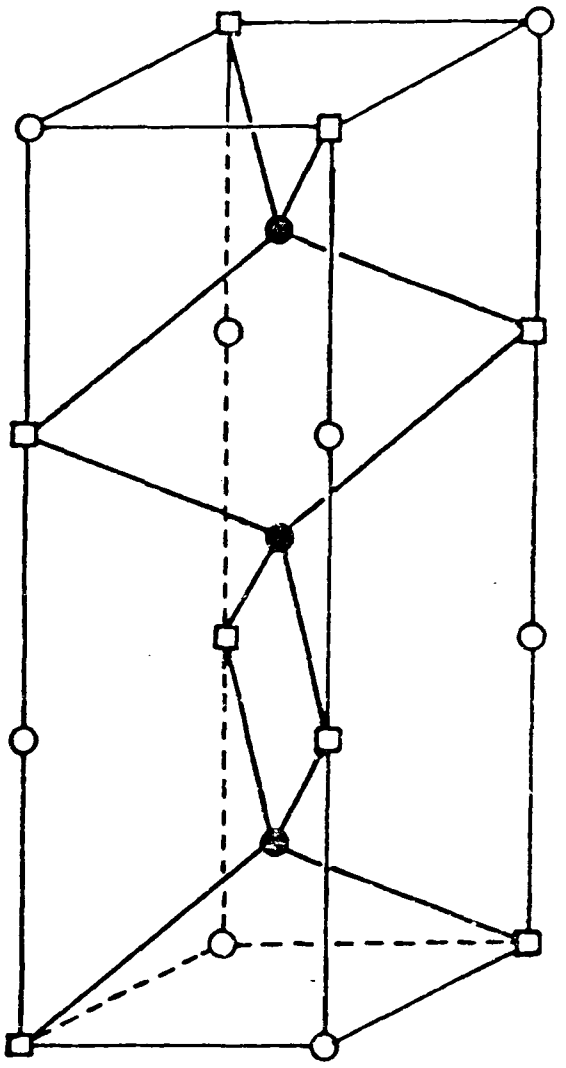
The first evidence for the condensation of 4:1 clusters comes from the X-ray work of Koch and Cohen [28] on a single crystal of the P' phase (Figure 2.1). The superlattice peaks mentioned previously are indexed



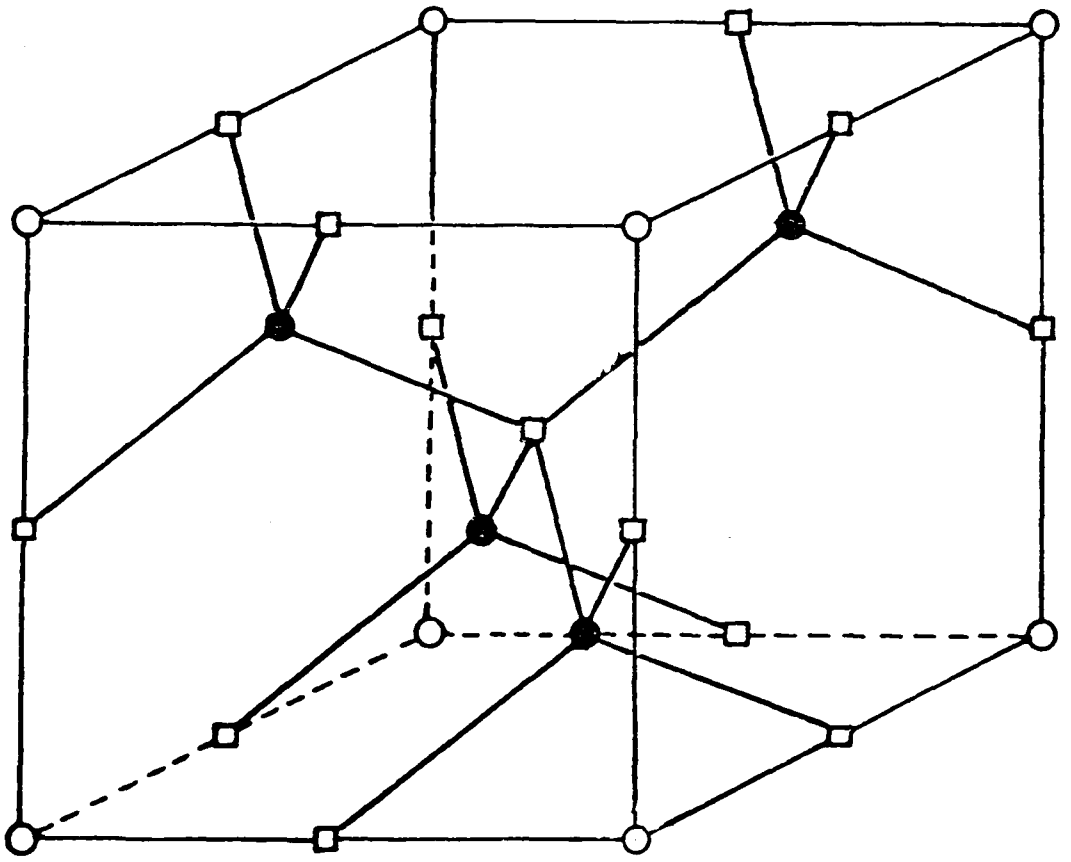
(3a)



(3b)



(3c)



(3d)

O oxygen
● interstitial
□ vacancy

Figure 2.3 Some possible defect clusters in ferrous oxide: (a), (b), (c) 4:1, 6:2 and 8:3 clusters, (d) Koch-Cohen (13:4) cluster.

on a cubic cell three times (3x) the dimension of that giving rise to the fundamental peaks, and a partial Patterson synthesis then reveals the defect cluster shown in Figure 2.3d. However, the R-value is high (15.7%) and the evidence for the 3x cubic cell is weak. The latter deficiency has been confirmed by electron microscopy studies[35,36] of the quenched phases P' and P" in which, respectively, monoclinic and orthorhombic symmetries are observed. No firm evidence for the structure of the clusters results from the use of electrons, although Anderson and Sletnes [36] suggest that the 8:3 cluster (Figure 2.3c) is a possibility. The occurrence of this and other edge-sharing structures is supported by lattice energy calculations [37], which demonstrate the stability of the 4:1 cluster and its 6:2 (Figure 2.3b) and 8:3 complexes, although the 10:4 cluster appears less favourable.

Neutron diffraction is an attractive method for the study of ferrous oxide because of the ease of making measurements at both high and low temperatures and the ability to differentiate between elements of similar atomic number. Although the method only gives information on the average state of the lattice, the number of cation vacancies and iron interstitials per unit cell can, in principle, be determined, and the ratio between them gives an indication of the average defect cluster size. Three powder neutron studies have superseded the work of Roth[34], one, by Battle and Cheetham [3], being concerned with the quenched phases, and the others [38,39,40] studying the equilibrium region. In the most recent high temperature measurements, by Gavarri and co-workers [39,40], the vacancy:interstitial ratio at different temperatures and defect concentrations is always close to 2.4. This value suggests that 8:3 or 10:4 clusters predominate at high temperatures and is consistent with the ratios observed in the room temperature work of Battle and Cheetham[3].

The experiments of Cheetham et al [38] were performed on samples between 800°C and 1180°C and reveal vacancy:interstitial ratios between 3 and 4. This data suggests dissociation of defect clusters into the basic 4:1 cluster occurs at the highest temperatures and lowest defect concentrations. The lack of agreement between this work and that of Gavarri et al may result from the use, in the latter experiment, of a much higher flux diffractometer, and the assignment of independent Debye-Waller factors to the octahedral and tetrahedral sites. The occupancy of the tetrahedral site is very small, and minimal changes to the analysis of the scattering from it may markedly affect the results.

Further indirect evidence for the 4:1 cluster and its edge-sharing derivitives has come from a study of the magnetic structure by Battle and Cheetham [3], in which the reduced coherent magnetic neutron scattering is correlated with magnetically ordered 8:3 or 6:2 clusters (see section 2.2.4). Various Mössbauer spectroscopy investigations have been reported [23,24,41,42,43], of which the most comprehensive (by Greenwood and Howe [24]) shows how the ferrous quadrupole splittings observed for a $Fe_{0.947}O$ sample can be accounted for by the presence of 4:1 rather than Koch-Cohen clusters. Unfortunately, the interpretation of ferrous oxide Mössbauer spectra is hampered by the large number of overlapping resonances (see Chapter 6.1).

While there is no experimental evidence for defect clustering in NiO [44], experiments [45,46,47] showing the formation of defect complexes in MnO and CoO have been supported by calculations [30,31], which also suggest that ionic transport occurs by concerted movement of the complexes. While experiments show this to be true in $Fe_zO$ [45], it is not in CoO at 1200°C [48]. Catlow, Fender and Muxworthy [30] have made predictions as to the form and mode of aggregation of clusters in MnO,

CoO and NiO. They show that the basic defect is again the 4:1 cluster, and simple vacancy:hole clusters are only favoured at high temperatures and low defect concentrations. However, edge-sharing clusters are only to be expected if the interstitial cation is triply charged, and ligand field stabilisation energies exclude high-spin $Co^{3+}$ and $Mn^{3+}$, but favour both interstitial and octahedral site occupancy by high-spin $Ni^{3+}$, $Mn^{2+}$ and $Co^{2+}$. The occupation of the tetrahedral site by doubly charged ions is probably limited by their larger sizes.

### 2.1.2 Solid Solutions

The ionic sizes of $Mn^{2+}$, $Fe^{2+}$, $Co^{2+}$ and $Ni^{2+}$ are very similar, and the room temperature lattice parameters of the monoxides are 4.14 Å (NiO), 4.25 Å (CoO), 4.29 - 4.31 Å ($Fe_zO$, dependent on the stoichiometry) and 4.44 Å (MnO). On this basis alone, it is to be expected that the four oxides will be completely miscible, and that the lattice parameter will have a linear composition dependence (Vegard's Law). However, the phase stability may depend on the different redox behaviour of the component oxides, as in NiO-$Fe_zO$ [49], where a large miscibility gap is caused by the ease of reduction of NiO by $Fe_zO$, and alloy and spinel co-exist at all temperatures. The five other possible combinations of the four oxides can be obtained across the whole range of composition, above certain minimum temperatures, but those containing iron tend to be non-stoichiometric and are difficult to prepare in single-phase form. A recent, comprehensive review of the data available on the solid solutions formed by ferrous oxide has been given by Gleitzer [50]. Equimolar metal:oxygen ratios can only be obtained when the non-ferrous ion is in very large excess; even in $Fe_zO$-MgO, stoichiometry is only attainable when less than 30% iron is present. The knowledge of the phase diagrams (up to 1974) of all the systems under consideration has been collated

by Levin, Robbins and McMurdie [51]. Some relevant data will now be summarised.

MnO-$Fe_zO$ The phase diagram at 1000°C has been determined by Aubry et al [52] and by Tret'yakov and co-workers [53]; the results of the latter are shown in Figure 2.4.

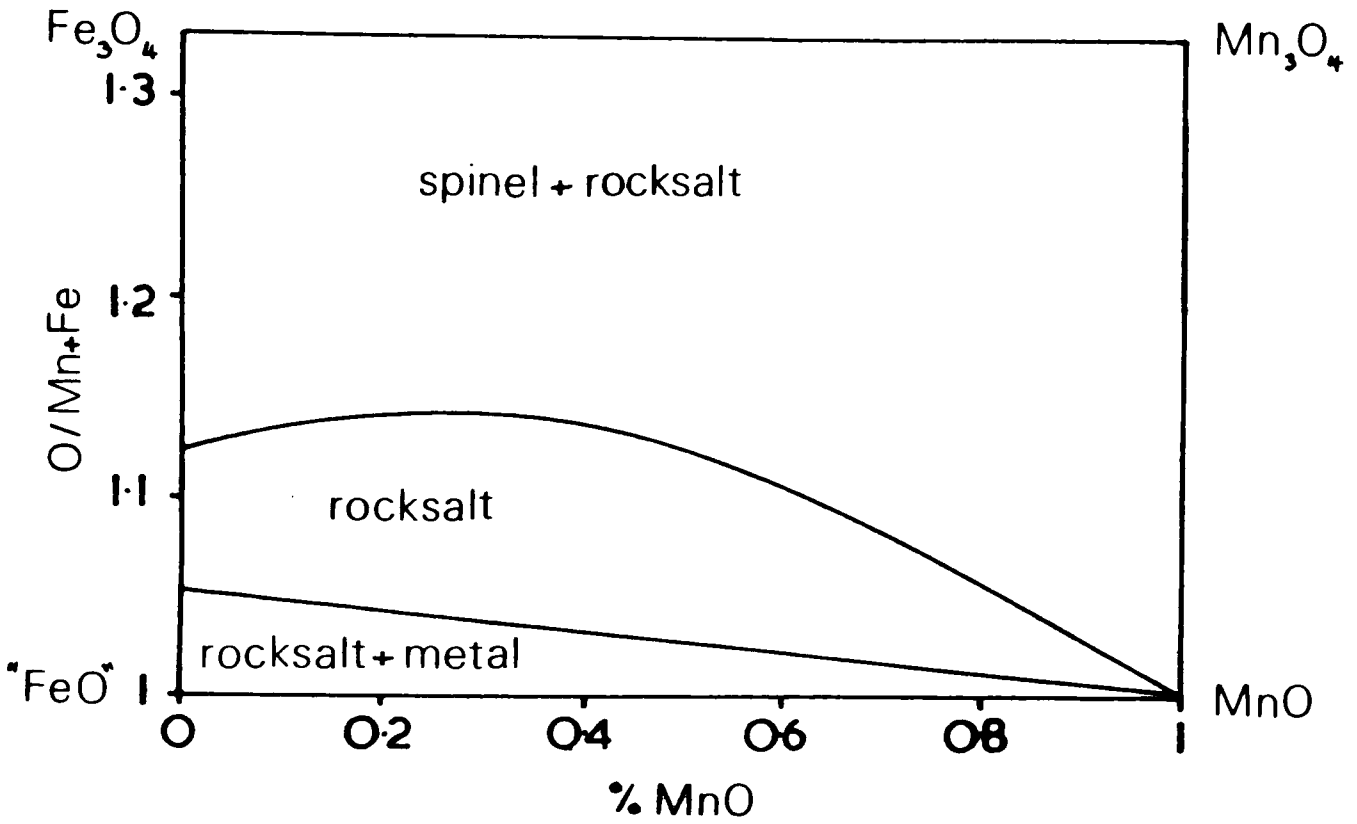



Figure 2.4 Schematic Phase Diagram for MnO-$Fe_zO$ at 1000°C.

No detailed investigation of the structure has been reported, but a lamellar arrangement of Mn and Fe has been proposed [54] to account for some magnetic susceptibility results. Foster and Welch [55] have determined the lattice parameter as a function of composition and stoichiometry, and have shown that the solution is ideal. However, Schwerdtfeger and Muan [56] suggest that the activities of the components show slight positive deviations from Raoult's Law. Phase separation may occur in samples maintained below 900°C [57].

MnO-CoO This solid solution was previously [58] thought to be ideal at 1200°C, but recent work [59,60] reveals a significant positive deviation

from Raoult's Law. The solution obeys Vegard's Law but, bar the randomness demonstrated by neutron diffraction [61], no other structural measurements have been made.

MnO-NiO The system shows substantial positive deviations from Raoult's Law [60,62], and Hampson et al [60] have suggested that the marked asymmetries in the heats and entropies of mixing can be explained by partial oxidation of $Mn^{2+}$ in the contracted nickel-rich lattices. Barrett and Evans[63] have observed a slight negative deviation from Vegard's Law.

$Fe_zO$-CoO As is the case for MnO-$Fe_zO$, the structure of this solid solution has not been studied. Although Bénard [64] reports complete solubility at 900°C, Touzelin [65] observes that the system is predominantly biphasic at this temperature. Aukrust and Muan [66] have determined the phase diagram at 1200°C (Figure 2.5) and demonstrate that the activities show

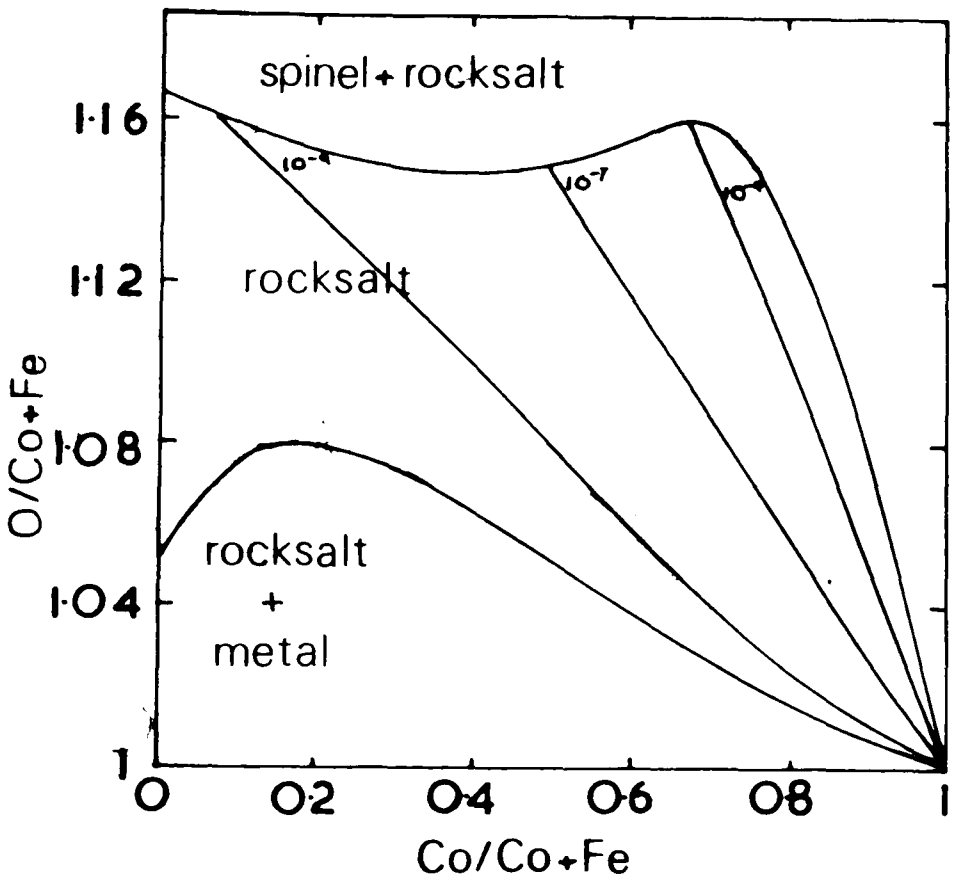



Figure 2.5 Schematic Phase Diagram for CoO-$Fe_zO$ at 1200°C. The rocksalt phase limits for different oxygen partial pressures are shown.

a slight positive deviation from ideality at this temperature. Other thermodynamic studies [60,61] have been reported, some of which are in conflict with the above results.

$Fe_zO$-NiO The limited composition range of this solid solution is demonstrated by the phase diagram at 1000°C shown in Figure 2.6.[49] This work is at variance with earlier suggestions [64] that the two oxides are

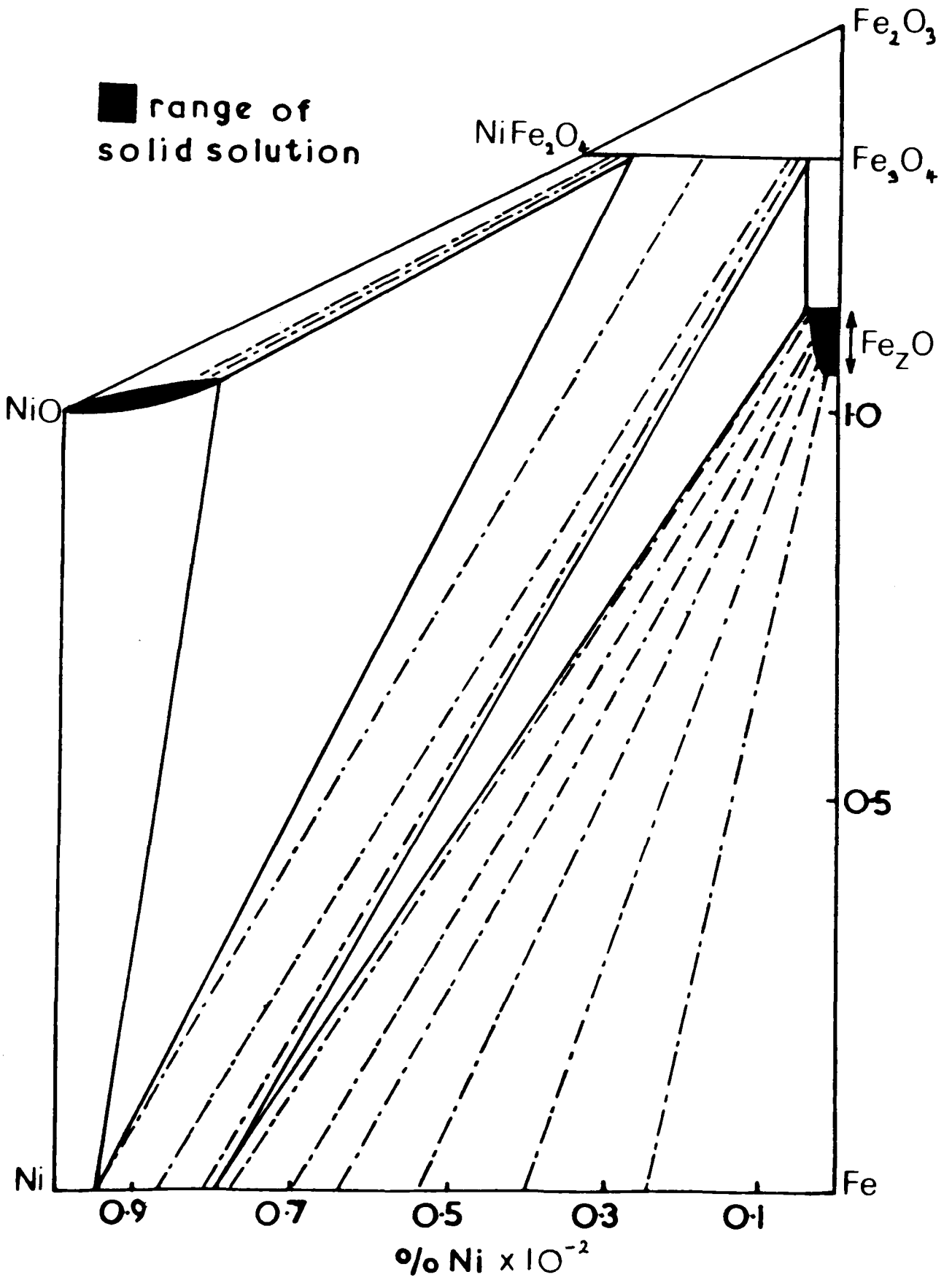



Figure 2.6 Phase Diagram for part of the Fe-Ni-O System at 1000°C.[49]

completely miscible. The composition $Ni_{0.95}Fe_{0.05}O$ has been studied by powder X-ray diffraction [69] at room temperature and, surprisingly, appears to be cubic, although nickel oxide is rhombohedral. NiO is antiferromagnetically ordered below 523 K (section 2.2.2) and the Néel temperature of the solid solution should be close to this. The exchange-strictions associated with the magnetic ordering might have been expected to be similar in both compounds.

CoO-NiO The phase diagram has been determined by Robin [70], and all the solid solutions can be prepared by sintering in air, although some phase separation may occur below 800°C [71]. The defect structure of this system has been studied at high temperatures by X-ray diffraction [72] and the results suggest that between 2 and 5 percent of cations are located on tetrahedral sites, depending on the temperature, partial pressure of oxygen and cobalt content. The lattice distortions of the magnetically ordered phases have been studied by Battle, Cheetham and Gehring [2].

## 2.2 Magnetic Ordering in Transition Metal Oxides, $MO(M^{2+} \equiv 3d^5-3d^8)$

### 2.2.1 General

The magnetic properties of the isomorphous Mott insulators (semi-conductors) MnO, $Fe_zO$, CoO and NiO can be interpreted in terms of ligand field theory (essentially localised electrons). The magnetic ordering behaviour is similar in all four oxides and is dominated by isotropic interionic superexchange between next-nearest neighbour spins. However, the details of the ordering are affected by the electronic structure of the ion involved and, in particular, the presence of an unquenched or induced orbital magnetic moment has a profound effect upon the sizes of the overall magnetic moment and the magnetocrystalline anisotropy energy (single and multiple ion). Although these oxides are considered to be

ionic, covalent mixing is important with regard to the exchange interactions, as will become evident from the subsequent discussion. Ferrous oxide is further complicated by the presence of significant amounts (10-20%) of ferric ion, and the resulting deviations from stoichiometry have a marked effect on the magnetic behaviour. Before considering the properties of the individual compounds, some features common to all four will be reviewed.

(a) Paramagnetism and Magnetic Structure MnO and its isomorphs are paramagnetic at high temperatures, and thermal energy, kT, is large compared with the interionic exchange energies. The Russell-Saunders coupling scheme is a good approximation for the first row transition metals, and the ground state of an ion can be identified with a single set of values for the quantum numbers L, S and J. Although J is not a good quantum number, it is possible to calculate some properties of such a paramagnet if it is assumed that all excited states corresponding to other combinations of L, S and J are of such high energy that they have negligible populations.

In an applied field, $H_a$, a state having total angular momentum, J, undergoes a Zeeman splitting into (2J+1) sublevels identified by the magnetic quantum numbers, $m_J$. These levels have energies

$$Em_J = -g\beta m_J H_a \quad , \quad m_J = J, J-1, \ldots, -J \tag{2.1}$$

The mean moment of a mole of ions is then given by [73]

$$M = Ng\beta JB_J(x) \tag{2.2}$$

where N is Avogadro's number, g is the Landé splitting factor, β is the Bohr magneton,

$$x = gJ\beta H_a/kT \tag{2.3}$$

and

$$B_J(x) = \frac{2J+1}{2J} \coth\left(\frac{2J+1}{2J} \cdot x\right) - \frac{1}{2J} \coth \frac{x}{2J} \qquad (2.4)$$

$B_J(x)$ is a Brillouin function. $B_J(x)$ only approaches unity in very high fields or at very low temperatures. For $x << 1$,

$$M = \frac{Ng^2 \beta^2 J(J+1) \cdot H_a}{3kT} \qquad (2.5)$$

The paramagnetic susceptibility is defined as the rate of change of magnetisation with respect to field and is therefore a measure of the response of a substance to a magnetic field. Hence,

$$\chi_m = \frac{M}{H_a} = \frac{Ng^2 \beta^2 J(J+1)}{3kT} \qquad (2.6)$$

where $\chi_m$ is the molar susceptibility. Writing the Curie constant

$$C = \frac{Ng^2 \beta^2 J(J+1)}{3k} \qquad (2.7)$$

one obtains

$$\chi_m = \frac{C}{T} \qquad (2.8)$$

which is the Curie Law. When $B_J(x) \simeq 1$, the sample becomes magnetically saturated, and the magnetic moment of an individual ion is given by

$$m = g\beta J \qquad (2.9)$$

This also gives the magnitude of the sublattice moments measured by neutron diffraction in a magnetically ordered solid (Chapter 3.2.1). Figure 2.7 shows the full Brillouin function for various values of J. Excellent agreement between theory and certain experimental data has been obtained [74].

To a first approximation, interactions between ions can be represented by the Heisenberg exchange Hamiltonian,

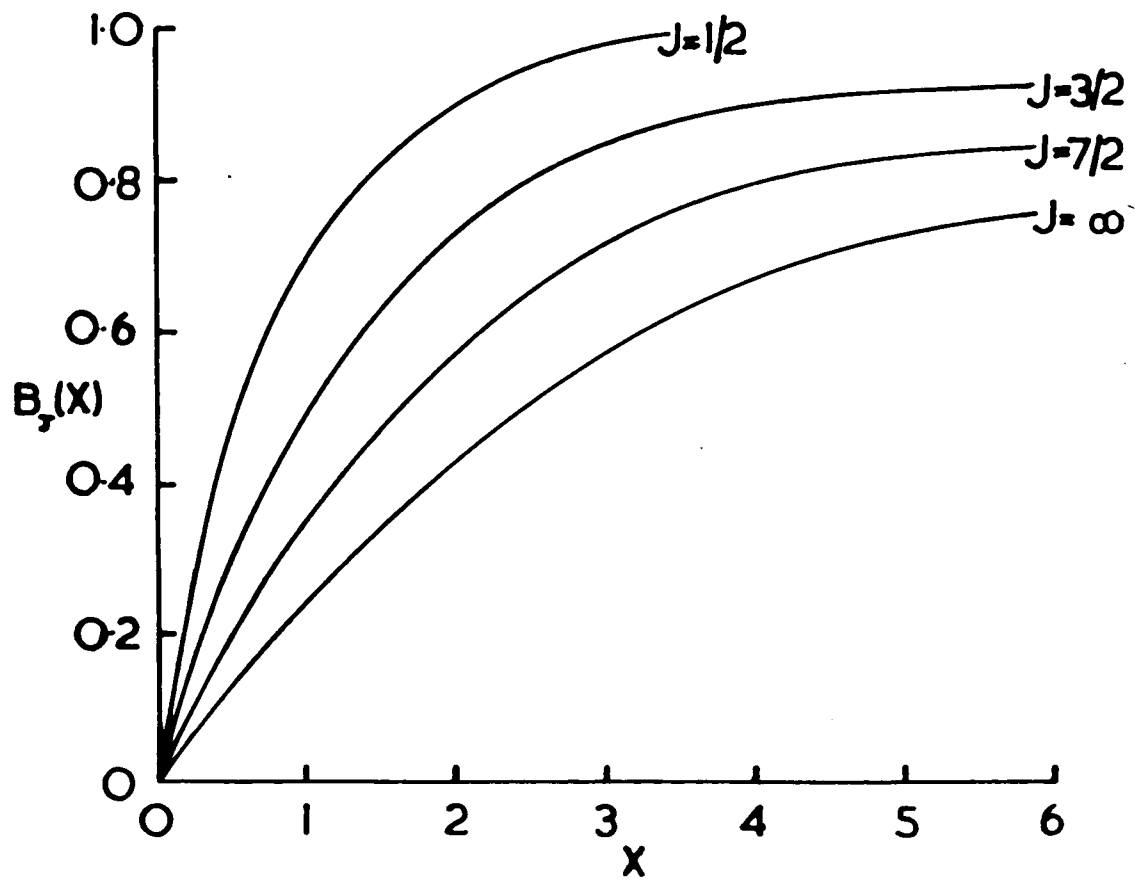



Figure 2.7 Brillouin Function ($B_J(x)$) for J = $\frac{1}{2}$, $\frac{3}{2}$, $\frac{7}{2}$, ∞.

$$\mathcal{H}_{ex} = -2\sum_{i<j} J_{ij}\, \underline{S}_i \cdot \underline{S}_j \qquad (2.10)$$

where $J_{ij}$ is the constant for exchange between the ions at i and j, and $S_i$ is the magnitude of the spin vector of ion i (Equation 2.18). The presence of interionic exchange necessitates an empirical modification of (2.8) to give the Curie-Weiss Law

$$\chi_m = \frac{C}{T-\theta} \qquad (2.11)$$

The paramagnetic Curie temperature is positive for ferromagnetic ordering, but is negative if the interionic exchange is antiferromagnetic overall. The onset of antiferromagnetism is characterised by a peak in the magnetic susceptibility or specific heat at a finite temperature, the Néel temperature ($T_N$), and in many antiferromagnets the absolute values of θ and $T_N$ are very different.

In the magnetically ordered state, each magnetic moment is acted upon by an intense internal magnetic field, or molecular field [75],

which is proportional to the magnetic moment of the surroundings. Even in zero applied field, this molecular field causes a Zeeman splitting of states with different $m_J$, and the theory given for the paramagnetic case can be used to calculate some properties of an antiferromagnet below $T_N$. The particular problem of magnetic ordering in the f.c.c. lattice, in which a given ion has twelve nearest (n.n.) and six next-nearest (n.n.n.) neighbour metal ions, has been discussed by Smart [76] using the Molecular Field Theory (MFT). In order to take into account all the interactions between near neighbours it is necessary to decompose the lattice into at least four simple cubic sublattices, and the total field acting on an ion of the $i^{th}$ sublattice is

$$H_T = H_a + \sum_{j=1}^{n} \gamma_{ij} M_j \qquad (2.12)$$

where n is the number of sublattices, $M_j$ is the magnetic moment of the $j^{th}$ sublattice and $\gamma_{ij}$ is a constant of proportionality (molecular field coefficient) for the field exerted on an ion on the $i^{th}$ sublattice by neighbours on the $j^{th}$ sublattice. $\theta$ is then found to be proportional to the sum of the $\gamma_{ij}$'s and thence to the sum of all the exchange interactions involving a given ion. However, the value of $T_N$ depends upon the particular type of ordering, which in turn depends upon the relative sizes of the $\gamma_{ij}$'s. If next-nearest neighbour exchange is most important, ordering of the second kind is observed and

$$T_N = - C\gamma_2 \qquad (2.13)$$

where $\gamma_2$ is the molecular field coefficient between n.n.n's. This is the case for the oxides MnO to NiO, and considerably simplifies the interpretation of the Néel temperatures of the pure oxides and their mixed crystals (section 2.3). Ordering of the second kind within the f.c.c. lattice is

predicted for $|\theta|/T_N < 5$; the value for MnO is close to the theoretical maximum (Table 2.2).

The simplest arrangement of sublattice moments within the above constraints has trigonal configurational symmetry [78] and is shown in Figure 2.8a. This single spin axis structure is now known to be adopted by all four oxides under consideration [79], although an alternative single

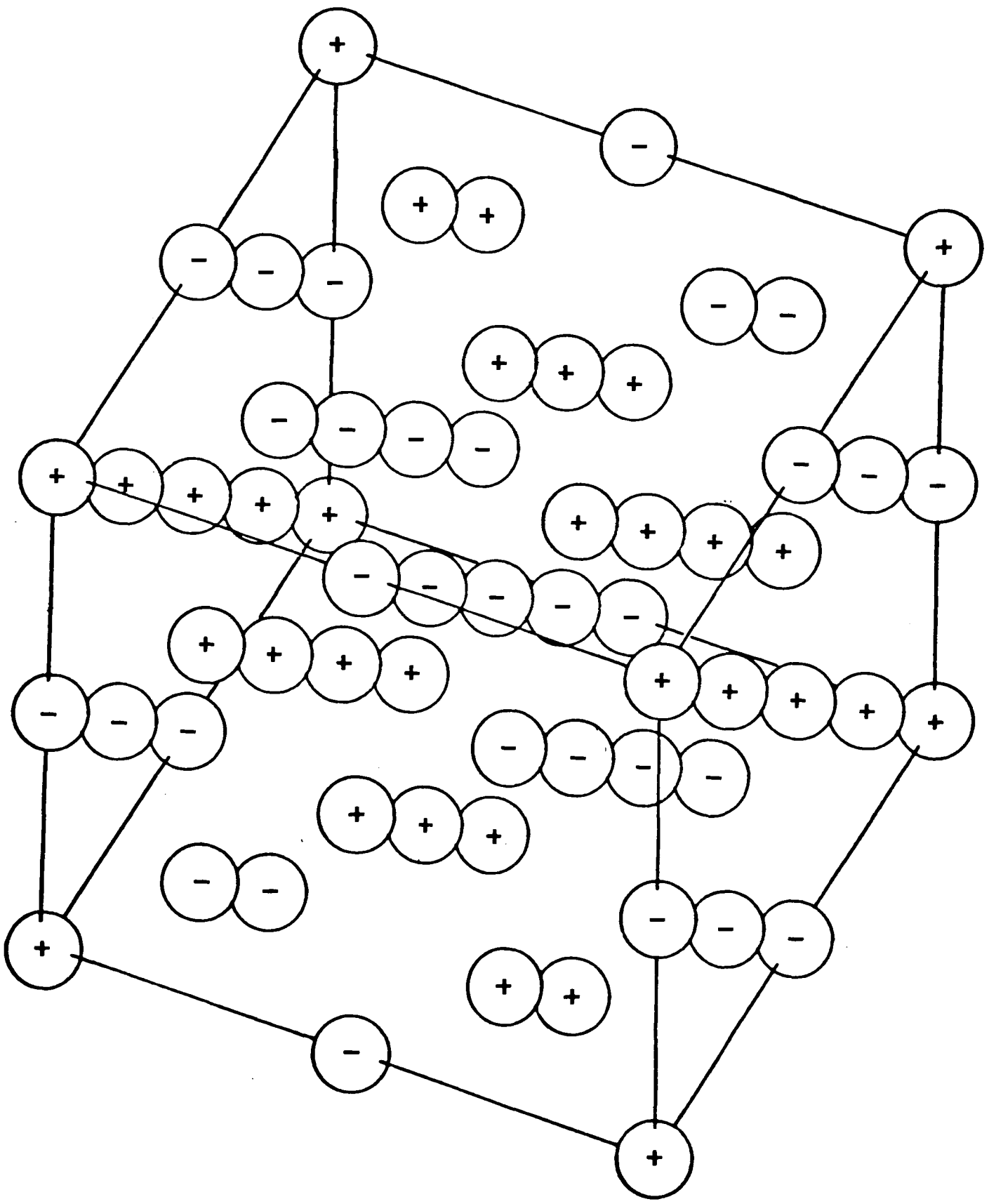


Figure 2.8a The Magnetic Structure of MnO, $Fe_zO$, CoO and NiO, after Shull and Smart [77].

spin axis structure has been suggested [80], and is shown in Figure 2.8b. Many multi-axis arrangements are also possible [79]; a number may be

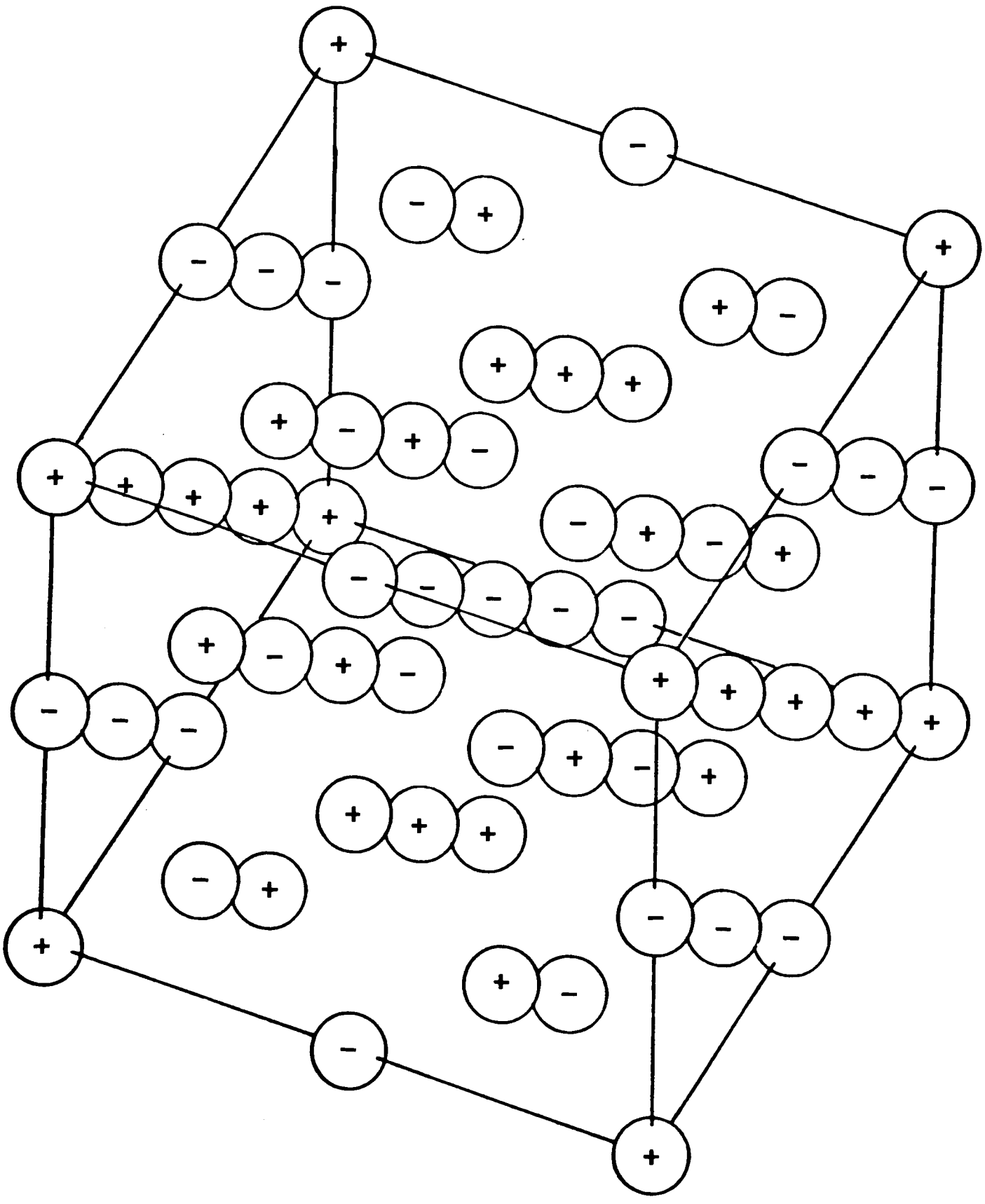


Figure 2.8b Single Axis Magnetic Structure Proposed by Li [80].

excluded on group-theoretical grounds, but it is sometimes difficult to exclude a particular multi-axis arrangement with the available experimental data, as has been the case with CoO in particular [81,82]. The arrangement of magnetic moments shown in Figure 2.8a generates complex domain structures,

the description and observation of which have been discussed by Tanner [83]. In MnO and NiO, for example, each T domain is associated with three S domains, which arise from the three symmetry-equivalent positions of the magnetic moment within the (111) plane. The domain configuration of a single crystal can be modified by the application of a magnetic field, temperature gradient or stress.

The nature of the paramagnetic-antiferromagnetic phase change in these compounds has been extensively studied. For example, the transition is thought to be second order in NiO and first order in MnO [84], becoming second order when a stress is applied along [111] [85]. The behaviour of MnO appears to be associated with the large lattice distortion.

It is possible to treat the temperature variation of the sublattice magnetisation of a ferro - or antiferromagnet in an analogous manner to the magnetisation of a paramagnet. The field acting on an ion, however, is now the sum of the applied and internal fields ($H = H_a + H_i$). As in the paramagnetic case, the reduced magnetisation of a particular sub-lattice is

$$\sigma_j = \frac{M_j}{Ng\beta J} = B_J(x) \qquad (2.14)$$

but equation (2.3) becomes

$$x = gJ\beta(H_a + H_i)/kT \qquad (2.15)$$

Since $H_i = \sum_{j=1}^{n} \gamma_{ij} M_j$ (equation (2.12)), the variable x is given by the linear function

$$x = \frac{H_a gJ\beta}{kT} + \frac{\gamma_{ij}\sigma_j Ng^2\beta^2J^2}{kT} \qquad (2.16)$$

or, in zero applied field,

$$\sigma_j = \frac{kTx}{\gamma_i N g^2 \beta^2 J^2} \qquad (2.17)$$

x now appears on both sides of (2.14) and it is necessary to solve the simultaneous equations (2.14) and (2.17) to obtain the reduced magnetisation, $\sigma_j$, at a particular value of x, as is shown in Figure 2.9. For $T > T_N$, the curves cross only at $\sigma_j = 0$, but a second intersection occurs

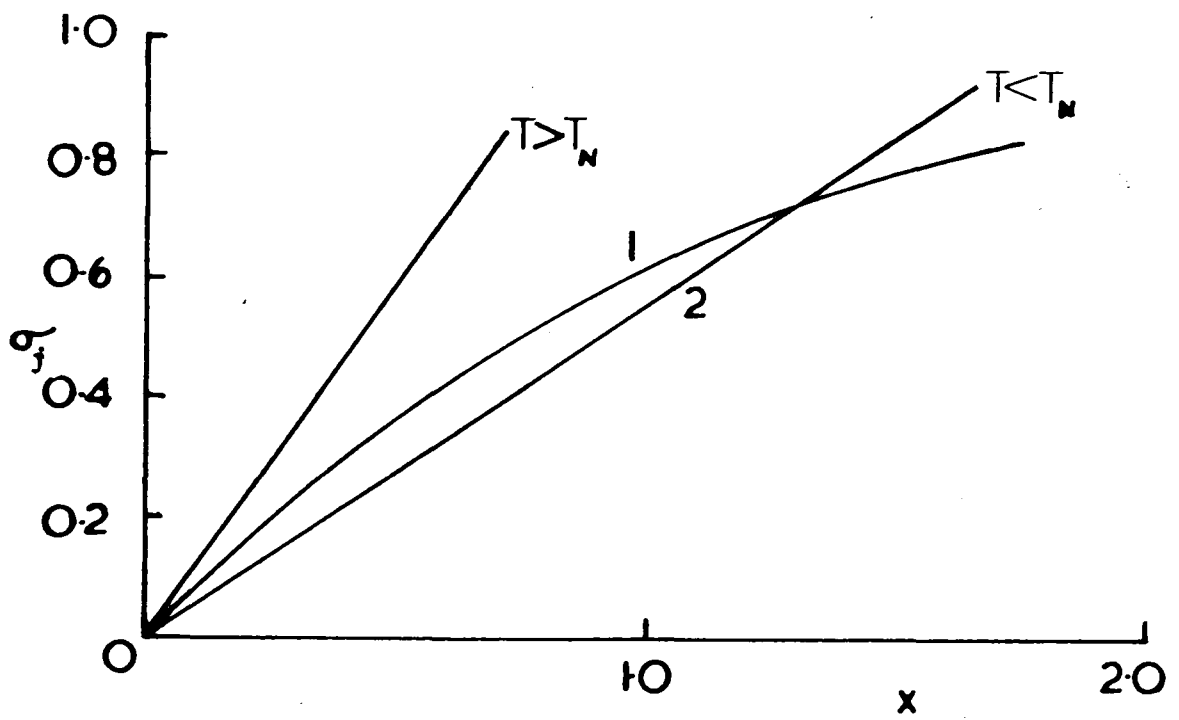



Figure 2.9 Solution of Equations 2.14 (1) and 2.17 (2) for the Spontaneous Sublattice Magnetisation of an Antiferromagnet.

for $T < T_N$, even in zero applied field.

The Néel temperature is related to the molecular field coefficients by expressions such as (2.13) and it is possible to express the reduced magnetisation, $\sigma_j$, in terms of a reduced temperature, $\tau = T/T_N$. This theoretical curve can be compared with the results of variable temperature neutron diffraction experiments, but is found to be inaccurate in the calculation of the temperature variation of the magnetisation at very low temperatures and just above the Néel temperature. These discrepancies stem from the neglect of the effects of spin waves and short range order above $T_N$ by the simple theory outlined above, and better agreement with experiment has followed from more sophisticated theories

such as the random-phase Greens function approximation [86], in which spin-waves are taken into account.

(b) Exchange. These effects arise from the stabilisations to be gained from the orientation of electron spins in certain favourable ways. In an atom, for instance, the electronic motions are most correlated, and the Coulomb repulsions minimised, if the individual spin vectors are parallel. This conforms to Hund's first rule, in which the state of highest multiplicity lies lowest in energy. On the other hand, the formation of a hydrogen molecule, $H_2$, is the result of the decrease in energy obtained by increasing the amount of negative charge between two positively charged nuclei and corresponds to a state with S = 0, because the bonding molecular orbital formed must, according to the Pauli exclusion principle, contain two electrons with spins antiparallel. Then, if the separation between the singlet (S = 0) and triplet (S = 1) is $J_{12}$, the orientation-dependent energy is

$$E_{ex} = - J_{12} (S_1 . S_2) \qquad (2.18)$$

In $H_2$, the antiparallel state has lowest energy and $J_{12}$ is negative; positive $J_{12}$ corresponds to the parallel, or ferromagnetic, alignment of spins.

These considerations can be extended to the insulating ionic crystals MnO, $Fe_zO$, CoO and NiO, in which the Heisenberg model, equation (2.10), can be used, although the exchange interactions are predominantly the results of electron transfer rather than direct electrostatic mechanisms such as the electron correlation. Despite this, the compounds have anomalous electrical conduction properties, in that band theory predicts them to have partially filled conduction bands and therefore to show metallic conductivity. The insulating behaviour arises from the strong

repulsion between electrons, but is linked to the strong exchange by the presence of a small number of electrons in the narrow conduction bands. This is accompanied by a binding of the "conduction electrons" to the corresponding holes (as in an exciton)[87] and the finite width of the conduction band corresponds to the "virtual" electron exchange. This often gives rise to an antiferromagnetic exchange stabilisation, and Anderson [88] named the process "superexchange", in contrast to interionic direct exchange, which is always ferromagnetic for orthogonal orbitals. However, superexchange is sometimes ferromagnetic, and the ideas of Anderson were expanded by Goodenough [89] and Kanamori [90], who formulated a set of semi-empirical rules for the sign of $J_{ij}^{SE}$ between two orbitals. Briefly, these are as follows:-

(i) overlap of two half-filled orbitals: this is always anti-ferromagnetic because any orbital can contain only one electron of a certain spin (Pauli exclusion principle). The transferred electron, which does not change spin during the exchange, then must be aligned antiparallel to the spin of the accepting orbital.

(ii) overlap of a half-filled and an empty orbital (on an ion which has net spin): the virtual electron exchange here does not depend on the sign of the electron spin, but the intraatomic exchange of the ion to which the electron is transferred will be a maximum if the spin of the electron is parallel to that of the receiving ion. The effect is then ferromagnetic, but is one degree higher a perturbation than (i) (as is (iii)).

(iii) overlap of a half-filled and a full orbital (on an ion having net spin): the transfer can only occur from the ion having the

full orbital (A) and the electron spin must be antiparallel to that of the receiving orbital on B. The intraatomic exchange of A is a maximum if the transferred electron is antiparallel to the overall spin; the relative orientation of the spins A and B is therefore ferromagnetic.

According to Goodenough [91], there are three important superexchange mechanisms in the rocksalt structure, (a) 180° cation-anion-cation, (b) 90° cation-anion-cation and (c) cation- -cation*. Of these, (a) is the largest and acts through the $e_g$ orbitals of the cations concerned, linking next nearest neighbours along a cell edge. In MnO, $Fe_zO$, CoO and NiO, the 180° superexchange is always antiferromagnetic because the $e_g$ orbitals are never more than half full, and the interaction is smallest for the most ionic material, as reflected by the increase in $T_N$ from MnO to NiO. The couplings (b) and (c) involve nearest neighbours and in many cases it is difficult to separate all the possible contributions. The first and second nearest neighbour exchange constants in the rocksalt structure, $J_1$ and $J_2$ can be obtained by fitting theoretical expressions derived from the Heisenberg hamiltonian to the magnon energies measured in inelastic neutron [92,93] and photon [94,95] scattering experiments. The

---

* The cation-anion-cation couplings are further classified into those involving correlation and delocalisation superexchange. The correlation effect results in simultaneous covalent bond formation on either side of the anion, while delocalisation superexchange arises from a drift of electrons from one cation to another through the anion (as in the original Anderson [88] formulation).

values obtained in this way seem to be more reliable than those calculated from θ and $T_N$ using MFT.

Although the rhombohedral distortion of NiO at low temperatures was originally attributed to a mismatch of the ionic sizes of $Ni^{2+}$ and $O^{2-}$ in their interlocking lattices, this deformation and that of MnO are now believed to arise from the dependence of the n.n. exchange constants on interionic separation. Similar effects may occur in $Fe_zO$ and CoO, but are negligible compared to the magnetostrictive distortions (section (c)). The volumestrictions observed in these oxides below $T_N$ (Table 2.2) result from an analogous effect involving the n.n.n. exchange. The contractions along [111] observed in MnO and NiO can be explained if both the intra- (111) layer and inter - (111) layer exchanges are antiferromagnetic, leading to an attraction between n.n. ions in adjacent planes and a repulsion between ions in the same plane. The equilibrium distortion is reached when the exchange forces are balanced by the elastic restoring forces, and the size of the deformation has been shown to vary approximately as the square of the sublattice magnetisation, disappearing above the Néel temperature [98,99].

The trigonal distortions of NiO and MnO do not depend upon the directions of the magnetic moments, only on the symmetry of the spin arrangement, and these compounds are said to undergo exchangestrictive distortions, as opposed to the magnetostrictions which cause the lowering of symmetry in CoO and $Fe_zO$ below $T_N$. The latter deformations depend upon the directions of the magnetic moments.

(c) Electronic Structures The electrons in MnO, $Fe_zO$, CoO and NiO are effectively confined to atomic orbitals and a description of the electronic structure of a cation in the solid can be developed from that of the free ion. Moreover, for light elements, electronic repulsion is

appreciable, the separation of free ion terms is larger than the crystal field splittings of those terms and the weak field limit of crystal field theory is applicable. When considering magnetic properties, one is chiefly concerned with the ground states of the ions involved; Table 2.1 sets out the electron configurations and ground states of some iron group ions under both free ion and weak crystal field conditions. Ferric ion is included because it is a minor, but important, constituent of ferrous oxide.

Although L and J are not good quantum numbers in the presence of a crystal field, they are used as a guide in Table 2.1. While the orbital contribution of $Ni^{2+}$ is quenched when it is located in an octahedral interstice, $Mn^{2+}$ has no orbital moment even in the free ion, and undergoes no crystal field stabilisation. However, $Co^{2+}$ and $Fe^{2+}$ have degenerate, partially filled $t_{2g}$ orbitals in octahedral symmetry which preserve an orbital contribution. A pictorial representation of this is the ability to transform the orbitals into one another by rotation about any principal axis, giving rise to three-fold orbital degeneracy. A quantum mechanical derivation of the behaviour of the corresponding T terms has been given by Mabbs and Machin [100]. In $Fe^{2+}$ and $Co^{2+}$, the J levels resulting from spin-orbit coupling are obtained by considering the T terms to carry azimuthal quantum numbers $M_L = 0, \pm 1$, and the levels having smallest J are lowest in energy because $Co^{2+}$ and $Fe^{2+}$ have more than half-filled d-shells [101].

In the crystal, further stabilisation can be obtained by a spontaneous, co-operative crystallographic distortion, as in $Mn_3O_4$ or $CuCr_2O_4$ [102]. These effects are manifestations of the Jahn-Teller theorem [103], which states that when the ground state of a molecule is degenerate in circumstances of high symmetry, the molecule will generally distort so as to

| ION | FREE ION | | CUBIC CRYSTAL FIELD | | | AXIAL CRYSTAL FIELD | |
|---|---|---|---|---|---|---|---|
| | Valence Shell Configuration | Ground Term | High-Spin Configuration | Ground Term | J = L + S | Tetragonal | Trigonal |
| $Mn^{2+}$, $Fe^{3+}$ | $d^5$ | $^6S$ | $t_{2g}^3 e_g^2$ | $^6A_{1g}$ | $\frac{5}{2}$ (L = 0) | $^6A_{1g}$ | $^6A_{1g}$ |
| $Fe^{2+}$ | $d^6$ | $^5D$ | $t_{2g}^4 e_g^2$ | $^5T_{2g}$ | 1 | $^5B_{2g} + {}^5E_g$ | $^5A_{1g} + {}^5E_g$ |
| $Co^{2+}$ | $d^7$ | $^4F$ | $t_{2g}^5 e_g^2$ | $^4T_{1g}$ | $\frac{1}{2}$ | $^4A_{2g} + {}^4E_g$ | $^4A_{2g} + {}^4E_g$ |
| $Ni^{2+}$ | $d^8$ | $^3F$ | $t_{2g}^6 e_g^2$ | $^3A_{2g}$ | 1 (L = 0) | $^3B_{1g}$ | $^3A_{2g}$ |

TABLE 2.1 The Electronic Structures of Some Iron-Group Ions[104]

relieve the orbital degeneracy. $Mn_3O_4$ and $CuCr_2O_4$ contain $Mn^{3+}$ and $Cu^{2+}$ in $^5E$ and $^2T$ states respectively; E states undergo large Jahn-Teller stabilisations which are much greater, in general, than those of T states. At high temperatures the distorted structure is less stable than the high-symmetry one because of the effect of electronic entropy.

Table 2.1 and Figure 2.10 show the effect of a uniaxial distortion from cubic symmetry on the T states of octahedral high-spin $Fe^{2+}$ and $Co^{2+}$. In the absence of other perturbations the static Jahn-Teller distortion leading to the stabilisation of an orbital singlet is more favourable because of conservation of the centre of gravity of the manifold of levels (Figure 2.10). However, Kanamori [102] has identified a mechanism giving rise to inversion of the order of levels, which depends upon the presence of an ordered, collinear arrangement of magnetic moments, and therefore upon the presence of a molecular field, $H_i$. Spin-orbit coupling is present in the E state arising from a uniaxial distortion, and $H_i$ may cause sufficient Zeeman splitting of the resultant J levels to stabilise this state. The ordering of magnetic moments results in an anisotropic electronic distribution around each ion, and the interstices must co-operatively distort until a balance with the elastic forces of the crystal is achieved. The co-operative Jahn-Teller (J.T.) and spin-orbit (S.O.) distortions are mutually exclusive and occur in opposite senses. If $T_c$ is the magnetic ordering temperature and $T_t$ the transition temperature to the lower symmetry, $T_t > T_c$ for the J.T. distortion and $T_t \sim T_c$ for the S.O. effect. The latter deformation is termed a magnetostriction, since the direction of distortion is linked to that of the magnetic moment (or spin) vector through the spin-orbit coupling. The magnetostriction also is the source of a deformation-dependent single-ion anisotropy energy (to be discussed in section 2.2.1 (d)).

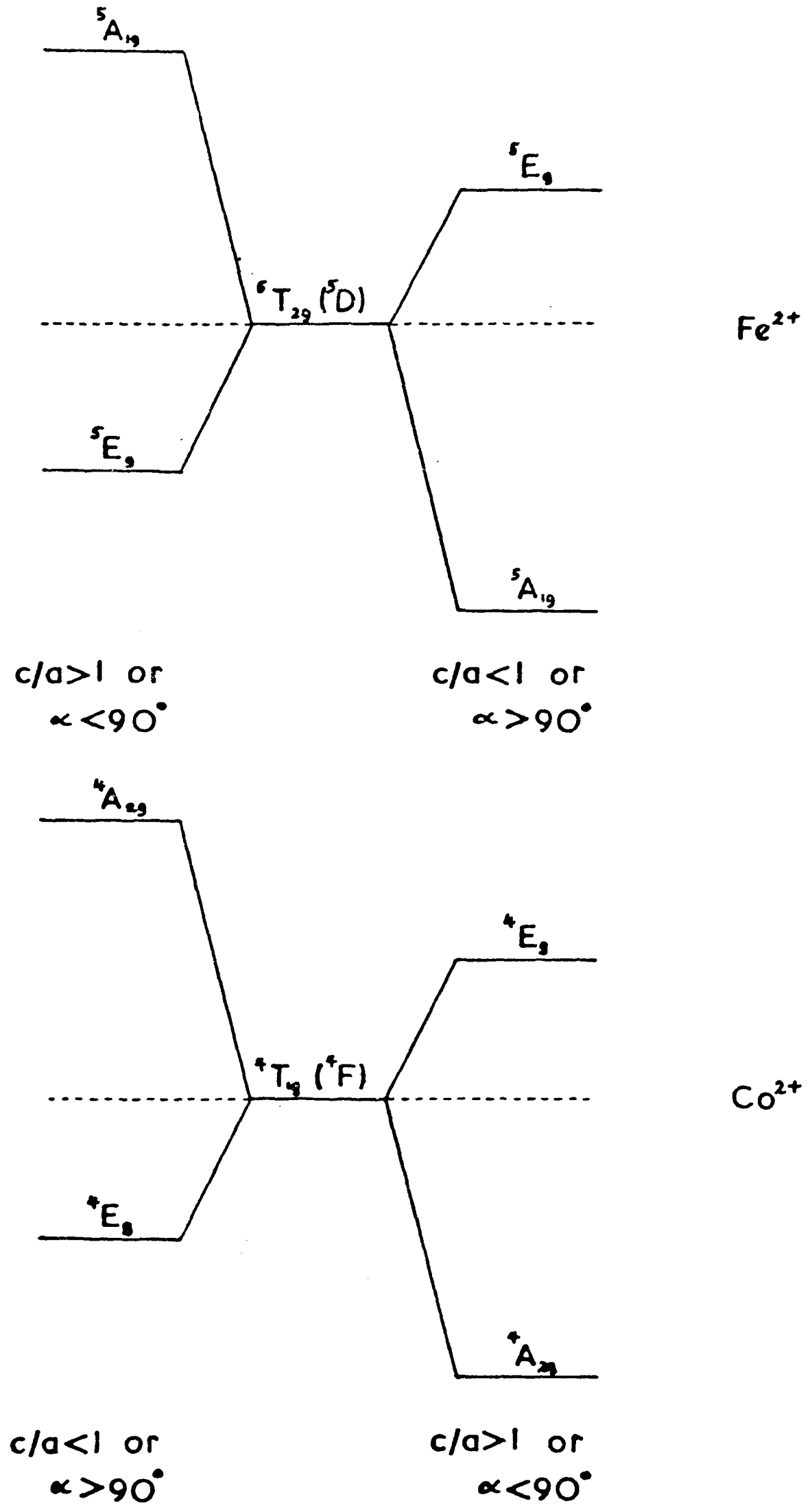



Figure 2.10 Schematic crystal-field terms for uniaxially distorted octahedral high-spin $Fe^{2+}$ and $Co^{2+}$, neglecting the influences of spin-orbit coupling and the molecular field (after ref. 104).

Although the above discussion of electronic structures has been within the framework of localised electrons, the discussion of exchange has suggested that these compounds can be considered in the context of band theory, especially from the tight-binding viewpoint. The band structures thereby obtained have been discussed by Mattheis [105], Skriver et al [106] and Brandow [107].

(d) Magnetic Anisotropy The anisotropy of an antiferromagnet having the magnetic structure shown in Figure 2.8a can be expressed in terms of a free energy, $E_a$, which is a function of the direction cosines $\alpha_1$, $\alpha_2$ and $\alpha_3$ of the sublattice magnetisation, M, with respect to the crystallographic axes. This energy has two contributing terms, one arising from the essentially cubic crystallographic symmetry, and the other resulting from the trigonal symmetry of the moment arrangement. To a first approximation,

$$E_a = K(\alpha_1^2\,\alpha_2^2 + \alpha_2^2\,\alpha_3^2 + \alpha_3^2\,\alpha_1^2) + T(\alpha_1\alpha_2 + \alpha_2\alpha_3 + \alpha_3\alpha_1) \qquad (2.19)$$

The many possible causes of anisotropy in the first row transition metal monoxides have been discussed by Kanamori [108]. Different possible easy axes correspond to the alternative signs of the anisotropy constants K and T: positive K favours {001}, negative K {111}, positive T a direction within a (111) plane and negative T [111]. The number of different sources of anisotropy is determined by whether an orbital magnetic moment is present or not. The anisotropy arising from the magnetostrictions of $Fe_zO$ and CoO was noted in section 2.2.1(c), and other anisotropic effects occur through the exchange and orbital multipole interactions because spin-orbit coupling can link the direction of spin to the shape of the electronic charge clouds. Anisotropic effects due to an induced orbital moment are of secondary inportance in NiO and very

small in MnO, the largest contribution arising from magnetic dipole forces.

Figure 2.11 shows the easy directions of the four oxides, and some other magnetic and structural parameters for these compounds are set out in Table 2.2. Some anisotropy constants for NiO and MnO appear in the table, but none are shown for $Fe_zO$ and CoO because of the large number of contributions.

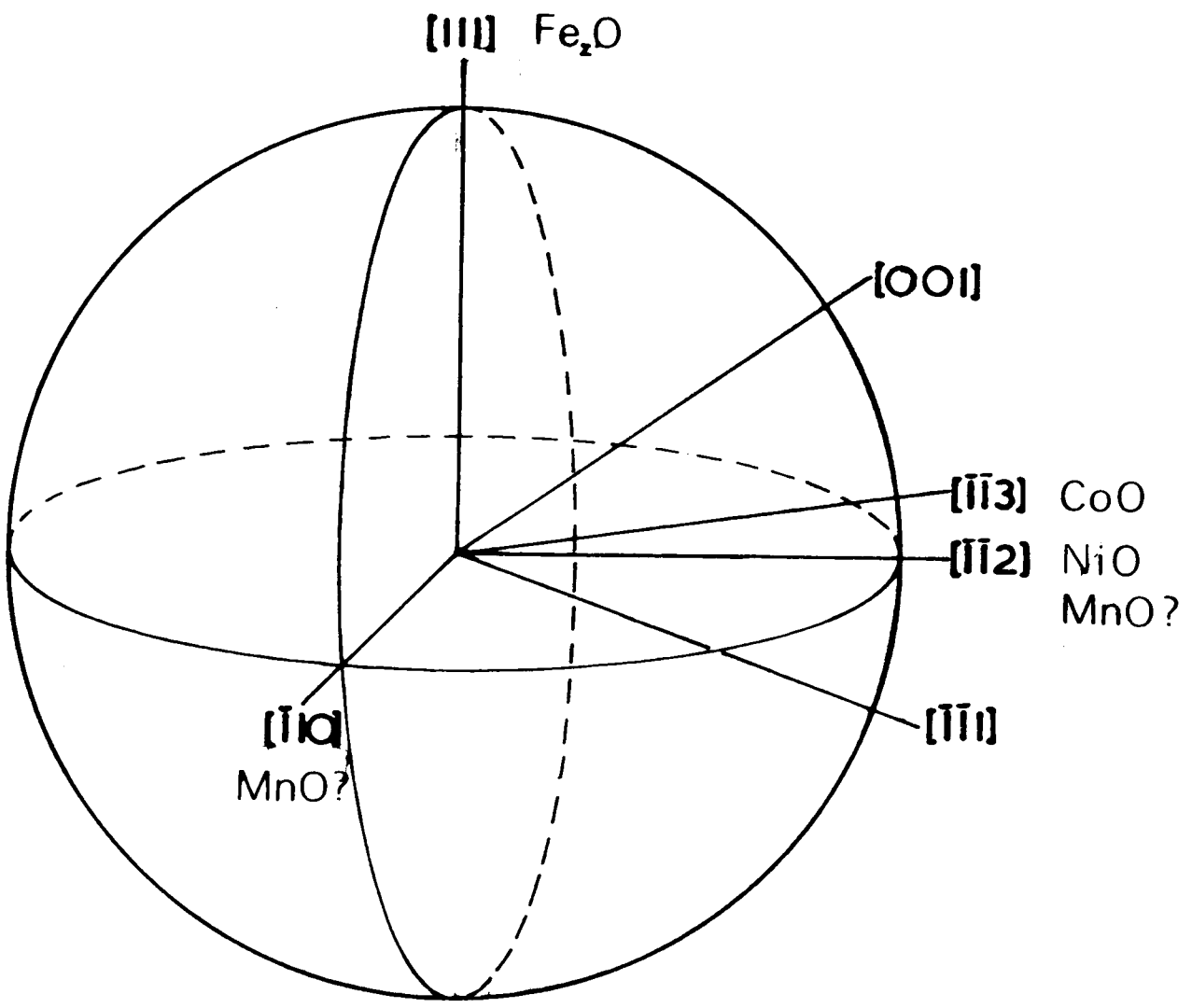



Figure 2.11 Some Important Directions in Antiferromagnetic Oxides with the Rocksalt Structure.

## 2.2.2 Manganous and Nickel Oxides

The $|\theta|/T_N$ ratios of MnO and NiO (Table 2.2) suggest that antiferromagnetic n.n. interactions are dominant in both oxides. In MnO, a value of $|\theta|/T_N = 5.2$ is close to the theoretical maximum and reflects the comparable magnitudes of $J_1$ and $J_2$. Here, all interactions are between

| COMPOUND | $T_N$(K) | θ(K) | $\lvert\theta\rvert/T_N$ | $J_1$(K) | $J_2$(K) | MOMENT DIRECTION |
|---|---|---|---|---|---|---|
| MnO | 118 (exp)[109] | - 610 [76] | 5.2 | - 8.4 (exp)[93]<br>-10 (calc)[119] | - 9.8 (exp)[93]<br>-11 (calc)[119] | ? [122,123] |
| NiO | 523 (exp)[110,111]<br>532 (calc) [112] | -1310 [76]<br>-2000[117] | ~ 3.0 | +16 (exp)[120] | -221 (exp)[120] | $[\bar{1}\bar{1}2]$ [124,125,126] |
| $Fe_zO$ | 179-209[54,113,114] | - 57 [114,118]<br>- 136 | ~0.7 | + 4.2(exp)[121] | - 9.4(exp)[121] | [111 ][127] |
| CoO | 287-292[110,115, 116] | - 330 [76] | ~1.1 | - 1.0(exp)[92] | - 16.8(exp)[92] | $[\bar{1}\bar{1}3]$ [81] |

TABLE 2.2 Some Magnetic and Structural Parameters of MnO, $Fe_zO$, CoO and NiO. Values for Exchange and Anisotropy Constants, and Lattice Parameters refer to 5K unless stated.

| COMPOUND | CELL PARAMETERS | $T_1$(erg.cm$^{-3}$) | $T_2$(erg.cm$^{-3}$) | $\delta a/a$* | $\delta \ell/\ell$+ |
|---|---|---|---|---|---|
| MnO | a=b=c= 4.432 Å [98]<br>α=β=γ=90.62° | $1.6 \times 10^7$(calc)[129,130]<br>$3.8 \times 10^6$ (exp)[131] | $2.2 \times 10^{-5}$(calc)[123]<br>$3 \times 10^4$ (exp) [130]<br>$2.8 \times 10^2$ (exp) [133] | $1.1 \times 10^{-3}$ [135] | $-4 \times 10^{-6}$(est) [136] |
| NiO | a=b=c= 4.173 Å [128]<br>α=β=γ=90.1° | $3.3 \times 10^6$(calc)[132]<br>$1.0 \times 10^6$(exp) [131] | $5.1 \times 10^2$ [134]<br>(exp, 288K) | $1.5 \times 10^{-3}$ [135] | $-5.4 \times 10^{-4}$<br>(exp, 293K) [125] |
| $Fe_zO$ | a=b=c= 4.301,4.291 Å [3]<br>α=β=γ=89.54,89.84°<br>(z = 0.943, 0.929) | | | | |
| CoO | a=b=4.260, c=4.210 Å [82]<br>α=β=γ= 89.98° | | | | |

TABLE 2.2 (Contd) * Isotropic volume contraction, + Orthorhombic Magnetostriction.

half-filled orbitals and are antiferromagnetic, the cation--cation exchange is large and is responsible for the appreciable exchangestriction.

Any cation--cation interactions in NiO are precluded by the presence of filled $t_{2g}$ orbitals, but a number of competing $90^{o}$ cation-anion-cation mechanisms can be visualised, the resultant of which is difficult to predict. These are:- [91]

(i) cation ($e_g$) $\underline{\quad\sigma\quad}$ anion (s) $\underline{\quad\sigma\quad}$ cation ($e_g$); (delocalisation s.e.); antiferromagnetic

(ii) cation ($e_g$) $\underline{\quad\sigma\quad}$ anion(2s's) $\underline{\quad\sigma\quad}$ cation ($e_g$); (correlation s.e.); antiferromagnetic

(iii) cation ($e_g$) $\underline{\quad\sigma\quad}$ anion (p) $\underline{\quad\pi\quad}$ cation ($t_{2g}$);(correlation s.e.); ferromagnetic

(iv) cation ($e_g$) $\underline{\quad\sigma\quad}$ anion(2p's) $\underline{\quad\sigma\quad}$ cation ($e_g$); (correlation s.e.); ferromagnetic

The greek symbols refer to the type of overlap between metal and ligand orbitals. (iv) is ferromagnetic because the $e_g$ orbitals interact through orthogonal anion orbitals, and the oxide intraatomic exchange is a maximum if the spins in each orbital are parallel.

The $\alpha > 90^{o}$ exchangestriction and $|\theta|/T_N$ value of NiO ($\sim 3.0$) are incompatible with the experimental, ferromagnetic exchange constant [120] (Table 2.2); the positive $J_1$ suggests that superexchange through the p orbitals of the oxygen is more important than that through the s, which might be expected from the smaller radial extent of the s orbitals. The exchangestriction may be the result of a greater sensitivity of the antiferromagnetic exchanges to interionic distance since an $\alpha > 90^{o}$ rhombohedral distortion increases the antiferromagnetic components, as has been pointed out by Goodenough [137]. Motida [138] has discussed the n.n. exchange in NiO and compared it to that in $NiTeO_3$, but a satisfactory explanation

to the above paradox has not been reached.

The variation of sublattice magnetisation with temperature in both MnO and NiO has been accounted for by the Greens function approximation using the ratio $J_2/J_1 = 1.5$ in both cases[99,119]. Although this ratio is compatible with experiment in the case of MnO (Table 2.2), it appears unreasonable for NiO ($J_2/J_1 \simeq 14$), and must again reflect the lack of understanding of the nearest neighbour exchange in NiO.

The occurrence of appreciable diffuse scattering around the magnetic powder diffraction peaks in MnO, even at 4.2K, has been noted by Roth [139], and by Blech and Averbach [140]. These workers have attributed this behaviour to inelastic scattering or to the persistence of antiphase domains down to the lowest temperatures. The same may be true in NiO, but will be less obvious because of the much smaller magnetic moment of $Ni^{2+}$.

The anisotropies of MnO and NiO are dominated by magnetic dipole forces because the ground states of $Mn^{2+}$ and $Ni^{2+}$ in octahedral co-ordination are $^6A_{1g}$ and $^3A_{2g}$, derived from the free-ion $^6S$ and $^3F$ states respectively (Table 2.1). For $Mn^{2+}$ in MnO, no orbital contribution is present and high order perturbations involving simultaneously the crystal field and spin orbit coupling are thought necessary to split the free ion S state. The ground state splittings both in the free ion and the crystal are then very small, which is confirmed by the g-factor of $Mn^{2+}$ in an f.c.c. oxide matrix, 2.0014 [141]. The classical many-ion dipolar energy has the form [108]

$$E_{do} = T_1 (\alpha\beta + \beta\gamma + \alpha\gamma) \qquad (2.20)$$

where $E_{do}$ is the out-of-(111) plane anisotropy energy, $T_1$ is the corresponding anisotropy constant and $\alpha$, $\beta$ and $\gamma$ are the direction

cosines with respect to the cube axes. Kaplan [129] and others [130] have shown that the anisotropy energy, $E_{do}$, favours any direction within the (111) plane of the f.c.c. cell. The experimental and calculated values of $T_1$ for MnO are given in Table 2.2 and are of a similar order of magnitude.

The anisotropy energy within the (111) plane is believed to be much smaller and again in MnO probably stems from the dipolar interactions. This energy has the angular dependence [130]

$$E_{di} = -\frac{1}{2} T_2 \cos 6\eta \qquad (2.21)$$

where $E_{di}$ is the in-plane anisotropy energy, $T_2$ is the in-plane anisotropy constant and $\eta$ is the angle between the spin axis and the easy axis. The easy direction and magnitude of $T_2$ in MnO are a matter of some dispute and the problem of determining the easy axis has proved intractable. From the field dependence of the powder susceptibility, Keffer and O'Sullivan [130] and Bloch et al [142] calculate $T_2 = 3 \times 10^4$ and $9 \times 10^3$ erg. $cm^{-3}$ respectively, while a recent, accurate single crystal study[133] gives a value of $2.8 \times 10^2$ erg. $cm^{-3}$. These results compare with a theoretical estimate of $2.2 \times 10^{-5}$ erg. $cm^{-3}$ by Bidaux et al [123], who also find that the easy direction is close to $[\bar{1}\bar{1}2]$. This is in contrast with their earlier work [122], in which they settle for the direction at $90^o$ to $[\bar{1}\bar{1}2]$, $[\bar{1}10]$; Figure 2.11 shows both these directions.

Associated with the in-plane anisotropy of MnO is a very small magnetostriction which leads to monoclinic or orthorhombic symmetry [132] since the spins are confined to directions within, or very close to, the (111) plane. The magnetostriction of MnO has been attributed both to magnetoelastic coupling through the dipolar interactions [130] and to a single ion crystal field effect [136], but is very small and has not been

observed experimentally.

Similar considerations to the above also apply to NiO, although the orbital moment is now capable of contributing to the magnetic moment as a second order perturbation, and through the spin-orbit coupling further sources of anisotropy and a much larger magnetostriction are introduced. Covalency is also especially important in NiO (cf. the appreciable superexchange) and anisotropy may arise through spin-orbit coupling in the non-ionic configurations. Consequently, an anisotropic and enlarged g-factor, 2.227, is observed [141]. However, all these orbit-induced effects are small in comparison with the first order perturbation energy of the magnetic dipolar interaction, given by equation (2.20).

Four mechanisms capable of choosing the easy axis within the (111) plane of NiO have been introduced by Yamada [132] and discussed by Kanamori [108]. These are (i) magnetic dipole interaction, (ii) pseudo-dipolar interaction between [100] neighbour spins, (iii) anisotropic exchange interaction between [110] neighbour spins and (iv) crystalline field acting on each ion. Each interaction has a magnetostriction associated with it, and observations of the overall distortion have clearly demonstrated that the easy axis of NiO is $[\bar{1}\bar{1}2]$ (Table 2.2). Theoretically, either $[\bar{1}10]$ or $[\bar{1}\bar{1}2]$ are possible, and for $[\bar{1}\bar{1}2]$ a small deviation from the (111) plane may occur owing to a cubic anisotropy energy.

### 2.2.3 Cobaltous Oxide

It has been suggested [143] that the overlap between the $t_{2g}$ orbitals of $Co^{2+}$ and $Fe^{2+}$ in their respective oxides is much smaller than that in MnO, and any related exchangestriction is expected to be much smaller in the former compounds. In CoO, the majority of cation-cation interactions are between full and half-full orbitals, giving rise to

ferromagnetic coupling and an $\alpha < 90^{o}$ exchangestriction. However it is possible that these exchanges are comparable in magnitude to the $90^{o}$ cation-anion-cation couplings discussed previously for NiO, and the sign of the overall n.n. exchange constant is unclear. The experimental values of $|\theta|/T_N$ and $J_1$ (Table 2.2) suggest that the antiferromagnetic exchange is slightly more powerful, although an $\alpha < 90^{o}$ exchangestriction is observed [82].

According to the considerations set out in section 2.2.1(c), the large tetragonal contraction of CoO below $T_N$ should be accompanied by an alignment of the sublattice magnetisation parallel to the unique axis. However, a number of independent experiments[2,79,81,144,145] demonstrate that the magnetic moment is inclined at an angle of $\sim 27^{o}$ to the c axis, i.e. approximately parallel to $[\bar{1}\bar{1}3]$ (Figure 2.11) and only $8^{o}$ out of the (111) plane. In the context of the collinear magnetic structure known to be adopted by MnO, $Fe_zO$ and NiO (Figure 2.8a) this is surprising because it requires a ratio of anisotropy constants $T/K = 1.37$ with $K > 0$, $T > 0$ (Equation 2.19). Calculations[146,147] suggest that a large proportion of K arises from the magnetoelastic coupling and show that this stabilisation is much greater than the contribution to T from the dipole-dipole forces. As a solution to the problem, Van Laar [81] proposed an alternative multi-axis magnetic structure of tetragonal symmetry which models the observed powder and multi-domain magnetic neutron Bragg peaks equally well. This arrangement finds support in the work of Khan and Erickson [144] and Bertaut[148], but other measurements favour the collinear structure. For example, the X-ray data of Saito et al [82] shows a peak splitting characteristic of a small exchangestrictive rhombohedral distortion which, as discussed in section 2.2.1(b), is only compatible with the MnO-like

magnetic structure. Direct observation of a magnetic structure is only possible by neutron techniques, however, and the two models have been distinguished by applying a uniaxial stress to a single crystal during data collection, so as to modify the domain structure [79]. The marked changes in scattering observed are only compatible with the collinear model.

An explanation for the large deviation of the magnetic moment from the tetragonal axis, which also supports the collinear model, has been obtained [149] by considering an anisotropic exchange mechanism omitted from the original [146] treatment of the anisotropy energies of CoO. The calculations suggest that orbital dependent, anisotropic cation-cation superexchange between nearest neighbours introduces a cubic anisotropy energy of negative sign which favours the directions {111} and causes the sublattice magnetisation to rotate away from the c axis. Unfortunately, this treatment does not explain the lack of any magneto-striction associated with the unusual direction of the magnetic moment vector. The analogous distortion in NiO is caused by the second order contribution, and has been observed in careful measurements on single crystals (section 2.2.2).

Usual considerations of the electronic structure of CoO assume that the maximum spin-orbit coupling occurs in the ground state and, because $Co^{2+}$ has a more than half-filled valence shell, the spin and orbital angular momenta are parallel. Mixing of higher J states then causes a precession of $\underline{L}$ and $\underline{S}$, and hence $\underline{J}$, around the axis of quantisation. However, Okada and Yasuoka [150] point out that the orbital and spin momenta need not be parallel when the spin moment deviates from a high-symmetry axis, as is the case in antiferromagnetic CoO. This is confirmed by their n.m.r. results, showing that the hyperfine field,

which is mainly composed of orbital and Fermi contact terms, is $21.1 \pm 0.5^{o}$ from [001]. Since the contact term is associated with the spin vector, they deduce that the orbital and spin vectors are non-collinear with the orbital moment $22.8^{o}$ from the c axis.

The magnetic behaviour of CoO may be further complicated by the effects of non-stoichiometry. While magnetic susceptibility measurements [151] on $Co_zO$ with different values of z show that the Néel temperatures are approximately the same, a sample with z = 0.99 demonstrates an increase in susceptibility below 100K. Since the likely impurity $Co_3O_4$, is antiferromagnetic, this behaviour is attributed to the uncompensated moments of $Co^{3+}$ ions adjacent to vacancies.

### 2.2.4 Ferrous Oxide

Neutron diffraction experiments [3,127,139] have demonstrated that the magnetic moment vector in ordered $Fe_zO$ is parallel to a three-fold axis of the rocksalt cell. This configuration is consistent with the retention of an orbital magnetic moment, and with the observed trigonal magnetostrictive distortion, but it also maximises the dipole-dipole energy. The many other sources of anisotropy associated with the ferrous ion have been discussed by Kanamori [146], who relates the observed easy axis to a combination of anisotropy energies associated with orbital multipole and anisotropic exchange interactions, rather than the magnetoelastic coupling energy. The calculations suggest that the latter term should favour the [001] moment direction, and emphasise the theoretical difficulty of attempts to distinguish between the alternative trigonal ($\alpha < 90^{o}$) and tetragonal ($c/a > 1$) distortions (Figure 2.10), either of which preserve an orbital moment.

A further ambiguity arises when the Goodenough-Kanamori rules are

applied to ferrous oxide [104], since the magnetostriction and exchange-striction may be mutually dependent by virtue of their identical symmetries. For instance, in the limit of a large trigonal ($\alpha < 90^{o}$) distortion the relatively large splitting of the $t_{2g}$ orbitals promotes ferromagnetic cation-cation couplings within a (111) plane, rather than the antiferromagnetic exchange predicted for $\alpha = 90^{o}$. The distorted state is thereby stabilised, and these conclusions are supported by the values of $|\theta|/T_N$ and $J_1$ shown in Table 2.2. Koch and Fine [114] previously attributed the value of $|\theta|/T_N$ to double exchange [152] between $Fe^{2+}$ and $Fe^{3+}$, but the Mössbauer spectra [24] give no indication of fast electron hopping between these ions.

The important influence of the defects associated with the non-stoichiometry on the magnetic properties of ferrous oxide was first recognised by Roth [34], who related the unexpectedly small magnetic neutron Bragg peaks to paramagnetic regions in the vicinity of defect clusters. However, this picture does not explain a number of observations, the most noteworthy of which are (i) a decrease in intensity of the magnetic diffraction peaks as the non-stoichiometry becomes more severe [3], (ii) unlike non-stoichiometric CoO [151], a consistent increase in $T_N$ with increasing oxygen content [54,113,114] and (iii) a decrease in rhombohedral distortion as the number of defects increases [153] (Figure 2.12). Battle and Cheetham [3] account for these results by considering the influence of magnetically ordered 6:2 and 8:3 defect clusters on the antiferromagnetic bulk structure. They postulate that the tetrahedral ferric ion is antiferromagnetically coupled to the occupied nearest neighbour cation sites (Figure 2.13) and suggest that the defective region thereby constitutes a ferrimagnetic domain. If the moment direction within the resulting cluster is perpendicular to that of the

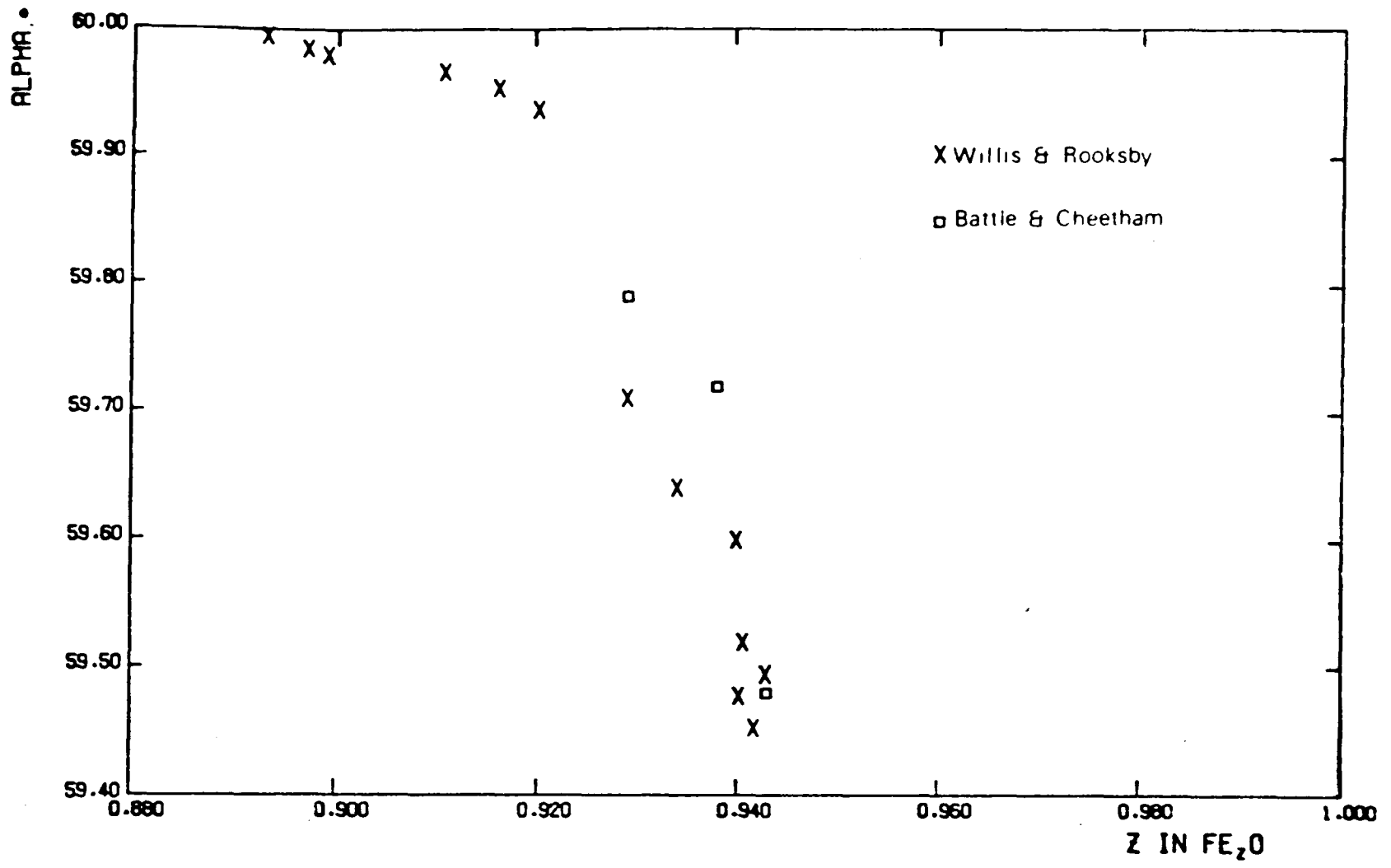



Figure 2.12. Dependence of Angular Distortion on the Stoichiometry of Ferrous Oxide (after Battle and Cheetham [3], and Willis and Rooksby [153]).

surrounding matrix and uncorrelated with the magnetisations of other clusters, the associated neutron scattering is incoherent and the Bragg peaks are reduced in magnitude, as observed.

In addition, the presence of magnetically ordered clusters accounts for the property (ii) above, and the lack of any significant lattice distortion in highly defective samples (Figure 2.12) is attributed to the contribution of an $\alpha > 90^{o}$ exchangestriction (as in MnO). The ordering around the defects is similar to that in MnO and involves ions which have no orbital contribution ($Fe^{3+}$) or whose orbital moment is quenched by the low symmetry in the neighbourhood of the cluster ($Fe^{2+}$).

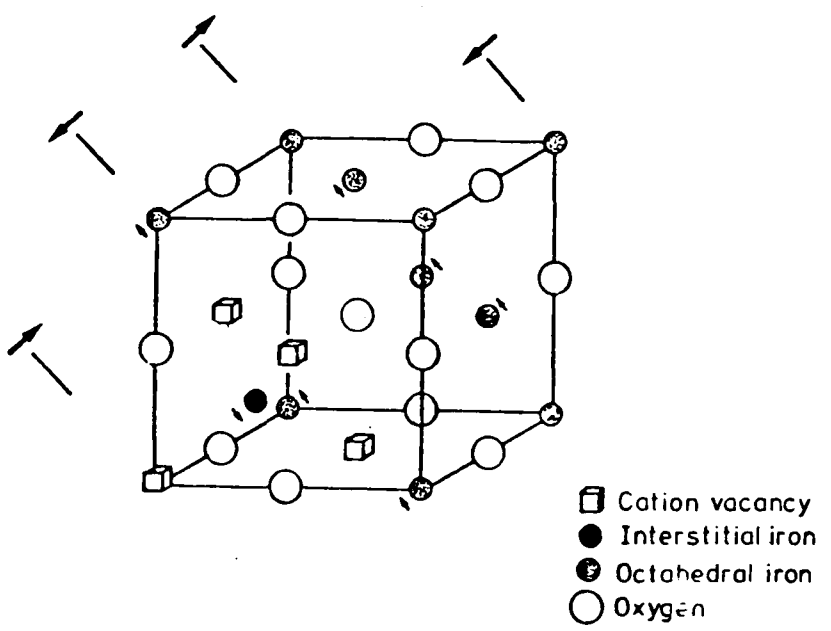



Figure 2.13 A Magnetically Ordered 4:1 Defect Cluster, after Battle and Cheetham [3]. Large Arrows Represent Spins Along [111] in the Bulk Structure; Cations Whose Spins Lie in the (111) Plane are Represented by Smaller Arrows.

### 2.2.5 Summary

Some of the important similarities and differences between the magnetic and related properties of the four oxides dealt with in this section of the chapter are:-

(a) all have the same single axis magnetic structure, which is determined by the appreciable $180^{o}$ cation-oxygen-cation super-exchange interactions. The Néel temperatures increase from 118K (MnO) to 523K (NiO), in line with the increasing electronegativities of the elements.

(b) Crystallographic distortions occur below the magnetic ordering temperatures of all four compounds. MnO and NiO undergo trigonal ($\alpha > 90^{o}$) exchangestrictions which reflect the symmetry of the magnetic structure, while $Fe_{z}O$ and CoO experience trigonal ($\alpha < 90^{o}$) and tetragonal ($c/a < 1$) magnetostrictions, respectively, and are such that an orbital magnetic moment about a high symmetry axis is conserved.

(c) The magnetic moment directions of MnO and NiO are primarily determined by magnetic dipole interactions. These favour a (111) easy plane, and the easy axis within the plane depends upon much weaker effects. The preferred direction within the (111) plane of MnO is unknown, while the easy axis of NiO is $[\bar{1}\bar{1}2]$.

(d) The magnetic vectors of $Fe_zO$ and CoO are linked to the trigonal and tetragonal axes via the spin-orbit coupling. While the moment of ferrous oxide is parallel to the three-fold axis [111], that of CoO is $\sim 27^o$ to [001] and this direction remains to be conclusively explained.

(e) Under normal conditions, only ferrous oxide is appreciably non-stoichiometric and contains a sufficient concentration of defect clusters to affect the magnetic behaviour. The defects substantially diminish the magnetic diffraction peaks, increase the Néel temperature and remove the trigonal magnetostriction.

## 2.3 Magnetic Properties of Disordered Ionic Antiferromagnets

Systems comprising two or more metal ions disordered over the cation sites of a non-metallic lattice may show a wide range of magnetic properties depending upon the cations and anions present. Examples include (i) $Eu_xSr_{1-x}S$ [154], a non-metallic spin glass for $x < 0.5$, (ii) $Mn_xHg_{1-x}Te$ [155], a "semimagnetic semiconductor" in which the band structure of HgTe is perturbed by the exchange interactions between manganous ions, producing unusual magneto-optical effects, (iii) $(Ti_xV_{1-x})_2O_3$ [156], a Pauli paramagnet, spin glass, mictomagnet or antiferromagnet depending on the values of composition and temperature, and (iv) the range of mixed crystals composed of antiferromagnets having different magnetic structures e.g. $(Cr_xFe_{1-x})_2O_3$ [157,158], $(Mn_xFe_{1-x})_2O_3$ [159], $BaCo_xMn_{1-x}O_3$ [160] and $Fe_xMn_{1-x}WO_4$ [161]. These

compounds show changes in magnetic structure, Néel temperature and electronic structure as the composition is varied. In addition, solid solutions of magnetic ions with the transparent ferromagnet $Rb_2CrCl_4$ [162] and weak ferromagnet $FeBO_3$ [163] are being prepared and characterised. These may give rise to unusual magneto-optical properties, for instance.

Many examples exist of mixed crystals composed of an antiferromagnet and a diamagnet, or of two isomorphous antiferromagnets having effectively the same magnetic structure. The magnetic phase relations, excitations and critical behaviour of such mixed magnets have received a great deal of attention recently. In the former category, the properties of $Mg_xNi_{1-x}O$ [164,165] $Mg_xCo_{1-x}O$ [165], $(Cr_xAl_{1-x})_2O_3$ [166] and $Fe_xMg_{1-x}Cl_2$ [167], for example, have been related to the effects of site and bond percolation on the exchange couplings present. The magnetic behaviour of the latter class of compounds is determined by a competition between the interionic exchanges and magnetic anisotropies. The exchange energy is a minimum if spins are parallel, and involves AA, BB, and AB interactions; the anisotropy energy of an ion is smallest when the magnetic moment vector points in the easy direction. This effect is determined by single ion (crystal field) or multiple ion (e.g. dipole-dipole or anisotropic exchange) terms.

The vast majority of previous work on mixed antiferromagnets has been concerned with cases in which the anisotropies of one or both ions are a greater perturbation than the exchange. In particular, mixed magnets made up of good representations of the two dimensional Heisenberg, XY and Ising models have been studied. The presence of weak anisotropies in the Heisenberg and XY systems induces 3-D long range order, but the exchange leading to this order is weak and the anisotropy can be considered to dominate the exchange.

Theoretical work has considered a random mixture of antiferromagnets with opposed anisotropies of similar magnitude, particularly the case when the easy axes are at right angles. The similarity between the phase diagram determined by renormalisation group [168] and mean field treatments [169] and that observed experimentally for $Fe_xCo_{1-x}C\ell_2.2H_2O$ [170], for instance, is striking (Figure 2.14). A noticeable feature is the

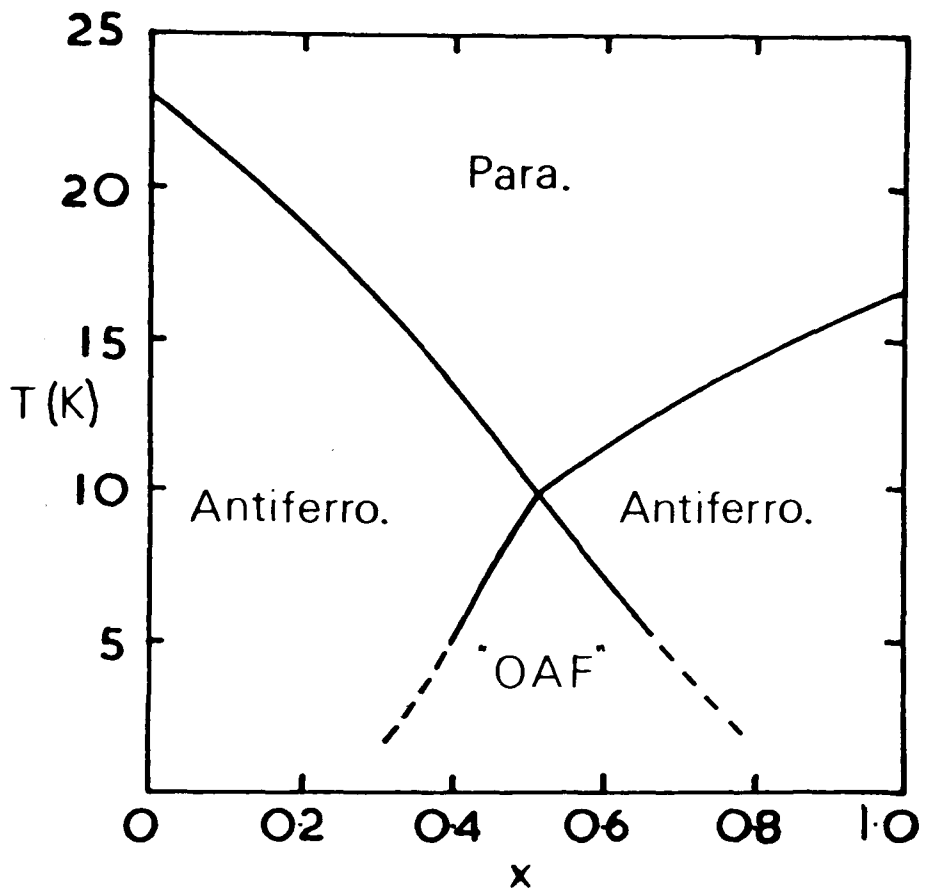



Figure 2.14. The Néel Temperature-Composition Phase Diagram for $Fe_xCo_{1-x}C\ell_2.2H_2O$, after Katsumata, Kobayashi, Sato and Miyako [170].

occurrence of a tetracritical point at intermediate compositions, indicative of a new magnetic phase. Similar behaviour is observed in the 2-D magnets $Fe_xCo_{1-x}C\ell_2$ [171] and $K_2Fe_xMn_{1-x}F_4$ [172], and the 1-D magnet $CsMn_{1-x}Co_xC\ell_3.2H_2O$ [173].

This novel behaviour has been investigated by calorimetric, magnetic susceptibility and neutron scattering techniques, and by optical spectroscopy, Mössbauer spectroscopy and torque measurements. Particular attention has been paid to the intermediate "mixed ordering" or "oblique antiferromagnetic" (OAF) phase. The neutron diffraction[174,175]

Mössbauer [176] and magnetisation [170,171] experiments suggest that the directions of the spins are distributed widely through the crystal in the OAF phase, but the mean magnetisation direction, as measured by neutron diffraction, can still be determined, and is intermediate between the easy axes of the components. The different spin species appear to behave almost independently, as is found in the vicinity of the percolation threshold of a diamagnetically diluted magnet, and the decrease in $T_N$ towards the tetracritical point demonstrates the disruption of the exchange interactions leading to 3-D long range order. The width of the OAF and its region of occurrence depend upon the relative strengths of the anisotropies of the ions involved. In $K_2Fe_xMn_{1-x}F_4$, for example, the weak axial dipolar anisotropy of $Mn^{2+}$ is easily overcome by the very strong planar single ion anisotropy of $Fe^{2+}$, and the OAF only exists over a range $0.022 < x < 0.028$ [172].

The anisotropy of the OAF is found to be much smaller than that of the end members. In $Fe_xCo_{1-x}C\ell_2 . 2H_2O$ [170], a spin-flop transition occurs upon the application of a magnetic field, in contrast to the metamagnetic transitions of the pure substances, and the susceptibility becomes almost isotropic for a sample with ~ 60% $Co^{2+}$ [177]. The spin-flopping is characteristic of a pseudo 2-D Heisenberg antiferromagnet (very weak anisotropy) [178].

Some halides closely related to those mentioned above do not show OAF behaviour, although their Néel temperatures and the exchanges leading to 3-D ordering are small. These compounds include $Co_xNi_{1-x}C\ell_2.6H_2O$ [179,180] and $Mn_xCo_{1-x}C\ell_2.6H_2O$ [181], and it has been demonstrated that, in the former, the spin direction changes gradually with composition owing to the non-orthogonality of the easy axes of the pure compounds. It is also noteworthy that in neither of the above compounds, nor in the 3-D magnet

$Mn_xFe_{1-x}F_2$ [182], is $T_N(x)$ a linear function. Apart from demonstrating the complexity of the competing exchanges, this suggests that the exchange constant between different spins, $J_{AB}$, is not the geometric mean of $J_{AA}$ and $J_{BB}$, as is usually assumed in theoretical treatments of the problem of mixed magnets.

In a random antiferromagnet, therefore, the orientation adopted by a particular ionic moment depends on a large number of factors: the strengths of the single and multiple ion anisotropies of a particular ion and the ions surrounding it, and the sizes of the exchange interactions which, in addition to enabling an ion to "feel" the anisotropies of the surrounding ions, endeavour to align the moments parallel or antiparallel. Two limiting cases can be identified, (i) systems of the XY or Ising type whose anisotropy dominates the exchange, leading to the formation of the "mixed ordering phase" (OAF) and (ii) isotropic Heisenberg exchange (equation 2.10).

Amongst 3-D magnets, EuO, with the rocksalt structure, is a near classical Heisenberg ferromagnet. Its isomorphs MnO, $Fe_zO$, CoO and NiO show strong isotropic superexchange leading to antiferromagnetic order, but have many sources of anisotropy (as discussed in section 2.2). In some respects, it is difficult to understand fully the behaviour of the undoped oxides in the ordered states, but in all the solid solutions formed between the four oxides (except NiO-$Fe_zO$, which exists over a limited composition range [49] and has not been investigated), $T_N$ shows an approximately linear composition dependence [54,116,183,184,185] MFT (section 2.2.1(a)) shows that the only interactions contributing to 3-D ordering are very strong, isotropic $180^o$ cation-anion-cation superexchanges, and an explanation [61] for the linear $T_N(x)$ function demonstrates that the n.n.n. molecular field coefficient of a rocksalt

solid solution is the geometric mean of the coefficients of the end members. The part of the $180^{o}$ exchange energy which is a measure of the energy difference between parallel and antiparallel arrangements is a constant for each oxide and all the solid solutions for the following reason. The more stable antiferromagnetic situation occurs in the correlation superexchange process when a promoted p electron enters the metal d shell antiparallel to the d electrons, for in the parallel (ferromagnetic) case, the Pauli exclusion principle forces the excited electron into the 4s shell. For all the ions concerned the energy difference between 3d and 4s is approximately constant, and the average exchange constant in the solid solution is then only a function of the overlap between oxygen 2p and metal 3d orbitals (the covalency), which increases steadily with increasing nuclear charge from $Mn^{2+}$ to $Ni^{2+}$.

Owing to the dominance of the isotropic n.n.n. superexchange exemplified by the linear Néel temperature-composition diagrams, it is unlikely that any OAF behaviour appears in the mixed iron group monoxides. However, opposed exchange mechanisms involving like and unlike nearest neighbour cations may occur, as is found in $Mn_xCo_{1-x}(HCO_2)_2.2H_2O$ [186] and $Fe_xCo_{1-x}C\ell_2$ [187]. Here, ESR and magnetically-induced light scattering have been used to probe the isotropic and anisotropic exchange between dissimilar metal ions.

Amongst the possible combinations of transition metal monoxides, the systems NiO-CuO [188] and NiO-CoO[2] have been studied recently. In the former, the rhombohedral distortion of NiO is diminished by doping with small amounts of CuO, which has monoclinic crystal and magnetic structures [189]. The powder neutron diffraction study of $Ni_xCo_{1-x}O$[2]

clearly shows the strong influence of the $Co^{2+}$ single ion anisotropy, its linear dependence on composition, and approximate dependence upon the sublattice magnetisation. The dipolar anisotropy of $Ni^{2+}$ is weak and any exchangestriction is only evident for large concentrations of NiO.

# CHAPTER THREE

# EXPERIMENTAL TECHNIQUES

## 3.1 Sample Preparation and Analysis

### 3.1.1 Undoped Oxides

Quantities of MnO, CoO and NiO were required both for neutron diffraction experiments and as precursors for solid solutions prepared by conventional high temperature solid state methods. Olive green manganous oxide was synthesised in a mullite tube by the decomposition of manganous oxalate contained in an alumina boat under a stream of hydrogen at 1000°C. Nickel oxide was a light green Johnson Matthey "Specpure" sample, fired at 1000°C in a platinum boat to increase the particle size. Brown cobaltous oxide was prepared in a mullite tube by firing cobaltous carbonate under a stream of carbon dioxide at 500°C for 4 hours and then at 1000°C in vacuo for a further 24 hours.

Ferrous oxide samples having different stoichiometries were made by grinding the required amounts of iron sponge and $Fe_2O_3$ together in an agate mortar, pelleting, and firing at 1000°C for 24 hours in silica tubes. The products were quenched into liquid nitrogen and their stoichiometries determined by gravimetric oxidation to $Fe_2O_3$ at 1000°C.[55] The samples were contained in alumina boats lined with $Fe_2O_3$, and the resulting stoichiometries are given in Table 6.1.

### 3.1.2 Solid Solutions

#### (a) Preparation of MnO-CoO and MnO-NiO

Two different methods were employed in the syntheses of samples belonging to these solid solution series, both of which utilised a mullite tube attached to a vacuum/gas line. The first involved mixing

appropriate amounts of MnO and CoO or NiO in an agate mortar, pelleting and firing at 1000°C for 24 hours. A static vacuum or $CO_2$ atmosphere was used, and the samples were contained in alumina boats which, in the case of MnO-NiO, were lined with platinum foil [190]. The firings were repeated until adequate sample homogeneities were obtained (see section 3.1.2(c)).

Alternatively isomorphous basic carbonates were coprecipitated to form a precursor which was then decomposed at a higher temperature. Aqueous solutions of $MnC\ell_2.4H_2O$ and $Ni(NO_3)_2.6H_2O$ or $Co(NO_3)_2.6H_2O$ were mixed to give the required proportions of the two ions. The resulting solution was added with stirring to an excess of saturated aqueous $KHCO_3$ at 80°C, and the suspension was allowed to digest for five minutes. After filtration, the precipitate was washed well with distilled water, and left to dry in a vacuum desiccator for a week. Organic solvents were not used as drying agents for the mixed manganese-nickel carbonates because they were adsorbed by the solid and caused reduction of $Ni^{2+}$ during the subsequent decomposition process. A number of batches of each feathery mixed carbonate were then fired under a stream of $CO_2$ at 600°C until a sufficient weight of raw oxide for neutron diffraction was obtained. The homogeneity and average particle size of the product were improved by firing at 1000°C under a static $CO_2$ atmosphere for a further 24 hours.

(b) Preparation of $MnO-Fe_zO$ and $CoO-Fe_zO$

The requisite amounts of MnO or CoO, iron sponge and ferric oxide were ground together in an agate mortar until a fine, uniform powder was obtained. This mixture was formed into pellets, which were fired in evacuated silica tubes at 1000°C for 24 hours and then quenched into

liquid nitrogen. If necessary, the firings were repeated until homogeneous samples were obtained. While this method gave good results for $(Mn_xFe_{1-x})_zO$, diffraction methods showed that samples of $(Co_xFe_{1-x})_zO$ containing more than ~ 40% iron incorporated significant amounts of impurity, a difficulty which must result from the unfavourable phase relationships existing in this system [65,66] (Figure 2.5). Moreover, attempts to synthesise solid solutions containing 20-30% cobalt invariably resulted in multi-phase products, of which the rocksalt phase was not the major constituent. Substantial reaction appeared to have taken place with the silica tube, and it was necessary to attempt a synthesis employing platinum tubes and a temperature of $1200^{o}C$. Unfortunately, no rate of quenching fast enough to halt appreciable disproportionation could be achieved, and the cost of platinum precluded the use of this method for the preparation of the large quantities necessary for neutron diffraction.

(c) Sample Assessment

The quality of each preparation was analysed by powder X-ray diffraction in a Guinier camera. This technique only showed the presence of impurities in the case of the 20-30% cobalt compositions referred to above, but subsequent neutron diffraction studies of the three iron-rich $CoO-Fe_zO$ solid solutions revealed spinel or metallic impurities. Thus the neutron powder profiles of $(Co_{0.04}Fe_{0.96})_{0.939}O$ and $(Co_{0.5}Fe_{0.5})_{0.935}O$ contained minor iron metal and alloy peaks, and that of $(Co_{0.12}Fe_{0.88})_{0.911}O$ indicates the presence of a significant amount of spinel (Figure 6.12(b)). Magnetic measurements extended down to ca. 50K for four $MnO-Fe_zO$ compositions (Chapter 6.2.1) show increases in susceptibility characteristic of the onset of magnetic ordering of $Mn_3O_4$ [191]. Previous measurements

on MnO-NiO [184] show similar behaviour, but the concentration of impurity is insufficient to interfere with any other measurements of the MnO-containing solid solutions.

The metal-metal ratios of the mixed crystals were obtained by atomic adsorption analyses, and their homogeneities were gauged from the width of the X-ray diffraction lines. When the microscopic quality of the crystallites was in doubt, the samples were examined further using a JEOL 100CX TEMSCAN analytical electron microscope. The spread of values obtained in the elemental analyses of ten different thin crystals of each solid solution was determined and, if necessary, further firings were carried out. The applicability of the electron microscope to analytical problems has been discussed by Cheetham and Skarnulis [192], and they include some results obtained for the MnO-$Fe_zO$ system. Impurity concentrations were also monitored in this way, but in all cases they were below the detection level of the instrument.

In general, the ferrous oxide solid solutions were grossly non-stoichiometric, and it was necessary to determine the excess oxygen by volumetric analysis [193]. Assuming all oxidation is accommodated by the formation of iron(111), the total iron content of a sample was realised by passing a solution of the oxide in dilute HCℓ through a Jones reductor and titrating the washings with standard 0.1M $KMnO_4$. The proportion of iron(11) was estimated by dissolving the oxide under air-free conditions and titrating with the standard $KMnO_4$. Both sets of titrations were repeated twice and the results agreed to within 0.5%. In both cases, a quantity of Zimmerman-Reinhardt reagent was added to minimise oxidation of chloride by permanganate, and the end-point was indicated by the appearance of the purple colour of $MnO_4^-$. The compositions calculated from the analytical results are set out in Table 6.1. Two $^{57}Fe$-enriched

MnO-FeO solid solutions, containing 90 and 97.5% manganese, were prepared for Mössbauer spectroscopy experiments. These were necessarily in such small quantities that they could not be analysed by the above method, but their green colours indicated negligible oxidation.

## 3.2 Neutron Diffraction

### 3.2.1 Principles

Although the neutron is uncharged, it possesses a magnetic moment, and, in addition to being scattered by the nucleus of an atom, it may interact with any magnetic moment resulting from the presence of unpaired valence electrons. Neutrons moderated to thermal energies after generation in a nuclear reactor or a particle accelerator have wavelengths comparable to the separations of atoms in solids and, by analogy with X-rays, may be diffracted by regular arrangements of these atoms. Likewise, the ordered dispositions of moments in a magnetically ordered solid give rise to neutron diffraction patterns characteristic of the magnetic symmetry. These coherent, elastic scattering processes are accompanied by other incoherent and inelastic mechanisms, but they only contribute to the background in a diffraction experiment and will not be discussed further here. The principles of chemical and magnetic structure analysis using neutrons will now be briefly reviewed. Many comprehensive discussions appear elsewhere [194,195,196,197].

A diffraction pattern provides information on the sizes and symmetries of the chemical and magnetic unit cells comprising a magnetically ordered crystalline solid and may reveal the positions and nature of the scattering centres within these cells. The locations of peaks in the pattern are related to the diffracting lattice by the Bragg equation

$$\lambda = 2d_{hk\ell} \sin\theta \qquad (3.1)$$

where $\lambda$ is the neutron wavelength, $d_{hk\ell}$ is the spacing between "reflecting" planes, and $\theta$ is the angle between the incident neutrons and these planes. Apart from the systematic absences produced by translational symmetry elements in the structure, the fundamental quantity determining the intensity of a reflection is the corresponding structure factor, $F_{hk\ell}$. In an unpolarised neutron diffraction experiment, this is the sum of two independent nuclear and magnetic contributions:

$$F_{hk\ell}^2 = \left(\sum_i b_i \exp\{2\pi i(hx_i + ky_i + \ell z_i)\}\right)^2 + \left(\sum_i q_i p_i \exp\{2\pi i(hx_i + ky_i + \ell z_i)\}\right)^2 \qquad (3.2)$$

The summations embrace all the scattering centres in each cell and $x_i$ $y_i$ and $z_i$ are their fractional co-ordinates. The peak intensity is diminished by the effect of thermal vibrations, and the nuclear and magnetic scattering factors, $b_i$ and $q_i p_i$, are modulated by a Debye-Waller temperature factor. In the isotropic approximation, this is $e^{-W}$, where

$$W = 8\pi^2 \bar{U}_s^2 \sin^2\theta/\lambda^2 \qquad (3.3)$$

and $\bar{U}_s^2$ is the mean square displacement of the atoms along the normal to the reflecting planes.

Unlike the magnetic scattering factor, the nuclear scattering length, $b_i$, does not vary with scattering angle, $2\theta$, because the range of the neutron-nuclear interaction is very much less than the neutron wavelength. Nor does it increase smoothly with atomic number, owing to the different contributions of potential and resonance scattering for different nuclei. Therefore neighbouring elements of the periodic table can be distinguished, as can isotopes of the same element.

In addition to the magnetic moment of an ion, the magnetic scattering factor includes terms which take into account the variation in intensity with scattering angle, $2\theta$, and with the angle between the magnetic moment and scattering vectors. The former is analogous to the form factor of X-ray diffraction and occurs because the electronic cloud causing the magnetic moment has a radial extent comparable to the neutron wavelength. The latter arises from the requirement that the magnetic moment have a projection onto the reflecting plane for scattering to occur. The magnetic interaction vector, $\underline{q}_i$, is defined by

$$\underline{q}_i = \underline{\varepsilon}(\underline{\varepsilon}.\underline{K}) - \underline{K} \qquad (3.4)$$

where $\underline{\varepsilon}$ is the unit scattering vector for the hkℓ planes and $\underline{K}$ is a unit vector parallel to the magnetic moment. If $\alpha$ is the angle between $\underline{\varepsilon}$ and $\underline{K}$, the magnitude of $\underline{q}$ is $\sin\alpha$; when $\underline{\varepsilon}$ and $\underline{K}$ are collinear, no reflection occurs.

The preceding cursory discussion applies equally well to steady state and pulsed sources, and to powder and single crystal samples. However, only the conventional steady state powder diffraction technique was employed in the present work and this will be considered more fully in subsequent sections.

### 3.2.2 Powder Methods

The suitability of powder diffraction methods for the solution of problems in solid state science is well established and documented [198]. However, it is necessary to stress that the data obtained are less informative than those from the corresponding single crystal experiments because reflections from all symmetry-equivalent planes occur at the same Bragg angle. Consequently, the expression for the intensity of a powder diffraction peak is

$$I_{hk\ell} = \frac{pmAk|F_{hk\ell}|^2}{L} \qquad (3.5)$$

where p is a polarisation correction (X-rays only), m is the multiplicity of the (hkℓ) reflection, A is an absorption correction, k is a scaling constant and L is the Lorentz (velocity) factor ($\sin^2\theta.\cos\theta$).

The loss of information in a powder experiment is particularly limiting when attempts are made to determine magnetic structures, since certain different magnetic moment configurations may produce exactly the same powder intensities. If the configurational symmetry[78,199] (the symmetry of the magnetic structure when the vector properties of the magnetic moments are disregarded) is orthorhombic or lower, the direction of the moments may be uniquely defined, but if this symmetry is uniaxial, only the angle with respect to the unique axis can be determined. No deductions at all can be made when cubic configurational symmetry is encountered.

A further drawback with powders is the extensive peak overlap for cells with low symmetries and large lattice parameters, even when diffractometers having very good resolution are available. It is then difficult to deconvolute the resulting envelope into individual peak intensities, to carry out structure factor calculations, and to perform least squares refinements against trial models. A solution to this problem, which also provides more parameters for the least squares process, is the profile refinement technique of Rietveld[200]. This was originally developed for the analysis of neutron powder data obtained at fixed wavelength, owing to the ease with which the peak shape can be fitted to an analytical function, and it has found wide applicability[201]. The method has recently been extended to the analogous X-ray technique[202,203,204]

and time-of-flight neutron diffraction [205].

Perfect collimation of a neutron beam of fixed wavelength would lead to an infinitely narrow peak at position $2\theta_k$ having an intensity given by equation 3.5. However, the arrangement of a conventional powder neutron diffractometer (Figure 3.1) leads to broadening of the reflection,

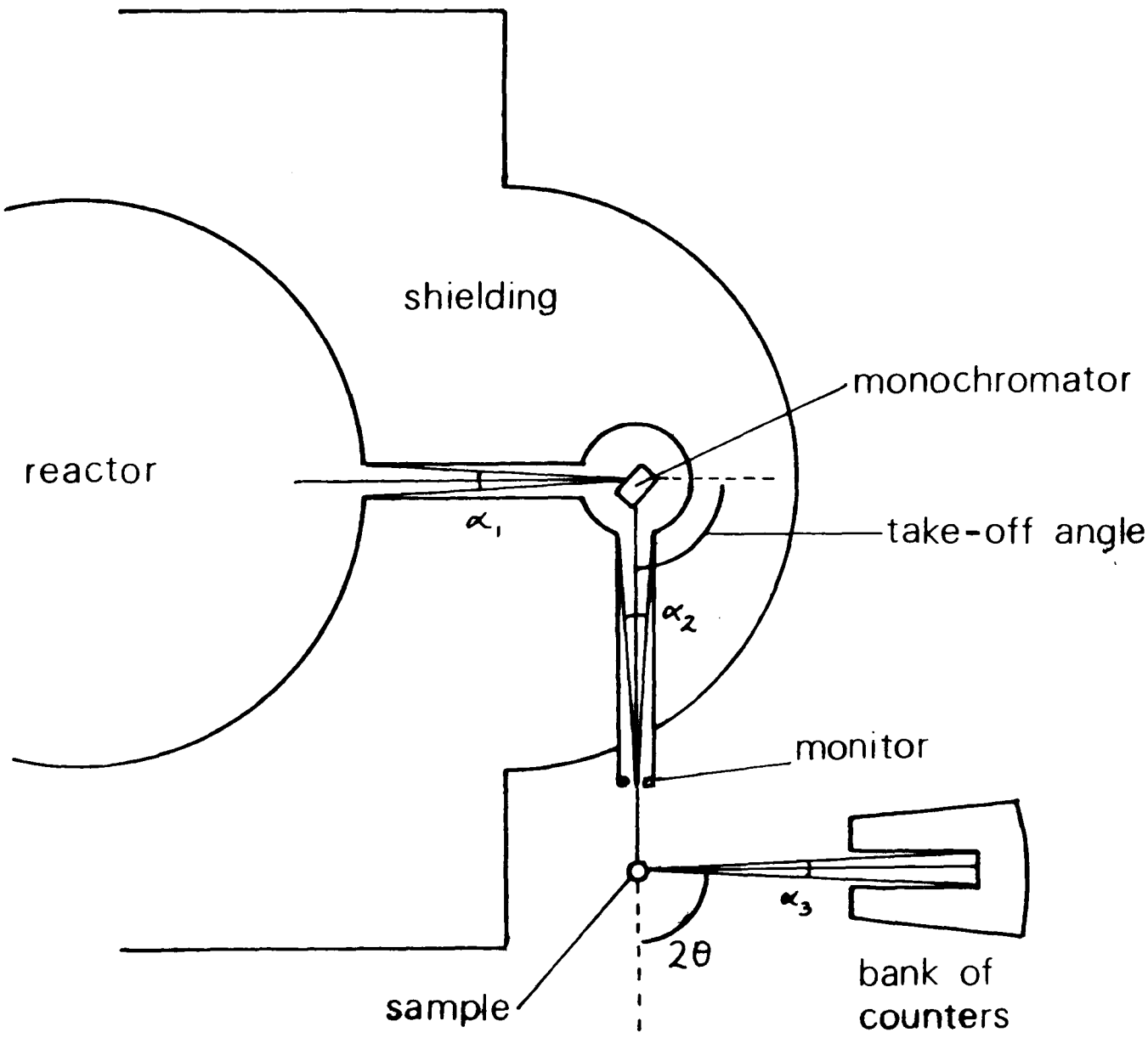



Figure 3.1 The Layout of a Conventional Powder Neutron Diffractometer.

in such a way that its shape is accurately described by a Gaussian function. The contribution, $y_i$, of the Bragg reflection (hkℓ) to the intensity measured at position $2\theta_i$ (after subtraction of the background) is

$$y_i = \frac{ctM_K L_K F^2_{hk\ell}}{H_K} \cdot \exp\left\{ - \frac{4\ell n2}{H_K^2} (2\theta_i - 2\theta_k)^2 \right\} \qquad (3.6)$$

where c is a constant, t is the counter step width, and $H_K$ is the full

width at half height of the peak. The dependence of $H_K$ on $2\theta_k$ for different diffractometers is shown in Figure 3.2 and is described by [206]

$$H_K^2 = U \tan^2\theta_K + V \tan\theta_K + W \qquad (3.7)$$

where U, V and W are treated as adjustable parameters in the refinement procedure.

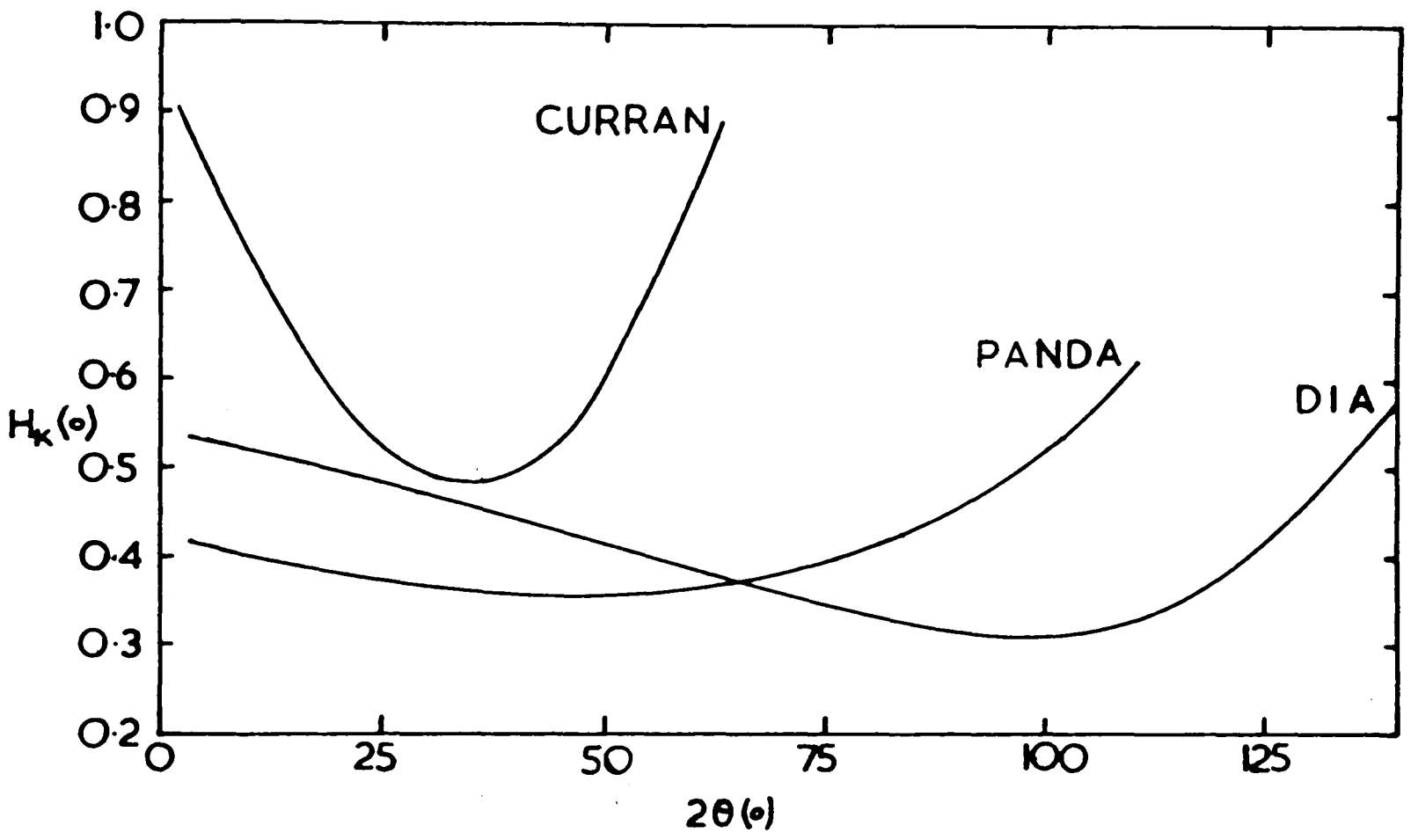



Figure 3.2 Resolution Curves for Certain Powder Neutron Diffractometers.

Other variables which affect the form of a profile are a scale factor, counter zero point, cell parameters, temperature factors, atomic co-ordinates and occupancies, and components of any ordered magnetic moments. Using these, a series of Gaussian peaks centred at $2\theta_k$ can be generated, and refinement carried out by minimising the quantity

$$\chi^2 = \sum_i w_i \left[ y_i(\text{obs}) - \frac{1}{c} y_i\ (\text{calc}) \right]^2 \qquad (3.8)$$

Here, $y_i(\text{obs})$ is the observed intensity at the ith profile point after subtraction of the background, and $y_i(\text{calc})$ is the sum of the contributions

from all reflections which overlap at the point i. c is a scale factor and $w_i$ is a weight calculated according to

$$w_i = \{(y_i + b_i) + \sigma^2 (b_i)\}^{-1} \qquad (3.9)$$

where $b_i$ is the background at point i and $\sigma (b_i)$ is usually taken as $\sim \sqrt{b_i}$ .

In practice, the crystallites may not be randomly oriented, and a correction for preferred orientation is necessary. This has the form

$$I_{cor} = I_{obs} \exp(-G\alpha^2) \qquad (3.10)$$

where $I_{obs}$ is the observed intensity, $\alpha$ is the acute angle between the scattering vector and the preferred orientation axis, and G is a parameter refined in the least squares calculations. It is a measure of the width of a Gaussian distribution of the preferred orientation axes of the individual crystallites about the axis of the sample.

Peak symmetry is often a problem at small scattering angles and stems from the greater curvature of the Debye-Scherrer rings close to $2\theta = 0^{o\ 207}$; different detector levels do not sample the powder line at the same position in $2\theta$ since the detectors must have sufficient height to furnish adequate counting statistics. When small deviations from the Gaussian shape occur, a correction to the peak shape can be applied. This is

$$c_a = \left(1 - \frac{P(2\theta_i - 2\theta_k)^2 S}{\tan\theta_i}\right) \qquad (3.11)$$

where P is the asymmetry parameter and S is unity, but with sign $(2\theta_i - 2\theta_k)$. However, peaks occurring at scattering angles less than $25^o$ on the D1A or PANDA diffractometers (section 3.2.3) normally cannot be included in a least squares refinement because the asymmetry is so large. The loss is

unfortunate for magnetic structure work because the most intense magnetic reflections tend to occur at low angles.

The agreement between observed data and calculated model after a refinement sequence can be assessed using a number of residuals. These are

$$R_{profile} = \frac{\Sigma|y_i(obs) - cy_i(calc)|}{\Sigma|y_i(obs)|} \tag{3.12}$$

$$R_{weighted\ profile} = \left\{ \frac{\Sigma\ w_i(y_i(obs) - cy_i(calc))^2}{\Sigma\ w_i(y_i(obs))^2} \right\} \tag{3.13}$$

$$R_{nuclear} = \frac{\Sigma_{hk\ell} |I^{hk\ell}_{nuc}(obs) - c\ I^{hk\ell}_{nuc}(calc)|}{\Sigma_{hk\ell} I^{hk\ell}_{nuc}(obs)} \tag{3.14}$$

$$R_{magnetic} = \frac{\Sigma_{hk\ell} |I^{hk\ell}_{mag}(obs) - c\ I^{hk\ell}_{mag}(calc)|}{\Sigma_{hk\ell} I^{hk\ell}_{mag}(obs)} \tag{3.15}$$

The nuclear and magnetic R values are obtained by deconvoluting the observed profile into individual peak intensities using the halfwidth parameters determined. For comparison, a statistical value of $R_{wp}$ may be calculated according to

$$R_E = \left\{ \frac{N}{\Sigma w_i(y_i(obs))^2} \right\} \tag{3.16}$$

where N is the number of data points minus the number of variable parameters.

Since the Rietveld method was originally formulated, the ability to perform refinements of anisotropic temperature factors has been

incorporated [208] and the calculation of standard deviations improved[209] The latter have been shown to increase by a factor of 2-3 when the correlation between neighbouring data points is taken into account. The results obtained from the integrated intensity and profile refinement methods may also be slightly different.

### 3.2.3 Data Collection

In addition to the ease of structural refinement according to the Rietveld technique, powder neutron diffraction has a number of advantages over X-ray or single crystal methods for the present work. Neutrons have much smaller absorption cross sections for many materials than X-rays, which enables a sample to be easily surrounded by cryogenic equipment, and the magnetic and crystallographic structures extant at low temperatures can be readily examined. It is often very difficult to obtain single crystals of sufficient size for neutron diffraction, and extinction and multi-domain effects can then limit the usefulness of the results obtained. These problems are negligible with powders and the samples may be obtained easily and studied quickly: in this programme of work more than thirty distinct experiments were carried out.

The layout of a conventional powder neutron diffractometer is depicted in Figure 3.1. Thermal neutrons from a nuclear reactor are monochromated by a large single crystal and scattered by the sample into a bank of detectors. The intensity at the sample and the angular resolution are dependent on the vertical and horizontal divergences determined by the collimators $\alpha_1$, $\alpha_2$ and $\alpha_3$. The take-off angle at the monochromator determines the range of $\sin\theta/\lambda$ in reciprocal space over which good resolution is obtained, although the incident neutron flux at the sample is somewhat diminished by using large values of this angle.

In the present work, the samples were contained in 12 x 44 mm vanadium cans, this material being used because it has a negligible coherent neutron scattering cross section. All experiments were carried out using vanadium or aluminium-tailed cryostats; that employed at the Institut Laue-Langevin, Grenoble enables data to be recorded at any temperature between 2.5K and ambient, using a controller incorporating a calibrated silicon diode. The wavelengths were measured using standard nickel metal or aluminium oxide powder.

Data were collected on three diffractometers: CURRAN and PANDA at AERE, Harwell [210] and D1A at ILL, Grenoble [211]. These can be used to scan the ranges $0 < 2\theta < 105^{o}$, $0 < 2\theta < 115^{o}$ and $0 < 2\theta < 162^{o}$, respectively, and their resolution curves are given in Figure 3.2. Although each instrument employs a bank of detectors, is automatically controlled by a microprocessor, and experiences approximately the same flux, D1A is the most modern and versatile of the three and deserves a fuller description [212].

While CURRAN and PANDA are situated against the reactor faces of the Harwell reactors DIDO and PLUTO, D1A occupies a position on a neutron guide tube approximately 60m from the face of the high flux beam reactor at ILL. The background at the sample is consequently very low and even, and the reflectance of the guide tube is such that the collimators $\alpha_1$ and $\alpha_2$ (Figure 3.1) are unnecessary. A focussing monochromator, with a take-off angle of $122^{o}$, necessitates the use of small quantities of sample (6-8g) and the time for a typical complete $2\theta$ scan is 12-24 hours, depending on the wavelength used and the sample quality. The ten $^{3}He$ counters, preceded by mylar foil collimators, are separated by $6^{o}$, and this matrix can be moved in steps of minimum size $0.05^{o}$. The diffracto-meter is controlled by a Plessey Micro 1 microcomputer incorporating the DEC RT11 operating system, and this also enables automatic wavelength,

temperature and magnetic field changes to be carried out.

The large take-off angle of D1A is primarily intended to extend the range of chemical structure investigations and appears not to produce the best conditions for the study of magnetic structures. Since magnetic Bragg peaks are most intense at small values of $\sin\theta/\lambda$ owing to the magnetic form factor, such investigations should be carried out using small take-off angles (e.g. D2 and D1B at ILL) or long wavelengths [213]. Some compromise must be reached in any attempt to simultaneously examine magnetic and nuclear scattering, and on D1A or PANDA this is normally weighted in favour of the chemical structure. Although most experiments described in this thesis were carried out at a wavelength of ~ 1.5 Å, it was possible to obtain longer wavelengths on D1A and to analyse the magnetic scattering more accurately. Although fewer peaks appear in the diffraction pattern, longer wavelengths (e.g. 1.9 Å, 2.98 Å) are additionally more favourable because the magnetic peaks occur at 2θ positions where asymmetry is less pronounced. The flux from the monochromator also increases markedly when λ is changed from 1.5 to ~ 3.5 Å.

### 3.2.4 Data Analysis

Details of particular refinements and their results are set out in Chapters 4-6, while Appendix 1 provides a pictorial indication of the agreement obtained. Some features common to all experiments will be discussed here.

Powder profiles recorded on D1A were collated and scaled directly after data collection using the central computer facilities of the ILL, Grenoble [214]. Data sets obtained at Harwell were collated using one of a suite of programs implemented on the ICL 1906A at Oxford University [215] and subsequent refinements of all data were carried out using both this

| | | | |
|---|---|---|---|
| $P\bar{1}$ | metal | at | 0, 0, 0 (1a) |
| | oxygen | at | 0, 0, $\frac{1}{2}$ (1b) |
| C2/m | metal | at | 0, 0, 0 (2a) |
| | oxygen | at | 0, $\frac{1}{2}$, $\frac{1}{2}$ (2d) |
| | interstitial | at | $\frac{1}{4}$, 0, $\frac{1}{4}$ (4i) |
| $R\bar{3}$ | metal | at | 0, 0, 0 (3a) |
| | oxygen | at | 0, 0, $\frac{1}{2}$ (3b) |
| | interstitial | at | 0, 0, $\frac{1}{4}$ (6c) |
| Fm3m | metal | at | 0, 0, 0 (4a) |
| | oxygen | at | $\frac{1}{2}$, $\frac{1}{2}$, $\frac{1}{2}$ (4b) |
| | interstitial | at | $\frac{1}{4}$, $\frac{1}{4}$, $\frac{1}{4}$ (8c) |

TABLE 3.1 Space Group Co-Ordinates Employed in Refinements Discussed in this Work.

pseudocubic - rhombohedral (trigonal)

$$\underline{a_r} = \tfrac{1}{2}\,\underline{b_c} + \tfrac{1}{2}\,\underline{c_c}$$
$$\underline{b_r} = \tfrac{1}{2}\,\underline{c_c} + \tfrac{1}{2}\,\underline{a_c}$$
$$\underline{c_r} = \tfrac{1}{2}\,\underline{a_c} + \tfrac{1}{2}\,\underline{b_c}$$

pseudocubic - C-centred (monoclinic)

$$\underline{a_m} = \underline{c_c} - \tfrac{1}{2}\,\underline{a_c} - \tfrac{1}{2}\,\underline{b_c}$$
$$\underline{b_m} = \tfrac{1}{2}\,\underline{a_c} - \tfrac{1}{2}\,\underline{b_c}$$
$$\underline{c_m} = \tfrac{1}{2}\,\underline{a_c} + \tfrac{1}{2}\,\underline{b_c}$$

pseudocubic - primitive (triclinic)

$$\underline{a_t} = \tfrac{1}{2}\,\underline{a_c} - \tfrac{1}{2}\,\underline{c_c}$$
$$\underline{b_t} = \tfrac{1}{2}\,\underline{b_c} - \tfrac{1}{2}\,\underline{c_c}$$
$$\underline{c_t} = \tfrac{1}{2}\,\underline{a_c} + \tfrac{1}{2}\,\underline{c_c}$$

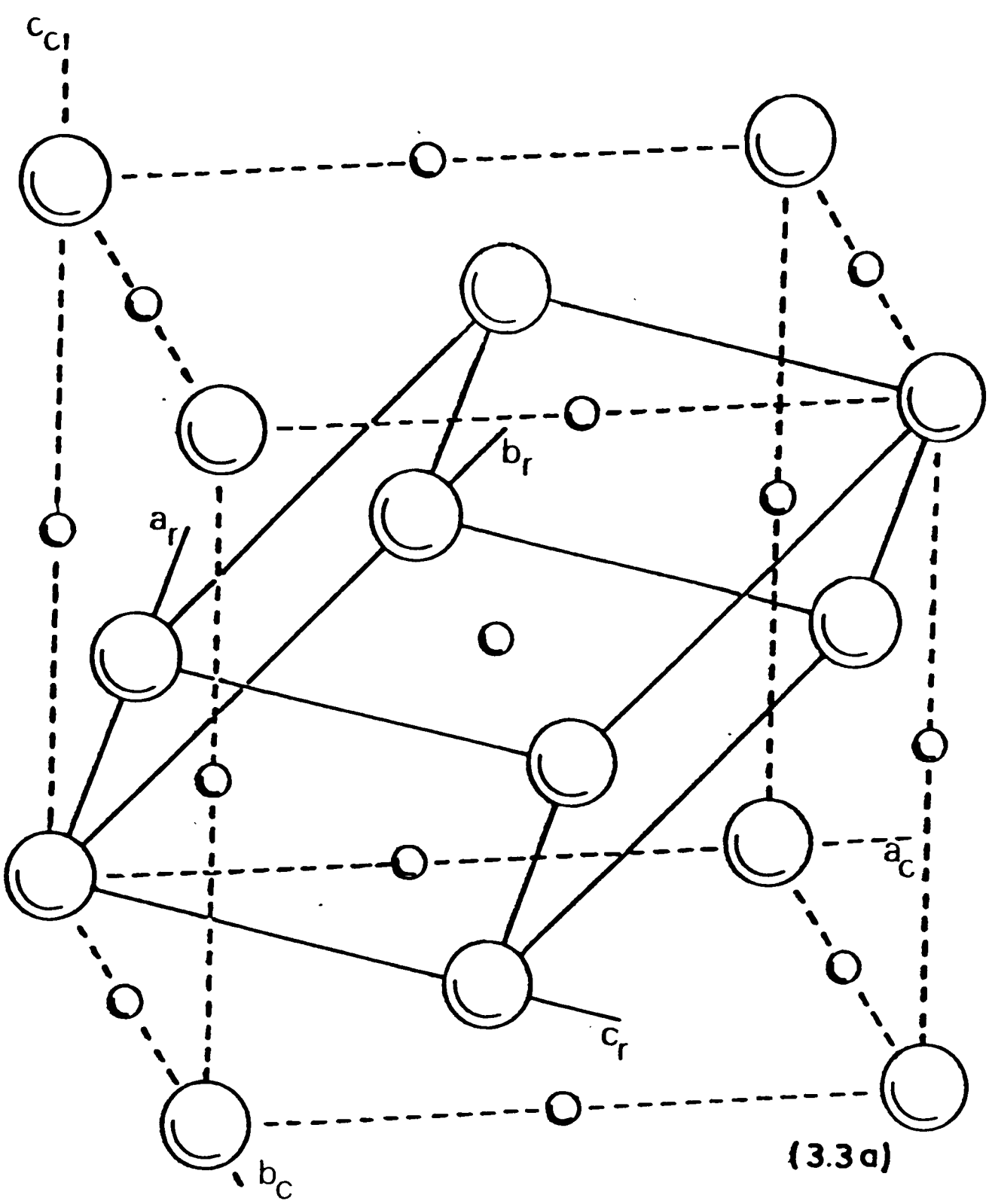
TABLE 3.2 Transformations Between Lattice Vectors of Pseudocubic and Component Cells

package and an interactive version of the same system located on a DEC-10 machine at UMIST [216].

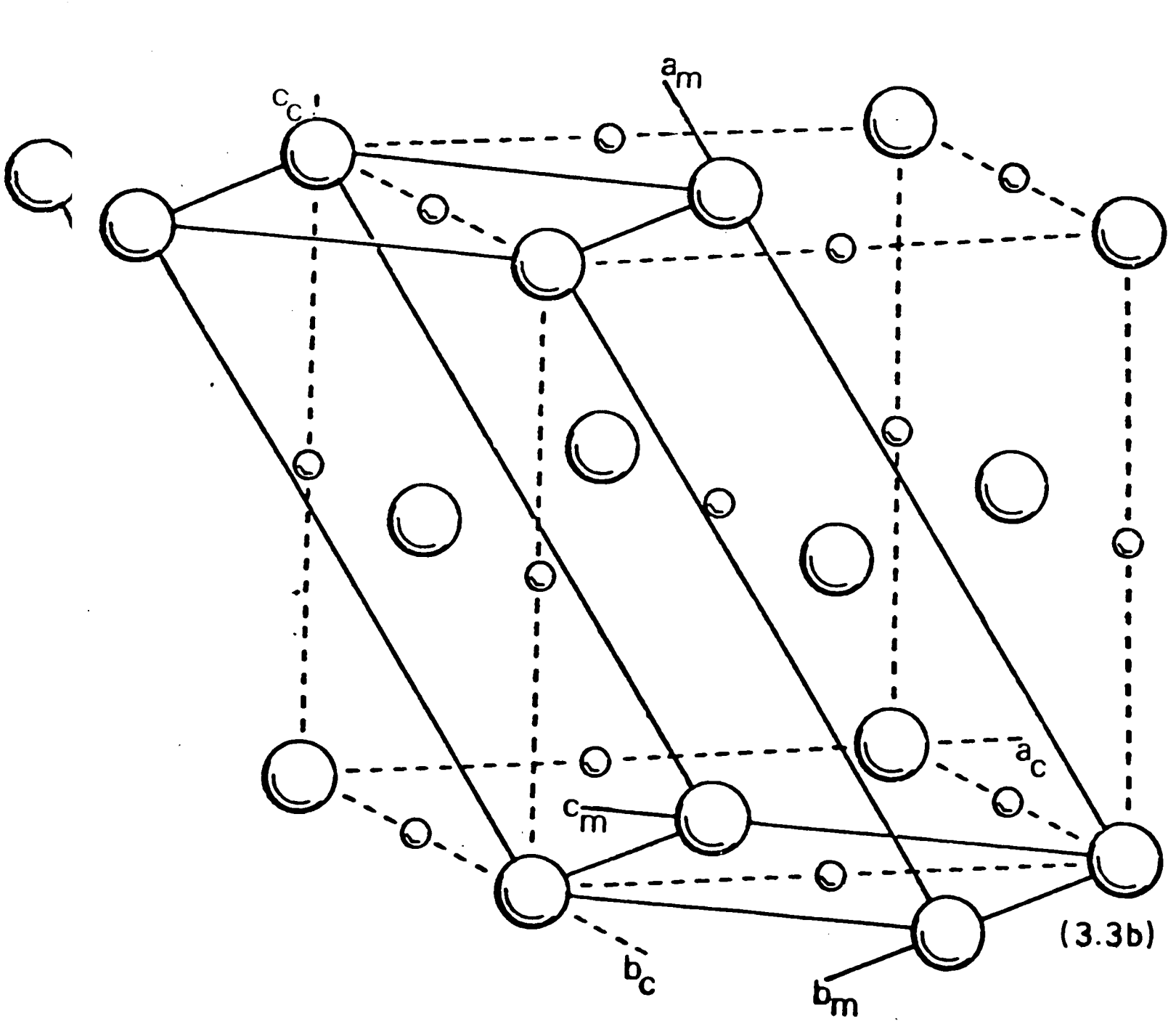
Depending upon the lattice distortions present, the data were analysed according to face-centred, trigonal, C-centred or primitive cells. The space group co-ordinates are set out in Table 3.1, and the transformations between the face-centred pseudocubic and smaller cells are summarised in Table 3.2 and Figure 3.3. It should be noted that the ab planes of the $R\bar{3}$ (hexagonal setting), C2/m and $P\bar{1}$ cells correspond to the (111) plane of the pseudocubic cell, so that the deviation of a magnetic moment from the (111) plane can easily be gauged from the size of the component along the c axis.

Scattering lengths for the elements involved were taken from Bacon [194], and those applied to the cation sites of the solid solutions were calculated from the atomic absorption analytical data. Subsequent refinement of the cation site occupancy (and hence the scattering length) led to good agreement with the analytical results when good quality data sets were involved, but it was necessary to adjust the occupancy to unity (for stoichiometric samples) in order to ensure the magnetic moments of different compositions were on the same scale. It is noteworthy that very little crystal disorder scattering was observed in any of the experiments, despite the random nature of the solid solutions and the large differences in scattering length between the components. The background levels of the mixed crystals profiles all have comparable count rates to those of the end members.

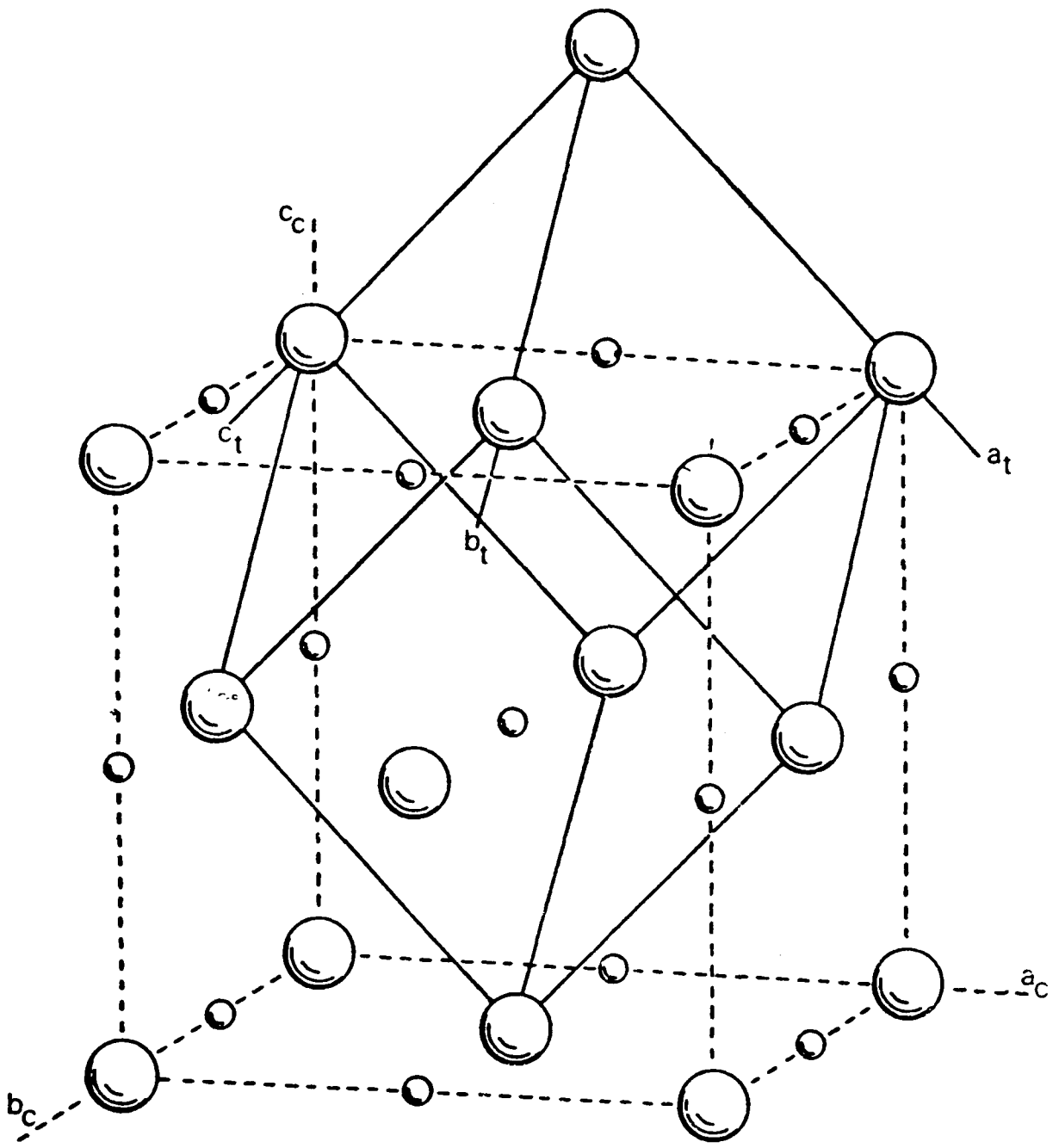
The neglect of peaks occurring at angles less than $2\theta = 25^{o}$ owing to the gross asymmetry was mentioned in section 3.2.2, but it was found that an asymmetry correction (equation 3.11) applied in the range




(3.3a)




(3.3b)




(3.3c)

Figure 3.3 Transformations Between The Face-centred Pseudocubic and (a) Trigonal (rhombohedral setting), (b) C-centred monoclinic and (c) Primitive triclinic cells.

$25 < 2\theta < 48^{o}$ (D1A data) substantially improved the agreement between observed and calculated profiles. The upper limit was set to $38^{o}$ for PANDA data, but the asymmetry was negligible for the CURRAN data set. Only magnetic reflections having $0.17 < \sin\theta/\lambda < 0.4$ were included in the calculations since peaks occurring at larger scattering vectors are very weak, the form factor is less well defined and possible anisotropic contributions, arising from aspherical charge distributions, are more severe.

A critical parameter involved in the treatment of the magnetic scattering is the form factor, which is the Fourier transform of the electronic distribution and consequently can be calculated for the d electrons of free ions using Hartree-Fock methods [217]. However, only in the case of $Mn^{2+}$ in MnO do the calculated and observed curves coincide [218]. In NiO [219,220] and CoO [144], the form factors are expanded relative to those of the free ion, an effect which can be attributed to the combined influences of covalency (the importance of which has been mentioned with regard to the superexchange coupling mechanism), orbital contributions, spin polarisation of 4s and 4p metal orbitals, and crystal field effects [221]. Covalency and zero point spin deviations also reduce the amplitude of the 3d form factor and thus diminish the observed moment. In fact, the reduction of magnetic moment in certain systems may be used to derive covalency parameters for the bonding between metal and ligand [222,223,224].

Although concentration-weighted form factors have been applied to solid solution magnetic neutron data elsewhere [175], the contributions listed above both expand and contract the form factor and the best curve to be applied cannot be calculated easily. For instance, the orbital contributions to the moments of octahedral $Co^{2+}$ and $Fe^{2+}$ in MnO-CoO and MnO-$Fe_zO$ (Chapters 5 and 6) are probably not present across the whole range of composition. Consequently, when determining the most appropriate solid solution form factor the following empirical procedure was used.

The concentration-weighted average was calculated, and this was then both contracted and expanded until the best fit, as indicated by the profile R value (equation 3.12), was obtained. Use of the magnetic R value was found to be less reliable. For some members of the MnO-CoO system, the best results were obtained using the concentration-weighted

average, but the converse was true in MnO-NiO, where better R values were obtained with form factors biased towards that of MnO. This may partly reflect the apparent overestimation of the expansion of the free ion $Ni^{2+}$ form factor in previous work [219] (Chapter 4.2.1).

Changes in the form factor carried out according to the above procedure suggested that the errors in the magnetic moments are larger than those forthcoming from the Reitveld analyses. For this reason, both errors are quoted in Tables 4.1 and 5.3.

## 3.3 Mössbauer Effect Spectroscopy

### 3.3.1 Principles

Unlike optical spectroscopy, where the recoil energy on emission of a photon is insignificant compared to the energy of a transition, the more energetic gamma rays involved in nuclear transitions impart much larger amounts of momentum to the emitting atoms. Conservation of energy requires that the energy of the emitted gamma ray is less than that of the transition by the kinetic energy of the recoiling nucleus, and the condition for resonant absorption is destroyed. However, when an atom is bound into a crystal, the recoil may be transferred to the centre of mass of the whole crystal if this energy is insufficient to change the vibrational state of the emitting atom or separate it from the lattice. The recoil velocity is then practically zero and the gamma ray emission carries away most of the energy. This occurs when low energy $\gamma$-ray transitions are involved, such as those of $^{57}Fe$, $^{119}Sn$, $^{61}Ni$, $^{123}Sb$ and a number of other nuclides, and the process is known as the Mössbauer effect, after its discoverer [225].

In the particular case of iron, a $^{57}Co$ source nucleus decays to an excited state of $^{57}Fe$ by K-electron capture. Nine percent of the

excited $^{57}Fe$ nuclei go directly to the ground state ($I = \frac{1}{2}$) with emission of a 137 KeV photon, but 91% decay to an intermediate state ($I = \frac{3}{2}$), which has a half-life of $10^{-7}$ seconds. In the transition between this and the ground state, a $\gamma$-ray of low energy, 14.4 KeV, is emitted which may experience resonant absorption by other iron nuclei under recoil-free conditions. Naturally occurring iron contains 2.17% of the $^{57}Fe$ isotope, an amount often sufficient for the observation of Mössbauer absorptions. If iron is in small concentrations, enrichment with $^{57}Fe$ must be carried out (as in some manganese-rich $Mn_xFe_{1-x}O$ solid solutions, Chapter 6.1.2). The subsequent discussion refers briefly to the characteristics of $^{57}Fe$ Mössbauer spectra; the theory and practice of the technique are treated thoroughly elsewhere [226].

The lifetime of the $I = \frac{3}{2}$ excited state is such that, according to the Heisenberg uncertainty principle, the linewidth of the nuclear levels is a very small fraction of the energy of the gamma ray. Owing to this, the extremely small hyperfine interactions between the nucleus and surrounding electrons, which cause minute shifts in relative energy between emitter and absorber, can be detected. This is accomplished by restoring resonance using the Doppler effect, whereby the sample and source are moved relative to one another at speeds of the order of a few mm per second. The hyperfine interactions reflect the chemical environment of an atom and stem from the finite radial distribution function of s electrons at the nucleus. Electrons having other azimuthal quantum numbers only affect the nuclear energy levels indirectly, for instance by screening. Figure 3.4 depicts the three effects which give rise to the main features of Mössbauer spectra, (i) the nuclear isomer shift ($\delta$), (ii) the nuclear quadrupole coupling ($\Delta E_Q$), (iii) the magnetic hyperfine interaction. All will now be

briefly discussed, although the Mössbauer work in this thesis is primarily concerned with paramagnetic samples and only involves the measurement of (i) and (ii).

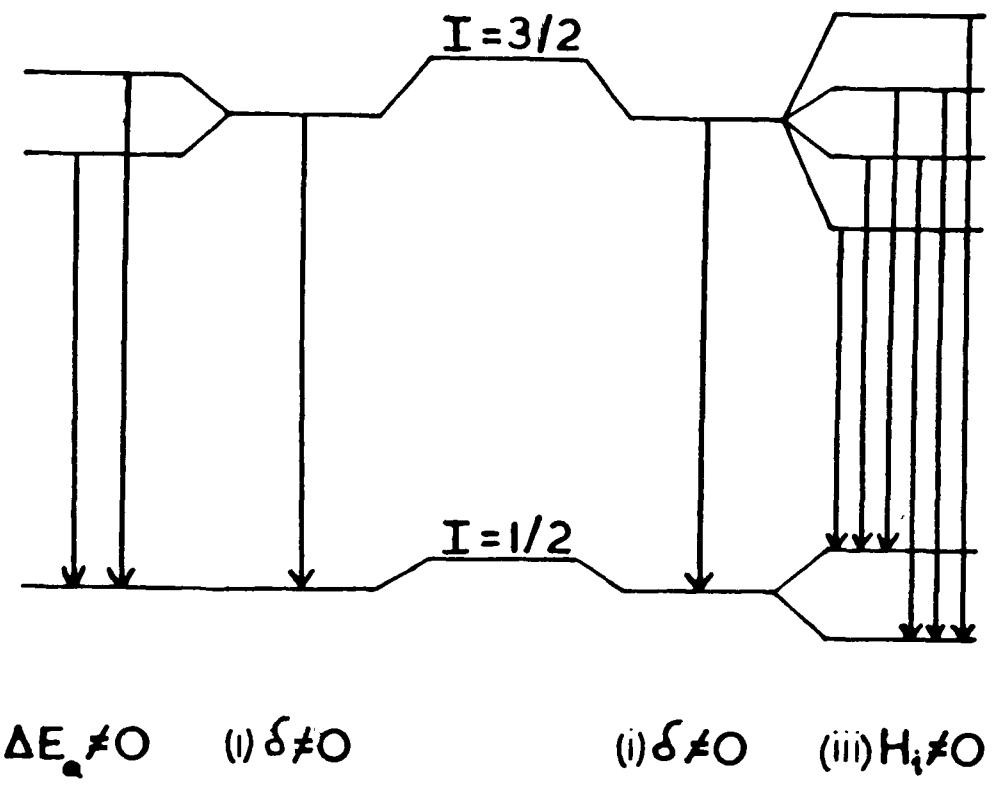



Figure 3.4 Changes in the Nuclear Energy Levels of $^{57}Fe$ Invoked by (i) Surrounding Electrons, (ii) An Electric Field Gradient, (iii) A Molecular Field.

The isomer shift, $\delta$, is sensitive to the s electron density at the nucleus and occurs because the nuclear charge radius is different in the ground and excited states. For $^{57}Fe$, increasing s electron density produces a negative shift in $\delta$, which is the case when covalency spreads the valence orbitals and decreases the shielding of the s electrons.

The $I = \frac{3}{2}$ state of $^{57}Fe$ possesses a quadrupole moment also, and the degeneracy of this level is removed by a finite electric field gradient. Point symmetries lower than cubic, which may arise from charges external to the atom (lattice contribution) or from incompletely filled d subshells (valence contribution), cause peak splittings for this reason. These quadrupole splittings furnish further information on the chemical environment of a $^{57}Fe$ atom.

In applied magnetic fields, or when incorporated into magnetically ordered materials, the nuclear levels of $^{57}Fe$ experience a Zeeman splitting, as shown in Figure 3.4. The six line spectrum is caused by interaction of the nuclear magnetic moment with the surrounding magnetic field, predominantly through the Fermi contact interaction. This requires unpaired s electron density at the nucleus and occurs even when the s shells are full via spin polarisation caused by the unpaired d electrons. The splitting between the first and sixth lines of the spectrum is proportional to the size of the applied or internal magnetic field. Shifts in lines 2 and 5 occur when an electric field gradient is simultaneously present, the magnitude of which is dependent both on the angle between the magnetic field and the principal axis of the EFG tensor and on the magnitude of the principal axis. The complex spectra of magnetically ordered ferrous oxide powders [24] must result from appreciable quadrupole interactions and a variety of sites of different symmetry. In polycrystalline materials, the six lines have the intensity ratio 3:2:1:1:2:3, but in single crystal experiments the intensity of the (2,5) lines depends on the angle between the hyperfine field and the incident $\gamma$-ray.

### 3.3.2 Experimental Procedure

The spectra were recorded either on a Ranger Electronic or a Harwell constant acceleration spectrometer, both of which used a room temperature rhodium matrix source. In this type of spectrometer, the source is moved cyclically so that the range of velocities of interest is covered several times a second. The counts from the detector are fed into a multi-channel analyser at accurate time intervals such that each channel corresponds to the same velocity increment. The spectrum is scanned

repeatedly until an adequate signal-noise ratio is obtained, and then calibrated by recording the spectrum of natural α-iron foil at room temperature.

Analyses of the spectra were performed using least squares minimisation programs implemented on the IBM 370/168 at Harwell and the Amdahl-7 at the University of Missouri-Rolla. All the spectra discussed in Chapter 6.1.2 were modelled using a single broad high-spin iron (111) resonance and up to three high-spin iron (11) quadrupole doublets in which the components were constrained to be equal in width and area. The parameters reported in Table 6.2 have errors of approximately 0.02 mm/s.

## 3.4 Magnetic Susceptibility Measurements

The quantity known as the magnetic susceptibility is defined in equation 2.6, and may be referred to unit mass ($\chi$), one mole ($\chi_m$) or unit volume ($\kappa$) of a specimen. It gives an indication of the reaction of a substance to a magnetic field, a property which may be related to the electronic characteristics of the atoms or ions constituting the material. All methods of measurement depend on the detection of the force (dF) experienced by a material when placed in an inhomogeneous magnetic field (H) [227]. When the magnetisation, M, is uniform throughout the specimen and the field varies with position (dH/dx), the force is given by

$$dF = -mM \frac{dH}{dx} = -m \chi H \frac{dH}{dx} \qquad (3.17)$$

where m is the mass of the specimen. The most common measurement techniques are those based on the Faraday method, in which the force is measured directly, and the Gouy method, where the force is integrated

over a large difference in field gradient. A Faraday balance was used in the investigations referred to in this thesis and will be described here.

A small quantity (~ 25 mg) of sample was placed in a teflon bucket and suspended in a region of constant dH/dx by a torsion fibre attached to a microbalance. The sample chamber was flushed out with helium and the region of constant dH/dx was extended by the use of specially shaped magnetic pole pieces. The displacement of the bucket was kept to a minimum and the field gradient was in the vertical direction (x). Temperatures between 50 and 300K were obtained using a Janis Supervaritemp cryostat and a Lake Shore cryotronics temperature controller incorporating a calibrated silicon diode. The magnetic field was measured with a Hall probe gaussmeter and forces were determined for nine fields up to nine KGauss.

Beforehand, the factor dH/dx ($\beta$) was realised for each field using a standard whose susceptibility is accurately known ($Hg[Co(CNS)_4]$. Likewise, a diamagnetic correction ($\delta$) for the teflon cup at each field was determined, and a similar correction for the diamagnetism of the inner electron shells of the ions concerned was calculated. The mass susceptibility is then

$$\chi = \frac{\beta(dF + |\delta|)}{m} \quad \text{erg. Oe}^{-2}\text{. g}^{-1} \qquad (3.18)$$

The molar susceptibilities obtained at the nine fields for five $MnO\text{-}Fe_zO$ samples are set out in Appendix 2, and the field-weighted averages of these measurements are plotted in Figure 6.11.

# PART II

# RESULTS AND DISCUSSION

# CHAPTER FOUR

# MAGNETIC ORDERING IN $Mn_xNi_{1-x}O$

## 4.1 Magnetic Phase Diagram

Susceptibility measurements[184] show that $T_N$ varies approximately linearly with composition for $Mn_xNi_{1-x}O$ ($x < 0.5$), but no data are available for the manganese-rich portion of the phase diagram. We have examined the region with $x > 0.5$ by monitoring the {111} magnetic neutron diffraction peak of $Mn_{0.77}Ni_{0.23}O$ as a function of temperature. The Néel temperature determined by extrapolating to zero intensity is plotted, together with the previous values [184], in Figure 4.1, and an approximately linear variation over the whole range is confirmed.

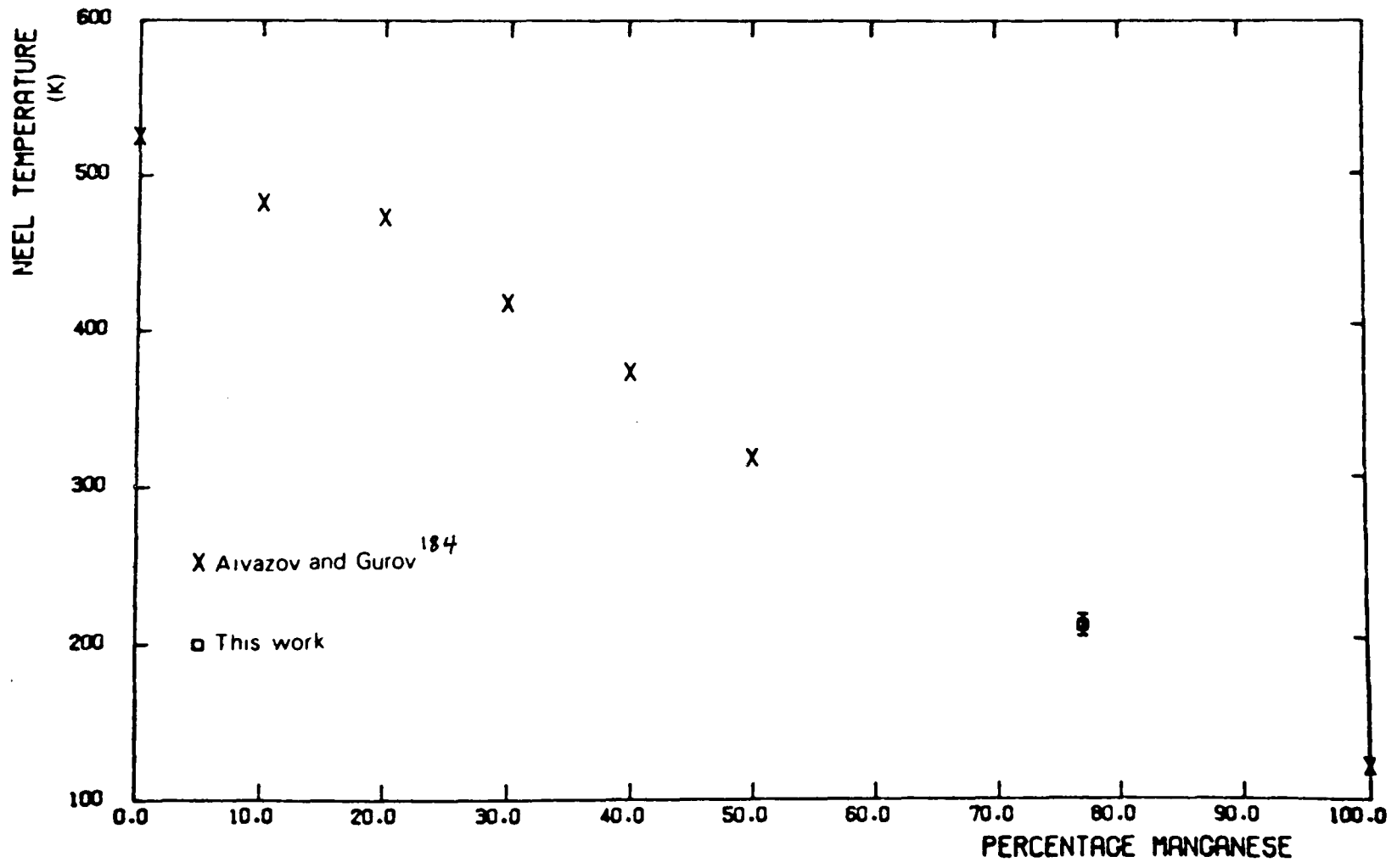



Figure 4.1 Néel Temperature as a Function of Composition for $Mn_xNi_{1-x}O$.

Although NiO and MnO both have (111) easy planes, the discussion in section 2.2.2 shows that the easy axis of MnO is experimentally undetermined and that theoretical treatments [122,123] inconclusively favour both the $[\bar{1}10]$ and $[\bar{1}\bar{1}2]$ directions of the pseudocubic cell. While the latter vector is the same as the easy axis of NiO, the former is perpendicular to it, and the possibility of a non-collinear 'OAF" phase arises. However, this is ruled out by the linear $T_N(x)$ function, and the large n.n.n. superexchange must dominate any differences in the planar anisotropies of MnO and NiO. The $180^o$ nickel-oxygen-manganese superexchange constant is then the geometric mean of the analogous exchange constants between like ions, as discussed by Bacon et al [61] (section 2.3).

A crude theoretical representation of the temperature variation of the sublattice magnetisation is obtained using the curve derived from the Brillouin function (section 2.2.1(a)), and this may be compared with experiment by taking the square root of the intensity of a magnetic Bragg peak at a particular temperature. According to equations 3.2 and 3.5, $\sqrt{I}$ is proportional to the mean sublattice moment. In MnO and NiO, the Brillouin-derived function falls off more rapidly than the observed magnetisation [228,229], and the theoretical treatment must be improved by the use of the Greens' function approximation and by taking into account exchange-induced lattice distortions[119]. In Figure 4.2, the observed decrease of the sublattice moment with increasing temperature in $Mn_{0.77}Ni_{0.23}O$ is compared with the Brillouin function (calculated using the mean of the spins of the different cations), and much better agreement is obtained than for the end members (MnO and NiO). Although this is probably somewhat fortuitous, it may be partially attributed to the presence of only a small exchangestriction

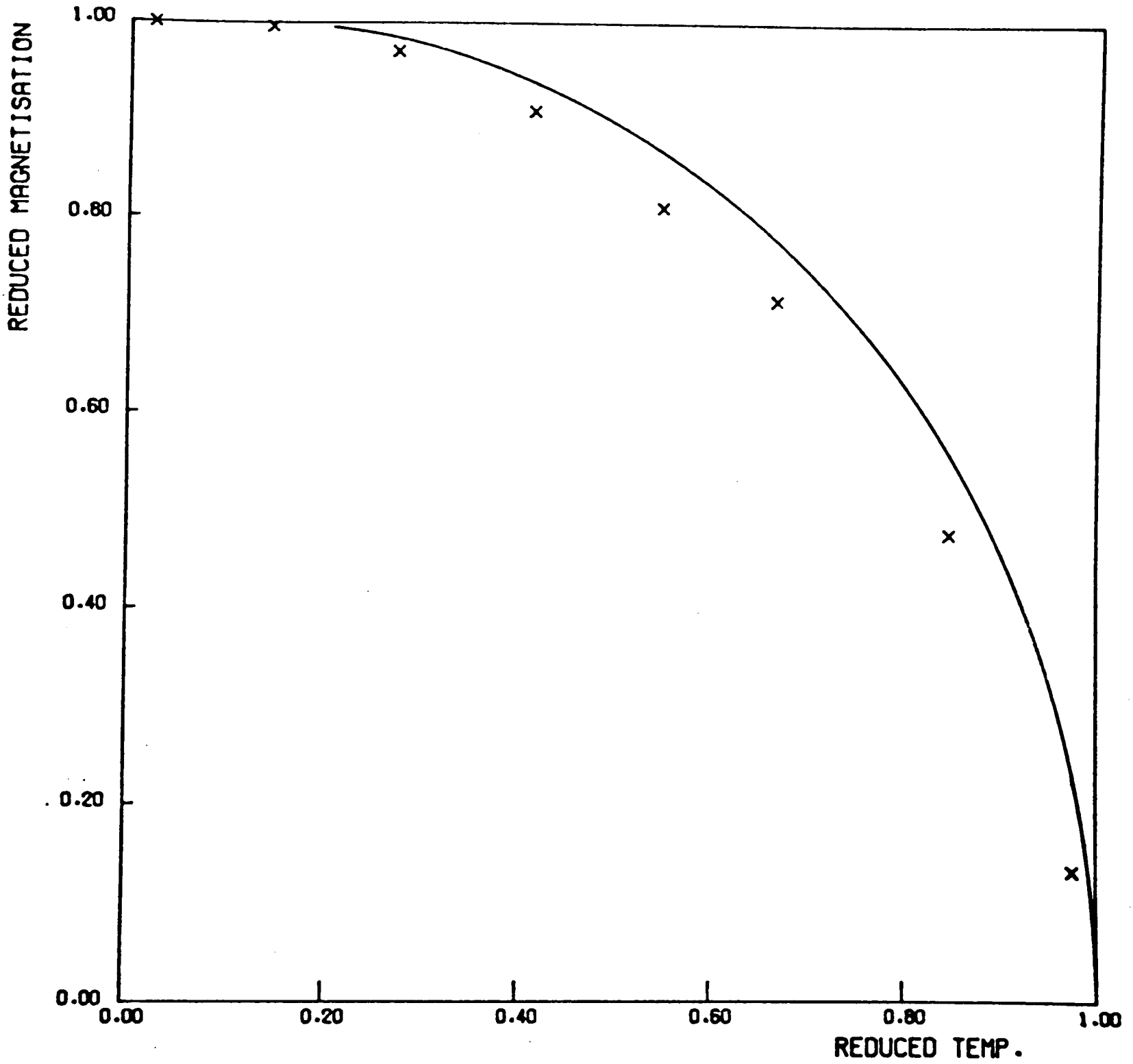



Figure 4.2 Temperature Variation of the Observed and Calculated Sublattice Magnetisation of $Mn_{0.77}Ni_{0.23}O$. Observed points-crosses, calculated-full line.

in this solid solution, for which further evidence and a discussion are presented in the final section of the chapter.

## 4.2 Magnetic Structure and Lattice Distortions at 5K

High resolution powder neutron diffraction profiles of MnO, NiO and solid solution samples containing 24, 48 and 77% manganese were recorded

| Composition | λ (Å) | a | b (Å) | c | α | β (°) | γ | B-overall + (Å$^2$) | μ* ($\mu_B$) | $R_{nuc}$ | $R_{mag}$ | $R_{pr}$ |
|---|---|---|---|---|---|---|---|---|---|---|---|---|
| NiO | 1.51 | 2.9510(1) | 2.9510(1) | 14.4266(5) | 90 | 90 | 120 | 0.0706(218) | 1.903(64) | 2.57 | 7.68 | 6.89 |
| | | 8.340 | 8.340 | 8.340 | 90.08 | 90.08 | 90.08 | | 1.903(100 | | | |
| $Ni_{0.76}Mn_{0.24}O$ | 1.51 | 2.9978(1) | 2.9978(1) | 14.6687(8) | 90 | 90 | 120 | 0.2353(164) | 2.532(32) | 1.52 | 4.57 | 4.76 |
| | | 8.478 | 8.478 | 8.478 | 90.03 | 90.03 | 90.03 | | 2.532(100) | | | |
| $Ni_{0.52}Mn_{0.48}O$ | 1.905 | 3.0440(2) | 3.0440(2) | 14.8974(8) | 90 | 90 | 120 | 0.5540(733) | 3.164(29) | 1.43 | 2.41 | 5.32 |
| | | 8.608 | 8.608 | 8.608 | 90.03 | 90.03 | 90.03 | | 3.164(40) | | | |
| $Ni_{0.23}Mn_{0.77}O$ | 1.51 | 8.7697(3) | 8.7697(3) | 8.7697(3) | 90.138(3) | 90.138(3) | 89.862(3) | 0.5404(226) | 3.907(62) | 3.07 | 4.85 | 7.84 |
| | | | | | | | | | 3.907(100) | | | |
| MnO | 1.51 | 3.1536(1) | 3.1536(1) | 15.2056(4) | 90 | 90 | 120 | 0.2530(184) | 4.575(28) | 2.77 | 2.75 | 7.04 |
| | | 8.864 | 8.864 | 8.864 | 90.61 | 90.61 | 90.61 | | 4.575(100) | | | |

* Two errors for each moment are shown. The first is that forthcoming from the profile analysis, and the second is estimated from changes in the form factor (section 3.2.4). Of the components of μ, $K_x=\mu$ and $K_y=K_z=0$ for all except $Mn_{0.77}Ni_{0.23}O$; here $K_x-K_y=2.766(44)$, $K_z=0$. + Isotropic temperature factor.

TABLE 4.1 Lattice and Magnetic Parameters for $Mn_xNi_{1-x}O$ (D1A diffractometer), referred to Pseudocubic and Trigonal (hexagonal) Cells.

using the PANDA and D1A diffractometers at wavelengths of 1.5 or 1.9 Å. The longer wavelength was used to provide more accurate magnetic parameters for $Mn_{0.48}Ni_{0.52}O$ (see section 3.2.3). The data were analysed by the Rietveld method according to the f.c.c. and trigonal (in the hexagonal setting) cells discussed in section 3.2.4, and the resulting magnetic and structural parameters are set out in Table 4.1. The agreement between observed and calculated profiles can be gauged from Appendix 1.

### 4.2.1 MnO and NiO

Although the end members of the $Mn_xNi_{1-x}O$ system have been the subjects of a number of previous powder neutron diffraction experiments (most recently by Roth [139], and Fender et al [218,222]), it was thought necessary to reconsider them in order to provide references for the analyses of the solid solution data. In addition, it seemed possible that the use of a high resolution diffractometer and profile analysis might reveal, in NiO, the small magnetostriction detectable by X-ray [124,125] and neutron topographical techniques [126].

Unfortunately, the resolution remains insufficient, and both MnO and NiO again appear trigonal with $\alpha > 90^o$ (Table 4.1). Likewise, both compounds have a (111) easy plane, as before, and the uniaxial configurational symmetry does not allow any deductions to be made as to the easy axis within this plane.

Initially, the $Mn^{2+}$ free ion form factor [218] was applied to the MnO data and a 17% expansion [219] along $\sin\theta/\lambda$ of the theoretical $Ni^{2+}$ curve was used for the NiO analysis. Although no improvement was obtained by

expanding or contracting the $Mn^{2+}$ form factor, equally good results were obtained for NiO with expansions of the $Ni^{2+}$ free ion curve less than the (previously accepted) 17%. Thus 11 and 17% expansions gave the same reliability indices, and the former value furnished a slightly better $R_{mag}$ (7.6 vs. 8.0), while increasing the observed moment from 1.85 to 1.93 Bohr magnetons. Consequently, the influences of covalency and spin-polarisation in NiO,for example, may be less than originally thought. The observed moments of MnO and NiO, $4{\cdot}6$ & $1{\cdot}9\ \mu_B$, are those expected when the reductions from 5 and $2.2\mu_B$ due to covalency and zero point spin deviation are taken into account (section 3.2.4).

### 4.2.2 Magnetic Scattering from the Solid Solutions

Good agreement with the solid solution magnetic intensities is obtained by calculating structure factors according to the magnetic structure adopted by MnO and NiO (Figure 2.8a). Table 4.1 shows that the moments are located within (111) planes and, as in the end members, the dipolar anisotropy **dominates,** as predicted for ions with orbital singlet ground states. In addition, the magnitudes of the magnetic moments fall on a straight line joining those of MnO and NiO (Figure 4.3), suggesting that a collinear spin structure is present at all compositions. This confirms the dominance of the $180^{\circ}$ n.n.n. super-exchange interactions revealed by the Néel temperature measurements (section 4.1).

If the MnO and NiO components have different easy axes, and the competing anisotropies are similar in size, intermediate moment directions may be adopted by the solid solutions. However, the moments are always within the (111) easy plane and, notwithstanding the limits set by the configurational symmetry (section 3.2.2), the neutron diffraction

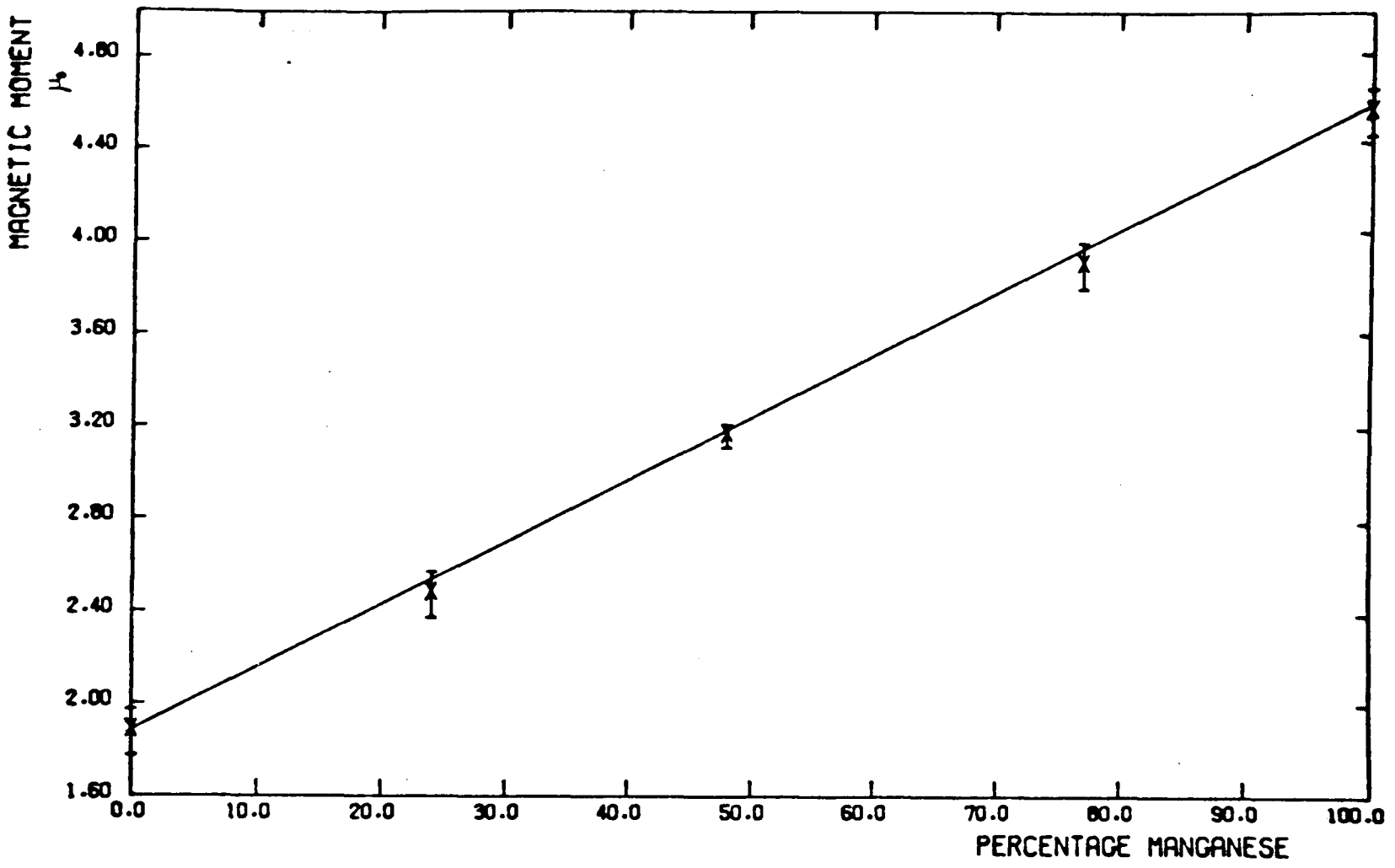



Figure 4.3 Mean Sublattice Moments for the Solid Solution $Mn_xNi_{1-x}O$.

experiment is very insensitive to small changes in the moment vector. Rather than being an example of a system where the effects of competing anisotropy energies are easily seen, the present study of $Mn_xNi_{1-x}O$ reveals a case where nearest neighbour exchange interactions of opposite sign lead to opposed trigonal lattice distortions, as described below.

### 4.2.3 Structural Changes across the Solid Solution Series

Only the reflections characteristic of the sodium chloride lattice are observed in any of the powder profiles, and therefore no long range ordering of nickel and manganese occurs. Neutron diffraction should be very sensitive to regular arrangements of the two atoms owing to the appreciable differences in their scattering lengths (Mn: $-0.372 \times 10^{-14}$m, Ni: $1.03 \times 10^{-14}$m).

However, unusual behaviour is evident from Table 4.1, in that the exchangestrictions of all the solid solutions are much smaller than those predicted by a linear interpolation between NiO ($\alpha = 90.08^{o}$) and MnO ($\alpha = 90.61^{o}$), an observation confirmed by inspection of parts of the high angle regions of the neutron powder profiles of MnO, $Mn_{0.77}Ni_{0.23}O$, $Mn_{0.24}Ni_{0.76}O$ and NiO (Figure 4.4). Except for MnO, the small peak splittings are evidence for symmetries very close to cubic, and this behaviour can be explained by recourse to an examination of the exchange interactions present.

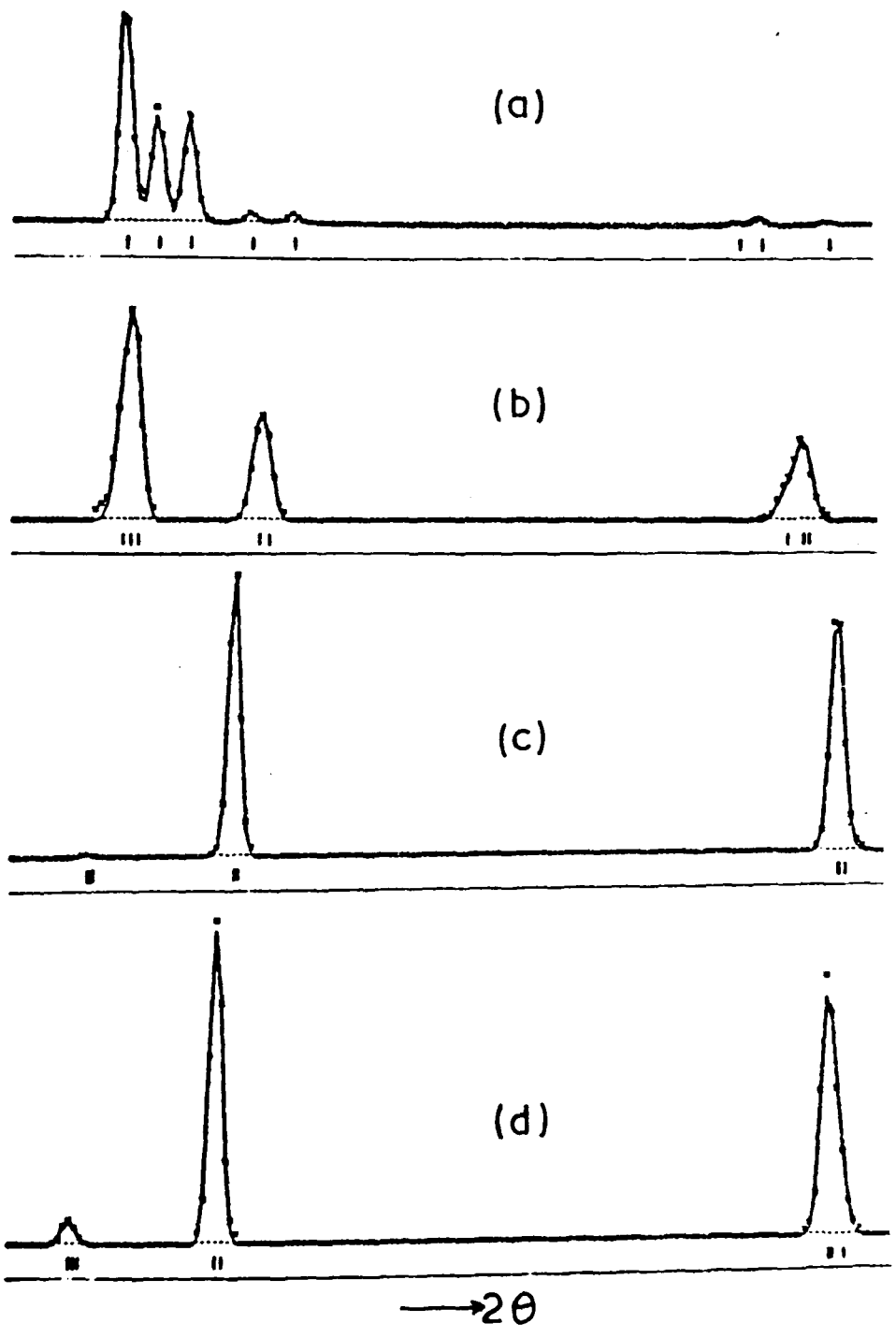



Figure 4.4 Pseudocubic {662}, {840} and {844} peaks of (a) MnO, (b) $Mn_{0.77}Ni_{0.23}O$, (c) $Mn_{0.24}Ni_{0.76}O$ and (d) NiO.

While the 180° cation-anion-cation superexchanges between like and unlike cations in $Mn_xNi_{1-x}O$ are antiferromagnetic since they always involve half-filled $e_g$ orbitals, the signs of the nearest neighbour interactions are influenced by the mechanism of the superexchange and the occupancies of the $t_{2g}$ orbitals (section 2.2.1(b)). The sign and size of the resultant exchangestriction then depends on whether the interactions are ferromagnetic or antiferromagnetic and on their sensitivities to changes in interionic distance. Thus, the large trigonal exchangestriction of MnO can be attributed to antiferromagnetic cation--cation superexchange, whereas the much smaller distortion of NiO depends on an antiferromagnetic 90° cation-anion (s orbital) - cation interaction.

In $Mn_xNi_{1-x}O$, the $\alpha > 90°$ exchangestrictions characteristic of MnO and NiO appear to be opposed by a distortion in the opposite sense, which can be associated with a new ferromagnetic component involving cation--cation exchange between $Ni^{2+}$ and $Mn^{2+}$. These are high-spin ions in oxides because the intra-ionic exchange stabilisation, $\Delta_{ex}$, is larger than the cubic crystal field splitting, $\Delta_c$, and in the ferromagnetic case a β-spin $Ni^{2+}$ electron is transferred such that the intra-atomic exchange of $Ni^{2+}$ is not disrupted (Figure 4.5). An antiferromagnetic alignment of the $Ni^{2+}$ and $Mn^{2+}$ spins would involve the virtual transfer of a $t_{2g}$ $Ni^{2+}$ α-spin electron, which has the additional stabilisation, $\Delta_{ex}$. It is noteworthy that the lattice parameter results discussed here are confirmed by previous susceptibility measurements[184] on the solid solution, where it is observed that $|\theta|/T_N$ decreases from ~ 3 in NiO and ~ 5.2 in MnO to ~ 1.5 in $Mn_{0.5}Ni_{0.5}O$, indicating an increase in ferromagnetic coupling (section 2.2.1(a)).

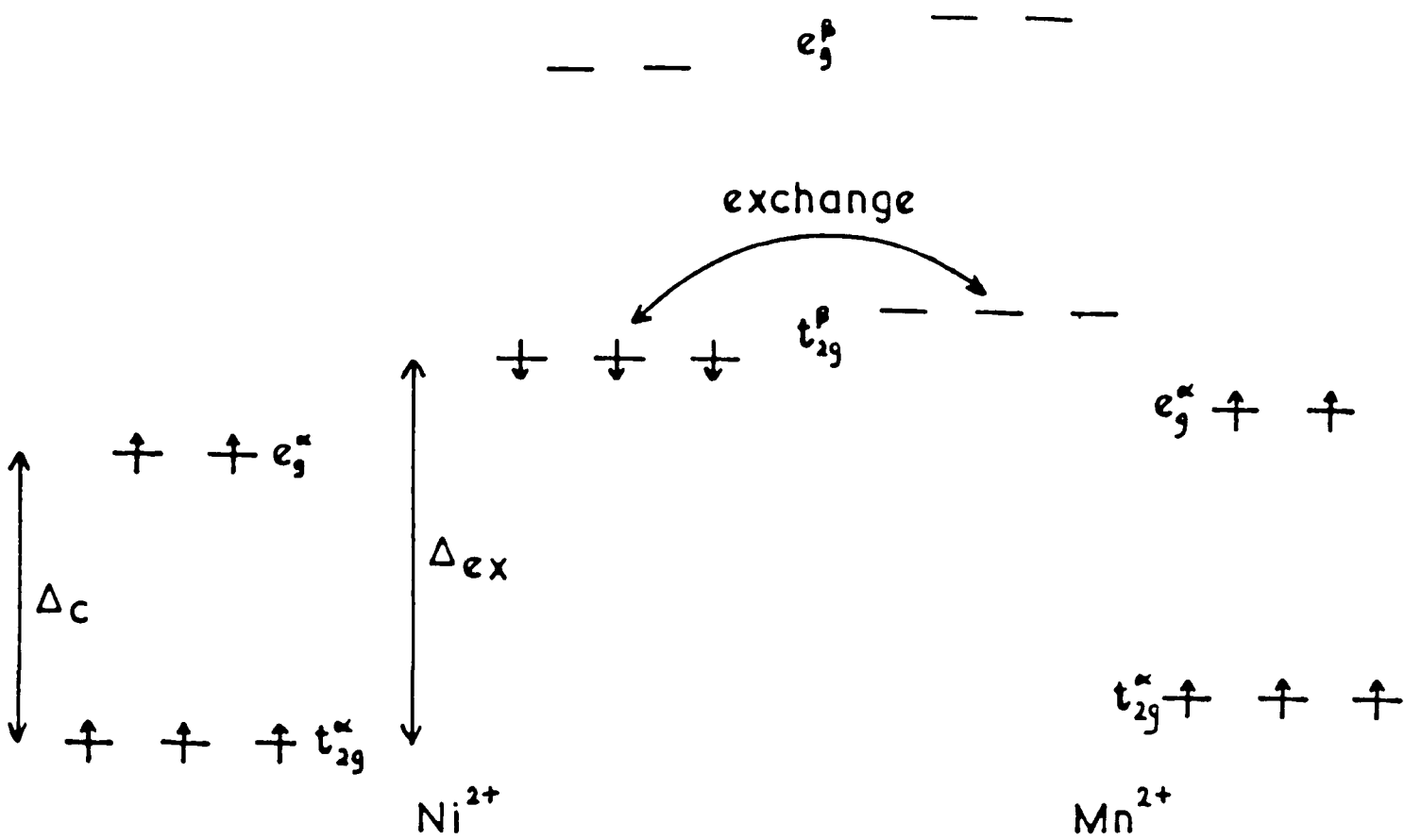



Figure 4.5 A schematic one-electron orbital diagram, showing the ferromagnetic $Ni^{2+}$- -$Mn^{2+}$ superexchange process.

In Table 4.1, it is noticeable that the 76% and 52% nickel compositions are represented both in the hexagonal and pseudocubic settings (with $a = b = c$, $\alpha = \beta = \gamma > 90^o$), while the 23% nickel sample is only shown to be pseudocubic, with $a = b = c$, $\alpha = \beta > 90^o$, $\gamma < 90^o$. Although the nuclear peaks could be refined equally well according to lattice parameters $a = b = c$, $\alpha = \beta = \gamma < 90^o$ (which, in fact, refer to the same cell as that shown in Table 4.1, projected along a different cube diagonal), the lattice symmetry and MnO-like magnetic structure could only be simultaneously accommodated using the lattice parameters quoted. While the latter furnished an $R_{pr}$ value of 7.8%, refinement according to the cell having $\alpha = \beta = \gamma < 90^o$ resulted in $R_{pr} = 10.7\%$. This can be seen by comparing the very poor fits to the magnetic peaks of Figure 4.6 with the full profile for this composition in Appendix 1.

The combination of magnetic and nuclear ordering therefore produces a propagation vector of the magnetic structure which is not parallel to

a three-fold axis. This suggests that appreciable magnetoelastic coupling is present, which is unreasonable in a system containing ions known to give rise to very small magnetostrictions. Conversely, the observed symmetry does not seem compatible with exchangestrictive distortions which, on the basis of the end members, are expected to reflect the trigonal symmetry of the magnetic structure. In order to try to explain this paradox, an attempt was made to fit the magnetic peaks to the alternative f.c.c. type 2 magnetic structure [80] shown in Figure 2.8(b), but without success. Another possibility is a three-axis magnetic structure resulting from the competition between exchange, dipolar anisotropy and crystal field effects, but this is ruled out because it requires, for equal sublattice magnetisations, moments directed out of the (111) plane [79]. This being so, the cause of this aspect of the behaviour of $Mn_{0.77}Ni_{0.23}O$ is unclear at present.

## 4.3 Summary

The main conclusions of this chapter are as follows:

(a) No superlattice ordering of $Ni^{2+}$ and $Mn^{2+}$ ions is evident in any of the three solid solutions studied.

(b) Contrary to earlier estimates, only a 11% expansion of the $Ni^{2+}$ free ion form factor is necessary in order to achieve good agreement with the NiO magnetic peaks.

(c) Each sample has a (111) easy plane, owing to the dominance of the dipolar anisotropy. Measurements of the Néel temperatures and magnetic moments indicate that the spin structure is collinear at all compositions. No "oblique antiferromagnetic" phase results from the possible competition between the magnetic anisotropies of NiO and MnO, and the

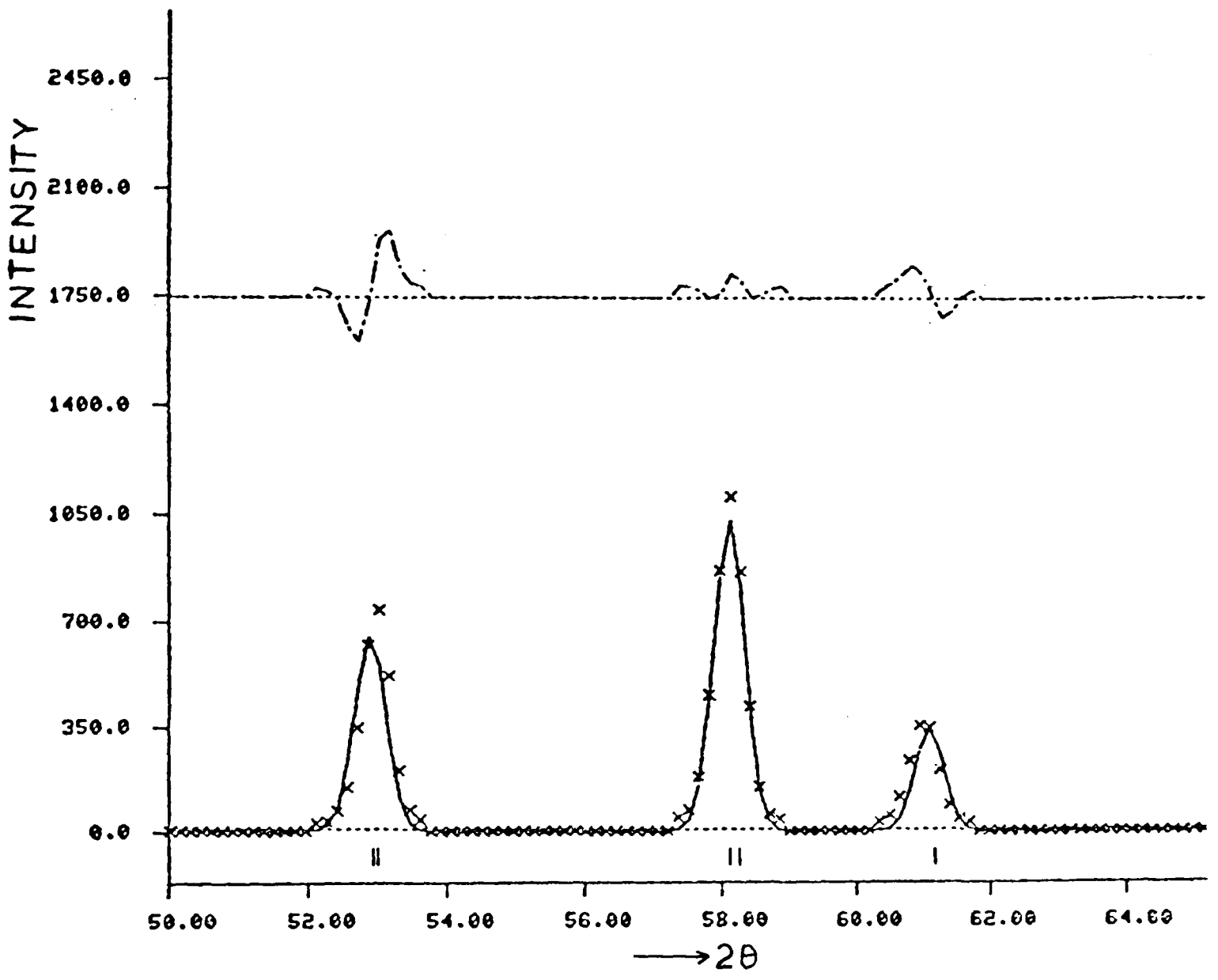



Figure 4.6 Pseudocubic {511,333}, {440} and {531} Peaks of $Mn_{0.77}Ni_{0.23}O$ Modelled for a=b=c, $\alpha=\beta=\gamma<90^{o}$.

$180^{o}$ cation-oxygen-cation superexchange is the most important interaction.

(d) The rhombohedral ($\alpha > 90^{o}$) distortions characteristic of MnO and NiO are largely quenched in the solid solutions because of ferromagnetic nearest neighbour exchange interactions between $Ni^{2+}$ and $Mn^{2+}$. However, the origin of the conflict between the apparent magnetic and nuclear symmetries of $Mn_{0.77}Ni_{0.23}O$ remains obscure.

# CHAPTER FIVE

# MAGNETIC ORDERING IN $Mn_xCo_{1-x}O$

## 5.1 Magnetic Phase Diagram of $Mn_xCo_{1-x}O$

The compositional dependence of the Néel temperature in $Mn_xCo_{k-x}O$ has been studied by Bacon, Street and Tredgold [61], and more recently by Kleinclauss et al [116]. Although the former determine the variation of magnetic susceptibility with temperature, and the latter measure specific heats, the agreement is very good and an approximately linear $T_N(x)$ function is observed (Figure 5.1). This rules out an "OAF" phase

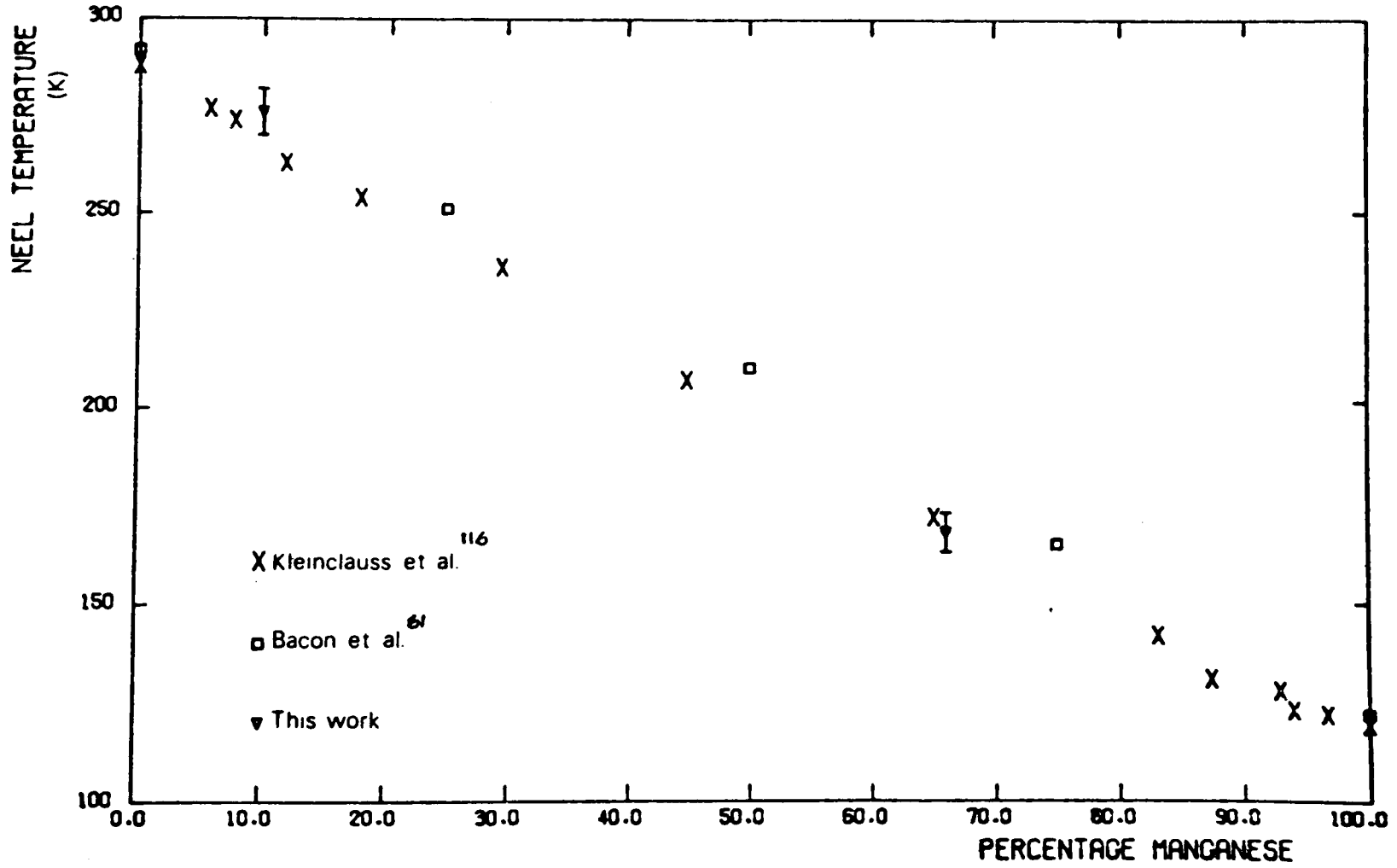



Figure 5.1 Composition dependence of the Néel temperature in $Mn_xCo_{1-x}O$.

and confirms the predictions of molecular field theory (MFT) for f.c.c. ordering of the second kind [61] (section 2.3). We have now extended the

available data using a third measuring technique, neutron diffraction, in which the average sublattice magnetisation is monitored as a function of temperature. The (111) peaks of two samples, containing 10 and 67% manganese, were extrapolated to zero intensity to give the Néel temperatures plotted in Figure 5.1, and it is evident that the three methods of measurement agree well.

Using concentration-weighted values of the spin angular momentum, S, the observed temperature dependences of the sublattice magnetisations of $Mn_{0.1}Co_{0.9}O$ and $Mn_{0.67}Co_{0.33}O$ are compared with those predicted by the Brillouin-derived function (section 2.2.1) in Figures 5.2 and 5.3. The level of agreement for the 10% manganese sample is comparable with

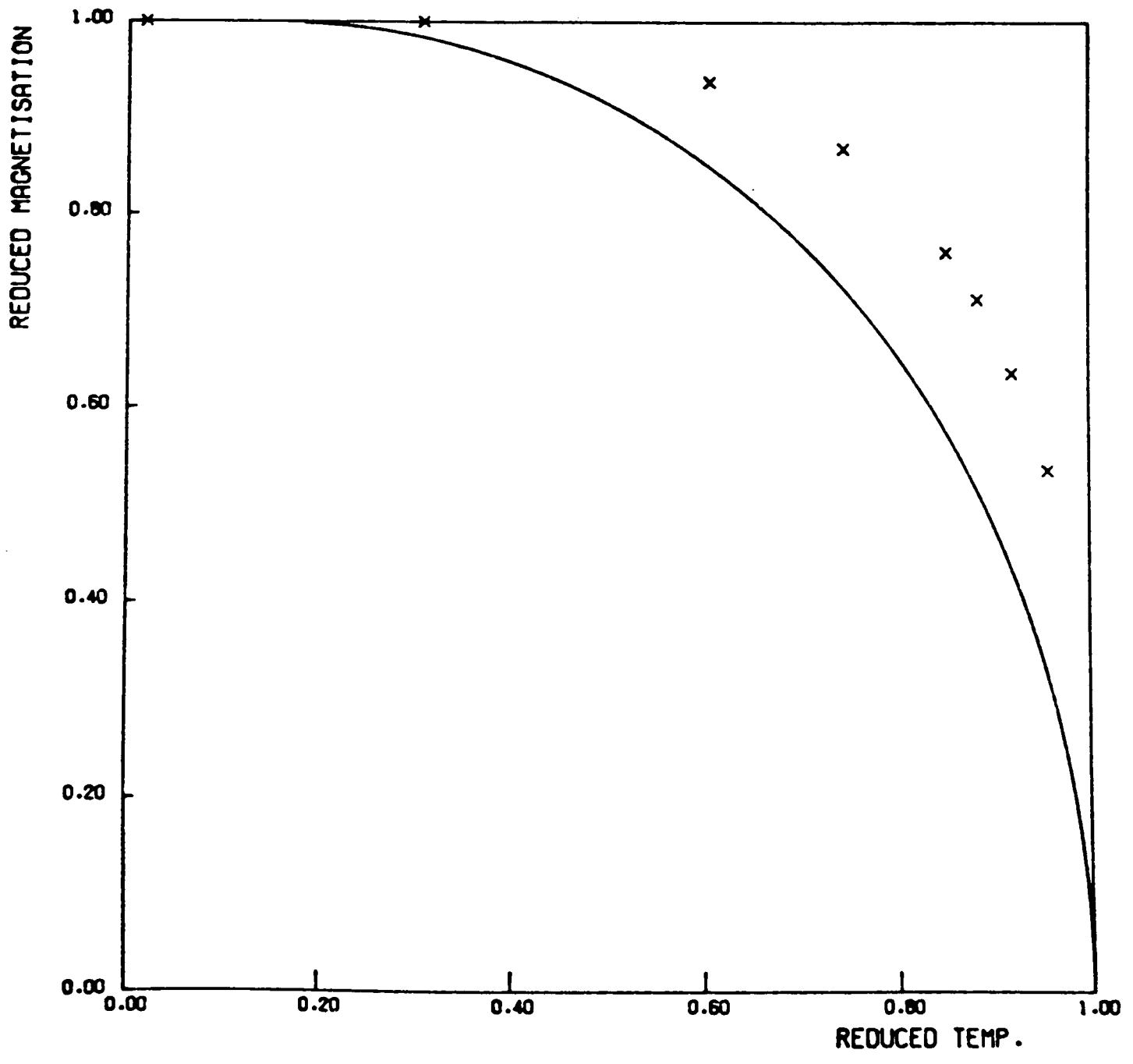



Figure 5.2 Temperature variation of the observed (crosses) and calculated (full line) sublattice magnetisation in $Mn_{0.1}Co_{0.9}O$.

that obtained in similar studies of CoO [230] and $Co_xNi_{1-x}O$ [2], in which the discrepancies are partially attributed to the residual orbital angular momentum of $Co^{2+}$, but mostly to the deficiencies of the MFT

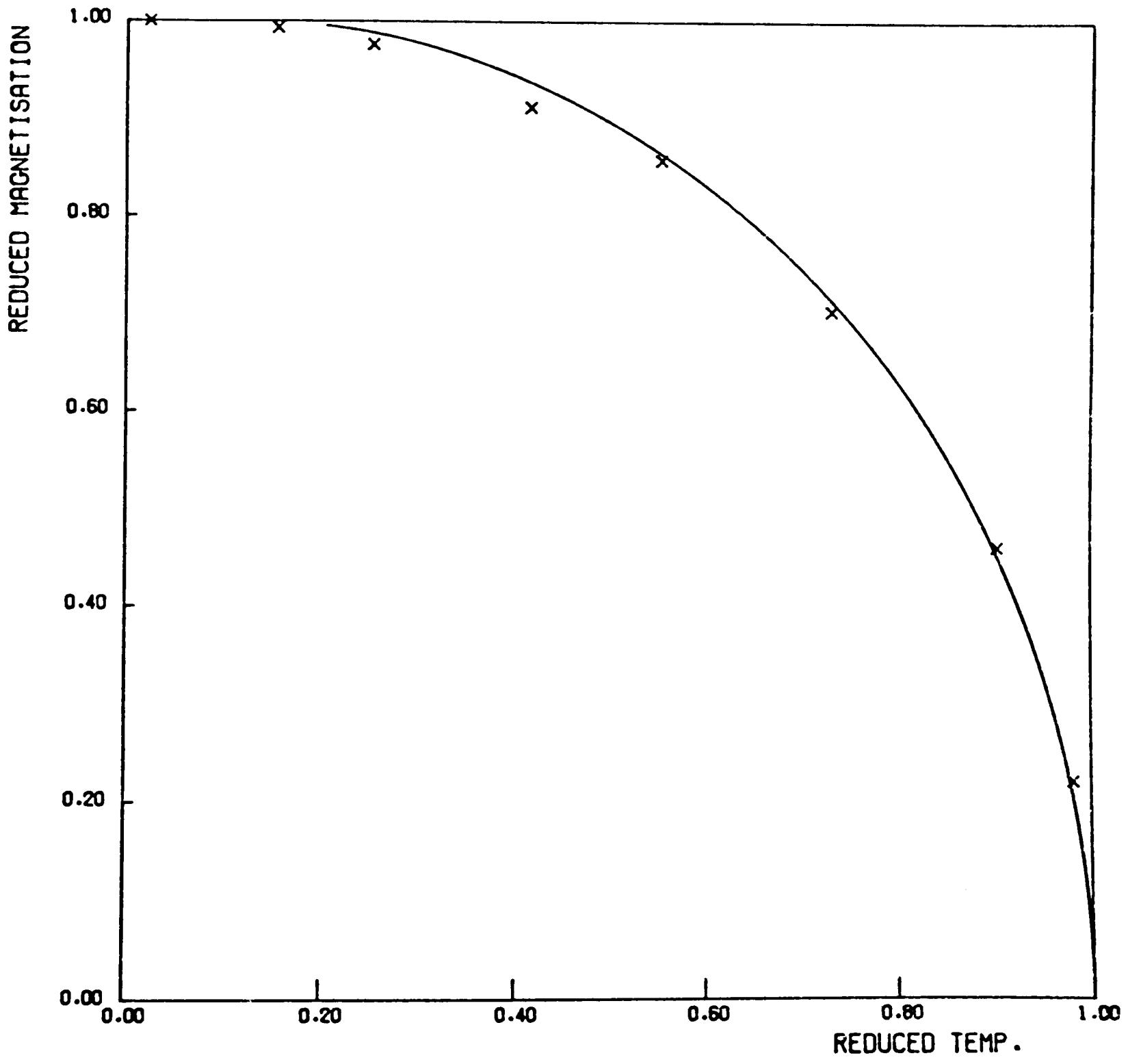



Figure 5.3 Temperature variation of the observed (crosses) and calculated (full line) sublattice magnetisation in $Mn_{0.67}Co_{0.33}O$.

approximation. The comparison is much better in the case of $Mn_{0.67}Co_{0.33}O$, which is surprising considering the bad agreement for the previous sample. A degree of improvement to the fit is likely if no orbital

contribution of $Co^{2+}$ is present (see section 5.2.3) but, by analogy with MnO [229], the trigonal distortion of this composition might be expected to lead to underestimation of the sublattice magnetisation at intermediate temperatures. Presumably, a large number of interactions are present here, which fortuitously cancel out.

## 5.2 Lattice Distortions and Magnetic Structure

### 5.2.1 Introduction

Unlike $Mn_xNi_{1-x}O$, the solid solution between CoO and MnO involves components having anisotropy energies and crystallographic distortions which arise from different single and multiple ion sources (section 2.2). Apart from the large exchangestriction of MnO, this system appears similar to $Co_xNi_{1-x}O$ [2], in which the single-ion anisotropy of cobaltous and its related magnetostriction are found to be dominant features. With the exception of an early, low resolution powder neutron diffraction study of the 50:50 composition [61], which demonstrates the absence of cation ordering in $Mn_xCo_{1-x}O$, no structural data is available for the low temperature phase of the system. However, the antiferromagnetic resonance (AFMR) spectra [231] of samples containing up to 6% cobalt show features similar to those observed in a similar study of $Co_xNi_{1-x}O$ [232]. The derived anisotropy constant, 32.8 $cm^{-1}$/ion, compares well with the magnetoelastic coupling energy of $Co^{2+}$ calculated by Kanamori [146], and it seems that the single ion anisotropy of $Co^{2+}$ is again the most important factor.

A powder neutron diffraction investigation of MnO, CoO and seven samples of their solid solution will now be described. The whole range of composition was studied at 5K, and two samples were additionally examined at temperatures up to the respective $T_N$'s. The same

high resolution diffractometer, D1A, was used for the two end members and the seven solid solutions, but two wavelengths were employed in an attempt to circumvent the unavoidable compromise which must be reached in a simultaneous analysis of nuclear and magnetic scattering (section 3.2.3).

The MnO results were discussed in detail in Chapter 4, but are repeated in Tables 5.1, 5.2 and 5.3 for comparison with the solid solution and CoO parameters. In most cases, it was desirable to analyse the diffraction patterns by decomposing the pseudocubic face-centred lattices into smaller primitive, C-centred or trigonal cells (section 3.2.4); where applicable, the lattice parameters appropriate to the reduced cells are given in Table 5.1, and the equivalent pseudocubic cell constants are set out in Table 5.2. The results of the magnetic refinements are presented in Table 5.3, and refer to the cells of Table 5.1. The derivation of the errors in the magnetic moment was discussed in section 3.2.4, but it should be stressed that those resulting from the profile analyses are underestimated. The next section is concerned with a discussion of cobaltous oxide, and this is followed by a consideration of the solid solution structural and magnetic data.

### 5.2.2 Cobaltous Oxide

A powder neutron diffraction investigation of CoO was carried out initially in order to provide a comparison with the solid solution magnetic data but, subsequently, a small exchangestriction was detected by profile analysis of the high resolution diffractometer data. This provides direct evidence for a single axis magnetic structure, but has only been observed previously by X-ray topography [82]. Table 5.1 shows that refinement according to a monoclinic, rather than tetragonal, unit

| COMPOSITION | | λ (Å) | a | b (Å) | c | α | β (o) | γ | B-overall* (Å$^2$) | $R_{nuc}$ | $R_{mag}$ | $R_{pr}$ |
|---|---|---|---|---|---|---|---|---|---|---|---|---|
| CoO | (a) | 1.904 | 8.5204(2) | 8.5204(2) | 8.4150(2) | 90 | 90 | 90 | -0.2105(371) | 1.59 | 4.75 | 5.56 |
| | (b) | 1.904 | 5.1738(9) | 3.0119(1) | 6.0258(14) | 90 | 54.413(10) | 90 | -0.1904(326) | 1.54 | 3.22 | 4.89 |
| $Co_{0.95}Mn_{0.05}O$ | | 1.513 | 8.5477(11) | 8.5299(11) | 8.4535(7) | 90 | 90 | 90 | 0.1521(542) | 4.52 | 4.35 | 8.63 |
| $Co_{0.90}Mn_{0.10}O$ | | 1.904 | 3.0096(2) | 3.0086(2) | 6.0104(5) | 60.327(6) | 90.467(2) | 60.288 | -0.232(398) | 3.25 | 3.55 | 5.96 |
| $Co_{0.75}Mn_{0.25}O$ | | 1.511 | 3.0386(4) | 3.0387(2) | 6.0693(7) | 60.139(9) | 90.368(4) | 60.154 | 0.2913(200) | 2.62 | 3.84 | 5.83 |
| $Co_{0.64}Mn_{0.36}O$ | | 1.512 | 3.0609(3) | 3.0599(2) | 6.1090(5) | 60.052(8) | 90.299(4) | 60.085 | 0.3404(165) | 3.38 | 2.75 | 6.15 |
| $Co_{0.49}Mn_{0.51}O$ | | 1.513 | 5.3341(4) | 3.0804(2) | 6.1340(3) | 90 | 54.767(4) | 90 | 0.6227(196) | 3.57 | 2.82 | 7.04 |
| $Co_{0.33}Mn_{0.67}O$ | | | | | | | | | | | | |
| | (a) | 1.511 | 5.3789(9) | 3.103(2) | 6.1678(9) | 90 | 54.608(9) | 90 | 0.3168(159) | 2.92 | 4.08 | 6.07 |
| | (b) | 1.904 | 5.3674(3) | 4.0973(2) | 6.1557(2) | 90 | 54.602(3) | 90 | 0.2961(234) | 1.73 | 3.61 | 5.16 |
| $Co_{0.17}Mn_{0.83}O$ | (a) | 1.512 | 5.4234(7) | 3.1297(4) | 6.204(7) | 90 | 54.449(8) | 90 | 0.2563(196) | 3.16 | 7.75 | 8.23 |
| | (b) | 1.512 | 5.4206(6) | 3.1311(3) | 6.2127(6) | 90 | 54.334(7) | 90 | 0.2553(201) | 3.22 | 3.25 | 7.35 |
| MnO | | 1.513 | 3.1536(1) | 3.1536(1) | 15.2056(4) | 90 | 90 | 120 | 0.2530(184) | 2.77 | 2.75 | 7.04 |

* Negative temperature factors are physically unreasonable and probably occur here because of the small range of $\sin\theta/\lambda$ sampled at 1.904 Å. Refinements in which B-overall was constrained to a positive value showed only slightly larger R factors.

TABLE 5.1 Lattice Parameters and R-values Obtained From Typical Refinements of Data from Samples in the $Mn_xCo_{1-x}O$ System at 5K (D1A diffractometer).

| SAMPLE | | a | b (Å) | c | α | β (o) | γ |
|---|---|---|---|---|---|---|---|
| CoO | (b) | 8.520 | 8.520 | 8.415 | 89.98 | 89.98 | 89.98 |
| $Co_{0.90}Mn_{0.10}O$ | | 8.541 | 8.554 | 8.471 | 89.96 | 90.08 | 90.01 |
| $Co_{0.75}Mn_{0.25}O$ | | 8.616 | 8.605 | 8.561 | 90.15 | 90.08 | 90.05 |
| $Co_{0.64}Mn_{0.36}O$ | | 8.671 | 8.650 | 8.626 | 90.22 | 90.12 | 90.09 |
| $Co_{0.49}Mn_{0.51}O$ | | 8.693 | 8.693 | 8.714 | 90.09 | 90.09 | 90.24 |
| $Co_{0.33}Mn_{0.67}O$ | (a) | 8.750 | 8.750 | 8.770 | 90.29 | 90.29 | 90.36 |
| | (b) | 8.733 | 8.733 | 8.751 | 90.29 | 90.29 | 90.36 |
| $Co_{0.17}Mn_{0.83}O$ | (a)* | 8.813 | 8.813 | 8.826 | 90.47 | 90.47 | 90.51 |
| | (b)+ | 8.821 | 8.821 | 8.808 | 90.50 | 90.50 | 90.45 |
| MnO | | 8.864 | 8.864 | 8.864 | 90.61 | 90.61 | 90.61 |

* $c/a > 1$,

\+ $c/a < 1$.

TABLE 5.2 Equivalent Pseudocubic Cells for $Mn_xCo_{1-x}O$ at 5K.

| SAMPLE | | $K_x$ | $K_y$ | $K_z$ | $\langle\mu\rangle^+$ ($\mu_B$) | $\theta^*$ (o) |
|---|---|---|---|---|---|---|
| CoO | (a) | 3.916(028) | - | -0.674(058) | 3.565(024) | 26.2 |
| | | | | | 3.565(040) | |
| $Co_{0.95}Mn_{0.05}O$ | | 1.029(089) | 1.029(089) | -3.143(179) | 3.464(019) | 24.9 |
| | | | | | 3.464(100) | |
| $Co_{0.90}Mn_{0.10}O$ | | 3.010(137) | 0.666(214) | 0.535(109) | 3.479(022) | - |
| | | | | | 3.479(050) | |
| $Co_{0.75}Mn_{0.25}O$ | | 1.525(295) | 2.365(241) | 0.585(194) | 3.636(023) | - |
| | | | | | 3.636(100) | |
| $Co_{0.64}Mn_{0.36}O$ | | 2.465(324) | 1.502(330) | 0.861(121) | 3.746(019) | - |
| | | | | | 3.746(100) | |
| $Co_{0.49}Mn_{0.51}O$ | | 0.405(638) | 3.633(149) | 0.824(179) | 3.798(025) | - |
| | | | | | 3.798(100) | |
| $Co_{0.33}Mn_{0.67}O$ | (a) | 1.599(348) | 3.158(243) | 1.186(126) | 4.017(063) | - |
| | | | | | 4.017(100) | |
| | (b) | 1.495(337) | 3.271(212) | 0.945(150) | 3.932(026) | - |
| | | | | | 3.932(050) | |
| $Co_{0.17}Mn_{0.83}O$ | (a) | - | 4.381(029) | - | 4.381(029) | - |
| | | | | | 4.381(029) | |
| | (b) | 4.395(030) | - | - | 4.395(030) | 35 |
| | | | | | 4.395(100) | |
| MnO | | 4.575(028) | - | - | 4.575(028) | 35 |
| | | | | | 4.575(028) | |

* Angle within $(1\bar{1}0)$ plane between moment and [001]

+ Two errors are shown, as discussed for $Mn_xNi_{1-x}O$ (Table 4.1).

TABLE 5.3 Components of Magnetic Vectors ($K_x$, $K_y$ and $K_z$)

cell furnished a profile R value improved by ~ 0.7%, and the fits to certain magnetic peaks were noticeably improved. The monoclinic parameters correspond to a small contraction of the pseudocubic cell angles (Table 5.2) and are compatible with ferromagnetic $Co^{2+}$--$Co^{2+}$ exchange[137]. The angles shown in Table 5.2 ($\alpha=\beta=\gamma=89.98^{o}$) are probably within the standard deviation for measurement of an angular distortion; otherwise the evidence for the exchangestriction seems strong.

Despite this confirmation of the nature of the CoO magnetic structure, the source of the anomalous magnetic moment direction remains to be conclusively explained. This experiment again shows that the cobaltous moment is ~ $26^{o}$ from [001] (Table 5.3), and the good resolution of the magnetic peaks, owing to the large tetragonal distortion and the use of a long wavelength, enables this result to be quoted with some confidence. In accordance with Kahn and Erickson [144], the best fit to the CoO magnetic data was obtained with a 15% expansion of the theoretical free ion form factor along $\sin\theta/\lambda$. The moment resulting, $3.57 \pm 0.04\mu_B$, is reasonable for an S = 3/2 ion with an appreciable orbital contribution.

In section 2.2.3, the apparent non-collinearity of the hyperfine field measured by solid state n.m.r. [150] and the magnetic moment determined by neutron diffraction was discussed briefly and the possibility of non-collinear spin and orbital angular momenta was raised. Okada and Yasuoka's [150] interpretation of the n.m.r. spectra assumes that the magnetic moment (measured by neutron diffraction) and spin directions are coincident, and an orbital moment $22.8^{o}$ from [001] is thereby derived. However, neutron diffraction does not reveal the spin direction when the spin and orbital moments are non-collinear, and an alternative explanation can be advanced. This is consistent with both n.m.r. and neutron measurements, and involves an orbital moment parallel to the

tetragonal axis of deformation, as predicted by the calculations of Kanamori [146].

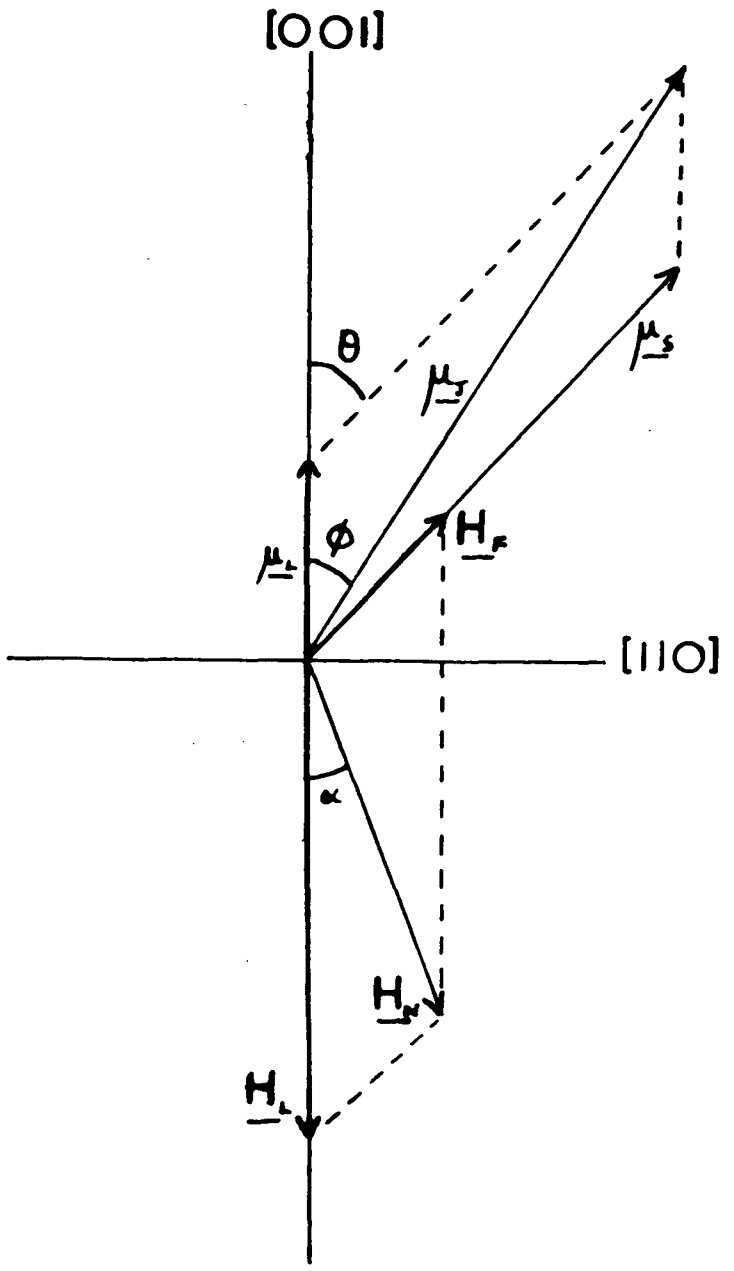



Figure 5.4 Vector diagram showing a possible non-collinear arrangement of the spin and orbital angular momenta of CoO. $\underline{\mu_S}$, $\underline{\mu_L}$ and $\underline{\mu_J}$ are the spin, orbital and total angular momentum vectors, and $\underline{H_N}$, $\underline{H_F}$ and $\underline{H_L}$ are the observed, Fermi contact and orbital hyperfine fields respectively.

Figure 5.4, which is adapted from a similar diagram of Okada and Yasuoka [150] shows that a total hyperfine field of +498 MHz at $\alpha = 21.1^{o}$ to [001] [150] can have components $H_L$ = +660 MHz along [001] and $H_F$ = -264 MHz at $\theta = 43^{o}$ to [001]. The value of $H_F$ was calculated by Okada and

Yasuoka [150], and their estimate of $H_L$ (+724 MHz) is close to that derived here. Combination of a spin moment of $gS = 2.7\mu_B$ (reduced by covalency from $3\mu_B$) in the direction of $H_F$ and an orbital moment of $1\mu_B$ along z then results in a magnetic moment of $3.5\mu_B$ inclined at $\phi = 31.7^o$ to the four-fold axis. These values are in remarkably good agreement with the neutron diffraction results, despite the very approximate nature of the calculation.

The model is attractive because it maximises the magnetoelastic coupling energy [146] and is consistent with the substantial tetragonal distortion observed, but some factor which compensates for the loss of spin-orbit coupling energy resulting from non-collinear $\underline{S}$ and $\underline{L}$ must be identified. A term which may account for the decoupling of $\underline{S}$ and $\underline{L}$, apart from the favoured maximisation of the magnetoelastic coupling energy, is the anisotropic n.n. exchange mechanism formulated by Yamada and Nakanishi [149]. The associated anisotropy constant favours {111}, but is again calculated on the assumption of collinear $\underline{S}$ and $\underline{L}$. However, the compensation in energy required from this term may not be very large since the spin-orbit coupling constant of $Co^{2+}$ in CoO is only 40% of its free-ion value ($-180$ cm$^{-1}$ vs. $-71$ cm$^{-1}$) [92]. A rough calculation of the spin-orbit coupling energy for configurations in which the orbital and spin momenta are (i) parallel and (ii) inclined at $43^o$ to one another illustrates this point. The spin-orbit coupling energy is given by

$$E_{S.O} = \lambda \underline{L}.\underline{S} = \lambda LS\cos\theta \qquad (5.1)$$

where $\lambda$ is the coupling constant and $\theta$ is the angle between $\underline{L}$ and $\underline{S}$. In the free ion, the difference in energy between the parallel and $\theta = 43^o$ situations is (270-197) = 72 cm$^{-1}$/ion, but in the crystal it is

29 $cm^{-1}$/ion.

### 5.2.3 Lattice Parameters of $Mn_xCo_{1-x}O$

According to Tables 5.1 and 5.2, the observed symmetry of $Mn_xCo_{1-x}O$ in the antiferromagnetic phase depends on the cationic ratio in a complicated way. As MnO is progressively doped into CoO, the symmetry changes from tetragonal-orthorhombic-triclinic-monoclinic-trigonal; these lattice parameters appear to be the products of exchangestrictions involving both cobaltous and manganese ions and, since $Mn^{2+}$ is in a $^6A_{1g}$ electronic state, of stabilisations to be gained by distortions of a $Co^{2+}$-containing octahedral site to lower symmetry (section 2.2.1(c)). Initially, exchange effects will be considered, and the remainder of the chapter is concerned with the implications of the orbital angular momentum of the cobaltous ion.

#### (a) Exchangestrictions at 5K

The exchangestrictions of MnO and CoO are caused by the sensitivity of antiferromagnetic and ferromagnetic cation--cation couplings, respectively, to ionic separation. Since the $Co^{2+}$ $t_{2g}$ orbitals are 5/6 full, the overall $Co^{2+}$-$Mn^{2+}$ cation--cation n.n. exchange should be ferromagnetic overall, and a cancellation of the $Mn^{2+}$--$Mn^{2+}$ exchangestriction (similar to that in $Mn_xNi_{1-x}O$) might be predicted. However, the $Mn^{2+}$--$Mn^{2+}$ exchange appears to be dominant here; Figure 5.5 shows the development of the pseudocubic {662} peak splitting (characteristic of a rhombohedral distortion) with increasing manganese concentration, and Figure 5.6 demonstrates that the striction increases gradually apart from a slight anomaly in the vicinity of the 50:50 composition. This may be caused by a trigonal Jahn-Teller ($\alpha < 90^o$) stabilisation of $Co^{2+}$ (Figure 2.10), which has the same symmetry as the $Mn^{2+}$-$Mn^{2+}$ exchange-

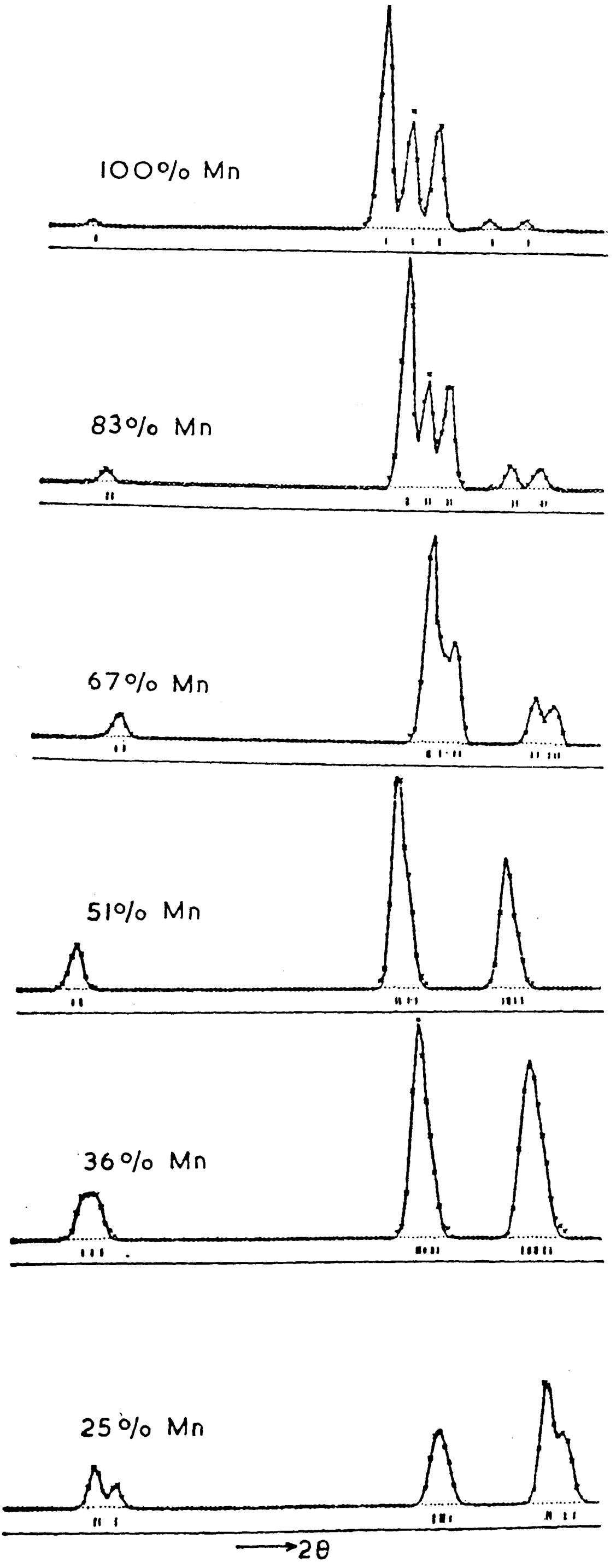



Figure 5.5 Pseudocubic {800},{662} and {840} peaks of $Mn_xCo_{1-x}O$.

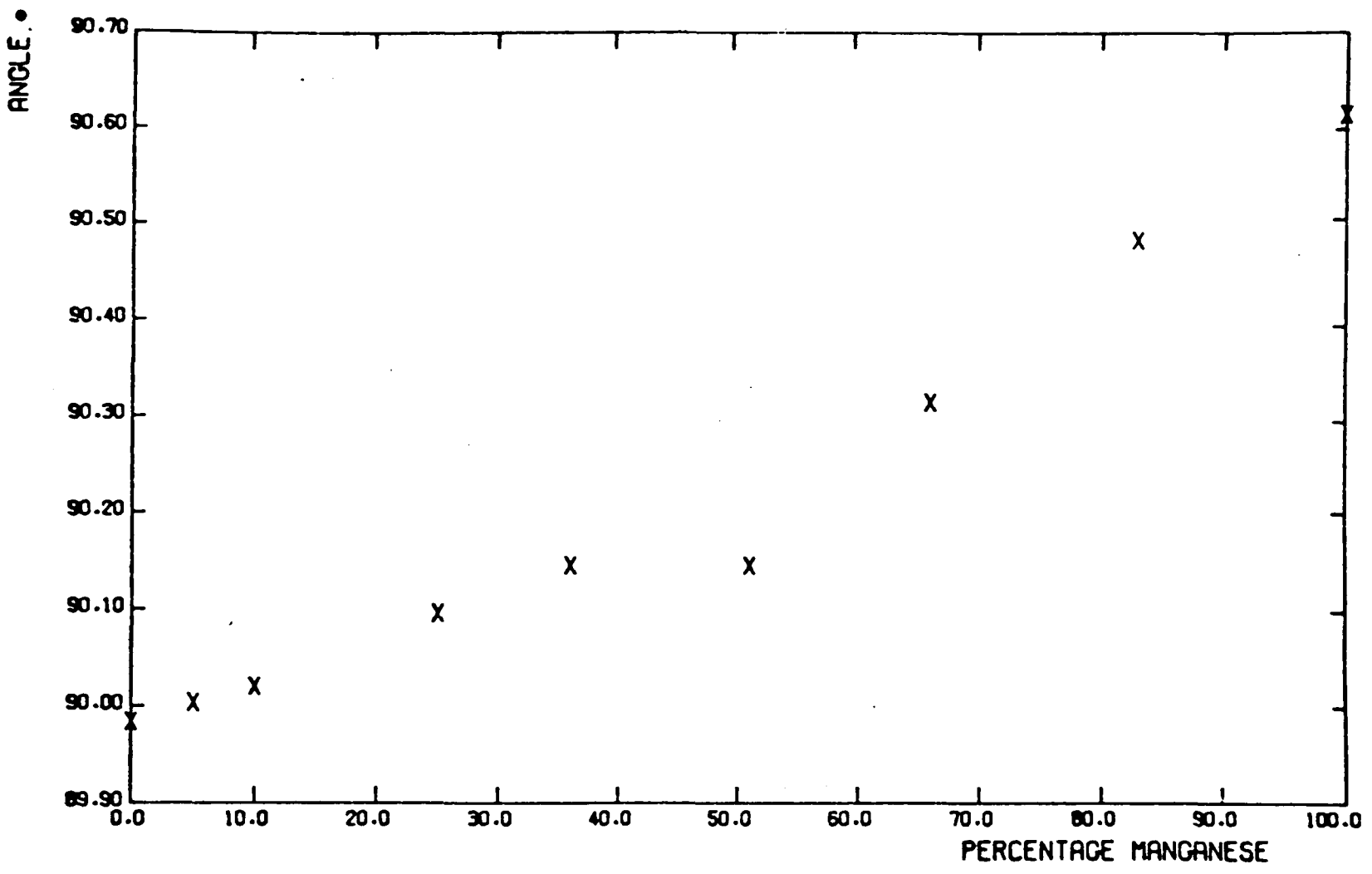



Figure 5.6 The average rhombohedral distortions of $Mn_xCo_{1-x}O$ plotted as a function of composition.

striction but produces a deformation in the opposite direction. However, the discussion in the next section suggests that this is never the major effect, despite the trigonal bias of the exchangestriction.

(b) Pseudocubic Axial Lengths at 5K

Evidence for the tetragonal distortion of CoO (a=b>c) is provided by the splitting of the pseudocubic {800} nuclear form into two components with intensity ratio 2:1, as shown in Figure 5.7(c). The same figure shows the equivalent peak at $\lambda$ = 1.904 Å for two solid solutions containing 90 and 33% cobalt, and it is clear that marked changes occur in the relative sizes of the axial lengths as the proportion of manganese increases. A further demonstration of this phenomenon is provided by

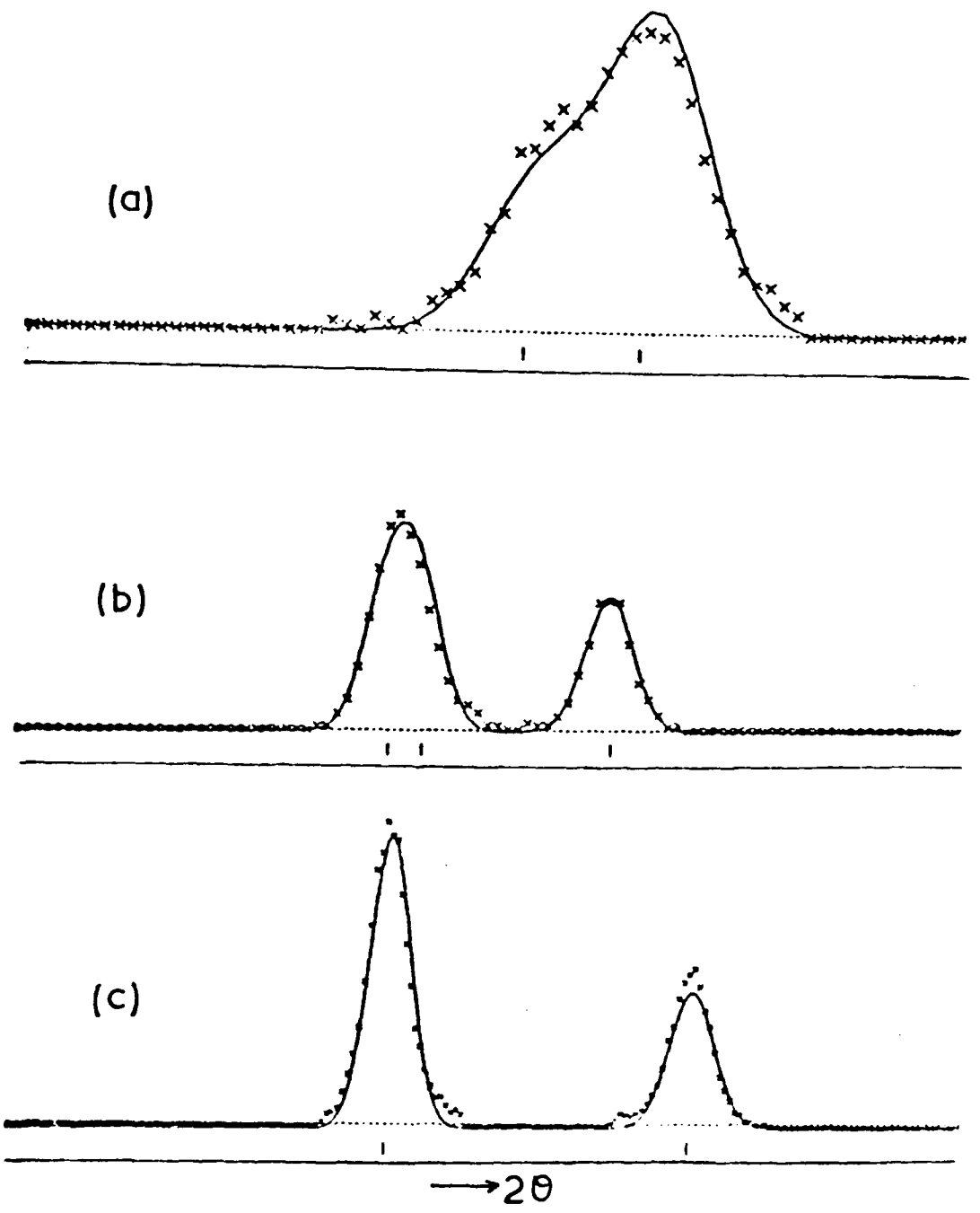



Figure 5.7 Pseudocubic {800} peaks of (a) $Mn_{0.67}Co_{0.33}O$, (b) $Mn_{0.10}Co_{0.9}O$ and (c) CoO. Reflection positions are marked.

the profile of $Mn_{0.36}Co_{0.64}O$ displayed in Figure 5.5, in which the {800} peak is split into three equally spaced components ($a \neq b \neq c$). The {800} form is also split into three, although not equally, in the 5-25% MnO samples; no trigonal distortion is apparent in orthorhombic $Mn_{0.05}Co_{0.95}O$, but the other compositions in this range all appear triclinic (Tables 5.1 and 5.2). However, in $Mn_{0.51}Co_{0.49}O$ and $Mn_{0.67}Co_{0.33}O$, monoclinic symmetry is observed which, unlike CoO, corresponds to a distorted cube having $a=b<c$ (a tetragonal elongation). The 67% manganese composition

was studied at two wavelengths (1.511 and 1.904 Å) and the longer revealed the pseudotetragonal expansion very clearly (Figure 5.7(a)). Part of the profile of $Mn_{0.83}Co_{0.17}O$ appears in Figure 5.5, and the dominance of the rhombohedral distortion is clear. Although the resolution is insufficient to observe any splitting of the {800} peak, the best refinement was obtained on the basis of a pseudocubic cell having a=b>c (c/a < 1), a setting similar to CoO (Tables 5.1 and 5.2).

Three regions of behaviour are apparent, therefore, and it is possible to explain these observations by postulating that the A ground state of octahedral $Co^{2+}$ (Figure 2.10) decreases in energy with progressive replacement of $Co^{2+}$ in CoO by $Mn^{2+}$. This behaviour seems to be related to the large trigonal distortion associated with the $Mn^{2+}$--$Mn^{2+}$ n.n. exchange (section 5.2.3(a)), since only features characteristic of the E ground state of $Co^{2+}$ are observed in $Co_xNi_{1-x}O^2$ and $(Co_xFe_{1-x})_zO$ (Chapter 6.2.2(b)); in these mixed crystals, the exchangestrictions are very small.

Initially, small concentrations of $Mn^{2+}$ in $Mn_xCo_{1-x}O$ seemingly quench the orbital contribution of $Co^{2+}$ to a limited extent, leading to triclinic or (when the overall trigonal magnetostriction is negligible) orthorhombic structures in which the magnetostriction (c/a < 1) and Jahn-Teller distortion (c/a > 1) coexist. These deformations are directed along different principle axes, producing the low symmetries observed (a≠b≠c), but the concomitant orbital splittings of $Co^{2+}$ are, apparently, insufficient to remove the orbital moment (and related magnetostriction) entirely. Larger exchangestrictions are associated with $Mn_{0.51}Co_{0.49}O$ and $Mn_{0.67}Co_{0.33}O$, which show monoclinic (a=b<c) symmetry, and here the $Co^{2+}$ orbital degeneracy must be lifted to such

a degree that only the Jahn-Teller stabilisation occurs. However, the AFMR data for 0.94 < % Mn < 1.0 (discussed in section 5.2.1) require that an orbital moment re-emerges in the manganese-rich region, which is consistent with the observed pseudotetragonal contraction of $Mn_{0.83}Co_{0.17}O$. Here, presumably, the cobalt concentration is too small to support a co-operative Jahn-Teller distortion of the $Co^{2+}$-containing octahedral sites, and a tetragonal magnetostriction develops despite the large trigonal $Mn^{2+}$--$Mn^{2+}$ exchangestriction.

The observed symmetries of samples having 0 < % Mn < 36 suggest that cobaltous ions having E and A ground states are simultaneously present. Consequently, the behaviour of a certain $Co^{2+}$ ion must be related to its environment and, in particular, to the exchangestriction determined by the number and distribution of manganous near neighbours. It appears that as little as 5% manganese is sufficient to affect a significant number of cobaltous ions, but (from the relative sizes of a, b and c) the proportion of Jahn-Teller $Co^{2+}$ ions does not increase markedly for manganese concentrations up to 25%. Presumably, a minimum number of manganese ions in the first co-ordination sphere of the majority of $Co^{2+}$ ions is necessary to produce a macroscopic predominantly Jahn-Teller distortion. This emphasises that the overall symmetry (for all the mixed systems studied in this thesis) is the resultant of the various local distortions. One might have expected the appreciable disorder to lead to large temperature factors but, bar $Mn_{0.51}Co_{0.49}O$, this is not the case (Table 5.1).

(c) Variable Temperature Experiments

In order to further examine the opposite tetragonal distortions, the {800} peaks of $Mn_{0.10}Co_{0.90}O$ and $Mn_{0.67}Co_{0.33}O$ were scanned at

temperatures up to, and above, the Néel temperatures. Both types of distortion should have temperature dependences similar to that of the sublattice magnetisation [102], but the Jahn-Teller tetragonal elongation is not linked to the magnetic ordering and should persist into the paramagnetic region [104]. Although thermal expansion is not taken into account in Figure 5.8, a,b and c of $Mn_{0.10}Co_{0.90}O$ all appear to have similar temperature dependences, and the predominance of the spin-orbit stabilisation at all temperatures is evident from the much shorter c axis. The Jahn-Teller effect may be present above $T_N$, but the resolution was insufficient to detect the associated distortion.

In $Mn_{0.67}Co_{0.33}O$, the behaviour is quite different, and is compared with the corresponding change in the rhombohedral distortion of the same compound in Figure 5.9. While the latter shows a similar temperature variation to that of MnO [98], c/a markedly decreases between 5 and 88K and then changes very slowly from 88K to 130K. Subsequently, the distortion diminishes sharply, and at 150K no significant tetragonality can be discerned, although appreciable broadening of the peaks was evident at lower temperatures, and summing over three counters of the diffractometer allowed accurate profile analyses to be carried out.

The unusual variable temperature behaviour of $Mn_{0.67}Co_{0.33}O$ must be related to the observation of a Jahn-Teller distortion at 5K, which is surprising since $x = 0.33$ is a smaller concentration than might be expected for co-operative coupling between interstices. For instance, in spinel solid solutions containing $Mn^{3+}$, the limiting composition ($x_t$) for the co-operative Jahn-Teller distortion varies from 0.4 to 0.73 [91], and in $Ni_xMg_{1-x}O$ [164,165] and other rocksalt solid solutions involving diamagnetic MgO [165], no long range magnetic ordering occurs for $x_t \leqslant 0.4$.

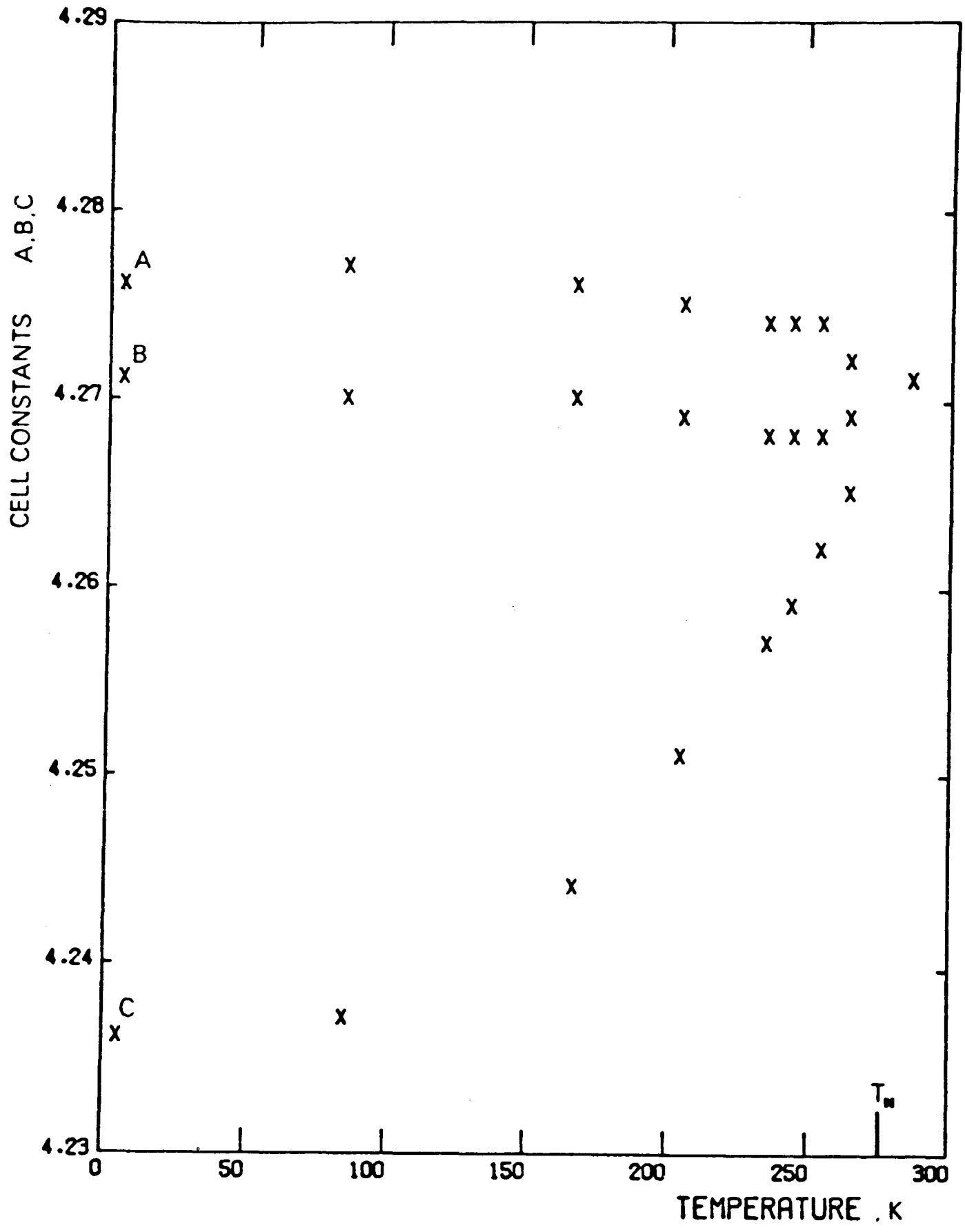



Figure 5.8 Temperature variation of the lattice parameters (A,B and C) of $Mn_{0.10}Co_{0.90}O$.

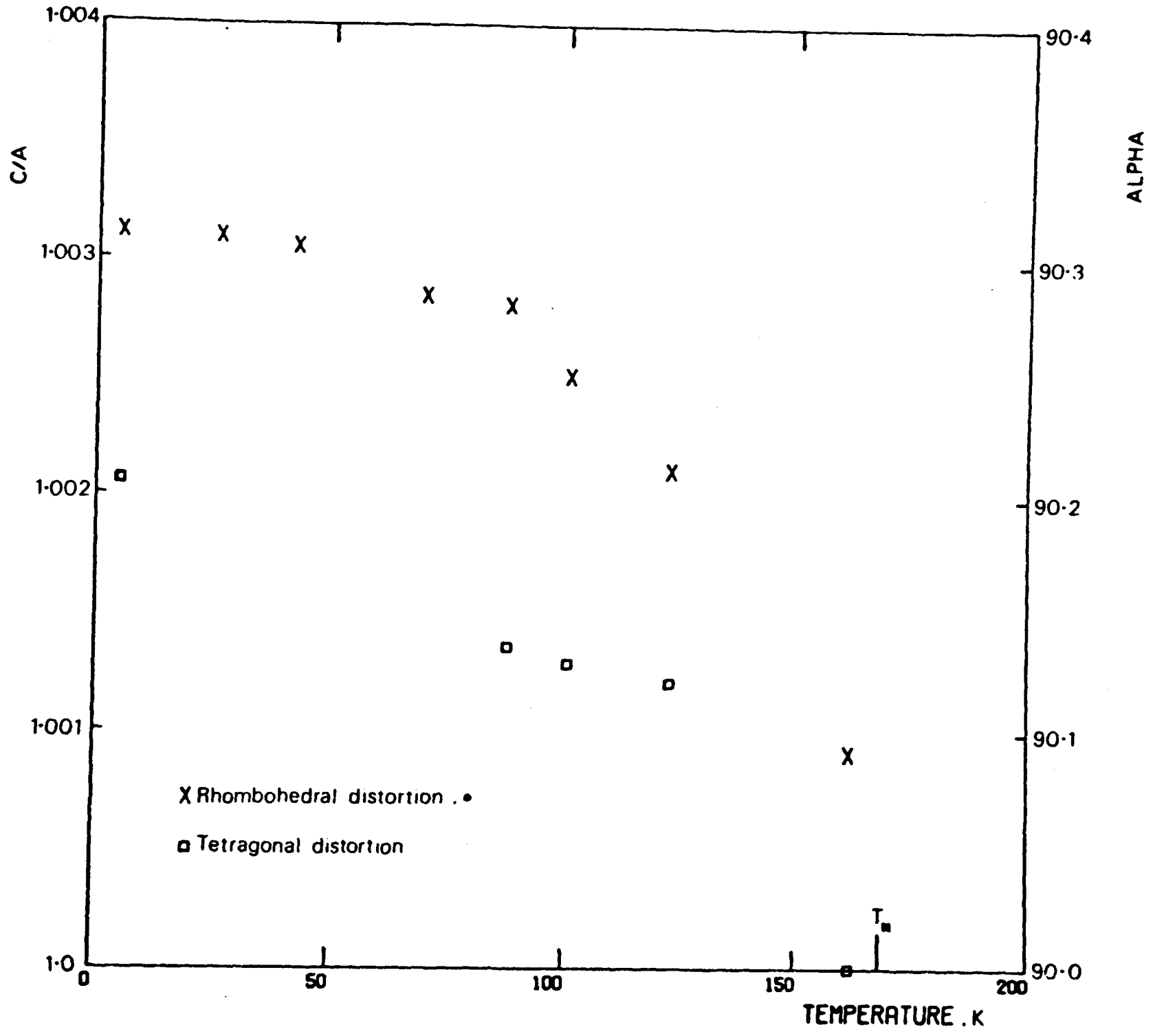



Figure 5.9 Temperature variations of the rhombohedral and tetragonal distortions of $Mn_{0.67}Co_{0.33}O$.

Although the magnesium oxide systems relate to co-operative magnetism, and the percolation limit of the f.c.c. lattice has been calculated to be as low as 0.18 for the site percolation mechanism [233,234], these examples provide approximate experimental values for the percolation limit in the rocksalt structure. The lack of a c/a > 1 distortion above, and slightly below, $T_N$ for $Mn_{0.67}Co_{0.33}O$ appears consistent with

the previous data for doped three-dimensional systems [91,164,165,166]; at lower temperatures it seems probable that the Jahn-Teller tetragonal expansion is induced by some magnetoelastic coupling generated upon magnetic ordering, despite this being associated with a tetragonal contraction.

### 5.2.4 Magnetic Parameters of $Mn_xCo_{1-x}O$ at 5K

No orbital angular momentum is present in the A ground state of a Jahn-Teller stabilised $Co^{2+}$ ion and, according to the results of the previous section, the magnetic moment of $Co^{2+}$ in $Mn_{0.67}Co_{0.34}O$ should be less than, for example, $Co^{2+}$ in CoO. This is confirmed by Figure 5.10, where the magnetic moment of each solid solution at 5K is plotted.

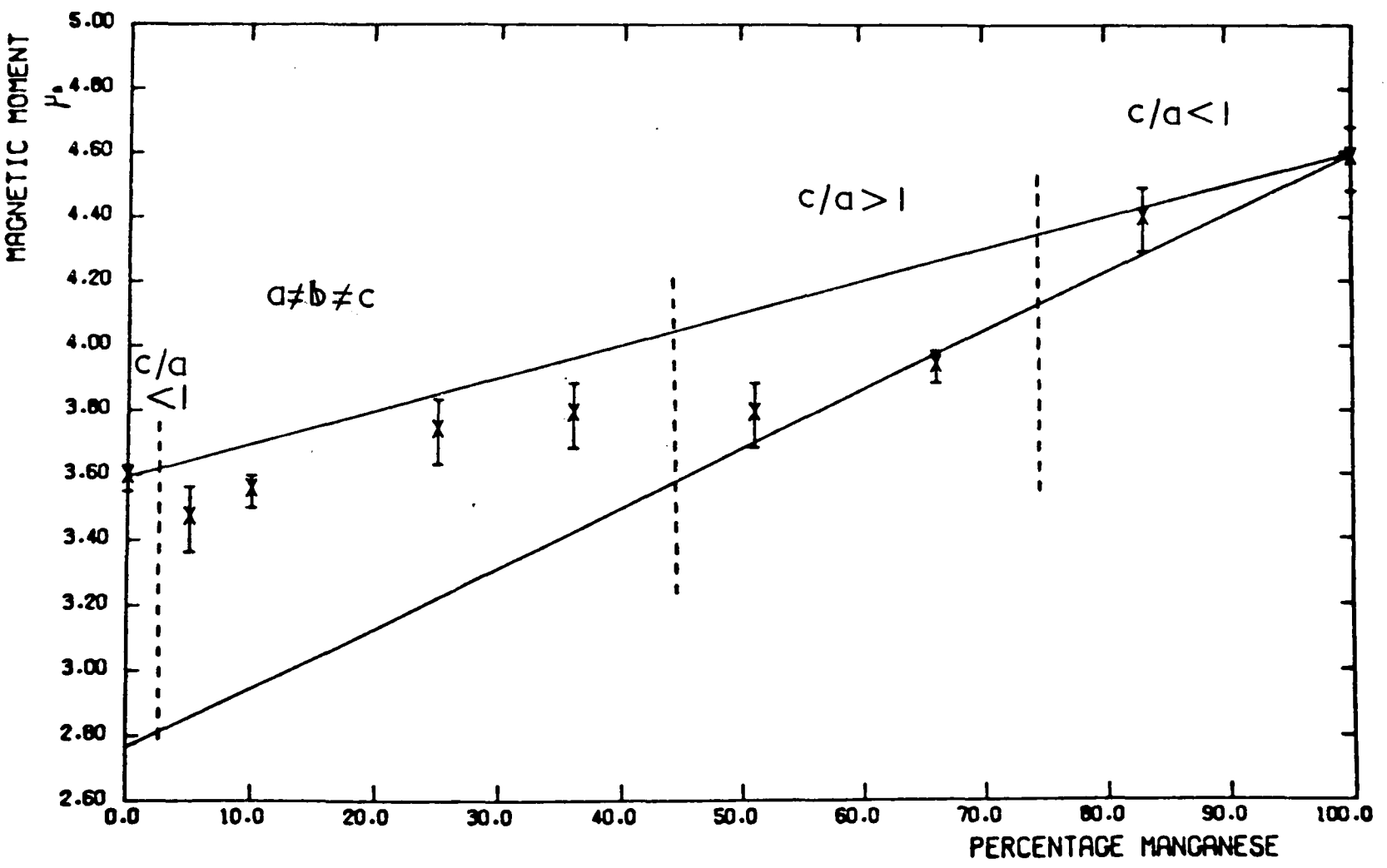



Figure 5.10 Mean sublattice moments of the solid solution $Mn_xCo_{1-x}O$.

Furthermore, it is evident that the $Mn_xCo_{1-x}O$ system is sub-divided into the same distinct regions identified by the lattice parameter measurements (Tables 5.1 and 5.2); these are delineated approximately by dotted lines in Figure 5.10. Compositions between 5 and 36% manganese show a reduction from the line joining the moments of CoO and MnO, which is compatible with the partial quenching of the $Co^{2+}$ moment postulated earlier, and the moments of the 5-25% MnO samples fall on a straight line, which suggests that they all involve similar degrees of quenching. Here, it will be recalled, the difference between the cell parameters a and b is much smaller than that between b and c. The decrease in the moment caused by the incorporation of as little as 5% MnO into CoO should also be stressed.

The magnetic moments of samples containing 51 and 67% manganese also fall approximately on a straight line, but this now joins $\mu$<MnO> with a value for CoO of $\sim 2.75\mu_B$, which is a reasonable estimate for a spin-only S = 3/2 ion with a small reduction for covalency. The loss of the $Co^{2+}$ orbital moment must be almost complete in these two samples. In the third region of Figure 5.10, the moment of the 83% MnO composition can be imagined to fall on either of the limiting lines. However, it tends towards the upper one, which is again consistent with the return of an orbital magnetic moment and single-ion anisotropy energy of $Co^{2+}$ at this composition. When drawing all the above conclusions, the assumption was made that approximate collinearity of the moments of different ionic species is maintained in all samples owing to the large $180^o$ superexchange interactions. The validity of this assertion is born out by much other evidence presented in this thesis.

Refinements of the components of the magnetic moments again exposed different characteristics for the same three ranges of composition

outlined above, although magnetic vectors close to, or within, the pseudocubic (111) plane are observed in all cases. It will be recalled (section 3.2.4) that the size of the component $K_z$ (in Table 5.3) for the trigonal (hexagonal), C-centred and primitive cells given in Table 5.1 indicates the degree of deviation of the magnetic moment from the pseudocubic (111) plane. For pseudo-f.c.c. cells, this quantity can be obtained from the value $\theta$ in Table 5.3, noting that the (111) planes are inclined at $\theta \simeq 35^{o}$ to [001].

In the cobalt-rich region, where partial quenching of the $Co^{2+}$ orbital moment occurs, the moments are found to adopt approximately the same direction as CoO, although they refined to positions somewhat closer to the pseudocubic [001] axis and removed from the $(1\bar{1}0)$ plane when an asymmetry correction was applied. However, the magnetic moments of the samples containing 51 and 67% manganese behave very differently; although CoO, $Mn_{0.51}Co_{0.49}O$ and $Mn_{0.67}Co_{0.33}O$ are all described well by monoclinic (C2/m) cells, the $K_z$ component of the end member (CoO) has an opposite sign to that of the two solid solutions (Table 5.3). Consequently, the easy axes of the latter appear to be on the opposite side of the (111) plane of the face-centred cell. The source of this result (if significant - see below) is unclear, since $Co^{2+}$ and $Mn^{2+}$ have orbital singlet ground states at these compositions and should have predominantly dipolar anisotropies, which favour the (111) plane.

The (111) plane is preferred by the average sublattice magnetisation of $Mn_{0.83}Co_{0.17}O$, which falls in the third region of Figure 5.10. Since the orbital contribution of $Co^{2+}$ seems to have re-emerged here, this may indicate that the dipolar $Mn^{2+}$ anisotropy is comparable with the single-ion effect of $Co^{2+}$ at this composition, although the contribution of the possible non-collinearity of the orbital and spin angular

momenta of $Co^{2+}$ is difficult to predict. The moment is shown to point along the pseudocubic $[\bar{1}\bar{1}2]$ direction for case (b) ($c/a < 1$) in Table 5.3; a slightly larger $R_{pr}$ value (7.60) was obtained by constraining the moment to $[\bar{1}10]$. The least squares refinement would not converge when the magnetisation was allowed a $K_z$ component.

In theory, the biaxial configurational symmetry [78] of all samples studied in this chapter (except MnO) should allow the absolute moment direction to be determined. Indeed, $K_x$, $K_y$ and $K_z$ could be refined independently in many cases but, unfortunately, by comparison with CoO the magnetic peaks of the solid solutions are not well resolved (Appendix 1) and their moment directions are less conclusively determined. The final parameters tended to be somewhat dependent on the starting model and often changed appreciably when an asymmetry correction was applied to peaks below $2\theta = 42^{o}$. The most intense magnetic peaks occur at low angles, and an attempt was made to improve their resolution and diminish the effects of asymmetry by measuring some profiles at a wavelength of 1.904 Å. However, refinements of solid solution data obtained under these conditions (for $Mn_{0.10}Co_{0.90}O$ and $Mn_{0.67}Co_{0.33}O$) retained a degree of uncertainty, and it seems that the powder method is rather insensitive here. Very good resolution of the magnetic peaks split by the small distortions must be necessary in order to distinguish between magnetic vectors close to the (111) plane, as highlighted by Table 5.4. This shows that similar $R_{pr}$ values were obtained whether or not the moments were constrained to the (111) plane.

Owing to these limitations, the relative sizes of the anisotropies of MnO and CoO cannot be readily contrasted using the $Mn_xCo_{1-x}O$ system. Moreover, the apparent $Mn^{2+}$ anisotropy may be much larger in the mixed system owing to the large effect of the associated exchangestriction on

| COMPOSITION | Moment Out Of (111) Plane | Moment In Plane ($K_z \approx 0$) |
|---|---|---|
| $Co_{0.90}Mn_{0.10}O$ | 5.96 | 6.10 |
| $Co_{0.75}Mn_{0.25}O$ | 5.83 | 5.86 |
| $Co_{0.64}Mn_{0.36}O$ | 6.15 | 6.32 |
| $Co_{0.49}Mn_{0.51}O$ | 7.04 | 7.10 |
| $Co_{0.33}Mn_{0.67}O$ | 5.16 | 5.29 |

TABLE 5.4 R-values for moments of $Mn_xCo_{1-x}O$ out of, and within, the (111) plane.

the electronic structure of $Co^{2+}$, which is apparent from the lattice parameter and magnetic moment measurements. The MnO-$Fe_zO$ and CoO-$Fe_zO$ systems (considered in Chapeter 6.2.2) probably provide a better comparison of the MnO and CoO anisotropies, not least because much larger changes in magnetic moment direction occur.

## 5.3 Summary

(a) The linear change of Néel temperature with composition in $Mn_xCo_{1-x}O$ precludes the existence of an "OAF" phase and the magnetic moments of different ions in all samples are effectively collinear.

(b) Previous neutron diffraction results concerning the magnetic structure of cobaltous oxide are confirmed, and high resolution diffractometry and a long wavelength have revealed a trigonal exchange-striction, compatible with a single axis magnetic structure. A model has been proposed for the electronic structure of $Co^{2+}$, wherein the spin and orbital angular momenta are non-collinear.

This appears consistent with both neutron diffraction and n.m.r. results.

(c) Unlike $Mn_xNi_{1-x}O$, the trigonal distortion due to $Mn^{2+}$--$Mn^{2+}$ exchange is not opposed by an opposite distortion due to ferromagnetic $Co^{2+}$--$Mn^{2+}$ interactions.

(d) The lattice parameters, and the magnitudes and directions of the magnetic moments all reveal three distinct areas of behaviour in $Mn_xCo_{1-x}O$. These can be attributed to changes in the electronic structure of $Co^{2+}$, although any inferences to be gained from the directions adopted by the magnetic moments in the three regions are restricted by the limitations of the powder neutron diffraction technique.

In the cobalt-rich ($x < 0.36$) regime, the orbital moments of some $Co^{2+}$ ions are quenched, distortions characteristic of both Jahn-Teller and magnetostrictive stabilisations are observed, and the magnetic moment directions are close to that of CoO. For $0.51 < x < 0.66$, spin-only $Co^{2+}$ moments and sole Jahn-Teller distortions are evident, and the moments have a slight preference for the opposite side of the (111) plane. However, when $Mn^{2+}$ is in large excess, indications of a magnetostrictive $Co^{2+}$ distortion reappear and the average moment is confined to the (111) plane; here the $Co^{2+}$ concentration may be insufficient to support a co-operative Jahn-Teller distortion.

(e) The tetragonal distortion of $Mn_{0.67}Co_{0.33}O$ shows an unusual temperature dependence, which suggests that the magnetostrictive and Jahn-Teller distortions are interlinked. At 5K, the latter deformation is supported by a composition which may be below the

percolation threshold for $Co^{2+}$ in the f.c.c. lattice. Consequently, a co-operative distortion of the interstices would not be predicted here, but some magnetoelastic coupling between interstices dependent on the magnetic ordering may introduce correlations between the individual Jahn-Teller distortions of $Co^{2+}$ sites.

# CHAPTER SIX

# THE CRYSTAL AND MAGNETIC STRUCTURES OF $(Mn_xFe_{1-x})_zO$ AND $(Co_xFe_{1-x})_zO$

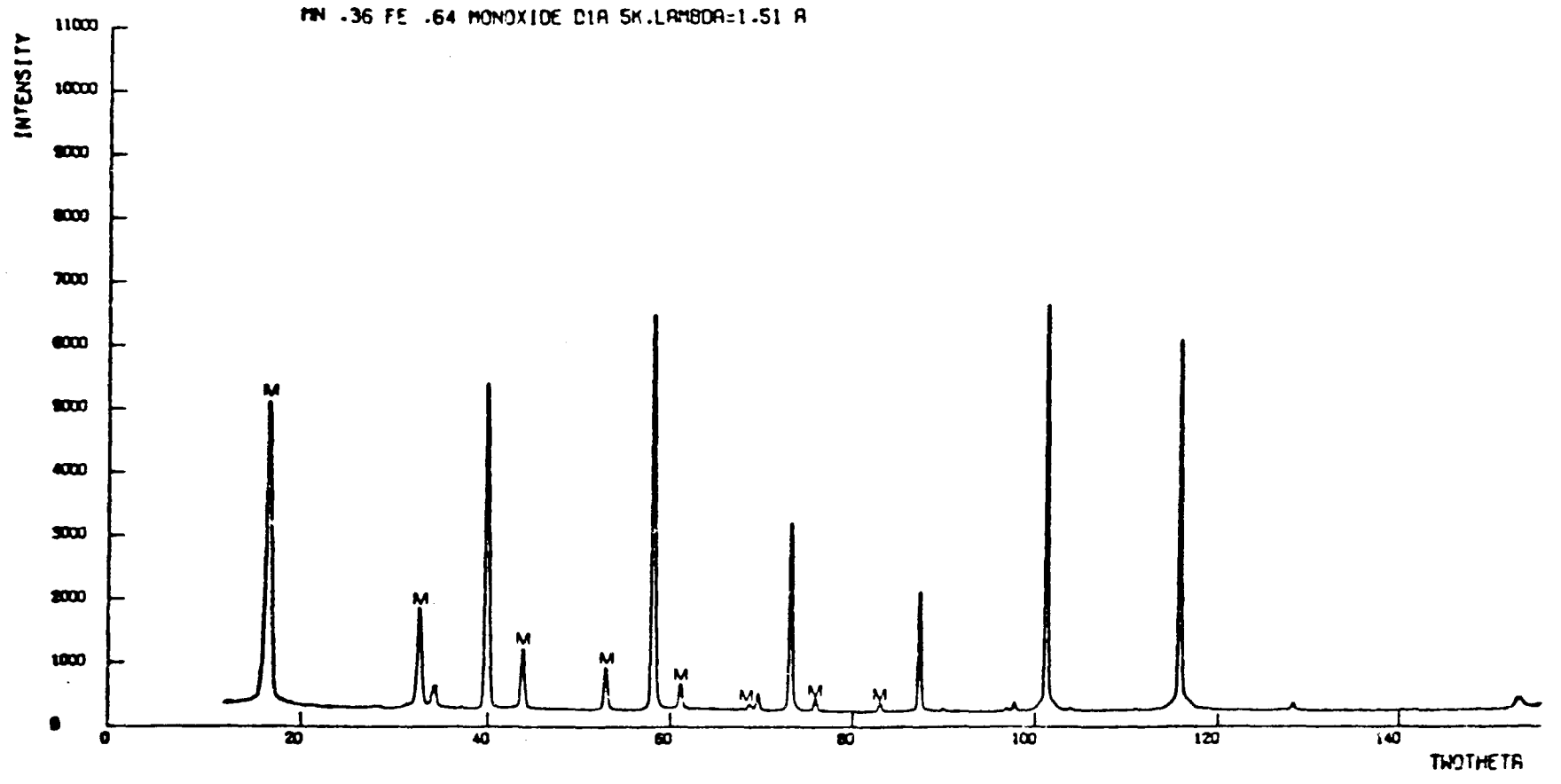
## 6.1 Defect Structures of the Solid Solutions

Unless MnO and CoO are in very large excess, their mixed crystals with $Fe_zO$ are always grossly non-stoichiometric (Chapter 2.1.2), and it is of interest to investigate the influence of the non-ferrous ions on the structural defects associated with cation deficiency. Other properties, such as the possibility of cation ordering, may also be associated with solid solution formation and, in the following two sections, studies employing neutron diffraction (on both systems) and Mössbauer effect spectroscopy (MnO-$Fe_zO$) will be described. The relationship between the nuclear and magnetic structures of each solid solution will be dealt with in the second part of the chapter.

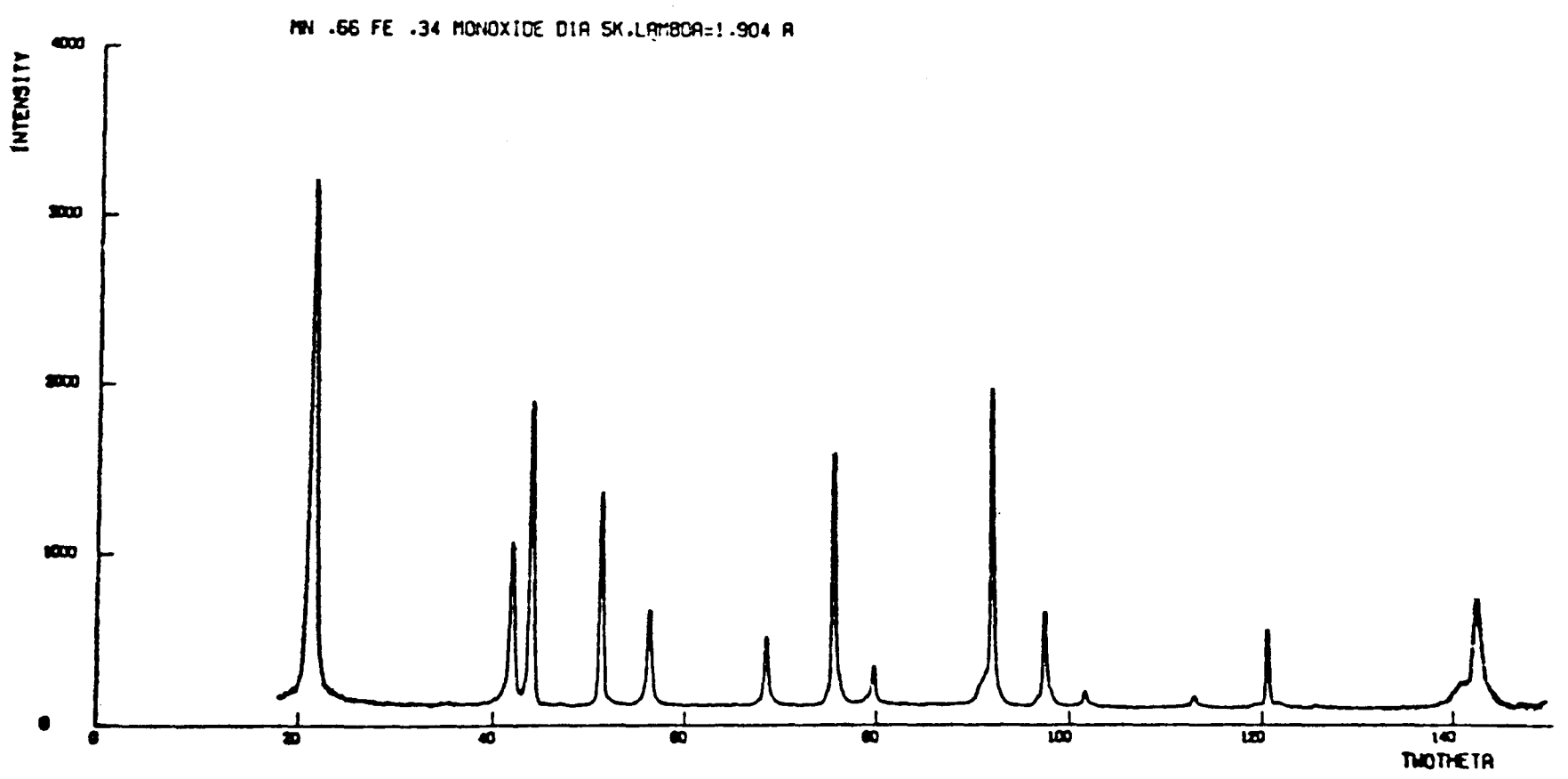
### 6.1.1 Neutron Diffraction Results

In Chapter 2.1.1, the application of neutron diffraction to the problem of defect clustering in ferrous oxide was discussed. From the contents of the unit cell, the number of octahedral vacancies and tetrahedral interstitials can be determined, and their ratio used to indicate the average defect cluster size. For instance, 4:1, 6:2 and 8:3 clusters (Figure 2.3) give rise to vacancy-interstitial ratios of 4,3 and 2.66 respectively. As the Introduction (Chapter 2) indicates, it is now generally accepted that the 4:1 cluster and its edge-sharing derivatives are the predominant defect units in ferrous oxide.

Some corresponding results, obtained at 5K for $(Mn_xFe_{1-x})_zO$ and $(Co_xFe_{1-x})_zO$, are set out in Table 6.1. These were extracted from




(a)




(b)

**Figure 6.1** Observed powder patterns of (a) $(Mn_{0.36}Fe_{0.64})_{0.954}O$ and (b) $(Mn_{0.66}Fe_{0.34})_{0.954}O$ at 5K. In (a) magnetic peaks are labelled "M".

profile analyses of the nuclear Bragg reflections, which are normally well separated from the magnetic peaks owing to the different magnetic and nuclear periodicities (Figure 6.1(a)). For non stoichiometric samples, it was presumed that all oxidation is associated with the formation of $Fe^{3+}$, and the scattering length of iron was assigned to the tetrahedral (interstitial) site since octahedral co-ordination is favoured for $Fe^{2+}$, $Mn^{2+}$, $Mn^{3+}$, $Co^{2+}$ and $Co^{3+}$ owing to ligand field stabilisation or size factors. The remaining $Fe^{3+}$, plus all the $Fe^{2+}$ and $Mn^{2+}$ or $Co^{2+}$ present, was assumed to occupy the octahedral site. The validity of these assumptions is confirmed by the Mössbauer results (Chapter 6.1.2) and by the consistency of the results forthcoming from the neutron profile analyses (Table 6.1).

Initially the occupancies of octahedral and tetrahedral sites were refined independently, furnishing a value for the tetrahedral iron occupancy. Using this quantity and the atomic absorption iron-manganese (cobalt) analytical data, a corrected octahedral scattering length was calculated and the sum of the occupation numbers of the octahedral and tetrahedral sites was constrained to equal z in the formula $(Mn_xFe_{1-x})_zO$, (M=Mn, Co). The vacancy-interstitial ratios shown in Table 6.1 were obtained from the occupancies calculated according to this procedure, and the same Table indicates that the tetrahedral occupancies and profile residuals resulting from constrained and unconstrained refinements are comparable in most cases, despite any inaccuracies arising from the bulk analyses, neutron data and the approximations made. The large overall isotropic temperature factors shown in Table 6.4 are somewhat larger than those of $Mn_xNi_{1-x}O$ and $Mn_xCo_{1-x}O$, and they reflect the additional disorder associated with the defects present in non-stoichiometric samples. This also leads to diffuse scattering in the vicinity of the

Bragg peaks, as shown in Figure 6.1 for $(Mn_{0.36}Fe_{0.64})_{0.954}O$ and $(Mn_{0.66}Fe_{0.34})_{0.954}O$. Although no impurities are apparent, the profile of the latter is of a poor quality, which is reflected by the large $R_{pr}$ values of constrained and unconstrained refinements and the difference between them; this behaviour will be considered further below.

Except for those samples close to stoichiometry (containing 56 and 89% manganese, and 81% cobalt), where the tetrahedral occupancy is too small to be detected, vacancy-interstitial ratios could be measured in every case. The values range from 2.7 to 4.1 for MnO-$Fe_zO$ and from 2.2 to 3.0 for CoO-$Fe_zO$; consequently all show evidence for defect clustering as in ferrous oxide itself. However, the ratios for CoO-$Fe_zO$ are, on the average, smaller in size, which must be linked to the larger tetrahedral site occupancies of iron-rich $(Co_xFe_{1-x})_zO$ (Table 6.1). This may reflect incipient disproportionation into spinel and metal, via the formation of larger clusters, under the conditions of preparation (1000°C) or quenching. It is noteworthy that these observations are compatible both with the phase diagrams at 900°C [65] and 1200°C [66] (Figure 2.5), and with the synthetic difficulties discussed in Chapter 3.1.2, in that the neutron patterns of the CoO-$Fe_zO$ samples containing greater than 50% iron also incorporate weak impurity peaks (e.g. Figure 6.12(b)). The profile of $(Co_{0.63}Fe_{0.37})_{0.958}O$ measured on D1A is free of extraneous lines and the tetrahedral occupancy and vacancy-interstitial ratio are consistent with the smaller clusters present in $Fe_zO$ and $(Mn_xFe_{1-x})_zO$. In the cobalt-rich region of the phase diagram, therefore, formation of the rocksalt solid solution appears more facile.

While it is fortunate that the spinel and metal peaks observed in some $(Co_xFe_{1-x})_zO$ patterns are normally separate from the rocksalt structure reflections, so that profile analyses can proceed, the impurity

| COMPOSITION | INSTRUMENT | $\lambda$(Å) | occ(Td,c)[a] | occ(Td,u)[a] | v[b] | $R_{pr}$(c)[a] | $R_{pr}$(u)[a] | $T_N$(K) |
|---|---|---|---|---|---|---|---|---|
| $(Mn_{0.05}Fe_{0.95})_{0.936}O$ | CURRAN | 1.4 | 0.025 (3) | 0.039(3) | 3.5(4) | 5.12 | 4.28 | - |
| $(Mn_{0.05}Fe_{0.95})_{0.954}O$ | DIA | 1.5 | 0.027 (4) | 0.036(5) | 2.7(4) | 9.76 | 9.34 | - |
| + preferred orientation | | | 0.015 (5) | 0.022(6) | 4.1(1.4) | 8.93 | 8.84 | - |
| $(Mn_{0.1}Fe_{0.9})_{0.931}O$ | PANDA | 1.5 | 0.034 (7) | 0.040(7) | 3.0(7) | 8.10 | 7.59 | 186[c] |
| $(Mn_{0.12}Fe_{0.88})_{0.926}O$ | DIA | 1.5 | 0.036 (4) | 0.041(5) | 3.1(1) | 6.66 | 6.36 | - |
| $(Mn_{0.23}Fe_{0.77})_{0.929}O$ | PANDA | 1.5 | 0.031 (5) | 0.031(5) | 3.3(5) | 4.49 | 4.49 | 178[c] |
| $(Mn_{0.36}Fe_{0.64})_{0.954}O$ | DIA | 1.5 | 0.027 (4) | 0.022(5) | 2.7(4) | 8.38 | 8.06 | 161[c] |
| $(Mn_{0.50}Fe_{0.50})_{0.971}O$ | - | - | - | - | - | - | - | 158[c] |
| $(Mn_{0.56}Fe_{0.44})_{0.993}O$ | DIA | 1.5 | - | - | - | - | - | - |
| $(Mn_{0.66}Fe_{0.34})_{0.954}O$ | DIA | 1.9 | 0.023 (6) | 0.018(6) | 3.0(8) | 18.84 | 15.14 | 141[c], 158[d] |
| $(Mn_{0.89}Fe_{0.11})_{0.997}O$ | PANDA | 1.5 | - | - | - | - | - | - |
| $(Co_{0.04}Fe_{0.96})_{0.939}O$ | DIA | 1.5 | 0.049 (4) | 0.054(5) | 2.2(2) | 4.70 | 4.55 | - |
| $(Co_{0.12}Fe_{0.88})_{0.911}O$ | PANDA | 1.5 | 0.044 (9) | 0.050(9) | 3.0(7) | 9.68 | 9.46 | - |
| $(Co_{0.50}Fe_{0.50})_{0.935}O$ | PANDA | 1.5 | 0.049 (5) | 0.047(6) | 2.4(3) | 9.76 | 9.67 | - |
| $(Co_{0.63}Fe_{0.37})_{0.958}O$ | DIA | 1.5 | 0.023 (4) | 0.023(4) | 2.8(5) | 5.81 | 5.79 | - |
| $(Co_{0.81}Fe_{0.19})_{0.980}O$ | PANDA | 1.5 | - | - | - | - | - | - |

TABLE 6.1 Summary of Neutron Diffraction and Magnetic Susceptibility Experiments, Defect Structure Parameters and Néel Temperatures for $(Mn_xFe_{1-x})_zO$ and $(Co_xFe_{1-x})_zO$.

a. The tetrahedral occupancies and profile residuals resulting from unconstrained refinements (u) and from refinements in which the sum of the octahedral and tetrahedral occupancies is constrained to be z in $M_zO$(c). b. The octahedral vacancy-tetrahedral interstitial ratio. c. Determined by magnetic susceptibility measurements. d. Determined by neutron diffraction. Estimated standard deviations are shown.

phases contribute to the metal:metal and metal:oxygen bulk analyses and render the application of these to the calculation of the octahedral and tetrahedral site occupancies more uncertain. However, the good agreement between constrained and unconstrained refinements (Table 6.1) suggests that the inaccuracies are not too severe. Except for $(Mn_{0.05}Fe_{0.95})_{0.936}O$, the diffraction patterns of $(Mn_xFe_{1-x})_zO$ do not reveal any decomposition products, but their presence (in very low concentrations) is indicated by magnetic susceptibility measurements (section 6.2.1).

In addition to being a good technique for the study of the effects of non-stoichiometry, the difference in scattering lengths between Mn, Fe and Co makes neutron diffraction an excellent method for the detection of long range atomic order, such as that found in FeCo [235]. Although such behaviour has been postulated in $(Mn_xFe_{1-x})_zO$ to account for some magnetic susceptibility results [54], no superlattice reflections are observed in any of the profiles of either $MnO-Fe_zO$ or $CoO-Fe_zO$ (see Figures 6.1 and 6.12, for example) and all the solid solutions appear to have random cation distributions. However, the profiles of $(Mn_{0.05}Fe_{0.95})_{0.954}$ (Appendix 1) and $(Mn_{0.66}Fe_{0.34})_{0.954}O$ (Figure 6.1(b)) show some unusual features.

The agreement between the observed and calculated profiles of the former is bad for high angle peaks split by the low temperature distortion. Although these reflections could only be indexed according to a trigonal ($R\bar{3}$) cell, no solution to the problem could be obtained by varying the co-ordinates and occupancies of the metal and oxygen sites. However, the application of a preferred orientation correction (equation 3.10), allowing the crystallites to lie preferentially on the close packed plane ((111) in cubic indices) perpendicular to the trigonal axis of

distortion, improved the $R_{pr}$ value by approximately 0.5%. This is not observed in any other sample and is very unexpected because the trigonal distortion only appears at low temperatures.

The nuclear peaks of $(Mn_{0.66}Fe_{0.34})_{0.954}O$ are associated with substantial diffuse haloes, which are responsible for the poor profile analysis residuals (Table 6.1). This scattering is probably due to a lack of gross homogeneity, although different electron microscope analyses agree well, the powder X-ray diffraction lines are sharp and the Néel temperature is well defined (Figure 6.11). It is appreciably larger than the diffuse scattering observed in other non-stoichiometric $(Mn_xFe_{1-x})_zO$ samples, which may be attributed to relaxation around the defects [236], and is much more pronounced than that observed for $(Co_{0.63}Fe_{0.37})_{0.958}O$, a sample containing approximately the same proportion of $Fe^{3+}$ as $(Mn_{0.66}Fe_{0.34})_{0.954}O$ (~ 30% of the total iron).

### 6.1.2 Mössbauer Spectroscopy Results

Fits to the spectra obtained for seven samples of $(Mn_xFe_{1-x})_zO$ are illustrated by Figures 6.2 and 6.3. The resulting parameters for these compositions are presented in Table 6.2, together with those for one other MnO-$Fe_zO$ composition ($Mn_{0.975}{}^{57}Fe_{0.025}O$) and two ferrous oxide samples. For the purpose of fitting the spectra, it was assumed that no appreciable exchange of the sort

$$Fe^{2+} + Fe^{3+} \rightleftarrows Fe^{3+} + Fe^{2+} \qquad (6.1)$$

or

$$Fe^{2+} + Mn^{3+} \rightleftarrows Fe^{3+} + Mn^{2+}$$

occurs at a rate comparable with the Mössbauer time scale. The first equilibrium is reflected by the Verwey transition of magnetite [237], and the second is the cause of the controversy surrounding the valence

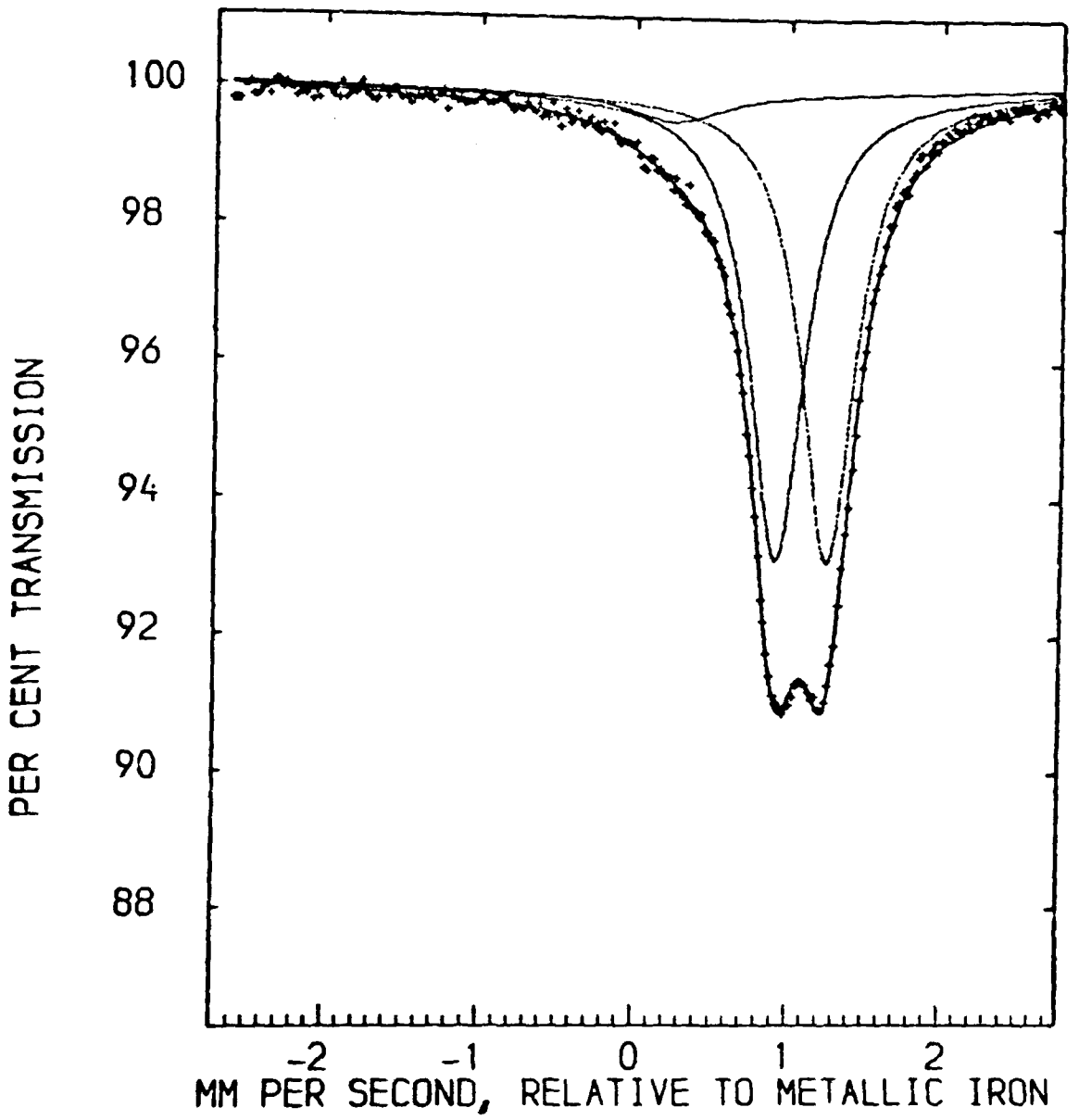



Figure 6.2 Observed and Calculated Mössbauer Spectra of $Mn_{0.9}{}^{57}Fe_{0.1}O$.

distribution of $(Mn_xFe_{1-x})_3O_4$ solid solutions [238,239]. Additionally, it was assumed that all the iron(11) and iron(111) is present in the high spin state and that contributions to the iron(11) quadrupole interaction arise from the proximity of cation vacancies, iron(111) and asymmetric near-neighbour iron/manganese distributions. Despite the large number of factors contributing to the quadrupole interaction and isomer shift, some clear trends can be distinguished.

The ferrous oxide spectra are well represented by an iron(111) singlet and two iron(11) quadrupole doublets, as has been reported previously [24]: little improvement was gained by attempts to fit the spectra to seven lines. Nevertheless, the spectra of solid solution

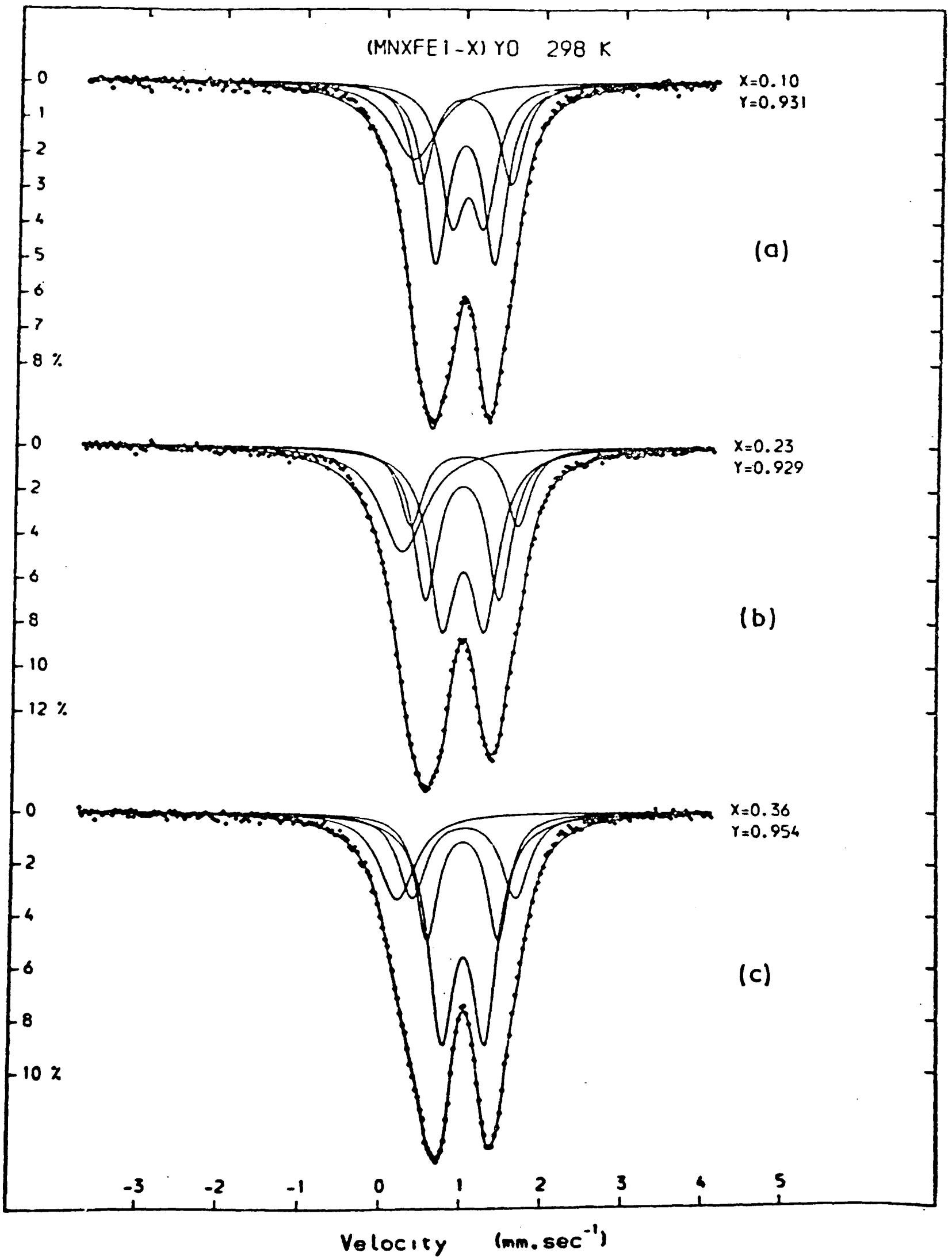



Figure 6.3(a) to (c) Room temperature Mössbauer effect spectra of $(Mn_{0.10}Fe_{0.90})_{0.931}O$, $(Mn_{0.23}Fe_{0.77})_{0.929}O$ and $(Mn_{0.36}Fe_{0.64})_{0.954}O$.

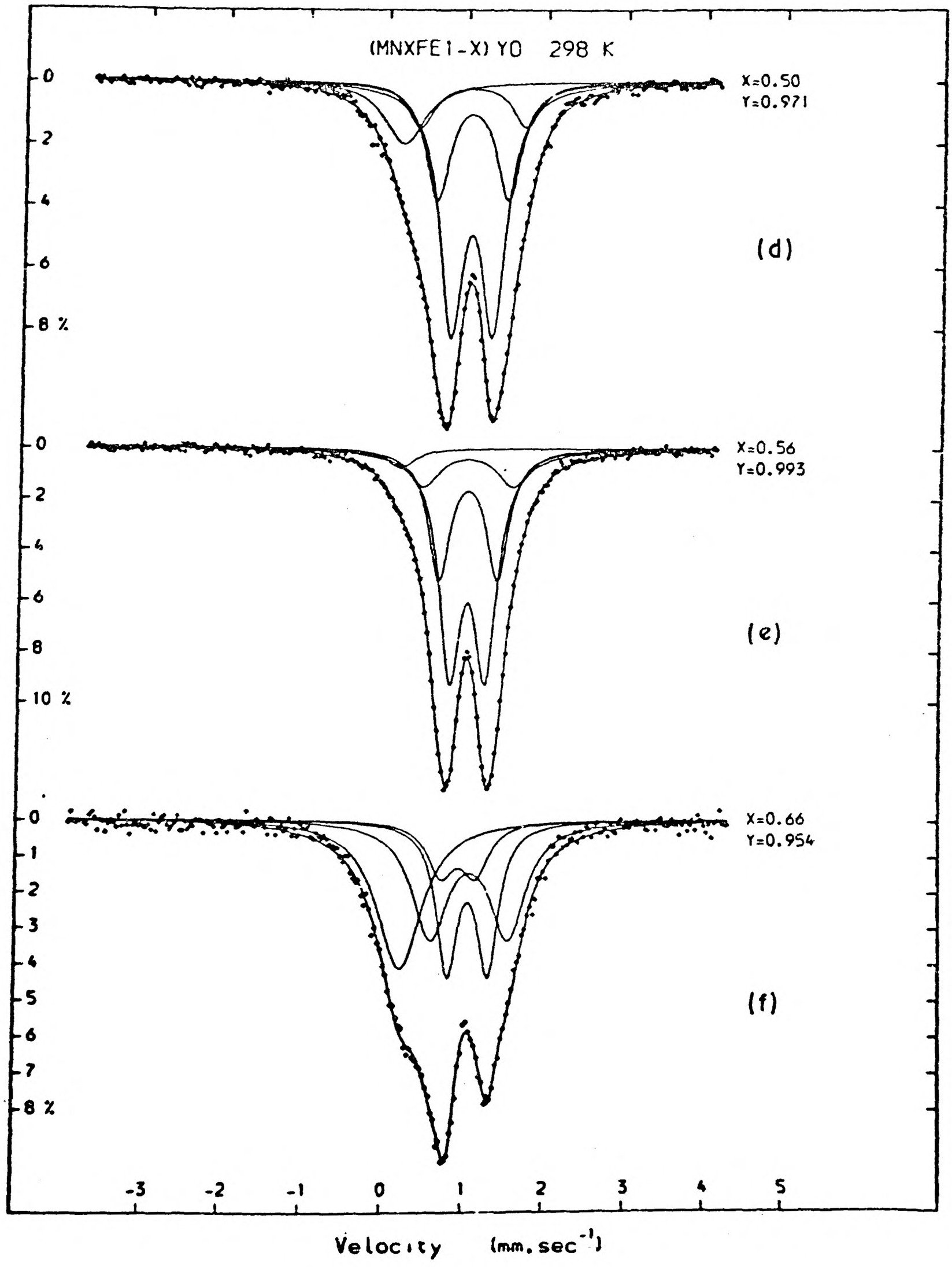



Figure 6.3(d) to (f) Room temperature Mössbauer effect spectra of $(Mn_{0.50}Fe_{0.50})_{0.971}O$, $(Mn_{0.56}Fe_{0.44})_{0.993}O$ and $(Mn_{0.66}Fe_{0.34})_{0.954}O$.

samples containing more than 40% iron could not be fitted satisfactorily with the five-line model, and required the inclusion of a third quadrupole Fe(11) doublet with a splitting in the range of 0.90 to 1.38 mm.s$^{-1}$. The composition dependence of the quadrupole splittings of these three doublets is shown in Figure 6.4, which demonstrates the combined effect

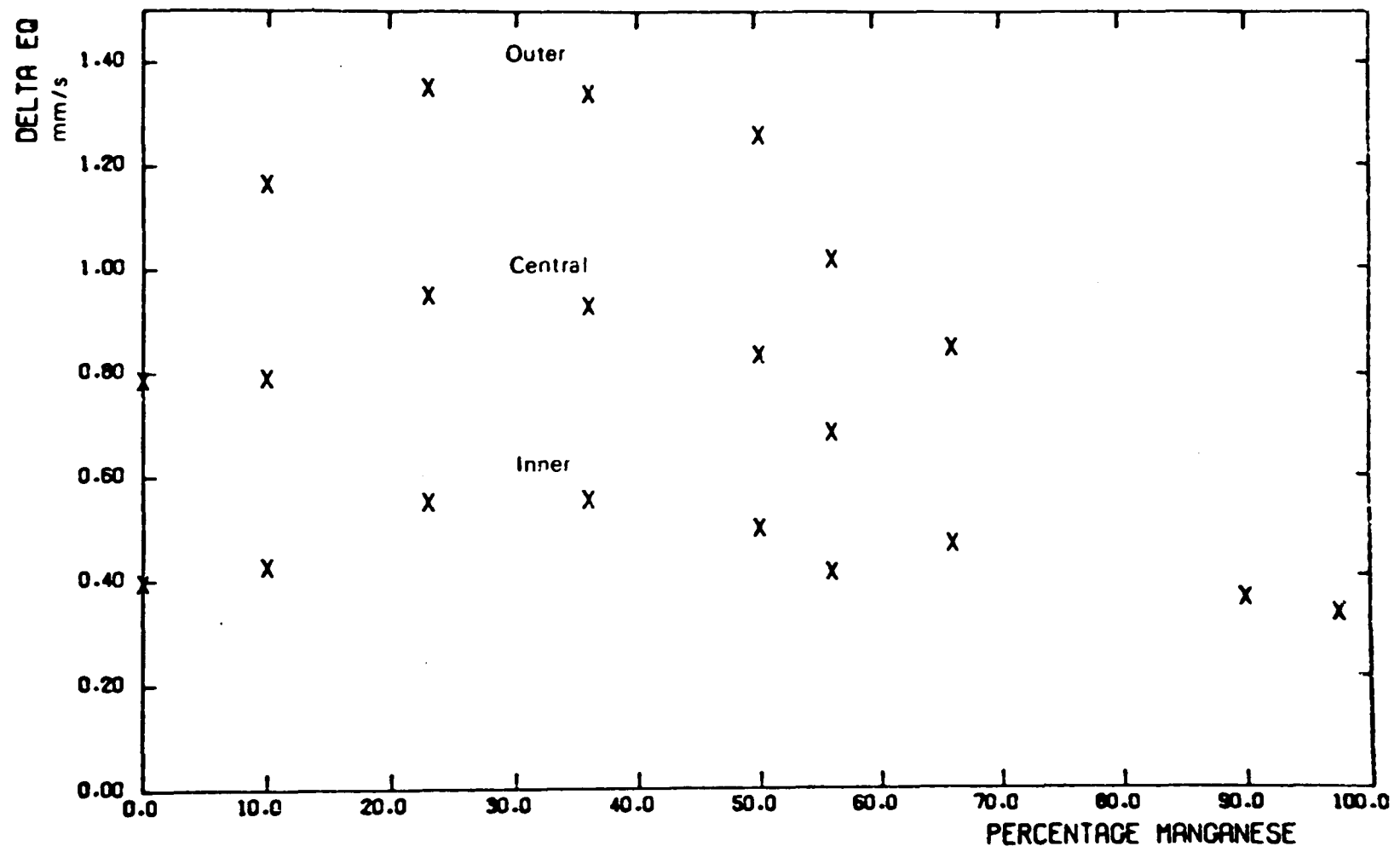



Figure 6.4 Composition Dependence of the Quadrupole Splittings in $(Mn_xFe_{1-x})_zO$.

of the lowering of the iron(11) site symmetry by the proximity of random iron and manganese distributions, and by the large number of vacancies and iron(111) ions. The influence of manganese upon the asymmetry of the iron(11) site is most easily seen in a plot (Figure 6.5) of composition versus the area-weighted average quadrupole splitting, defined by

$$AW = \sum_i A_i \Delta E_{Qi} \qquad (6.2)$$

where the summation is over all quadrupole components, whose areas and splittings are given by $A_i$ and $\Delta E_{Qi}$. The contribution of Fe(111) is

| COMPOSITION | Fe(111) | | | | Fe(11) | | | | | | | | | | | | | |
|---|---|---|---|---|---|---|---|---|---|---|---|---|---|---|---|---|---|---|
| | | | | | Inner Doublet | | | | Central Doublet | | | | Outer Doublet | | | | Total | |
| | δ | Γ | %A | %A* | δ | $\Delta E_Q$ | Γ | %A | δ | $\Delta E_Q$ | Γ | %A | δ | $\Delta E_Q$ | Γ | %A | Area+ | $\chi^2$ |
| $Fe_{0.910}O$ | 0.43 | 0.64 | 9.0 | 19.7 | 0.99 | 0.42 | 0.39 | 31.1 | 0.95 | 0.80 | 0.48 | 59.9 | | | | | 37.1 | 4.37 |
| $Fe_{0.918}O$ | 0.42 | 0.51 | 7.5 | 17.9 | 1.00 | 0.43 | 0.37 | 38.7 | 0.94 | 0.80 | 0.43 | 53.8 | | | | | 36.5 | 2.22 |
| $(Mn_{0.10}Fe_{0.90})_{0.931}O$ | 0.30 | 0.60 | 12.3 | 16.3 | 1.01 | 0.44 | 0.38 | 32.9 | 1.01 | 0.83 | 0.38 | 39.1 | 1.00 | 1.18 | 0.34 | 15.7 | 29.8 | 2.44 |
| $(Mn_{0.23}Fe_{0.77})_{0.929}O$ | 0.23 | 0.58 | 15.8 | 19.7 | 1.02 | 0.56 | 0.44 | 43.0 | 1.02 | 0.97 | 0.37 | 28.8 | 1.05 | 1.36 | 0.34 | 12.4 | 25.8 | 1.64 |
| $(Mn_{0.36}Fe_{0.64})_{0.954}O$ | 0.22 | 0.56 | 13.5 | 15.0 | 1.05 | 0.54 | 0.41 | 44.6 | 1.04 | 0.89 | 0.36 | 22.4 | 1.05 | 1.29 | 0.34 | 19.5 | 21.2 | 1.56 |
| $(Mn_{0.50}Fe_{0.50})_{0.971}O$ | 0.19 | 0.64 | 11.8 | 11.8 | 1.06 | 0.52 | 0.33 | 51.3 | 1.05 | 0.89 | 0.35 | 25.7 | 1.05 | 1.34 | 0.49 | 11.2 | 16.4 | 1.70 |
| $(Mn_{0.56}Fe_{0.44})_{0.993}O$ | 0.20 | 0.42 | 3.1 | 3.1 | 1.06 | 0.44 | 0.29 | 52.6 | 1.05 | 0.73 | 0.31 | 31.1 | 1.05 | 1.12 | 0.50 | 13.2 | 16.2 | 1.24 |
| $(Mn_{0.66}Fe_{0.34})_{0.954}O$ | 0.24 | 0.68 | 28.6 | 28.3 | 0.97 | 0.43 | 0.41 | 11.6 | 1.08 | 0.50 | 0.32 | 25.7 | 1.10 | 0.96 | 0.54 | 34.2 | 15.0 | 1.36 |
| | 0.25 | 0.69 | 28.6 | 28.3 | 0.98 | - | 0.81 | 11.7 | 1.06 | 0.50 | 0.31 | 25.8 | 1.10 | 0.92 | 0.53 | 34.3 | 15.0 | 1.48 |
| | 0.27 | 0.72 | 31.4 | 28.3 | 1.05 | 0.46 | 0.31 | 20.6 | | | | | 1.10 | 0.80 | 0.60 | 51.0 | 15.0 | 1.62 |
| $Mn_{0.90}{}^{57}Fe_{0.10}O$ | 0.24 | 0.76 | 5.2 | - | 1.08 | 0.34 | 0.42 | 94.8 | | | | | | | | | | 1.10 |
| $Mn_{0.975}{}^{57}Fe_{0.025}O$ | 0.03 | 1.2 | 15.1 | - | 1.08 | - | 0.42 | 43.7 | | | | | 1.06 | 0.28 | 0.39 | 41.2 | | 1.05 |

TABLE 6.2 Mössbauer Effect Spectral Data for $(Mn_xFe_{1-x})_zO$.

* The percentage of iron(111) as determined from analytical data. + In units of percent. $mm.s^{-1}$ for a constant absorber thickness.

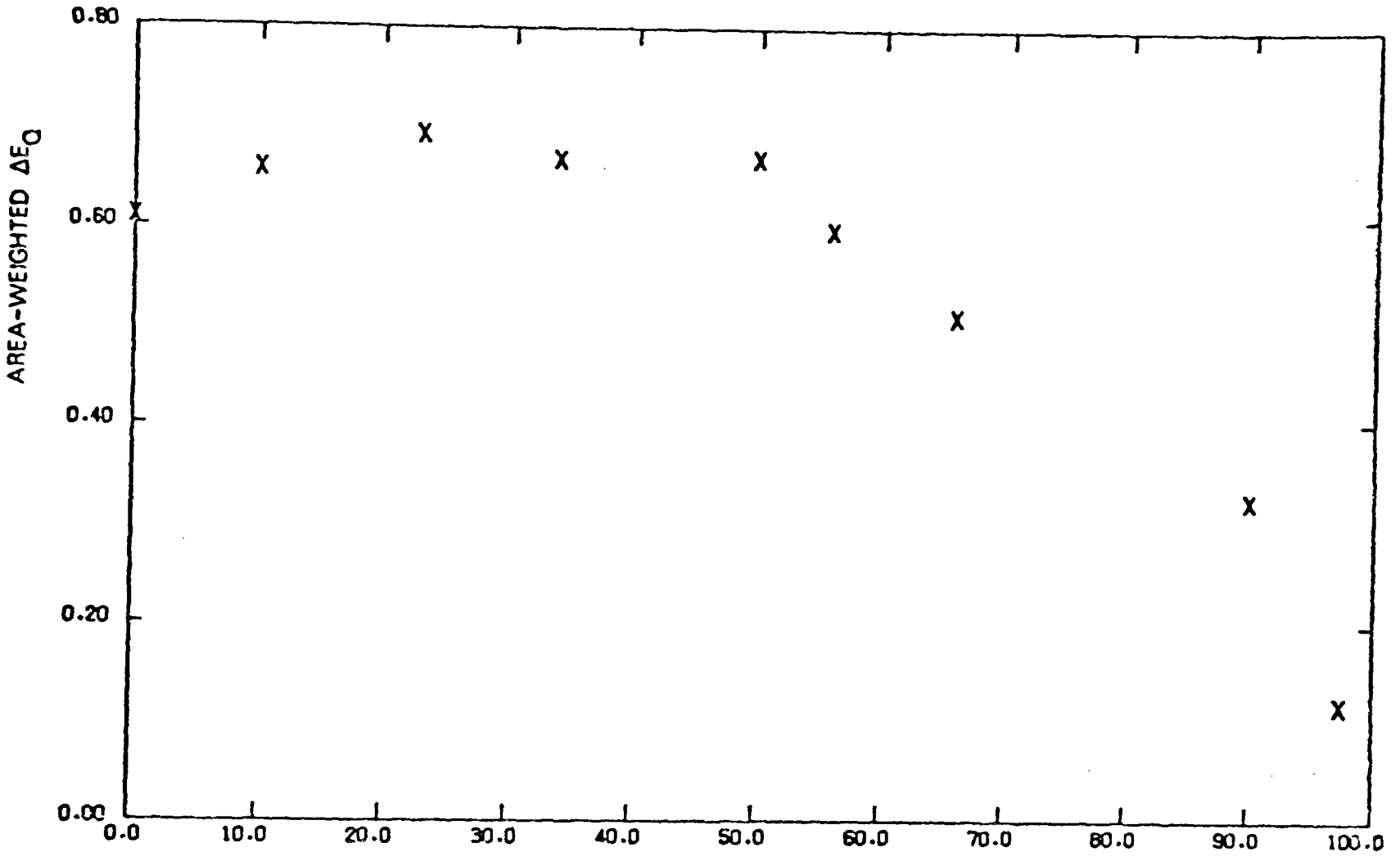



Figure 6.5 Composition Dependence of the Area-weighted Average Quadrupole Splitting in $(Mn_xFe_{1-x})_zO$.

always zero because it does not have any quadrupole splitting, and the quantity AW is essentially independent of the counting statistics and the components used to model the spectra.

For the two ferrous oxide spectra, the AW values are 0.597 and 0.610 mm.s$^{-1}$, and the average value of 0.603 mm.s$^{-1}$, shown in Figure 6.5, underlines the importance of the defects in determining the average quadrupole interaction in $Fe_zO$. The corresponding value for "stoichiometric" FeO[14] prepared under high pressure is approximately 0.21 mm.s$^{-1}$. The very small variation of AW with z in $Fe_zO$ presumably stems from the large concentration of defects present in both samples. However, despite the smaller degree of non-stoichiometry of all the solid solutions, the

area weighted quadrupole interaction increases slowly to a value of between 0.65 and 0.70 mm.s$^{-1}$ at the 50% composition. This increase must result from the presence of both manganese and iron near neighbours, providing an enhanced electric field gradient at the iron(11) sites, and it is reflected in the additional, outer quadrupole doublet mentioned previously.

Although $(Mn_{0.36}Fe_{0.64})_{0.954}O$ and $(Mn_{0.66}Fe_{0.34})_{0.954}O$ have the same metal to oxygen ratio, the Fe(11) absorption envelope of the latter is much simpler, the AW value is substantially smaller (Figure 6.5) and comparable fits to the spectrum are obtained using five, six or seven lines (Table 6.2). This suggests that, in the 66% manganese sample, a smaller proportion of Fe(11) occupies the low symmetry environments arising from the proximity of defects or asymmetric iron-manganese near neighbour distributions, and is compatible with the smaller concentration of total iron, and the much larger relative amount of iron(111), indicated by the appreciable absorption to low velocity (Figure 6.3(f)).

Similarly, the green colours of $Mn_{0.9}{}^{57}Fe_{0.1}O$ and $Mn_{0.975}{}^{57}Fe_{0.025}O$ indicate that their stoichiometries are comparable but are now close to the ideal monoxide composition, so that the effect of defects on the Mössbauer spectra is probably small and constant. The decrease in quadrupole splitting from 10% $^{57}Fe$ to 2.5% $^{57}Fe$ can then be attributed to an increase in the average iron(11) site symmetry of the latter composition as a result of the predominance of manganese on near neighbour sites. This trend is illustrated by a binomial calculation, presented in Table 6.3, of the fraction of octahedral iron sites which have i manganese and (12-i) iron near neighbours, and again the effect of site symmetry on the $Fe^{2+}$ quadrupole splittings (which is noticeable across the whole composition range) is emphasised. The similarity between the

spectra of $Mn_{0.975}Fe_{0.025}O$ and "FeO"[14], in which, again, more iron(11) ions are in high symmetry sites, is also worthy of note.

The Fe(11) isomer shift increases with increasing manganese content (Figure 6.6), which suggests that the $Fe^{2+}$ d electrons are becoming more localised compared with ferrous oxide (leading to increased s electron screening). This observation is compatible with the greater electronegativity of $Fe^{2+}$ compared to $Mn^{2+}$, and therefore suggests that $Fe^{2+}$-$Mn^{2+}$ charge transfer (via the cation- -cation interactions) is weaker than that involving two ferrous ions.

The Fe(111) isomer shift decreases markedly with increasing manganese concentration (Figure 6.7), which indicates that the s electron density at the nucleus is increasing. In order to preserve the local charge neutrality, the Fe(111) ions are concentrated around defect clusters, and in the solid solutions their nearest neighbour $Fe^{2+}$ ions are progressively replaced by $Mn^{2+}$. This again decreases the ease of charge transfer, and forces the ferric ions to be more like $Fe^{3+}$. These observations suggest that electrons with marked itinerant characteristics are present in the immediate vicinity of the defect clusters in ferrous oxide.

In the fits to the spectra, a broad singlet was adopted for the iron(111) line because high spin iron(111) has a $^6A_{1g}$ ground state and hence only a very small valence contribution to the electric field gradient. However, the 4:1 cluster and its surroundings should give rise to an overall lattice symmetry sufficient to broaden the Fe(111) band. In $Mn_{0.975}{}^{57}Fe_{0.025}O$, the $Fe^{3+}$ line is very broad and has a much smaller chemical shift (0.03 $mm.s^{-1}$). Measurements at 78 and 4.2K [240] show that this line is only split into a magnetic hyperfine

| i | $Mn_{0.975}{}^{57}Fe_{0.025}O$ | $Mn_{0.90}{}^{57}Fe_{0.10}O$ |
|---|---|---|
| 12 | 0.739 | 0.282 |
| 11 | 0.225 | 0.377 |
| 10 | 0.033 | 0.230 |
| 9 | 0.003 | 0.085 |
| 8 | 0 | 0.085 |
| 7 | 0 | 0.004 |

TABLE 6.3 Fraction of Fe(11) Sites with i Manganese Near Neighbour Atoms.

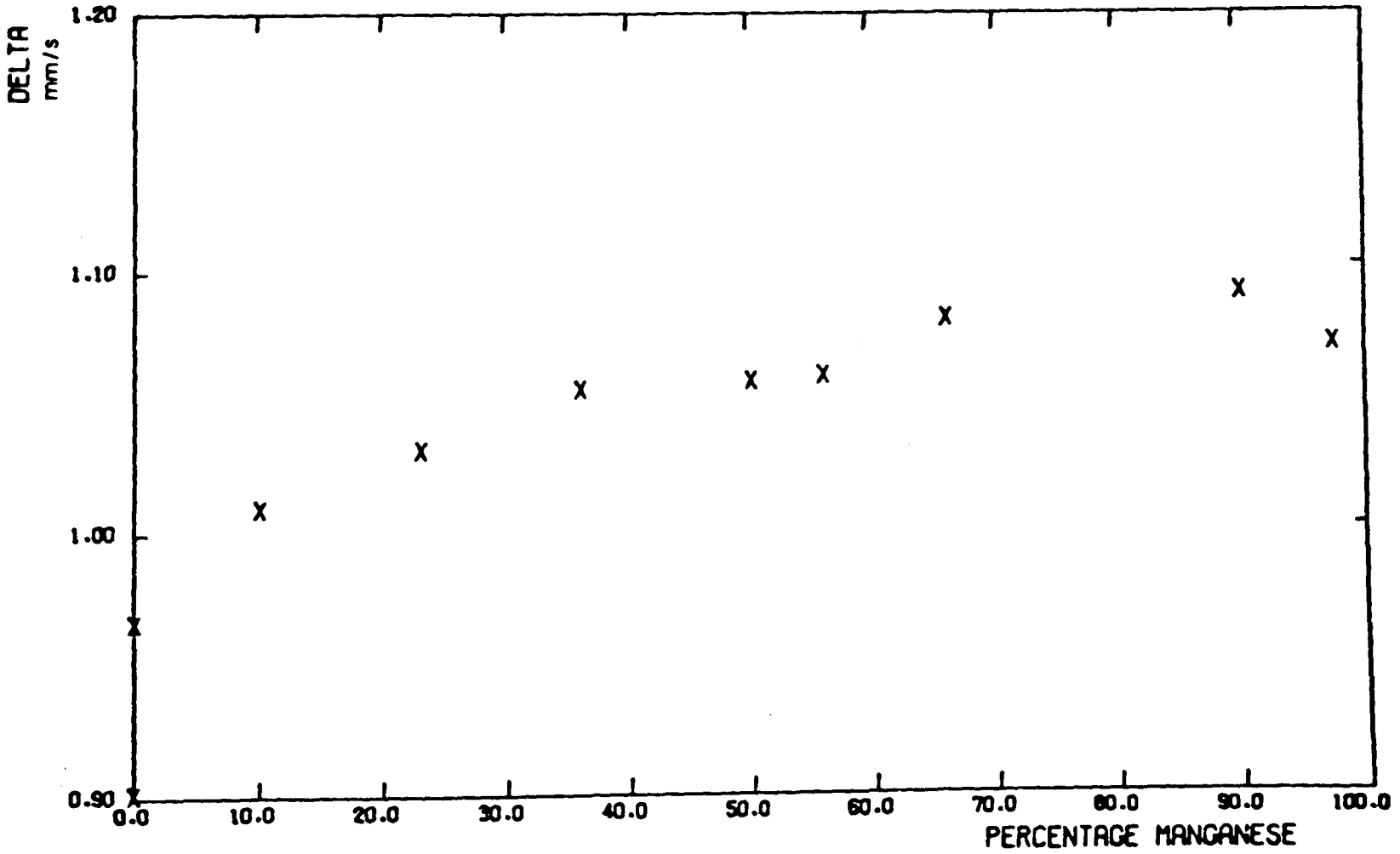



Figure 6.6 Variation in Fe(11) Isomer Shift as a Function of Manganese Content in $(Mn_xFe_{1-x})_zO$.

sextet at the lowest temperature, and it therefore must be associated with a manganese-rich $(Mn_xFe_{1-x})_3O_4$ solid solution which orders at

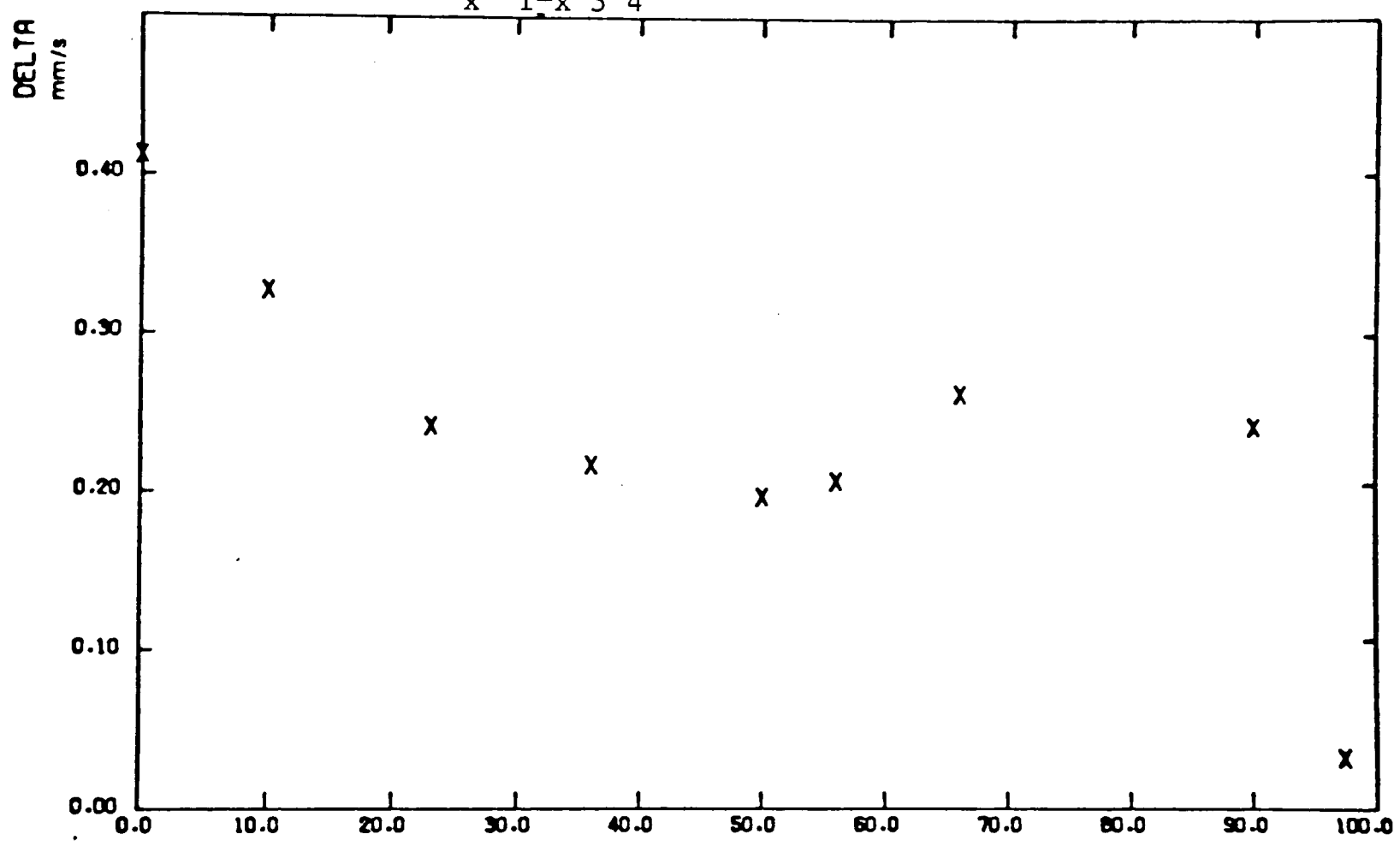



Figure 6.7 Compositional dependence of the Fe(111) isomer shift in $(Mn_xFe_{1-x})_zO$.

$\sim 42K$[241]. The width of this impurity line is probably caused by the appreciable tetragonal distortion of $Mn_3O_4$ and certain of its solid solutions[91].

The agreement between the volumetric iron(111) analyses and the proportion of Fe(111) detected by the Mössbauer effect improves as the proportion of manganese increases (Table 6.2). In iron-rich samples, the smaller amounts of Fe(111) forthcoming from the spectral analyses relative to those derived from the analytical results can again be attributed to the role of electron delocalisation around the clusters when both Fe(11) and Fe(111) are in large concentrations (as discussed with regard to the isomer shift data). The line at low velocity formally attributed to $Fe^{3+}$ in Table 6.2 probably corresponds to a

less positive state of Fe in these cases, and its relative area will then not coincide with the proportion of ferric ion determined by chemical methods.

6.1.3 Summary

(a) Neutron diffraction studies demonstrate that non-stoichiometry in $MnO-Fe_zO$ and $CoO-Fe_zO$ is accommodated by the formation of defect clusters similar to those observed in ferrous oxide; chemical analyses and Mössbauer spectroscopy indicate that their formation occurs via the oxidation of $Fe^{2+}$. Preparative difficulties and the phase diagram are consistent with the more extensive clustering found in $CoO-Fe_zO$.

(b) No long range order of iron and manganese or cobalt is detected by neutron diffraction.

(c) The room temperature Mössbauer effect spectra of $MnO-Fe_zO$ reveal an iron(11) isomer shift which increases with increasing manganese content. This is compatible with a greater electron localisation on the $Fe^{2+}$ ions, caused by the smaller electronegativity of $Mn^{2+}$ and diminished $Fe^{2+}$- -$Mn^{2+}$ charge transfer.

(d) The iron(111) isomer shift decreases with increasing manganese content; this, together with the anomalously small Fe(111) concentration detected by Mössbauer spectroscopy in iron-rich samples can be attributed to appreciable electron transfer between $Fe^{2+}$ and $Fe^{3+}$ in the vicinity of the defect clusters.

(e) Addition of manganese to ferrous oxide initially increases the range of quadrupole interactions experienced by Fe(11).

At levels of manganese greater than 50%, the average quadrupole interaction diminishes gradually, reaching a value of ca. 0.1 $mm.s^{-1}$ at 97.5% manganese. This behaviour may be understood in terms of the number of defects present and the nature and distribution of the iron/manganese near neighbour ions.

## 6.2 Magnetic Ordering in $(Mn_xFe_{1-x})_zO$ and $(Co_xFe_{1-x})_zO$

In subsequent sections, some studies of the magnetic and associated behaviour of the solid solutions between ferrous oxide and manganous and cobaltous oxides will be considered. Chapter 6.2.1 is concerned with an investigation of the exchange interactions leading to magnetic ordering in $MnO-Fe_zO$ by means of magnetic susceptibility and neutron diffraction measurements at different temperatures. In Chapter 6.2.2, the results of neutron diffraction experiments at 5K are used to provide information on the magnetic anisotropies of the component ions and their related magnetostrictions, together with any lattice distortions associated with the nearest neighbour exchange. Finally, the correlation between the reduced intensities of the magnetic neutron diffraction peaks and magnetic ordering around the defect clusters will be discussed in section 6.2.3.

### 6.2.1 Magnetic Phase Diagrams

Previous Néel temperature data for $(Mn_xFe_{1-x})_zO$ [54] and $(Co_xFe_{1-x})_zO$ [185] are plotted in Figures 6.8 and 6.9 and, as in the other systems considered in this work, an approximately linear dependence on composition is evident. Figure 6.8 additionally shows some data determined for the $MnO-Fe_zO$ system during the present investigation by magnetic susceptibility and neutron diffraction measurements. It is

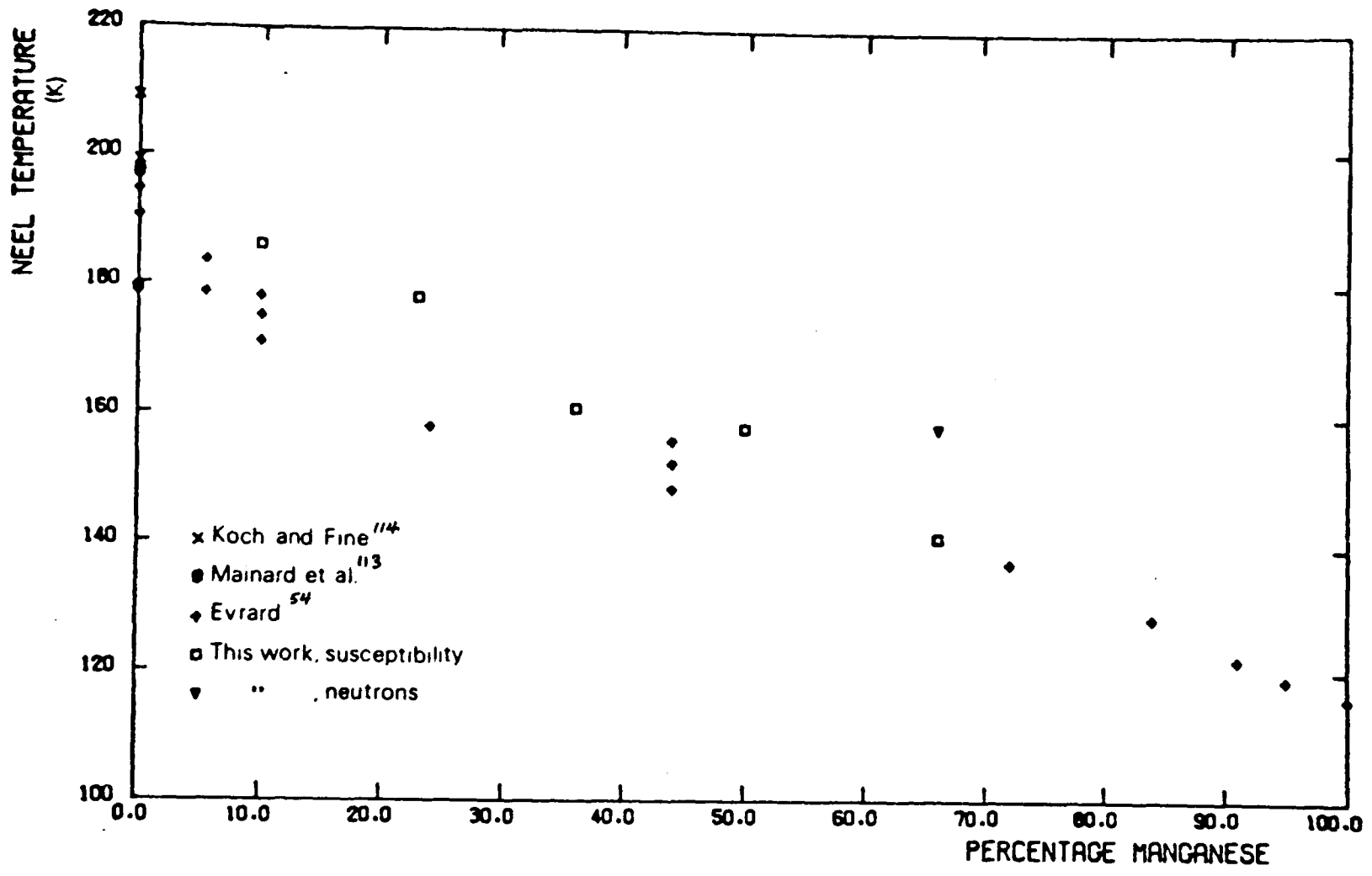



Figure 6.8 Néel Temperatures of the System MnO-$Fe_zO$; points at the Same Manganese Concentration Refer to Different Stoichiometries.

clear that the new values are broadly consistent with the older data; $T_N$ decreases with increasing manganese content (Table 6.1), but is also very sensitive to the stoichiometry. An unusual feature of Figure 6.8 is the difference, for $(Mn_{0.66}Fe_{0.34})_{0.954}O$, of the magnetic ordering temperatures determined by susceptibility and neutron techniques. This is probably due to errors in temperature calibrations or the difficulty of estimating the Bragg peak intensity in the presence of a substantial diffuse background, although similar differences observed elsewhere[242] are considered to be genuine.

As in certain examples of $Mn_xCo_{1-x}O$ and $Mn_xNi_{1-x}O$, a comparison of

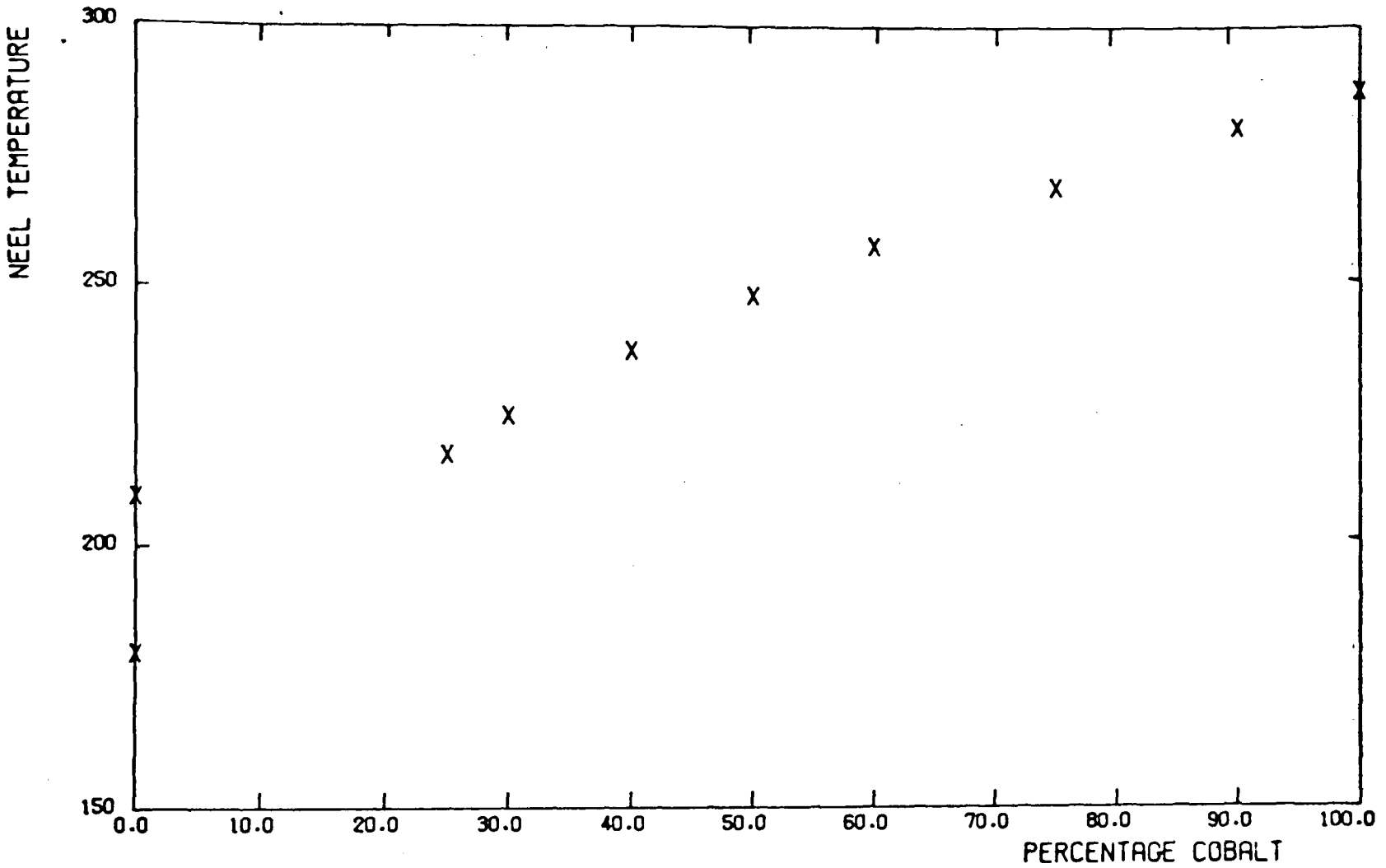



Figure 6.9 Néel Temperatures of Certain Compositions in the Solid Solution CoO-$Fe_zO$; after Boubel, Mainard, Fousse and Pointon [185].

the observed temperature variation of the sublattice magnetisation of $(Mn_{0.66}Fe_{0.34})_{0.954}O$ (measured by scanning the magnetic (111) peak) with that calculated using the Brillouin derived function (section 2.2.1(a)) is very good (Figure 6.10). The agreement obtained may be partially attributed to the lack of any significant distortion below $T_N$ and, possibly, a quenched orbital moment of $Fe^{2+}$ (section 6.2.2(b)).

The magnetic susceptibilities of the five $(Mn_xFe_{1-x})_zO$ samples were measured at temperatures between 50 and 300K; the values are tabulated in Appendix 2 and plotted in Figure 6.11. Features worthy of comment are the decrease in susceptibility at the Néel temperature between the 10% and 66% manganese samples, which can be attributed to the presence of decreasing amounts of ferrimagnetic $Fe_3O_4$ ($T_c$ = 858K) or iron-rich

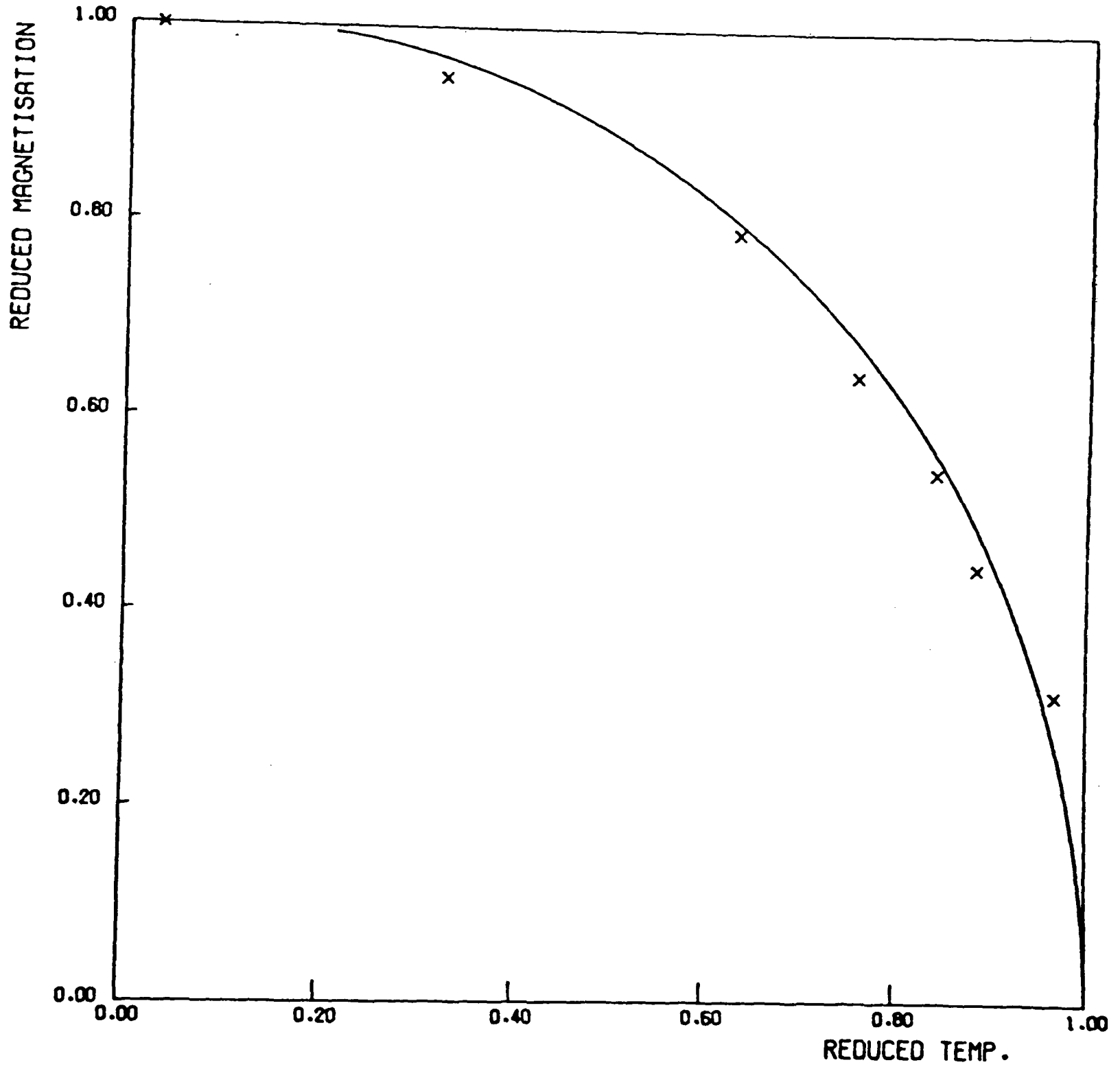



Figure 6.10 Observed (crosses) and Calculated (full line) Temperature Variation of the Sublattice Magnetisation of $(Mn_{0.66}Fe_{0.34})_{0.954}O$.

$(Mn_xFe_{1-x})_3O_4$ impurity, and the increase in susceptibility at temperatures below 60K for samples containing 23% or more manganese. The latter behaviour may be traced to small quantities of ferrimagnetic $Mn_3O_4$ or $(Mn_xFe_{1-x})_3O_4$ $(0.9 < x < 1.0)$, since $T_c$ for $(Mn_xFe_{1-x})_3O_4$ decreases monotonically from 858K to 323K at $x = 0.9$, but then drops sharply to

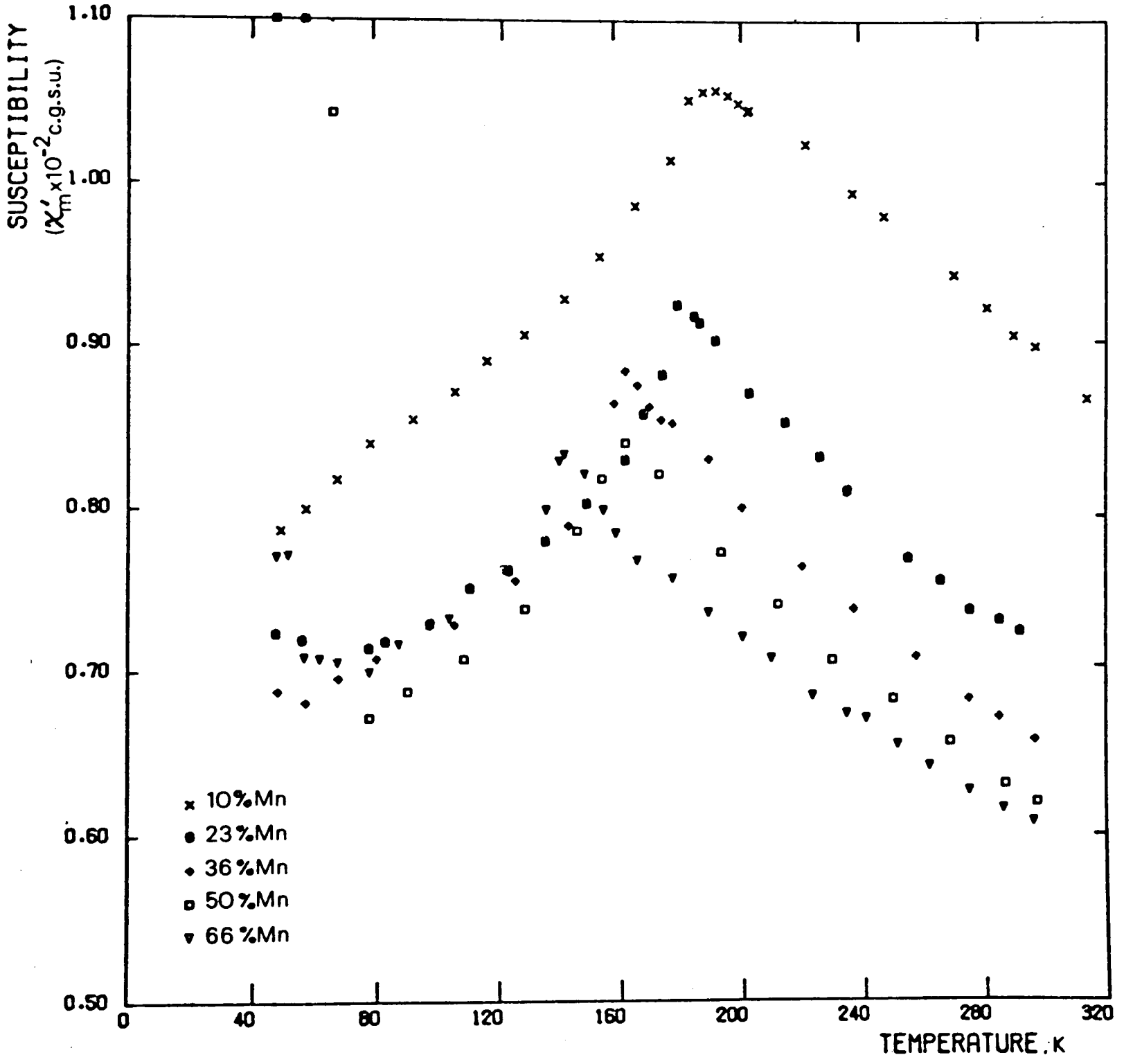



Figure 6.11 Magnetic Susceptibilities of $(Mn_xFe_{1-x})_zO$.

reach 43K at $Mn_3O_4$.[241] Similar increases in susceptibility at low temperatures have been observed in studies of MnO powder and single crystal samples, and attributed to small quantities of $Mn_3O_4$ [191].

### 6.2.2 Lattice Distortions and Magnetic Structures at 5K

#### (a) Introduction

Chapter 5 indicates how the magnetic anisotropies and lattice distortions of MnO, CoO and $Mn_xCo_{1-x}O$ are related to the electronic structures of the component ions. In the following pages, analogous neutron diffraction experiments designed to study the effects of doping by cobalt and manganese on the corresponding properties of ferrous oxide are considered. From the Introduction (Chapter 2), it will be recalled that high spin ferrous ion has a single ion anisotropy similar to that of cobaltous, which produces a trigonal ($\alpha < 90^o$) magnetostrictive distortion in ferrous oxide below ~ 200K. Unlike CoO, the moment is aligned parallel to the unique axis and $\underline{S}$ and $\underline{L}$ must be collinear, but the magnetic properties are complicated by non-stoichiometry and the presence of defect clusters. With regard to the contents of this section of the chapter, the influence of ferric ion on the trigonal magnetostriction of $Fe_zO$ [3,153] is especially relevant (Figure 2.12); ferrous oxide can be considered a solid solution also. Subsequently, $Mn^{2+}$ and $Co^{2+}$ will be seen to have equally profound effects on both the direction of the ferrous moment and on the lattice distortions related to the magnetic ordering.

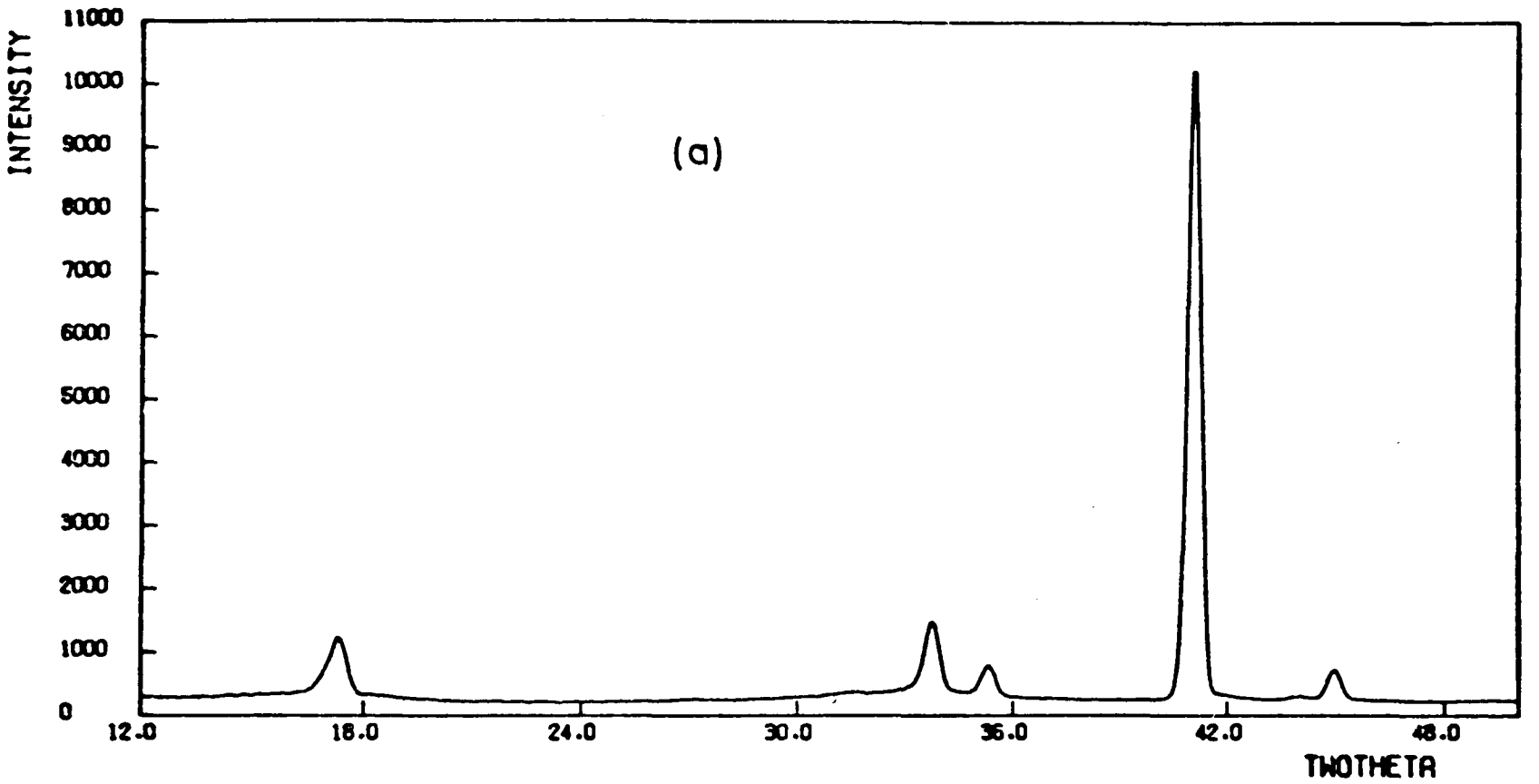
The compositions studied, the diffractometers used, and some details of the refinements of the nuclear structures are summarised in Table 6.1. More extensive information, showing the nuclear and magnetic parameters referred to pseudocubic cells and, in some cases, trigonal or monoclinic cells (Chapter 3.2.4), is set out in Tables 6.4, 6.5 and 6.6. Wavelengths between 1.38 and 1.904 Å were employed, although most experiments were carried out at ~ 1.5 Å. Plots showing a cross section of the final observed and calculated profiles resulting from application of the

Rietveld technique appear in Appendix 1.

(b) Anisotropies and Magnetostrictions

Surprisingly, substitution of $Co^{2+}$ and $Mn^{2+}$ into the ferrous oxide lattice has a dramatic effect upon the direction of the overall sub-lattice magnetisation, although $Fe^{2+}$ might be presumed to have a strong single ion anisotropy. The absence of a (111) magnetic Bragg reflection in $Fe_zO^3$ is evidence for magnetic moments parallel to [111] (Equation 3.4), but both cobalt and manganese cause this peak to appear when they are present in only small amounts (Figures 6.12 and 6.13). In addition to demonstrating the ease with which the orientation of the ferrous moments can be changed, these figures suggest that the anisotropy of $Co^{2+}$ is only slightly stronger than that of $Mn^{2+}$, and the magnitudes of the (111) peaks show how the effects of the strongly anisotropic species are transmitted to all ions via the appreciable $180^{o}$ cation-anion-cation superexchange interactions. Initially, $Co^{2+}$ was expected to have a much larger, single ion effect than the dipolar anisotropy of $Mn^{2+}$, but the present results, and those found for $Mn_xCo_{1-x}O$ (Chapter 5), demonstrate that this is not the case.

The two ferrous oxide solid solutions probably afford a more realistic comparison of the MnO and CoO anisotropies than does $Mn_xCo_{1-x}O$ and, bearing in mind the results obtained for $Co_xNi_{1-x}O^2$, it now seems that the anisotropy order for the iron group oxides is CoO>MnO>>$Fe_zO$≈NiO. This unexpected order must stem from the much smaller anisotropy of $Fe^{2+}$, to be discussed below, and the large exchange striction associated with $Mn^{2+}$. The latter contribution is not present in two-dimensional anti-ferromagnets such as $Fe_xCo_{1-x}C\ell_2.2H_2O$ [170] and $K_2M_xMn_{1-x}F_4$ (M = Fe, Co)[172], wherein the ferrous and cobaltous anisotropies are very similar.



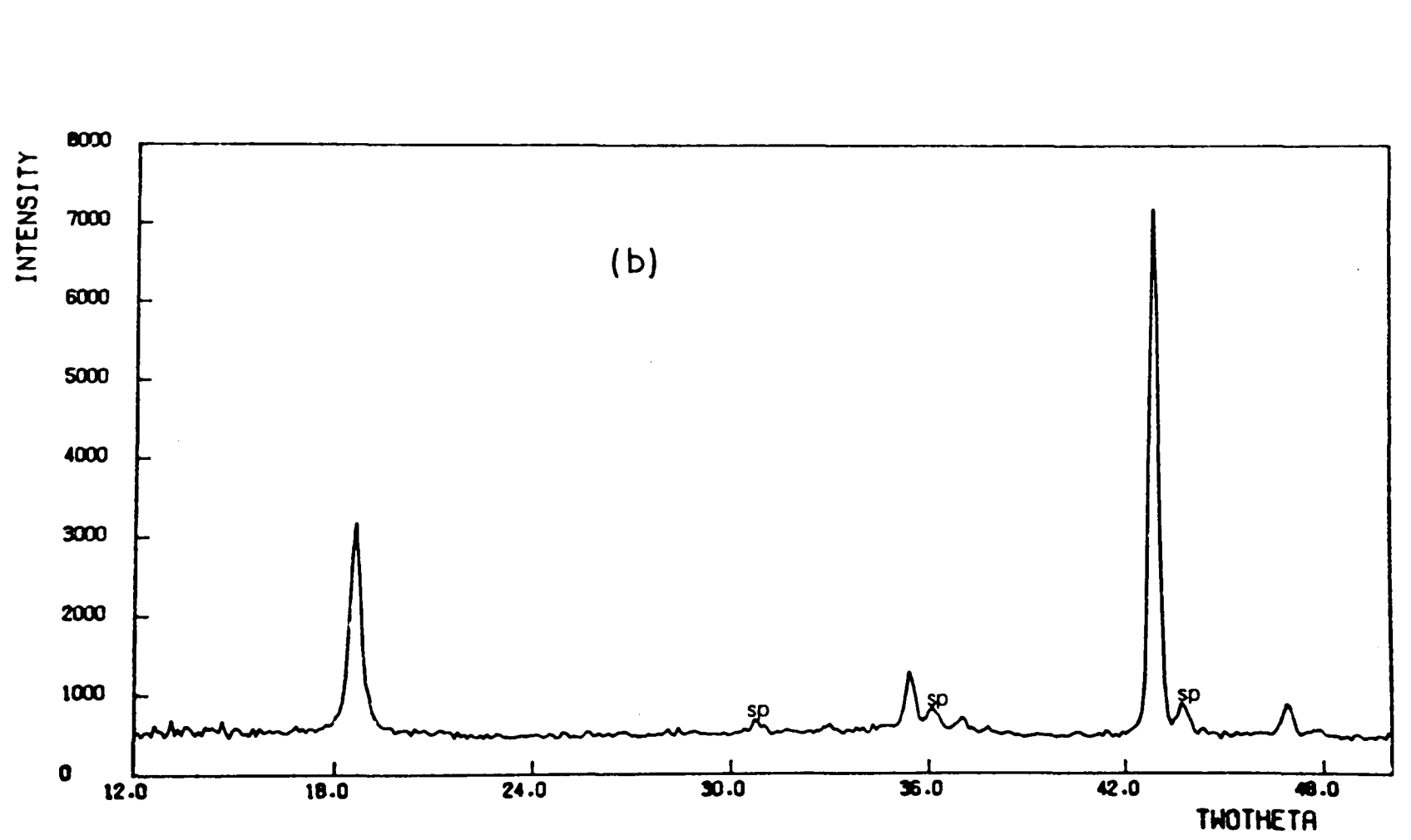
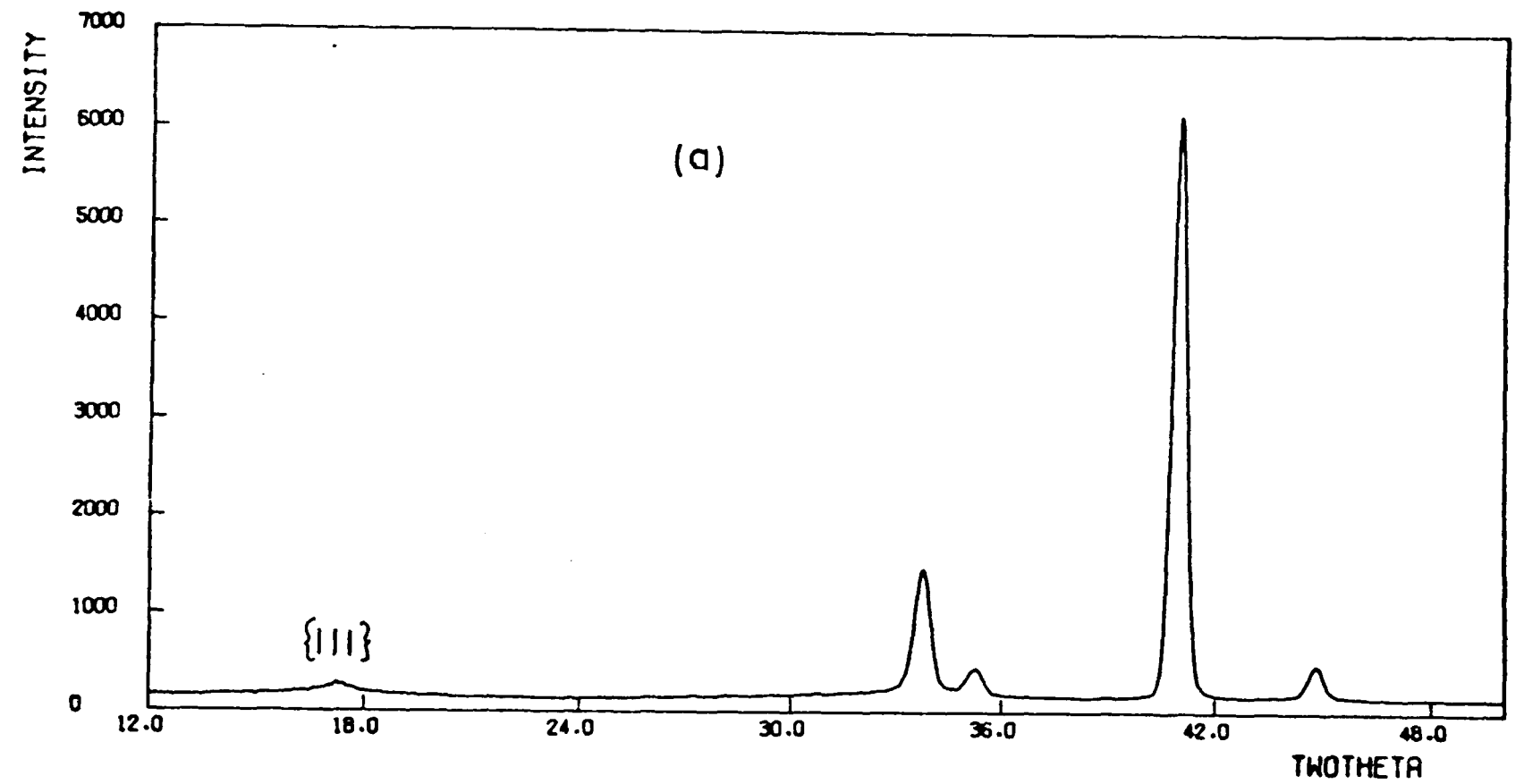




Figure 6.12 Low Angle Regions of the Profiles of (a) $(Co_{0.04}Fe_{0.96})_{0.939}O$ and (b) $(Co_{0.12}Fe_{0.88})_{0.911}O$. "sp" refers to spinel impurity peaks.



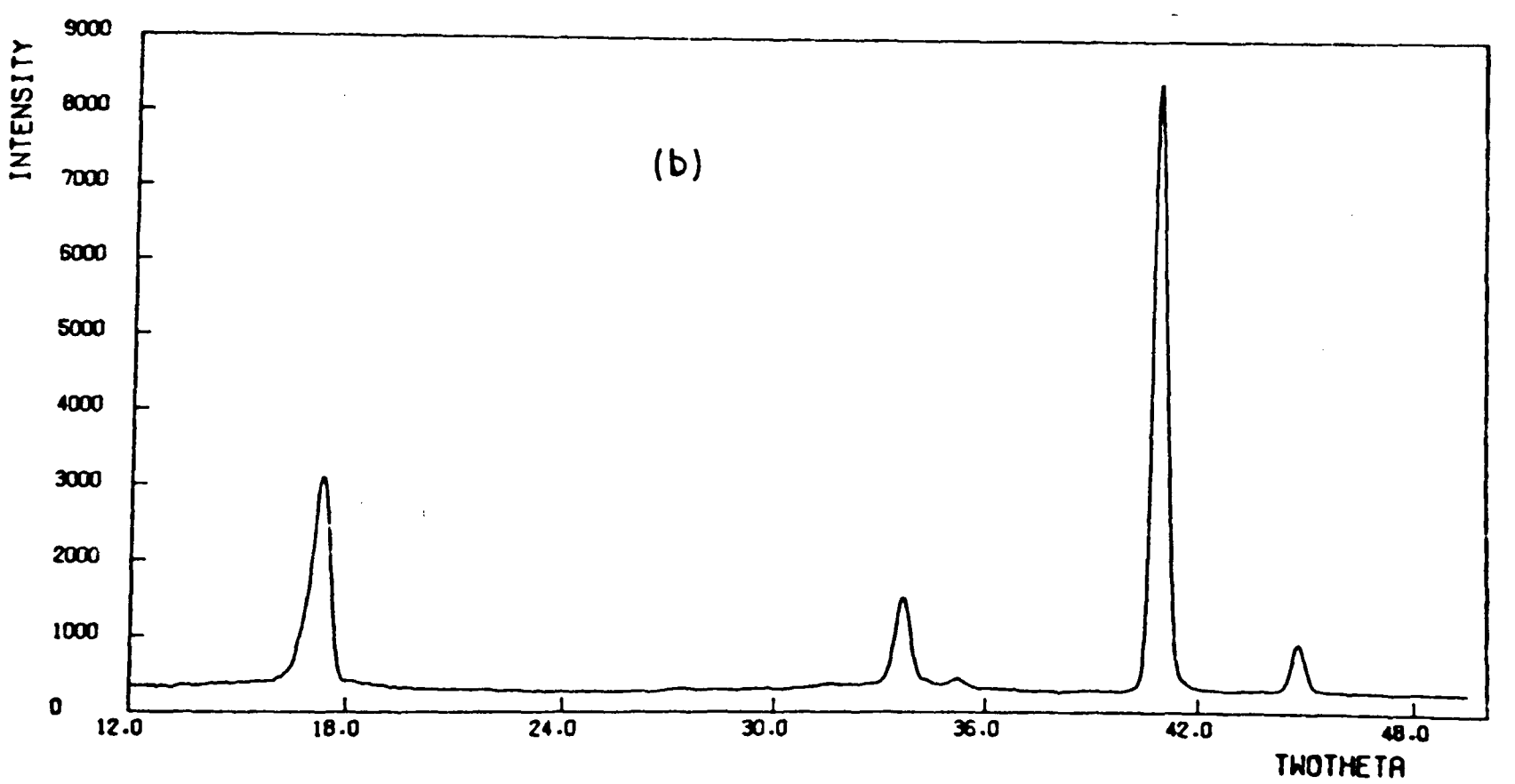




Figure 6.13 Low Angle Regions of the Profiles of (a) $(Mn_{0.05}Fe_{0.95})_{0.954}O$ and (b) $(Mn_{0.12}Fe_{0.88})_{0.926}O$.

| COMPOSITION | a | b (Å) | c | α | β (o) | γ | B-overall ($Å^2$) | $R_{nuc}$ | $R_{mag}$ | $R_{pr}$ |
|---|---|---|---|---|---|---|---|---|---|---|
| $(Mn_{0.05}Fe_{0.95})_{0.936}O$ | 8.6338(10) | 8.6338(10) | 8.6338(10) | 90 | 90 | 90 | 0.5199(386) | 2.64 | 14.87 | 6.97 |
| $(Mn_{0.05}Fe_{0.95})_{0.954}O$ | 3.0398(1) | 3.0398(1) | 14.9835(8) | 90 | 90 | 120 | 0.6248(285) | 4.15 | 7.82 | 9.87 |
| $(Mn_{0.10}Fe_{0.90})_{0.931}O$ | 8.6228(5) | 8.6228(5) | 8.6228(5) | 90 | 90 | 90 | 0.7815(529) | 3.69 | 9.98 | 9.66 |
| $(Mn_{0.12}Fe_{0.88})_{0.926}O$ | 8.6244(2) | 8.6244(2) | 8.6224(2) | 90.051(4) | 90.051(4) | 90.051(4) | 0.8553(275) | 2.85 | 10.04 | 7.25 |
| $(Mn_{0.23}Fe_{0.77})_{0.929}O$ | 3.0564(5) | 3.0564(5) | 14.9831(30) | 90 | 90 | 120 | 0.7118(404) | 2.76 | 10.52 | 6.70 |
| $(Mn_{0.36}Fe_{0.64})_{0.954}O$ | 8.7120(2) | 8.7120(2) | 8.7120(2) | 90.049(3) | 90.049(3) | 90.049(3) | 0.8998(304) | 3.91 | 8.96 | 9.07 |
| $(Mn_{0.56}Fe_{0.44})_{0.993}O$ | 5.3844(3) | 3.1028(1) | 6.2122(4) | 90 | 54.568(3) | 90 | 0.5865(170) | 2.55 | 1.95 | 4.89 |
| $(Mn_{0.66}Fe_{0.34})_{0.954}O$ | 3.0971(4) | 3.0971(4) | 15.1407(32) | 90 | 90 | 120 | 1.2475(1026) | 13.92 | 14.25 | 19.94 |
| $(Mn_{0.89}Fe_{0.11})_{0.997}O$ | 3.1458(5) | 3.1458(5) | 15.1784(18) | 90 | 90 | 120 | 0.5144(566) | 4.42 | 7.93 | 10.65 |
| $(Co_{0.04}Fe_{0.96})_{0.939}O$ | 3.0332(1) | 3.0332(1) | 14.8298(5) | 90 | 90 | 120 | 0.6654(223) | 1.72 | 14.47 | 5.52 |
| $(Co_{0.12}Fe_{0.88})_{0.911}O$ | 8.5498(9) | 8.5498(9) | 8.5498(9) | 90 | 90 | 90 | 1.1181(1128) | 4.30 | 22.30 | 12.48 |
| $(Co_{0.50}Fe_{0.50})_{0.935}O$ | 8.5429(13) | 8.5429(13) | 8.5429(13) | 90 | 90 | 90 | 0.4649(591) | 4.75 | 12.07 | 12.99 |
| $(Co_{0.63}Fe_{0.37})_{0.958}O$ | 5.2150(4) | 3.0152(1) | 6.0488(2) | 90 | 54.621(6) | 90 | 0.3964(171) | 3.10 | 4.37 | 6.02 |
| $(Co_{0.81}Fe_{0.19})_{0.980}O$ | 8.5373(6) | 8.5373(6) | 8.5373(6) | 90 | 90 | 90 | -0.0908(510) | 4.88 | 5.66 | 10.83 |

TABLE 6.4 Nuclear and Profile Parameters Resulting from Refinements of $(Mn_xFe_{1-x})_zO$ and $(Co_xFe_{1-x})_zO$ at 5K.

| COMPOSITION | a | b (Å) | c | α | β (°) | γ |
|---|---|---|---|---|---|---|
| $(Mn_{0.05}Fe_{0.95})_{0.954}O$ | 4.307 | 4.307 | 4.307 | 89.76 | 89.76 | 89.76 |
| $(Mn_{0.23}Fe_{0.77})_{0.929}O$ | 4.323 | 4.323 | 4.323 | 90.03 | 90.03 | 90.03 |
| $(Mn_{0.56}Fe_{0.44})_{0.993}O$ | 4.390 | 4.390 | 4.390 | 90.15 | 90.15 | 89.94 |
| $(Mn_{0.66}Fe_{0.34})_{0.954}O$ | 4.377 | 4.377 | 4.377 | 90.08 | 90.08 | 90.08 |
| $(Mn_{0.89}Fe_{0.11})_{0.997}O$ | 4.427 | 4.427 | 4.427 | 90.58 | 90.58 | 90.58 |
| $(Co_{0.04}Fe_{0.96})_{0.939}O$ | 4.287 | 4.287 | 4.287 | 90.08 | 90.08 | 90.08 |
| $(Co_{0.63}Fe_{0.37})_{0.958}O$ | 4.271 | 4.271 | 4.252 | 89.95 | 89.95 | 89.83 |

TABLE 6.5 Equivalent Pseudocubic Cells for $(Mn_xFe_{1-x})_zO$ and $(Co_xFe_{1-x})_zO$

| COMPOSITION | $K_x$ | $K_y$ | $K_z$ | $\mu(\mu_B)$ | $\theta(^o)$* |
|---|---|---|---|---|---|
| $(Mn_{0.05}Fe_{0.95})_{0.936}O$ | 1.741(1.00) | 1.741(1.00) | 1.903(1.886) | 3.112(057) | 3 |
| $(Mn_{0.05}Fe_{0.95})_{0.954}O$ | - | - | 3.090(042) | 3.090(042) | 0 |
| $(Mn_{0.10}Fe_{0.90})_{0.931}O$ | 0.369(198) | 0.369(198) | 2.963(350) | 3.008(343) | 29 |
| $(Mn_{0.12}Fe_{0.88})_{0.926}O$ | 0.169(132) | 0.169(132) | 2.978(071) | 2.988(076) | 50 |
| $(Mn_{0.23}Fe_{0.77})_{0.929}O$ | 3.223(079) | - | 0.139(890) | 3.226(053) | ~90 |
| $(Mn_{0.36}Fe_{0.64})_{0.954}O$ | 2.493(052) | -2.493(052) | - | 3.524(074) | 90 |
| $(Mn_{0.56}Fe_{0.44})_{0.993}O$ | 3.310(305) | 2.566(279) | -0.423(265) | 4.012(012) | ~90 |
| $(Mn_{0.66}Fe_{0.34})_{0.954}O$ | 3.659(074) | - | - | 3.659(074) | 90 |
| $(Mn_{0.89}Fe_{0.11})_{0.997}O$ | 4.432(054) | - | - | 4.432(054) | 90 |
| $(Co_{0.04}Fe_{0.96})_{0.939}O$ | 1.807(143) | - | -1.940(093) | 2.651(125) | 53 |
| $(Co_{0.12}Fe_{0.88})_{0.911}O$ | 0.501(343) | 0.501(343) | -2.653(555) | 2.745(574) | 70 |
| $(Co_{0.50}Fe_{0.50})_{0.935}O$ | 0.900(385) | 0.900(385) | -2.820(528) | 3.094(545) | 80 |
| $(Co_{0.63}Fe_{0.37})_{0.958}O$ | 3.714(068) | - | -0.721(163) | 3.348(024) | 82 |
| $(Co_{0.81}Fe_{0.19})_{0.980}O$ | 0.848(157) | 0.848(157) | -3.271(345) | 3.484(363) | 75 |

* Angle of Inclination to the [111] axis.

TABLE 6.6 Magnetic Parameters (referred to the cells set out in Table 6.4) of $(Mn_xFe_{1-x})_zO$ and $(Co_xFe_{1-x})_zO$ at 5K.

Owing to the appreciable peak asymmetry at low scattering angles (section 3.2.2), only data above $2\theta \sim 30^{o}$ could be refined by profile analysis. The moment orientations are presented in Table 6.6 and, again, we believe that the moments are collinear. Figure 6.14 allows the rate of change of direction with increasing amounts of non-ferrous ion to be gauged. For instance, 12% cobalt is sufficient to rotate the moment to a position only $11^{o}$ from the easy axis of CoO ($\sim 27^{o}$ from [001], Chapter 5.2.2), and in the more cobalt-rich solid solutions the moments are located close to the CoO direction. It appears that doping cobaltous oxide with $Fe^{2+}$ does not have the same effect on the $Co^{2+}$ moments as incorporation of $Mn^{2+}$ into CoO (Chapter 5), presumably because of the much smaller exchangestriction resulting from $Fe^{2+}$-$Fe^{2+}$ exchange (section 6.2.2(c)). However, the lack of any trigonal magnetostriction due to $Fe^{2+}$ in CoO-$Fe_zO$ (Table 6.5) is very significant, and will be discussed below.

In MnO-$Fe_zO$ samples containing more than 23% manganese, magnetic moment orientations almost parallel with the (111) plane are always adopted and only small lattice distortions are, in general, observed. No direct evidence for quenched $Fe^{2+}$ moments is available, although this is likely when they are inclined at approximately $90^{o}$ to [111], since a component parallel to the three-fold axis is required in order to maintain the orbital contribution [104]. The $(Mn_{0.05}Fe_{0.95})_{0.954}O$ composition shows a trigonal ($\alpha < 90^{o}$) distortion compatible with a moment very close to [111], and the size of the striction is similar to that of the ferrous oxide composition containing the same amount of $Fe^{2+}$ ($Fe_{0.932}O$: see Figure 2.12). In $(Mn_{0.05}Fe_{0.95})_{0.936}O$, the slight displacement of the moment from [111] ($3^{o}$) and the non-existence of a trigonal distortion are consistent with the presence of only 81.3% $Fe^{2+}$

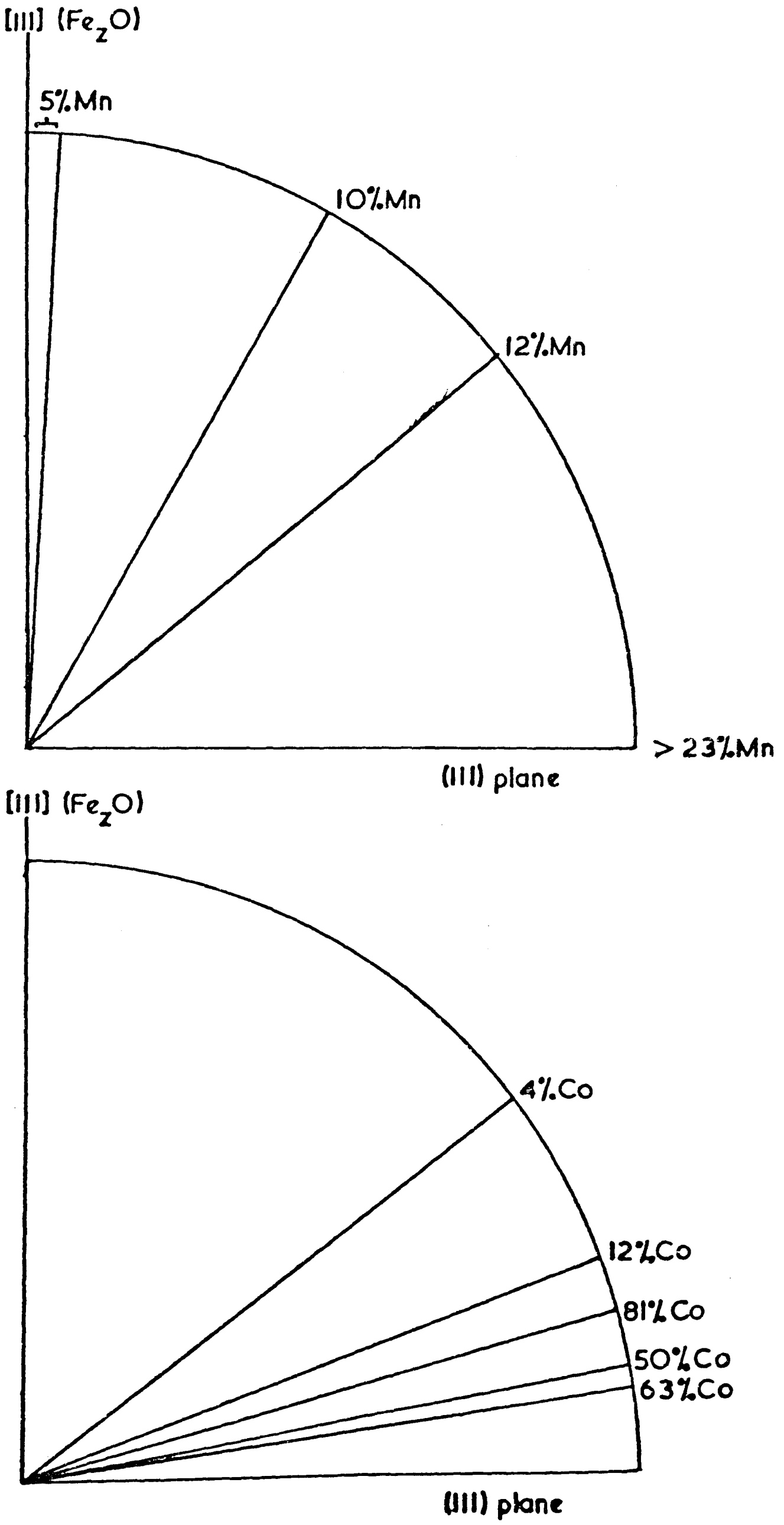



Figure 6.14 Moment directions in MnO-$Fe_zO$ and CoO-$Fe_zO$.

(equivalent to $Fe_{0.915}O$) and an increased amount of $Fe^{3+}$. Ferric ion has the same electronic structure ($^6A_{1g}$) and dipolar anisotropy as $Mn^{2+}$ and would be expected to have a similar influence, although this is probably somewhat tempered by the localisation of $Fe^{3+}$ around defect clusters.

The similarity between the dependence of $\alpha$ on z in $Fe_zO$ (Figure 2.12) and the disappearance of the trigonal ($\alpha < 90^o$) distortion in $MnO-Fe_zO$ and $CoO-Fe_zO$ is worthy of note. With regard to ferrous oxide itself, the loss of the striction has been attributed to the quenching of the $Fe^{2+}$ moments in the vicinity of the defect clusters [3] and to the opposition of the $Fe^{2+}$--$Fe^{2+}$ exchange interactions when near-cubic symmetry is attained [104] (section 2.2.4). In the solid solutions, the magnetostriction is additionally reduced by rotation of the overall moment away from [111] and by changes in the electronic structure of $Fe^{2+}$ induced by doping. In fact as little as 4% cobalt or 12% manganese reverse the sign of the trigonal distortion (to $\alpha > 90^o$) (according to the neutron refinements), results which may be attributed to either antiferromagnetic $Fe^{2+}$--$Fe^{2+}$ exchange, a Jahn-Teller stabilisation of $Fe^{2+}$ (Figure 2.10), or a trigonal magnetostriction due to $Co^{2+}$ in $(Co_{0.04}Fe_{0.96})_{0.939}O$ arising from the placement of moments close to [111]. In addition to these factors, others opposed to the deformation-dependent trigonal anisotropy energy of $Fe^{2+}$ ($\alpha < 90^o$) are possible.

The first is the unfavourable magnetic dipole-dipole repulsion between ferromagnetic sheets when the moments are perpendicular to these planes. Kaplan [129] shows that no torque acts on them when they are directed along [111], although the energy is appreciably smaller when the moments are parallel to the planes. However, any component parallel to the sheets introduced by $Fe^{3+}$, $Mn^{2+}$ or $Co^{2+}$ will furnish a driving

force for rotation away from the unique axis.

Secondly, the orbital angular momentum of $Fe^{2+}$ can also be maintained if a tetragonal expansion occurs along [001], by analogy with CoO (Figure 2.10). Although no suggestion of this stabilisation is found in MnO-$Fe_zO$, the variation of c/a with composition for samples of CoO-$Fe_zO$ containing > 50% $Co^{2+}$ provides evidence for its existence. Figure 6.15 compares the tetragonal distortions of this system with

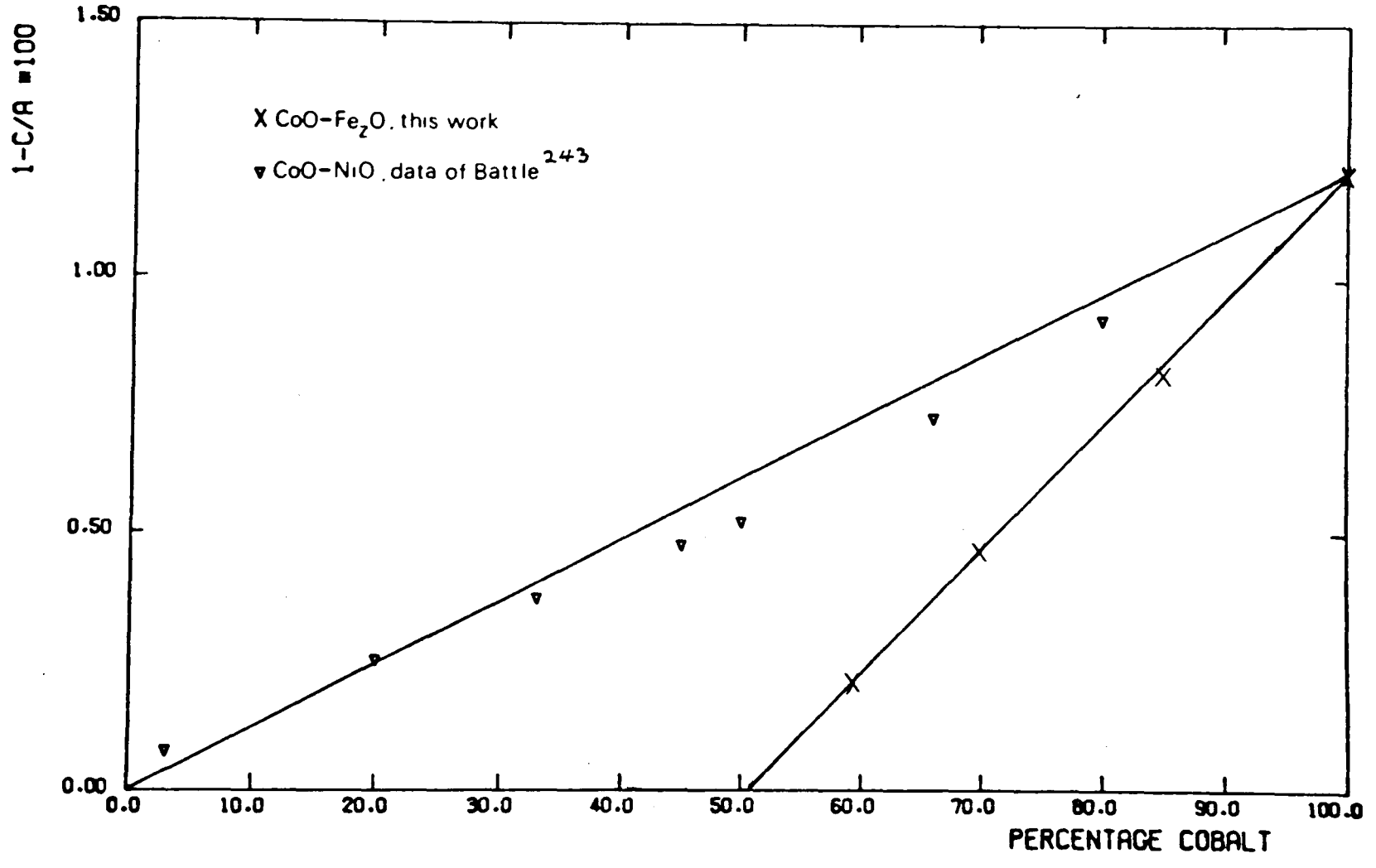



Figure 6.15 The Tetragonal Distortions of CoO-$Fe_zO$ and CoO-NiO [243] as a Function of Cobalt Content.

those of $Co_xNi_{1-x}O$ [243]. In the latter, the contraction along c changes approximately linearly with composition and disappears when the proportion of cobalt reaches zero, which is a clear demonstration of the single ion behaviour of CoO within the weakly anisotropic NiO lattice. The points plotted for $(Co_xFe_{1-x})_zO$ in Figure 6.15 represent the

measured distortions of cobalt compositions given by $[Co^{2+}/(Co^{2+} + Fe^{2+})] \times 100\%$. The variation remains linear, but the tetragonal contraction disappears at approximately 50% cobalt, which suggests that an expansion along c counteracts the $Co^{2+}$ single ion effect.

A possible explanation is the appearance of the alternative spin-orbit stabilisation of $Fe^{2+}$, which is induced by the tetragonal bias due to $Co^{2+}$ and the placement of moments close to [001]. It is significant that the calculations of Kanamori [146] suggest a marked preference by $Fe^{2+}$ for the four-fold axis ([001]) on magnetoelastic grounds alone. Apparently, other anisotropic exchange and quadrupole interactions lead to the choice of the [111]easy axis. Extrapolation of Figure 6.15 to zero cobalt content furnishes a value for the tetragonal distortion of stoichiometric FeO of c/a = 1.013, which compares with the CoO value of 0.988 (Chapter 5.2.2). If it had been possible to prepare samples in the 12-50% $Co^{2+}$ composition range, it would have been instructive to ascertain whether a $c/a > 1$ distortion appears here.

The similarities and differences between the lattice parameter behaviour of $(Co_xFe_{1-x})_zO$ and $Mn_xCo_{1-x}O$ (Chapter 5) are worthy of comment. For both systems, the observed symmetries must be accounted for in terms of variations in the local distortions from one region of the lattice to the other. The resulting disorder might then be expected to lead to increased temperature factors, although the average lattice parameters would still be defined. However, the temperature factors of MnO-CoO appear normal in size (Table 5.1), and in CoO-$Fe_zO$ any increase must stem, at least in part, from relaxation around the defects.

The difference in the observed symmetries of the two systems should

also be stressed. While triclinic symmetry is observed in $Mn_xCo_{1-x}O$ (see Figure 5.4), the least degenerate lattice type in $(Co_xFe_{1-x})_zO$ is monoclinic. In the former, the simultaneous presence of spin-orbit and Jahn-Teller stabilised $Co^{2+}$ leads to tetragonal $c/a < 1$ and $c/a > 1$ distortions directed along different unique axes, but in the latter the link between the sublattice magnetisation and the lattice for both $Co^{2+}$ and $Fe^{2+}$ requires that their opposite tetragonal distortions be coaxial.

(c) Exchangestrictions

The lattice distortions observed in $MnO-Fe_zO$ and $CoO-Fe_zO$ are the resultants of a number of contributions: exchangestrictions between like and unlike $Fe^{2+}$, $Co^{2+}$, $Mn^{2+}$ and $Fe^{3+}$ ions, and the magnetostrictions discussed in section (6.2.2(b). It is difficult to predict the combined influence of all these effects, although in certain cases, MnO for instance, assignment is unambiguous. Separation of the distortions due to cation--cation and cation-oxygen-cation interactions is especially problematical, although the former are predicted to be larger, in general. The signs of the cation--cation exchanges of the pure oxides have been discussed in Chapter 2; that between ferrous ions is ferromagnetic when an $\alpha < 90^o$ distortion is present, but antiferromagnetic otherwise, and the $Co^{2+}-Co^{2+}$ coupling should be ferromagnetic. The manganous-manganous exchange is antiferromagnetic, as are the interactions between $Fe^{2+}$ and $Mn^{2+}$ or $Fe^{3+}$, which mostly involve half-full orbitals. The couplings between $Co^{2+}$ and $Fe^{2+}$ are slightly weighted in favour of the ferromagnetic case (an excess of half-full over full interactions).

These predictions are confirmed by the cell angles observed in the

$(Co_xFe_{1-x})_zO$ system. Apart from the 4% Co sample, which was discussed in section 6.2.2(b), $(Co_{0.63}Fe_{0.37})_{0.954}O$ shows a very small rhombohedral component ($\alpha < 90^o$); this is compatible with ferromagnetic $Co^{2+}$-$Co^{2+}$ and $Fe^{2+}$-$Co^{2+}$ nearest neighbour cation--cation exchange and, in conjunction with the tetragonal magnetostriction, gives rise to the monoclinic cell parameters quoted in Table 6.4. The transformation between cells is considered in Chapter 3.2.4. No angular distortions are detected in the other samples, owing to their small magnitudes and the limitations of the PANDA diffractometer.

The cell parameters of all MnO-$Fe_zO$ compositions are given in Tables 6.4 and 6.5 and, amongst the members of this system, the sample containing 89% manganese shows a large $\alpha > 90^o$ rhombohedral distortion compatible with predominantly antiferromagnetic $Mn^{2+}$-$Mn^{2+}$ and $Mn^{2+}$-$Fe^{2+}$ exchange. Bar the 5% manganese samples (discussed in section 6.2.2(b)) and $(Mn_{0.56}Fe_{0.44})_{0.993}O$, all the other compositions exhibit small $\alpha > 90^o$ components. The signs of these distortions are compatible with the antiferromagnetic couplings thought to be present, but the small deviations from $90^o$ are anomalous since they suggest that the large effect of the $Mn^{2+}$--$Mn^{2+}$ exchangestriction must be counteracted by a competing ferromagnetic component favouring $\alpha < 90^o$. In this respect, the MnO-$Fe_zO$ system is similar to MnO-NiO (Chapter 4), but the origin of the ferromagnetic exchange is now unclear. All the readily identifiable terms, such as the $Mn^{2+}$-$Mn^{2+}$, $Fe^{2+}$-$Mn^{2+}$ and $Fe^{2+}$-$Fe^{2+}$ couplings, superexchange involving $Fe^{3+}$, and the co-operative Jahn-Teller distortion of $Fe^{2+}$, favour expansion of the cell angles. In this case, perhaps the effect of the cation--cation exchange between unlike ions on the exchangestriction is small, and a ferromagnetic cation-oxygen-cation mechanism, similar to those present in NiO (Chapter 2.2.2), negates

the $Mn^{2+}$--$Mn^{2+}$ exchangestriction.

Another aspect of the behaviour of $(Mn_{0.56}Fe_{0.44})_{0.993}O$ is reminiscent of the MnO-NiO system. Here, as in $Mn_{0.77}Ni_{0.23}O$ (section 4.2.3), consistency between the nuclear and magnetic periodicities requires a cell $a=b\simeq c$, $\alpha=\beta>90^{o}$, $\gamma<90^{o}$ and indicates that the magnetic structure does not propagate along a threefold axis. Again, the results suggest that an unreasonably large magnetostriction is present, but no explanation for the anomaly can be advanced. In fact, the data refined well on the basis of a monoclinic unit cell, the parameters of which are given in Table 6.4, although the nuclear peaks indexed satisfactorily according to the $R\bar{3}$ space group with $\alpha < 90^{o}$. In the pseudo-cubic setting of the monoclinic cell, a and b are slightly larger than c, suggestive of a Jahn-Teller stabilisation of $Fe^{2+}$ (Figure 2.10), although the distortion is probably within experimental error. Moreover, the monoclinic symmetry allows the absolute moment direction to be determined (section 3.2.2). Table 6.6. shows that this is close to the (111) plane and intermediate between $[\bar{1}10]$ and $[\bar{1}\bar{1}2]$. While the absolute direction is probably not meaningful owing to the smallness of the monoclinic distortion, it may be significant (with regard to the validity of the $Mn_xCo_{1-x}O$ magnetic moment results) that the moment now has a preference for the [CoO] and [FeO] side of the (111) plane, unlike the $Mn_{0.66}Co_{0.34}O$ and $Mn_{0.51}Co_{0.49}O$ solid solutions, where it lies on the opposite side of (111) (Chapter 5.2.4).

### 6.2.3 Defect and Magnetic Structures

The magnetic structural model of ferrous oxide due to Battle and Cheetham [3] was briefly reviewed in Chapter 2, but some salient points deserve reiteration here. The spins of the occupied nearest neighbour

octahedral sites of a tetrahedral interstitial are oriented perpendicular to the sublattice magnetisation of the surrounding matrix, and the interstitial is antiferromagnetically coupled to its octahedral nearest neighbours. The spins of the nearest neighbour ions are thereby decoupled from the magnetic ordering scheme and do not contribute to the magnetic Bragg peaks because the moment directions of different defect clusters are uncorrelated. The interstitial ions of 4:1, 6:2 and 8:3 clusters decouple 12, 16 and 20 neighbouring octahedral ions according to this model, and the moment reductions measured by Battle and Cheetham for three ferrous oxide samples of different composition are accounted for well in terms of the effect of the 8:3 defect cluster; the smaller units diminish the moment even further.

In their treatment, the above authors are forced to make assumptions as to the size of the $Fe^{2+}$ moment and the degree of expansion of the ferrous free ion form factor. It must be stressed that the analysis of the coherent magnetic neutron scattering from the non-stoichiometric ferrous oxide solid solutions involves further assumptions and approximations. Table 6.1 shows that most of the samples studied have comparable stoichiometries to the range of composition of ferrous oxide itself, and in order to compare the predictions of the Battle and Cheetham model with the observed magnetic moments, the metal:oxygen and iron:manganese or iron:cobalt ratios must be known very accurately. The scattering length applied to the octahedral site, and hence the measured moment (which depends on the site occupancy), will then be reliable. It is encouraging that the refinements of the nuclear structure described in Chapter 6.1.1 suggest that the use of the bulk analytical data is a good approximation. The nuclear structure results also indicate that 6:2 or 8:3 clusters are probably present in $MnO-Fe_zO$, with perhaps more extensive

clustering in CoO-$Fe_zO$. The Battle and Cheetham model applied to the 8:3 cluster therefore seems a good starting point for a consideration of the magnetic data obtained from the solid solutions.

The observed magnetic moments of the octahedral sites of all samples in the MnO-$Fe_zO$ and CoO-$Fe_zO$ systems are set out in Table 6.6, and were calculated using form factors which gave the minimum profile R, according to the procedure of section 3.2.4. Only the esd's resulting from the profile analyses are shown in the Table, but the actual errors are likely to be somewhat larger than those quoted for MnO-NiO and MnO-CoO. The magnetic R values are comparable in size to those obtained in the $Fe_zO$ analyses [3], except for $(Co_{0.12}Fe_{0.88})_{0.911}O$, where the counting statistics were very poor and the magnetic peaks weak. The reliability indices were sometimes slightly enhanced when models including the interstitial in the coherent ordering scheme were considered, but these improvements did not appear significant.

The observed octahedral site moments are plotted as crosses in Figures 6.16 and 6.17 and, as in $Fe_zO$, are much smaller for the non-stoichiometric samples than the predicted moment assuming no octahedral sites are decoupled. This moment ($\mu_{FULL}$) can be calculated as follows, assuming the tetrahedral sites do not contribute. For the formula $(M_xFe_{1-x})_zO$, (M = Mn or Co), the amount of $Fe^{3+}$ per formula unit is

$$a = 2(1 - z) \qquad (6.3)$$

and the tetrahedral occupancy (from Chapter 6.1.1) is t. Then,

$$\mu_{FULL} = \frac{xz\mu(M^{2+}) + \{(1-x)z-a\}\ \mu(Fe^{2+}) + (a-t)\mu(Fe^{3+})}{z-t} \qquad (6.4)$$

The magnetic moment of $Fe^{3+}$ is assumed to be $4.6\mu_B$, by analogy with $Mn^{2+}$

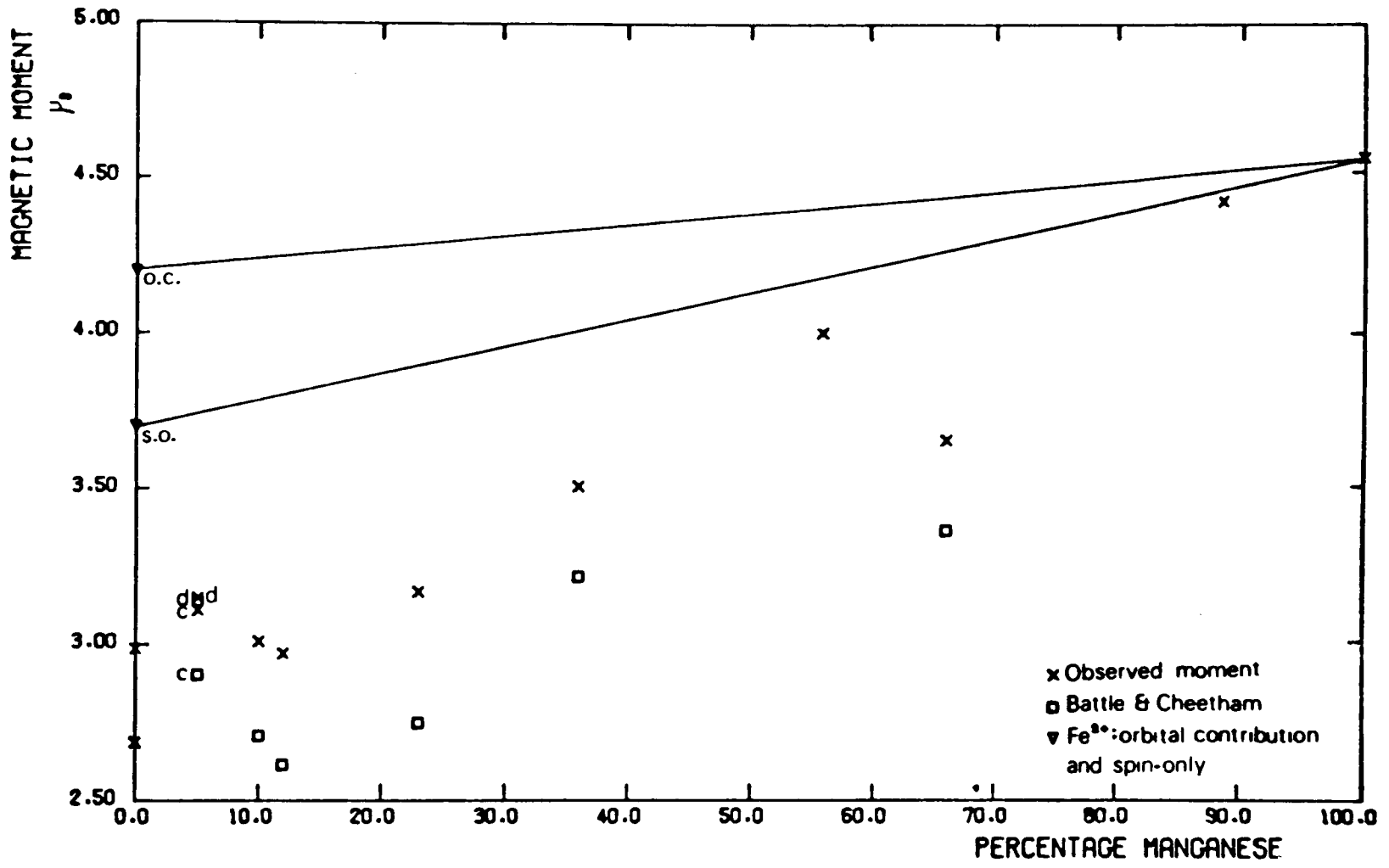



Figure 6.16 Comparison between the observed octahedral site moments of MnO-$Fe_zO$ and those calculated according to the model of Battle and Cheetham [3]. The points appertaining to the 5% manganese compositions measured on CURRAN and DIA (Table 6.1) are labelled c and d respectively. No errors are shown, but are estimated to be ~ $0.2\mu_B$ in all cases.

(Chapter 4). The $Fe^{2+}$ moment may or may not be quenched in $(Mn_xFe_{1-x})_zO$, and in Figure 6.16 the fully coherent moment of the octahedral sites then lies close to the lines joining the MnO value ($4.6\mu_B$) to the estimates (4.2 and $3.6\mu_B$) for "FeO" with and without an orbital contribution. According to the lattice parameter results of $(Co_xFe_{1-x})_zO$ (section 6.2.2(b)), $Fe^{2+}$ is presumed to maintain an orbital contribution across most of the composition range and only one line joining $4.2\mu_B$ ($Fe^{2+}$) and

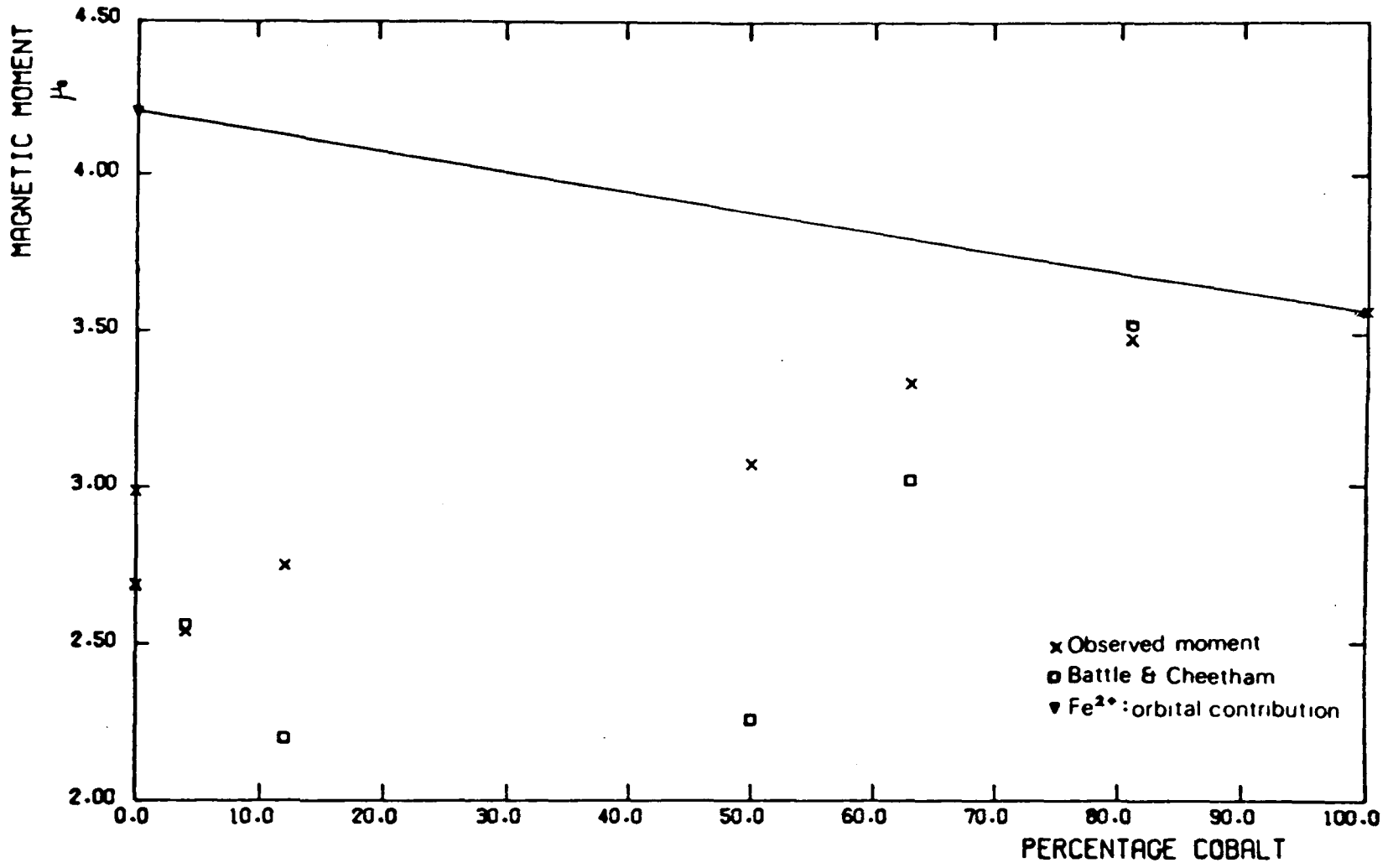



Figure 6.17 Comparison between the observed octahedral site moments of $CoO-Fe_zO$ and those calculated according to the model of Battle and Cheetham [3]. The errors are again estimated to be $\sim 0.2\mu_B$.

$3.6\mu_B$ ($Co^{2+}$) is depicted in Figure 6.17.

The Battle and Cheetham model [3] is applied as follows, assuming 8:3 defect clusters. The number of decoupled octahedral sites per 8:3 cluster is

$$d = \frac{v}{8} \times 3 \times 6.67 \qquad (6.5)$$

where v is the number of vacancies per unit cell (from the nuclear refinement) and 6.67 is the number of spins decoupled per tetrahedral interstitial for the 8:3 cluster. The number of contributing octahedral sites is then (1-v-d), and the predicted moment becomes

$$\mu_{EXP} = \mu_{FULL} (1-v-d) \qquad (6.6)$$

Although the ferrous moment may be quenched in some cases, the model is always applied assuming an $Fe^{2+}$ orbital contribution. A spin-only $Fe^{2+}$ moment for MnO-$Fe_zO$ would lead to predicted moments smaller than those plotted as squares in Figure 6.16.

The diminished moments observed for most of the samples confirm that the presence of defect clusters leads to a loss of coherent magnetic scattering, as in $Fe_zO$ itself. This is true even of $(Co_{0.81}Fe_{0.19})_{0.980}O$, which must have a smaller concentration of defect clusters, but the near-stoichiometric samples, $(Mn_{0.56}Fe_{0.44})_{0.993}O$ and $(Mn_{0.89}Fe_{0.11})_{0.997}O$, have moments lying close to the line joining the moments of MnO and spin-only $Fe^{2+}$ in "FeO". Assuming that the effect of defects is minimal here, this again suggests that the ferrous orbital momenta are quenched.

However, the more defective samples behave differently in comparison with ferrous oxide, in that only those containing 4-5% cobalt or manganese (where the moment vectors are closer to [111]) give good agreement with the moments calculated using the 8:3 cluster and the Battle and Cheetham model (as set out above). The more heavily doped compositions display larger observed moments than predicted moments, and it seems that when the overall sublattice magnetisation has a large component parallel to the (111) planes, the defect cluster and its surroundings partially contribute to the antiferromagnetic Bragg peaks. On the basis of the model of Battle and Cheetham, some increase in coherent scattering would be expected as the bulk moment rotates away from [111], since the spins around the cluster (uncorrelated in $Fe_zO$) will then experience a uniaxial torque tending to align them with the bulk magnetisation. However, any coherent scattering from ferrimagnetic clusters similar to that shown in Figure 2.13 should not lead to reinforcement of the type II f.c.c. magnetic peaks because the magnetic periodicity of the

defective regions does not coincide with the antiferromagnetic arrangement of the bulk structure.

Therefore, it seems that the Battle and Cheetham model for ferrous oxide may require modification, so that it takes into account the possibility of an antiferromagnetic cluster. The ferromagnetic arrangement (Figure 2.13) was assumed because it gives rise to the maximum antiferromagnetic exchange between the interstitial and its nearest neighbours, but it neglects the $180^{o}$ superexchange interactions between octahedral sites, which strongly favour an antiferromagnetic sequence. A possible antiferromagnetic moment configuration for the 6:2 cluster and some near-neighbour octahedral sites is shown in Figure 6.18; this is the opposite extreme to the ferrimagnetic cluster since the majority of the nearest neighbours of the interstitial are now ferromagnetically disposed to it. This figure also shows antiferromagnetically related interstitials, which appears to be a favoured orientation since the $90^{o}$ cation-oxygen-cation and cation- -cation interactions between ferric ions are presumably very similar to those between $Mn^{2+}$ ions. The lack of a completely coherent antiferromagnetic scattering contribution from the clusters probably stems from a situation intermediate between the limiting cases represented by Figures 2.13 and 6.18. The competing exchange requirements must then lead to a very complex arrangement of spins around the cluster.

### 6.2.4 Summary

The important conclusions of the second part of Chapter 6 are as follows:-

(a) The Néel temperatures of certain compositions of $MnO-Fe_zO$ show an approximately linear dependence on the concentration of manganese.

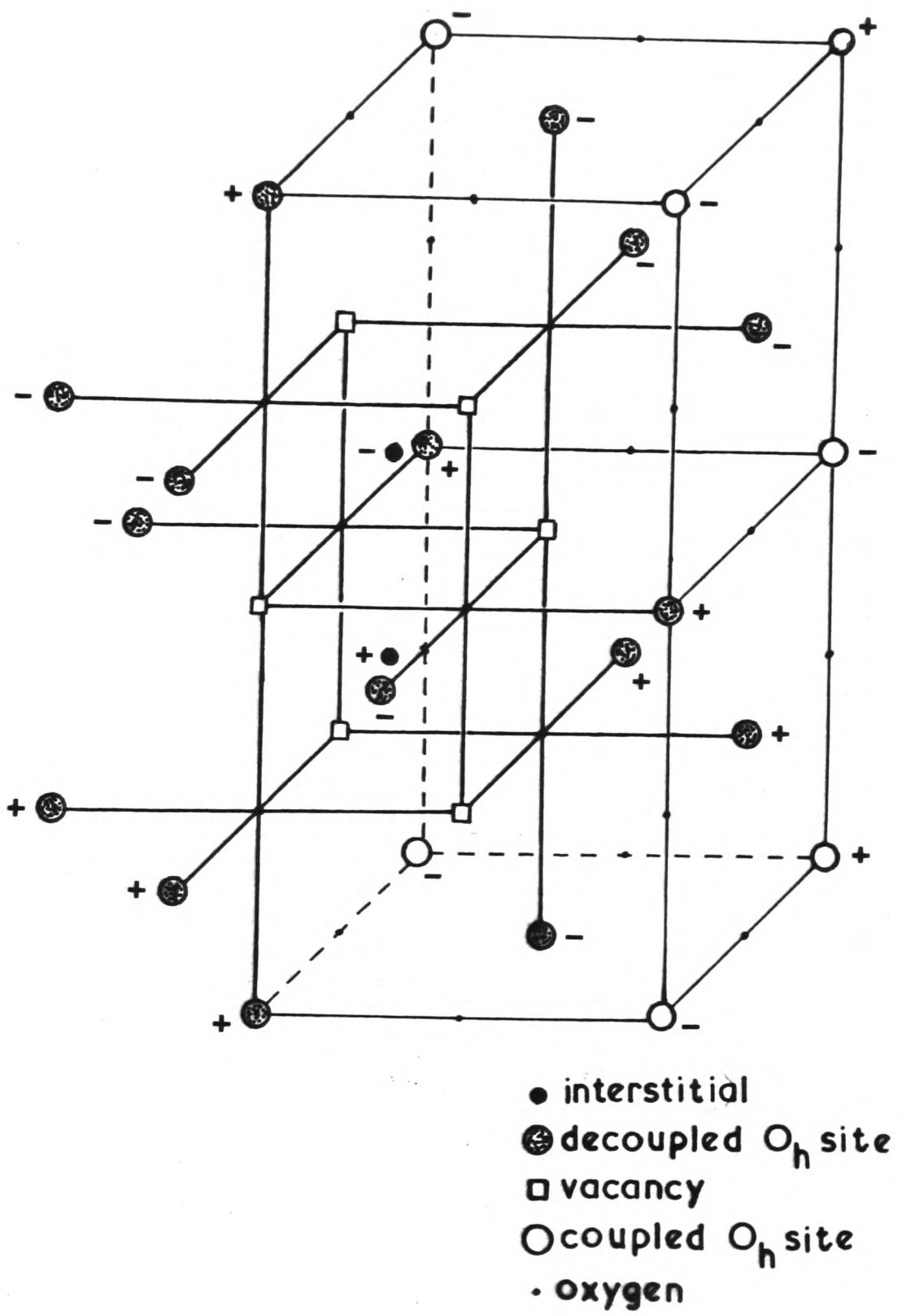



Figure 6.18 An antiferromagnetic 6:2 defect cluster and its relation to the f.c.c. type II magnetic structure. Opposite moment directions are signified by the signs +, -.

These values, together with previous data for $(Mn_xFe_{1-x})_zO$ [54] and $(Co_xFe_{1-x})_zO$ [185], rule out an OAF phase for both systems.

(b) Only small amounts of $Co^{2+}$ and $Mn^{2+}$ are necessary to divert the $Fe^{2+}$ moment from the [111] axis and remove the corresponding trigonal ($\alpha < 90^o$) magnetostriction. The cobaltous ion has a slightly greater effect than $Mn^{2+}$, and these results, together with those for $Mn_xCo_{1-x}O$ (Chapter 5) and $Ni_xCo_{1-x}O$[2], suggest that the anisotropy order for the iron-group monoxides is CoO>MnO>>$Fe_zO$≈NiO.

(c) The weakness of the ferrous anisotropy can be related to a number of factors: (i) quenching of the orbital angular momentum in the vicinity of the defect cluster, (ii) the unfavourable orientation of the bulk moments with respect to the magnetic dipole-dipole forces, (iii) the opposition of the $Fe^{2+}$--$Fe^{2+}$ exchangestriction when small trigonal magnetostrictions occur, and (iv) the presence of alternative (Jahn-Teller and spin-orbit coupling) modes by which the orbital degeneracy can be relieved.

(d) Magnetic moment directions close to those of CoO and MnO are observed for small concentrations of $Co^{2+}$ and $Mn^{2+}$ in $Fe_zO$. Since the magnetic vector is within, or very close to, the (111) plane in MnO-$Fe_zO$, the ferrous orbital moment is likely to be quenched here. This is not the case in CoO-$Fe_zO$ (see (e)).

(e) The tetragonal contraction due to $Co^{2+}$ in CoO-$Fe_zO$ is diminished relative to the analogous distortion of CoO-NiO [243]. The introduction of an opposite tetragonal magnetostrictive distortion due to $Fe^{2+}$ along the same axis may explain this effect, and extrapolation to zero cobalt content then reveals a hypothetical tetragonal

distortion for "FeO" of c/a = 1.013.

(f) The minor, or undetectable, trigonal distortions of all compositions in the CoO-$Fe_zO$ system are compatible with small exchangestrictions due to ferromagnetic and antiferromagnetic n.n. interactions between like and unlike ions. The large trigonal ($\alpha > 90^o$) exchangestriction due to $Mn^{2+}$--$Mn^{2+}$ antiferromagnetic couplings is negated in MnO-$Fe_zO$ by an opposite ($\alpha < 90^o$) deformation, the origin of which is unclear. The problem of the combined nuclear and magnetic symmetries of $Mn_{0.56}Fe_{0.44}O$ also remains unsolved.

(g) With a few exceptions, the measured magnetic moments of non-stoichiometric samples of $(Mn_xFe_{1-x})_zO$ and $(Co_xFe_{1-x})_zO$ are larger than those predicted by a model [3] for the magnetic structure of ferrous oxide. This can be qualitatively attributed to the introduction of a coherent component into the magnetic scattering from defective regions, owing to an overall sublattice magnetisation perpendicular to [111]. However, the previous model of $Fe_zO$[3] must be modified to take into account the possibility of an antiferromagnetic arrangement of spins around the cluster.

# CHAPTER SEVEN

# CONCLUSIONS AND FUTURE DEVELOPMENTS

## 7.1 SUMMARY OF RESULTS AND THEIR INTERPRETATION

A range of compositions belonging to the antiferromagnetic solid solutions MnO-NiO, MnO-CoO, MnO-$Fe_zO$ and CoO-$Fe_zO$ have been prepared by conventional high temperature and co-precipitation methods. The homogeneity and single-phase nature of these oxides, all of which have the rocksalt structure, were checked by X-ray diffraction and analytical electron microscopy, and the metal:metal ratios were obtained by atomic absorption spectrometry. By analogy with ferrous oxide itself, the mixed crystals incorporating iron tend to be non-stoichiometric, and the excess oxygen content was estimated by means of volumetric analyses for iron (11) and total iron.

Each preparation was subjected to a high resolution powder neutron diffraction investigation at 5K, from which both magnetic and nuclear structural parameters were obtained by means of the Rietveld profile analysis technique. In addition, certain members of the $Mn_xNi_{1-x}O$, $Mn_xNi_{1-x}O$ and $(Mn_xFe_{1-x})_zO$ systems were briefly examined by neutron diffraction over a range of higher temperatures, and the polycrystalline magnetic susceptibilities of five samples of $(Mn_xFe_{1-x})_zO$ were measured between 50 and 300K. Finally, the paramagnetic Mössbauer spectra of various samples of $(Mn_xFe_{1-x})_zO$ ($0 < x < 0.975$) were obtained by measurements at room temperature.

### 7.1.1 Magnetic and Related Properties

The magnetic behaviour of the solid solutions as a function of

composition has been found to be chiefly influenced by the interionic exchange energies between nearest and next-nearest neighbours, and the presence, or lack of, an orbital magnetic moment when an ion is situated in an octahedral site. The importance of the $180^{o}$ cation-oxygen-cation superexchange in determining the Néel temperature-composition phase diagrams has been demonstrated by collating data available in the literature and from further magnetic susceptibility and variable temperature neutron measurements carried out in this work. Each system clearly demonstrates the lack of the "oblique antiferromagnetic" phase observed in other mixed systems composed of anisotropic antiferromagnets, and the moments of unlike ions appear to be effectively collinear at all compositions. The magnetic susceptibility experiments are also very sensitive to small quantities of ferrimagnetic $Fe_3O_4$ and $Mn_3O_4$ impurities present in $(Mn_xFe_{1-x})_zO$.

The nearest neighbour exchange is important in determining the exchangestrictions revealed by lattice parameter measurements, although these may be masked by magnetostrictions of the same symmetry. It is also sometimes difficult to identify which n.n. interaction is the most important in causing the observed striction, as in NiO, $(Mn_xFe_{1-x})_zO$ and $Mn_xCo_{1-x}O$. However, the large exchangestriction of MnO is unambiguous, as is its removal in $Mn_xNi_{1-x}O$ by an opposed deformation due to ferromagnetic n.n. $Ni^{2+}$--$Mn^{2+}$ exchange; this is favoured because it maximises the intraionic exchange of the $Ni^{2+}$ ion. The MnO-NiO system involves ions without first order orbital contributions, and the size of the magnetic moment changes linearly with composition (again indicative of collinear spins), with the spins confined to the (111) plane of the face centred cube by repulsion between magnetic dipoles.

Reduced magnitudes of the magnetic moments per occupied octahedral site are observed for all non-stoichiometric ferrous oxide solid solutions. In most cases, these values do not coincide with the predictions of a previous model based upon similar behaviour in ferrous oxide, wherein ferrimagnetically ordered defect clusters are postulated[3]. A modified model involving partial antiferromagnetic order in the vicinity of the clusters is necessary in order to account for the solid solution observations.

Cobaltous and ferrous ions occupying octahedral sites have orbital triplet ground states in the absence of a deformation to lower symmetry, but it is possible for the degeneracy to be relieved by trigonal or tetragonal distortions that either maintain or quench the orbital contribution; the deformations are opposite in sign for Jahn-Teller and spin-orbit stabilisations and for $Co^{2+}$ and $Fe^{2+}$ ions, as discussed in chapter 2.2.1(c). The different possibilities appear to be very close in energy, and the behaviour of an ion must depend upon the elastic coupling between interstices and the exchange coupling between spins. Either stabilisation may occur at the expense of the other in a particular system, and the magnetic moments and lattice distortions are affected accordingly. The oxides CoO and $Fe_zO$, together with the mixed systems MnO-CoO, MnO-$Fe_zO$, CoO-$Fe_zO$ and CoO-NiO[2] reveal how the orbitally degenerate ions behave in slightly different environments within distorted rocksalt lattices. The results for the end members and solid solutions gleaned from this and previous work are summarised in Table 7.1.

The behaviour of $Co^{2+}$ is dependent upon the relative energies of the A and E states produced by a Jahn-Teller distortion. The critical parameter appears to be the degree of further stabilisation acquired

| $Co^{2+}$ in | | | |
|---|---|---|---|
| CoO | CoO-NiO | CoO-$Fe_zO$ | CoO-MnO |
| S.O. (c/a < 1) | S.O. (c/a < 1) | S.O. (c/a < 1) | 5-36% Mn, S.O. (c/a < 1)<br>J.T. (c/a > 1)<br>51-67% Mn, J.T. (c/a > 1)<br>51% Mn, J.T. ($\alpha < 90^o$)?<br>83% Mn, S.O. (c/a < 1) |

| $Fe^{2+}$ in | | | |
|---|---|---|---|
| $Fe_zO$ | MnO-$Fe_zO$ | CoO-$Fe_zO$ | NiO-$Fe_zO$ |
| S.O. ($\alpha < 90^o$) | 5% Mn, S.O. ($\alpha < 90^o$)<br>>23% Mn, J.T. ($\alpha > 90^o$)? | > 50% Co, S.O. (c/a > 1) ? | - |

TABLE 7.1 Summary of the magnetostrictions (S.O.) and Jahn-Teller (J.T.) distortions due to $Fe^{2+}$ and $Co^{2+}$ in ferrous oxide, cobaltous oxide and oxide solid solutions.

in the E state via the spin-orbit coupling and the Zeeman splitting of the resultant J levels in a magnetic field. Cobaltous ions in this state produce a large single ion anisotropy which, in CoO, is associated with a distortion to tetragonal symmetry. In $Mn_xCo_{1-x}O$, symmetries ranging from tetragonal and trigonal to triclinic are observed. The degeneracies of different $Co^{2+}$ ions are relieved by both spin-orbit (S.O) coupling and the Jahn-Teller (JT) effect for $0.05<x<0.36$, but only the JT stabilisation is observed for $0.51<x<0.67$; solely S.O. behaviour is apparent for $x>0.83$. These findings are consistent with measurements of the magnitudes and directions of the magnetic moments of each composition, and the AFMR data of other workers[231]. It is noteworthy that (i) only 5% manganese is sufficient to induce Jahn-Teller behaviour in a significant proportion of $Co^{2+}$ ions; (ii) small magnetostrictions linked to the magnetic ordering may give rise to elastic coupling between $Co^{2+}$ sites in $Mn_{0.67}Co_{0.33}O$, which aids a co-operative Jahn-Teller distortion of these sites. This occurs at a smaller cobaltous concentration than would be expected from a consideration of other co-operative behaviour in f.c.c. lattices; and (iii) the tetragonal Jahn-Teller distortion of $Co^{2+}$ is prevalent despite the trigonal exchangestriction. The trigonal ($\alpha < 90^{o}$) Jahn-Teller deformation may be present but will be masked; it only appears to be large in $Mn_{0.51}Co_{0.49}O$, where the overall trigonal ($\alpha > 90^{o}$) distortion is less than interpolation would predict.

The MnO-CoO system clearly shows the effect of $Mn^{2+}$ ions upon the relative proportion of $Co^{2+}$ ions having an orbital contribution. This must depend upon the range of site symmetries present and the opportunity for co-operative elastic coupling between cobaltous ions having A ground states. The factors that control the lowering of symmetry are (i) the

presence of $Mn^{2+}$ in the n.n. cation positions around $Co^{2+}$, and (ii) the sensitivities of the n.n. exchange interactions (predominantly cation- -cation) between like and unlike ions to changes in ionic separation. This effect gives rise to the appreciable exchangestriction of MnO. We believe that the first of these factors has a minor influence because the introduction of NiO into CoO does not produce quenched $Co^{2+}$ moments[2]. The dominant factor would appear to be the presence of cation- -cation exchanges ($Co^{2+}$-$Co^{2+}$, $Co^{2+}$-$Mn^{2+}$, $Mn^{2+}$-$Mn^{2+}$) of different magnitudes. The first two appear to be small, while the latter is large, and so the particular environment of a $Co^{2+}$ ion is likely to be somewhat distorted if an unequal and asymmetric $Co^{2+}/Mn^{2+}$ n.n. distribution occurs. Accordingly, these distortions should affect the dispositions of the oxide ligands, and produce crystal field splittings of the degenerate orbitals with $m_\ell = \pm 1$.

It is noteworthy that the model for $Co^{2+}$ in CoO involving non-collinear $\underline{S}$ and $\underline{L}$ (Figure 5.4) also favours the A ground state because the multiplet splitting will be smaller due to the reduced spin-orbit coupling. This model is supported by the n.m.r. data of other workers and is attractive for a number of reasons: (i) the very large tetragonal magnetostriction strongly suggests that the orbital moment is pinned to the [001] axis in the crystal; (ii) the spin orbit coupling parameter is much smaller in the crystal owing to the effects of covalency; and (iii) factors such as the dipole-dipole forces and anisotropic n.n. exchange[149] are present in the crystal which may compensate for the loss of spin orbit coupling energy.

The solid solutions involving iron, MnO-$Fe_zO$ and CoO-$Fe_zO$, demonstrate that the trigonal magnetostriction associated with $Fe^{2+}$ rapidly disappears upon progressive doping of ferrous oxide with $Mn^{2+}$

or $Co^{2+}$. These observations correlate with the apparently weak trigonal anisotropy of $Fe^{2+}$, which appears to stem from a number of effects, e.g. an unfavourable orientation with respect to the dipole-dipole forces and the ease with which the electronic structure of the ion can be changed in these three dimensional systems via perturbations emanating from the cation- -cation exchange. The apparent anisotropy order for the four oxides then appears to be CoO > MnO >> $Fe_zO$ ≈ NiO. However, this is somewhat misleading, as the dipolar anisotropy of $Mn^{2+}$ must be much weaker than the single ion anisotropy of $Fe^{2+}$ in the absence of other interactions, as demonstrated by studies of the layered halides $Co_xFe_{1-x}C\ell_2$ [171] and $K_2Mn_xFe_{1-x}F_4$ [172].

In CoO-$Fe_zO$, the symmetry remains pseudotetragonal as $Fe^{2+}$ is added to CoO, but the reduction in the magnitude of the tetragonal distortion is more rapid than in CoO-NiO[2]. This was ascribed to a competition between the c/a < 1 distortion of CoO and a magnetostrictive tetragonal distortion (c/a > 1) stemming from $Fe^{2+}$. However, Figure 6.15 shows that the tetragonal distortion disappears when both $Co^{2+}$ and $Fe^{2+}$ are present in equal proportions, as though each $Fe^{2+}$ ion removes the distortions of two $Co^{2+}$ ions. In CoO-NiO[2], the tetragonal distortion becomes zero at 100% Ni; here the decrease in distortion is simply caused by ionic substitution. An alternative explanation for these observations could be the occurrence of $Co^{2+}$-$Fe^{2+}$ pairs with very strong cation- -cation exchange involving the β-spin electrons. This would lead to pseudo-itinerant electronic properties within the Co-Fe "bond", and the Jahn-Teller and magnetostrictive stabilisation possibilities for the $Co^{2+}$ ion involved would be removed.

The above consideration again emphasises the importance of the cation- -cation exchange in these oxides. Other important examples

revealed in this thesis are (i) the lattice parameter data for MnO-NiO, which is interpreted in terms of the ease of transfer of the $Ni^{2+}$ β-spin electrons, and (ii) the Mössbauer effect data for MnO-$Fe_zO$. While the chemical shift of Fe(11) increases with increasing manganese content, that of Fe(111) decreases. These observations, together with the reduced proportion of Fe(111) detected in iron-rich samples, are attributed to a smaller degree of electron delocalisation when less electronegative $Mn^{2+}$ ions occupy the near neighbour sites of the Fe(11) or Fe(111) ions. Since Fe(111) ions are localised around defect clusters, it can be deduced from the appreciable change in the Fe(111) chemical shift that considerable itinerant electron character is present in the neighbourhood of the defect clusters of ferrous oxide itself.

### 7.1.2 Structures of the Solid Solutions

In conjunction with studies of the magnetic properties by neutron diffraction, some aspects of the chemical structures of the solid solutions have been investigated. These are the observations that (i) no long range ordering of different ions occurs in any system; (ii) the effect of non-stoichiometry is manifest by the presence of interstitial ferric ions and octahedral vacancies, as in ferrous oxide. Vacancy-interstitial occupancy number ratios suggest that 6:2 or 8:3 clusters occur in MnO-$Fe_zO$, but larger clusters are indicated in CoO-$Fe_zO$ and are compatible with the smaller stability of this system towards disproportionation; and (iii) the strains in the antiferromagnetic solid solutions are the product of a number of contributions, and the distortions on the atomic level must change depending upon the occupation by unlike cations of the co-ordination sphere of an ion. Despite this, the average state probed by the diffraction method is extremely well defined, and comparable to that of undoped systems.

In addition to the considerations set out in section 7.1.1, the Mössbauer spectra of $(Mn_xFe_{1-x})_zO$ at room temperature contain other features diagnostic of the environments of the $Fe^{2+}$ ions in the paramagnetic phases of the solid solutions. The iron(11) quadrupole splittings are indicative of the effect on the electric field gradient at a $Fe^{2+}$ site of vacancies, Fe(111) ions, and the disorder of $Mn^{2+}$ and $Fe^{2+}$ over the octahedral cation sites of the lattice. Consequently, a larger range of interactions is found in most of the solid solutions than in ferrous oxide (despite smaller deviations from stoichiometry), and only when 2.5% $Fe^{2+}$ is present does the average Fe(11) site symmetry approach cubic.

## 7.2 SUGGESTIONS FOR FUTURE WORK

With the exception of a magnetic susceptibility and room temperature Mössbauer effect study of $MnO-Fe_zO$, the main technique employed in this work has been conventional powder neutron diffraction. Although the large number of experiments carried out provide some insight into the four solid solution systems, scope still exists for additional study of other compositions using the same method. For instance, further insight may follow the analysis of lattice parameter data for ferrous oxide very lightly doped with $Co^{2+}$, and for the unexplored region between 12 and 50% $Co^{2+}$ in $Fe_zO$. This may be more easily achieved by low temperature X-ray diffraction, where much smaller quantities of material are necessary. It may also be of interest to study the limited range of the $NiO-Fe_zO$ system.

Investigation of the other solid solutions by techniques complimentary to powder neutron diffraction at fixed wavelength would also be rewarding. More precise values for the moment directions of $Mn_xCo_{1-x}O$,

in particular, would be of value, and might be deduced from single crystal neutron experiments or pulsed spallation source data measured by time of flight methods. Here, the resolution is excellent, especially at low Q vectors where the peaks have larger separations in time. Such apparatus should facilitate the detection of very small distortions resulting from exchange- or magnetostrictions and may enable, for instance, the magnetostriction of NiO to be observed using powder data.

It will be of interest to learn the results of a Mössbauer investigation of CoO-$Fe_zO$ currently in progress[244]. The magnetically ordered spectra of this, and the MnO-$Fe_zO$ system[240], are very complex owing to the wide variety of iron sites and the large quadrupole interactions, and it may be difficult to achieve adequate fits to the spectra. Information on the anisotropy constants of these solid solutions may also be derived from AFMR experiments, although this is limited by line-broadening at intermediate compositions.

Although the present investigation has demonstrated the complexity of the three dimensional, antiferromagnetic iron group monoxides, theoretical studies of CoO, $Fe_zO$ and their solid solutions (on the lines of those of Kanamori[146]) appear to be necessary in the light of the progress in experimental work since 1957. It would be interesting to evaluate theoretically the model for CoO involving decoupled $\underline{S}$ and $\underline{L}$, and to gain some insight into the interactions between the co-operative strictions present in the solid solutions, recalling the wide variety of behaviour in $Mn_xCo_{1-x}O$. The calculations would be aided by examination of the magnetic ordering of MnO, $Fe_zO$, CoO and NiO doped with diamagnetic ions such as magnesium, since further understanding of the percolation behaviour of these systems might thereby be obtained.

REFERENCES


1. N.G. Parsonage and L.A.K. Staveley, "Disorder in Solids", Oxford University Press (1978).

2. P.D. Battle, A.K. Cheetham and G.A. Gehring, J. Appl. Phys., 50, 7578 (1979).

3. P.D. Battle and A.K. Cheetham, J. Phys. C, 12, 337 (1979).

4. N.N. Greenwood, "Ionic Crystals, Lattice Defects and Non-stoichiometry", Butterworth (1968).

5. H.N. Ok and J.G. Mullen, Phys. Rev., 168, 550 (1968).

6. M.W. Davies and F.D. Richardson, Trans. Faraday Soc., 55, 604 (1959).

7. B. Fisher and D.S. Tannhauser, J. Electrochem. Soc., 111, 1194 (1964).

8. S.P. Mitoff, J. Chem. Phys., 35, 882 (1961).

9. L.S. Darken and R.W. Gurry, J. Am. Chem. Soc., 67, 1398 (1945).

10. B.E.F. Fender and F.D. Riley, J. Phys. Chem. Solids, 30, 793 (1969).

11. N.N. Greenwood and A.T. Howe, J. Chem. Soc. (Dalton), 1, 116 (1972).

12. V.P. Romanov, L.F. Checherskaya and P.A. Tatsienko, Phys. Stat. Sol., A15, 721 (1973).

13. T. Katsura, B. Iwasaki, S. Kimura and S. Akimoto, J. Chem. Phys., 47, 4559 (1967).

14. B. Simons and F. Seifert, Report of the Geophysical Laboratory, Carnegie Institute of Washington, 625 (1978).

15. C. Carel and J.R. Gavarri, Mat. Res. Bull., 11, 745 (1976).

16. J.R. Gavarri, D. Weigel and C. Carel, Mat. Res. Bull., 11, 917 (1976).

17. P. Vallet and C. Carel, Mat. Res. Bull., 14, 1181 (1979).

18. P. Vallet and P. Raccah, C. Rendu. Acad. Sc., 258, 3679 (1964).

19. M. Hayakawa, J.B. Cohen and T.B. Reed, J. Am. Ceram. Soc., 55, 160 (1972).

20. M. Hayakawa, J.B. Wagner and J.B. Cohen, Mat. Res. Bull., 12, 429 (1977).

21. I. Bransky and D.S. Tannhauser, Physica, 37, 547 (1967).

22. D.S. Tannhauser, J. Phys. Chem. Solids, 23, 25 (1962).

23. D.J. Elias and J.W. Linnett, Trans. Faraday Soc., 65, 2673 (1969).

24. N.N. Greenwood and A.T. Howe, J. Chem. Soc. (Dalton), 1, 110 (1972).

25. C.R.A. Catlow, W.C. Mackrodt, M.J. Norgett and A.M. Stoneham, Phil. Mag., A35, 177 (1977).

26. G.M. Joshi, M. Pai, H.R. Harrison, C.J. Sandberg, R. Aragon and J.M. Honig, Mat. Res. Bull., 15, 1575 (1980).

27. A.J. Bosman and H.J. van Daal, Adv. Phys., 19, 1 (1970).

28. F. Koch and J.B. Cohen, Acta Cryst., B25, 275 (1969).

29. B. Hennion, Personal Communication.

30. C.R.A. Catlow, B.E.F. Fender and D.G. Muxworthy, J. Phys., Supp. 12, 67 (1977).

31. C.R.A Catlow, W.C. Mackrodt, M.J. Norgett and A.M. Stoneham, Phil. Mag., A40, 161 (1979).

32. E.R. Jette and F. Foote, J. Chem. Phys., 1, 29 (1933).

33. C. Carel, D. Weigel and P. Vallet, C.Rendu. Acad. Sc., 260, (1965).

34. W.L. Roth, Acta Cryst., 13, 140 (1960).

35. S. Iijima, Proc. Conf. on Diffraction Studies of Real Atoms and Real Crystals, Melbourne, 217 (1974).

36. B. Anderson and J.O. Sletnes, Acta Cryst., A33, 268 (1977).

37. C.R.A. Catlow and B.E.F. Fender, J. Phys. C, 8, 3267 (1975).

38. A.K. Cheetham, B.E.F. Fender and R.I. Taylor, J. Phys. C, 4, 2160 (1971).

39. J.R. Gavarri, C. Carel and D. Weigel, J. Solid State Chem., 29, 81 (1979).

40. P. Vallet, J. Solid State Chem., 29, (1979).

41. G. Shirane, D.E. Cox and S.L. Ruby, Phys. Rev., 125, 1158 (1962).

42. D.P. Johnson, Solid State Commun., 7, 1785 (1969).

43. L.F. Checherskaya, V.P. Romanov and P.A. Tatsienko, Phys. Stat. Sol., A19, K177 (1973).

44. Yu. D. Tret'yakov and R.A. Rapp, Trans. A.I.M.E., 245, 1235 (1969).

45. B. Leroy, Y. Beronger and P. Lacombe, J. Phys. Chem. Solids, 33, 1515 (1972).

46. A.Z. Hed and D.S. Tannhauser, J. Electrochem, Soc., 114, 314 (1967).

47. A.Z. Hed, J. Chem. Phys., 50, 2935 (1969).

48. W.K. Chen and N.L. Peterson, J. Phys. Chem. Solids., 41, 647 (1980).

49. M.C. Trinel-Dufour, Thèse, Lille (1977).

50. C. Gleitzer, Mat. Res. Bull., 15, 507, 955 (1980).

51. E.M. Levin, C.R. Robbins and H.F. McMurdie, "Phase Diagrams for Ceramicists", American Ceramic Society (1964, and supplements 1969 and 1975).

52. J. Aubry, A. Berthet, R. Duchene, H. Etienne, O. Evrard, J. Jeannot, C. Gleitzer, C. Offroy and P. Perrot, Ann. Chim., t.5, 299 (1970).

53. Yu. D. Tret'yakov, Yu. G. Saksonov and I.V. Gordeev, Inorg. Mater., 1, 382 (1965).

54. O. Evrard, Rev. Chim. Miner., 8, 63 (1971).

55. P.K. Foster and A.J.E. Welch, Trans. Faraday Soc., 52, 1626 (1956).

56. K. Schwerdtfeger and A. Muan, Trans. A.I.M.E., 239, 1114 (1967).

57. C.A. Goodwin, H.K Bowen and W.D. Kingery, J. Am. Ceram. Soc., 58, 317 (1975).

58. E. Aukrust and A. Muan, Trans. A.I.M.E., 227, 1378 (1963).

59. P.J. Hampson, D. Phil. Thesis, Oxford (1968).

60. C.R.A. Catlow, B.E.F. Fender and P.J Hampson, J. Chem. Soc., (Faraday), 73, 911 (1977).

61. G.E. Bacon, R. Street and R.H. Tredgold, Proc. Roy. Soc., A217, 252 (1953).

62. W.C. Hahn and A. Muan, J. Phys. Chem. Solids, 19, 338 (1961).

63. C.A. Barrett and E.B. Evans, J. Am. Ceram. Soc., 47, 533 (1964).

64. J. Bénard, Ann. Chim., 12, 5 (1939).

65. B. Touzelin, J. Less Common Met., 77, 11 (1981).

66. E. Aukrust and A. Muan, Trans. A.I.M.E., 230, 1395 (1964).

67. R. Yu. Dobrovinskii, V.F. Balakirev, A.N. Men' and G.I. Chufarov, Russ. J. Phys. Chem., 42, 523 (1968).

68. V.A. Gutin, V.S. Zhaglov, D.I. Lisovskii and G.S. Viktorovich, Russ. J. Phys. Chem., 46, 883 (1972).

69. H.P. Rooksby, Trans. Brit. Ceram. Soc., 56, 581 (1957).

70. J. Robin, Ann. Chim., 10, 395 (1955).

71. M. Kinoshita, W.D. Kingery and H.K. Bowen, J. Am. Ceram. Soc., 56, 398 (1973).

72. J.J. Stiglich, D.H. Whitmore and J.B. Cohen, J. Am. Ceram. Soc., 56, 211 (1973).

73. J.H. Van Vleck, "The Theory of Electric and Magnetic Susceptibilities", Oxford University Press (1932).

74. W.E. Henry, Phys. Rev., 88, 559 (1952).

75. P. Weiss, J. Phys. Radium, 4, 661 (1907).

76. J.S. Smart, "Effective Field Theories of Magnetism", Saunders (1966).

77. C.G. Shull and J.S. Smart, Phys. Rev., 76, 1256 (1949).

78. G. Shirane, Acta Cryst., 12, 282 (1959).

79. D. Herrmann-Ronzaud, P. Burlet and J. Rossat-Mignod, J. Phys. C, 11, 2123 (1978); D. Herrmann-Ronzaud, Thèse, Grenoble (1978).

80. Y.Y. Li, Phys. Rev., 100, 627 (1955).

81. B. Van Laar, Phys. Rev., 138, A854 (1965).

82. S. Saito, K. Nakahigashi and Y. Shimomura, J. Phys. Soc., Japan, 21, 850 (1966).

83. B.K. Tanner, Cont. Phys., 20, 187 (1979).

84. P.V. du Plessis, S.J. van Tonder and L. Alberts, J. Phys. C, 4, 1983 (1971).

85. D. Bloch and C. Vettier, J. Magn. Magn. Mater., 15-18, 589 (1980).

86. M.E. Lines, Phys. Rev., 139, A1304 (1965).

87. N.F. Mott, Proc. Phys. Soc., A62, 416 (1949).

88. P.W. Anderson, Phys. Rev., 115, 2 (1959).

89. J.B. Goodenough, Phys. Rev. 100, 564 (1955); J. Phys. Chem. Solids, 6, 287 (1958); Phys. Rev., 117, 1442 (1960).

90. J. Kanamori, J. Phys. Chem. Solids, 10, 87 (1959).

91. J.B. Goodenough, "Magnetism and the Chemical Bond", Wiley Interscience (1963).

92. J. Sakurai, W.J.L. Buyers, R.A. Cowley and G. Dolling, Phys. Rev., 167, 510 (1968).

93. M. Bonfante, B. Hennion, F. Moussa and G. Pepy, Solid State Commun., 10, 553 (1972).

94. H. Chou and H.Y. Fan, Phys. Rev., 13, 3924 (1976).

95. K. Motizuki and T. Niwa, Physica, 89B, 116 (1977).

96. H.P. Rooksby, Acta. Cryst., 1, 226 (1948).

97. J.S. Smart and S. Greenwald, Phys. Rev., 82, 113 (1951).

98. B. Morosin, Phys. Rev., B1, 236 (1970).

99. L.C. Bartel and B. Morosin, Phys. Rev., B3, 1039 (1971).

100. F.E. Mabbs and D.J. Machin, "Magnetism and Transition Metal Complexes", Chapman and Hall (1973).

101. J.S. Griffith, "The Theory of Transition Metal Ions", Cambridge University Press (1961).

102. J. Kanamori, J. Appl. Phys., 31, 14S (1960).

103. H.A. Jahn and E. Teller, Proc. Roy. Soc., A161, 220 (1937).

104. J.B. Goodenough, Phys. Rev., 171, 466 (1968).

105. L.F. Mattheis, Phys. Rev., B5, 290 (1972); Phys. Rev., B5, 306 (1972).

106. H.L Skriver, O.K. Anderson and B. Johansson, J. Magn. Magn. Mater., 15-18, 861 (1980).

107. B.H. Brandow, Adv. Phys., 26, 651 (1977).

108. J. Kanamori, in "Magnetism" Vol 1 (Eds. G.T. Rado and H. Suhl), Academic Press (1963).

109. R. Boire and M.F. Collins, Can. J. Phys., 55, 688 (1977).

110. M. Foex, C. Rendu. Acad. Sc., 227, 193 (1948).

111. C.H. La Blachetais, J. Phys. Radium, 12, 765 (1951).

112. V.A. Gubanov and D.E. Ellis,Phys. Rev. Lett., 44, 1633 (1980).

113. R. Mainard, M. Boubel and H. Fousse, C. Rendu, Acad. Sc., 266, 1299 (1968).

114. F. Koch and M.E. Fine, J. Appl. Phys., 38 1470 (1966).

115. H. Bizette, J. Phys. Radium, 12, 161 (1951).

116. J. Kleinclauss, R. Mainard, H. Fousse, N. Ciret, D. Bour and A.J. Pointon, J. Phys. C, 14, 1163 (1981).

117. J.R. Singer, Phys. Rev., 104, 929 (156).

118. C. Carel and J.Y. Boudonnet, Mem. Sci. Rev. Met., 70, 179 (1973).

119. M.E. Lines and E.D. Jones, Phys. Rev., 139, A1313 (1965).

120. M.T. Hutchings and E.J. Samuelsen, Phys. Rev., B6, 3447 (1972).

121. G.E. Kugel, B Hennion and C. Carabatos, Phys. Rev., B18, 1317 (1978).

122. R. Bidaux, R. Conte and J.A. Nasser, J. Appl. Phys., 50, 1683 (1979).

123. R. Bidaux, R. Conte and J.A. Nasser, J. Phys., 41, 1317 (1980).

124. T. Yamada, S. Saito and Y. Shimomura, J. Phys. Soc., Japan, 21, 672 (1966).

125. K. Nakahigashi, N. Fukuoka and Y. Shimomura, J. Phys. Soc., Japan, 38, 1634 (1975).

126. J. Baruchel, M. Schlenker, K. Jurosawa and S. Saito, Phil. Mag., B43, 853 (1981); Phil. Mag. B43, 861 (1981).

127. C.G. Shull, W.A. Strauser, E.O. Wollan, Phys. Rev., 83, 333 (1951).

128. G.A. Slack J. Appl. Phys., 31, 1571 (1960).

129. J.I. Kaplan, J. Chem. Phys., 22, 1709 (1954).

130. F. Keffer and W.O'Sullivan, Phys. Rev., 108, 637 (1957).

131. A.J. Sievers and M. Tinkham, Phys. Rev., 129, 1566 (1963).

132. T. Yamada, J. Phys. Soc. Japan, 21, 664 (1966).

133. M.S. Jagadeesh and M.S. Seehra, Phys. Rev., B23, 1185 (1981).

134. S. Saito, M. Miuro and K. Kurosawa, J. Phys. C, 13, 1515 (1980); J. Phys. C, 13, 1521 (1980).

135. D.S. Rodbell and J. Owen, J. Appl. Phys., 35, 1002 (1964).

136. L. Alberts and W. Lee, Proc. Phys. Soc. (London), 78, 728 (1961).

137. J.B. Goodenough, in Progress in Solid State Chemistry, 5, 145 (1971).

138. K. Motida, J. Phys. Soc. Japan, 44, 1498 (1978).

139. W.L. Roth, Phys. Rev., 110, 1333 (1958).

140. I.A. Blech and B.L. Averbach, Phys. Rev., 142, 287 (1966).

141. W. Low, Solid State Physics, Suppl. 2, Academic Press (1960).

142. D. Bloch, J.L. Feron, R. Georges and I.S. Jacobs, J. Appl. Phys., 38, 1474 (1967).

143. K. Motida, and S. Miyahara, J. Phys. Soc. Japan, 28, 1188 (1970); J. Phys. Soc. Japan, 29, 516 (1970).

144. D.C. Khan and R.A. Erickson, Phys. Rev., B1, 2243 (1970).

145. M.D. Rechtin and B.L. Averbach, Phys. Rev., B6, 4294 (1972).

146. J. Kanamori, Prog. Theor. Phys. (Kyoto), 17, 197 (1957).

147. T. Nagamiya and K. Motizuki, Rev. Mod. Phys., 30, 89 (1958).

148. E.F. Bertaut, J. Phys. Chem. Solids, 30, 763 (1969).

149. T. Yamada and O. Nakanishi, J. Phys. Soc. Japan, 36, 1304, 1315 (1974).

150. K. Okada and H. Yasuoka, J. Phys. Soc. Japan, 43, 34 (1977).

151. M.S. Seehra and P. Silinsky, Solid State Commun., 31, 183 (1979).

152. C. Zener, Phys. Rev., 82, 403 (1951).

153. B.T.M. Willis and H.P. Rooksby, Acta. Cryst., 6, 827 (1953).

154. H. Maletta and W. Felsch, Phys. Rev., 20, 1245 (1979).

155. S. Nagata, R.R. Galazka, D.P. Mullin, H. Akbarzadeh, C.D. Khattak, J.K. Furdyna and P.H. Keesom, Phys. Rev., B22, 3331 (1980).

156. J. Dumas and C. Schlenker, J. Phys. C, 12, 2381 (1979).

157. D.E. Cox, W.J. Takei and G. Shirane, J. Phys. Chem. Solids, 24, 405 (1963).

158. T. Birchall and A.F. Reid, J. Solid State Chem., 13, 351 (1975).

159. S. Geller, R.W. Grant, J.A. Cape and G.P. Espinosa, J. Appl. Phys., 38, 1457 (1967).

160. H. Taguchi, M. Shimada, F. Kanamaru, M. Koizumi and Y. Takeda, J. Solid State Chem., 18, 299 (1976).

161. H.A. Obermayer, H. Dachs and H. Schrocke, Solid State Commun., 12, 779 (1973).

162. G. Munninghoff, W. Treutmann, E. Hellner, G. Heger and D. Reinen, J. Solid State Chem., 34, 289 (1980).

163. O. Muller, M.P. O'Horo and J.F. O'Neill, J. Solid State Chem., 23, 115 (1978).

164. F. Gesmundo and P.F. Rossi, J. Solid State Chem., 8, 287 (1973).

165. O. Evrard, F. Jeannot and J.M. Lecuire, Rev. Chim. Miner., 9, 463 (1972).

166. T.M. Sabine and E.R. Vance, J. Solid State Chem., 1, 554 (1970).

167. T.E. Wood and P. Day, J. Magn. Magn. Mater., 15-18, 782 (1980).

168. S. Fishman and A. Aharony, Phys. Rev., B18, 3507 (1978).

169. F. Matsubara and S. Inawashiro, J. Phys. Soc. Japan, 42, 1529 (1977).

170. K. Katsumata, M. Kobayashi, T. Sato and Y. Miyako, Phys. Rev., B19, 2700 (1979).

171. T. Tawaraya and K. Katsumata, Solid State Commun., 32, 337 (1979).

172. L. Bevaart, E. Frikkee, J.V. Levesque and L.J. de Jongh, Phys. Rev., B18, 3376 (1978).

173. I. Yamamoto, J. Phys. Soc. Japan, 49, 74 (1980).

174. K. Katsumata, M. Kobayashi and H. Yoshizawa, Phys. Rev. Lett., 43, 960 (1979).

175. T. Tawaraya, K. Katsumata and H. Yoshizawa, J. Phys. Soc. Japan, 49, 1299 (1980).

176. A. Ito, Y. Someya and K. Katsumata, Solid State Commun., 36, 681 (1980).

177. M. Kobayashi and K. Katsumata, J. Phys. Soc. Japan, 45, 697 (1978).

178. E. Stryjewski and N. Giordano, Adv. Phys., 26, 487 (1977).

179. K. Takeda, M. Matsuura and T. Haseda, J. Phys. Soc. Japan, 29, 885 (1970).

180. F. Matsubara and S. Inawashiro, J. Phys. Soc. Japan, 47, 1102 (1979).

181. H. Forstat and N.P. Lam, Phys. Lett., 72A, 167 (1979).

182. G.K. Wertheim and H.J. Guggenheim, Phys. Rev., 178, 804 (1969).

183. A. Serres, J. Phys. Radium, 21, 551 (1960).

184. M.I. Aivazov and S.V. Gurov, Inorg. Mater., 10, 738 (1974).

185. M. Boubel, R. Mainard, H. Fousse and A.J. Pointon, Phys. Stat. Sol., 35A, 459 (1976).

186. M. Lynch, G. Kokoshka and P. Szydlik, J. Phys. Chem. Solids, 40, 79 (1979).

187. F. Seitz, T.E. Wood and P. Day, Z. Naturforsch., 35A, 1013 (1980).

188. P. Grange, H. Charcosset, P. Gallezot, P. Turlier and J. Vaille, J. Solid State Chem., 11, 26 (1974).

189. B.N. Brockhouse, Phys. Rev., 94, 781 (1954).

190. H. Bizette, R. Mainard and J. Picard, Bull. Soc. Sci. Bretagne, 40, 107 (1965).

191. M.S. Jagadeesh and M.S. Seehra, Phys. Rev., B21, 2897 (1980).

192. A.K. Cheetham and A.J. Skarnulis, Anal. Chem., 53, 1060 (1981).

193. A.I. Vogel, "Textbook of Quantitative Inorganic Analysis", Longman (1978).

194. G.E. Bacon, "Neutron Diffraction", Oxford University Press (1975).

195. G.L. Squires, "Introduction to the Theory of Thermal Neutron Scattering", Cambridge University Press (1978).

196. W. Marshall and S.W. Lovesey, "The Theory of Thermal Neutron Scattering", Oxford University Press (1971).

197. O. Halpern and M.H. Johnson, Phys. Rev., 55, 898 (1939).

198. H.P. Klug and L.E. Alexander, "X-Ray Diffraction Procedures for Polycrystalline and Amorphous Materials", Wiley (1974).

199. C. Wilkinson and E.J. Lisher, Acta Cryst., A29, 453 (1973).

200. H.M. Rietveld, Acta Cryst., 22, 151 (1967); J. Appl. Cryst., 2, 65 (1969).

201. A.K. Cheetham and J.C. Taylor, J. Solid State Chem., 21, 253 (1977).

202. G. Malmros and J.O. Thomas, J. Appl. Cryst., 10, 7 (1977).

203. R.A. Young, P.E. Mackie and R.B. Von Dreele, J. Appl. Cryst., 10, 262 (1977).

204. R.A. Young and P.E. Mackie, Mat. Res. Bull., 15, 17 (1980).

205. R.B. Von Dreele, Unpublished Results.

206. G. Cagliotti, A. Paoletti and F.P. Ricci, Nucl. Instrum. Methods, 3, 223 (1958).

207. "International Tables for X-Ray Crystallography", Volume II, Kynoch Press (1959).

208. A.W. Hewat, AERE Report, RRL 73/239, Harwell (1973).

209. M. Sakata and M.J. Cooper, J. Appl. Cryst., 12, 554 (1979).

210. A.H. Baston and D.H.C. Harris (eds), AERE Report, R9278 (1978).

211. "Neutron Beam Facilities of the HFR", Institut Laue-Langevin, Grenoble, France (1977).

212. A.W. Hewat and I. Bailey, Nucl. Inst. Methods, 137, 463 (1976).

213. B.O. Loopstra, Nucl. Inst. Methods, 44, 181 (1966).

214. A.W. Hewat, "Powder Retrieval and Refinement System", Institut Laue-Langevin Report (1978).

215. P.J. Clarke, Unpublished Results (Oxford Rietveld Refinement User Manual (1976)).

216. A.R. Rae-Smith, A.K. Cheetham and A.J. Skarnulis, J. Appl. Cryst., 12, 485 (1979).

217. R.E. Watson and A.J. Freeman, Acta Cryst., 14, 27 (1961).

218. A.J. Jacobson, B.C. Tofield and B.E.F. Fender, J. Phys. C, 6, 1615 (1973).

219. H. Alperin, Phys. Rev. Lett., 6, 55 (1961).

220. M. Blume, Phys. Rev., 124, 96 (1961).

221. R.E. Watson and A.J. Freeman, Phys. Rev., 120, 1134 (1960).

222. B.E.F. Fender, A.J. Jacobson and F.A. Wedgewood, J. Appl. Phys., 48, 990 (1968).

223. A.J. Jacobson, in "Chemical Applications of Thermal Neutron Scattering", (ed. B.T.M. Willis), Oxford University Press (1973).

224. G.J. Long, G. Longworth, P.D. Battle, A.K. Cheetham, R.V. Thundathil and D. Beveridge, Inorg. Chem., 18, 624 (1979).

225. R.L. Mössbauer, Z. Physik, 151, 124 (1958).

226. N.N. Greenwood and T.C. Gibb, "Mössbauer Spectroscopy", Chapman and Hall (1971).

227. B.N. Figgis and J. Lewis, in "Modern Co-ordination Chemistry", (eds. J. Lewis and R.G. Wilkins), Wiley Interscience (1967).

228. D.S. Rodbell, I.S. Jacobs, J. Owen and E.A. Harris, Phys. Rev. Lett., 11, 10 (1963).

229. W.L. Roth, Phys. Rev., 111, 772 (1958).

230. D.C. Khan and R.A. Erickson, J. Phys. Chem. Solids, 29, 2087 (1968).

231. A.E. Hughes, Phys. Rev., B3, 877 (1971).

232. C.R. Becker, P. Lau, R. Geick and V. Wagner, Phys. Stat. Sol., B67, 653 (1975).

233. R.J. Elliott and B.R. Heap, Proc. Roy. Soc., A265, 264 (1961).

234. R.J. Elliott, J. Phys. Chem. Solids, 16, 165 (1960).

235. C.G. Shull and S. Seigel, Phys. Rev., 75, 1008 (1949).

236. K. Huang, Proc. Roy. Soc., A190, 102 (1947).

237. E.J.W. Verwey, P.W. Haaymann and F.C. Romeijin, J. Chem. Phys., 15, 181 (1947).

238. F.K. Lotgering and A.M. Van Diepen, J. Phys. Chem. Solids, 34, 1369 (1973).

239. M. Rotter, B. Sedlak, Z. Simsa and V.A.M. Brabers, Phys. Stat. Sol., A40, K169 (1977).

240. D.A.O. Hope, A.K. Cheetham and G.J. Long, Unpublished Results.

241. I. Yun, Mem. Coll. Sci. Univ. Kyoto, (Ser. B. Geol. and Mineral), 25, 125 (1958).

242. F. Grandjean and A. Gerard, J. Magn. Magn. Mater., 15-18, 1001 (1980).

243. P.D. Battle, D. Phil. Thesis, University of Oxford (1979).

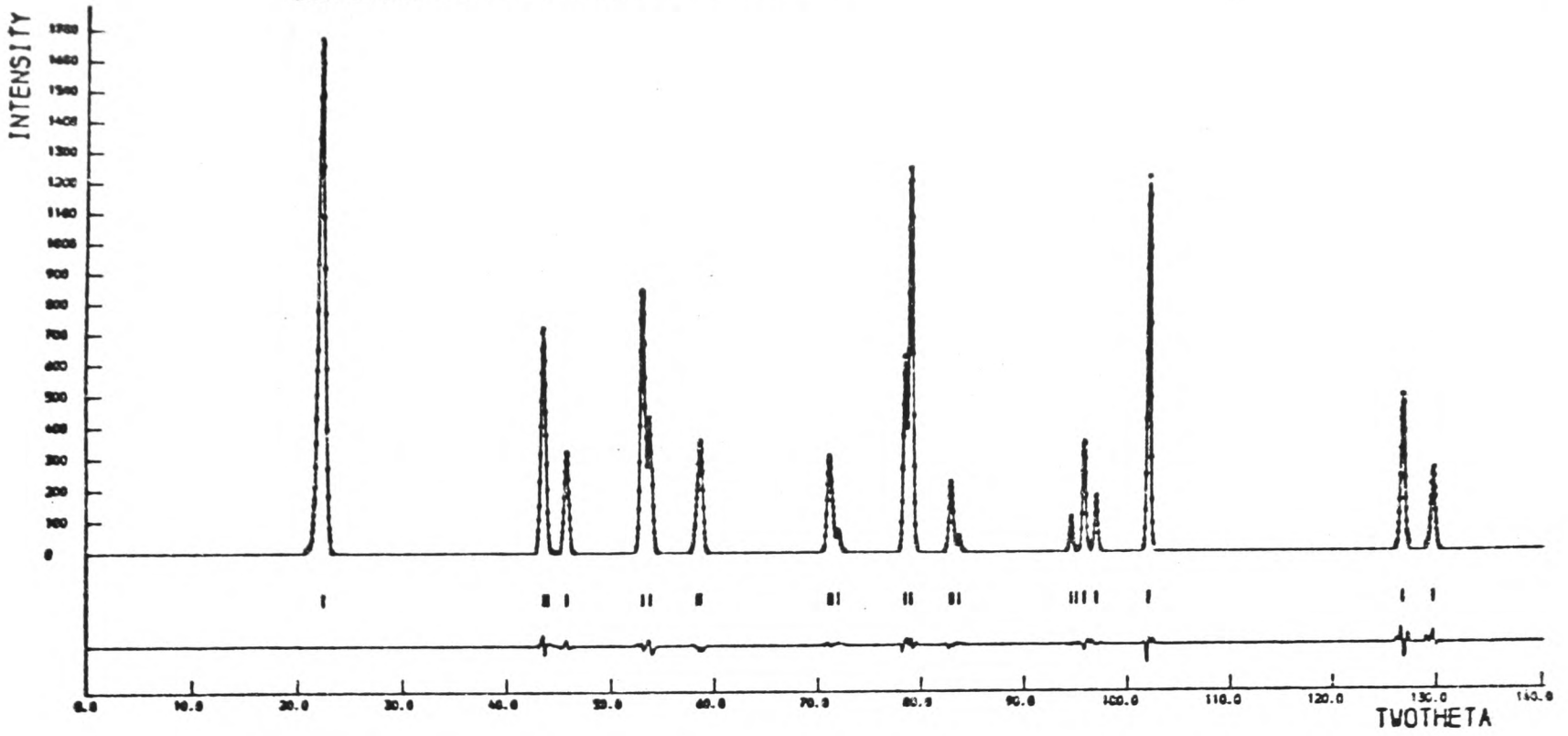
244. C. Gleitzer, Personal Communication.

# APPENDIX I

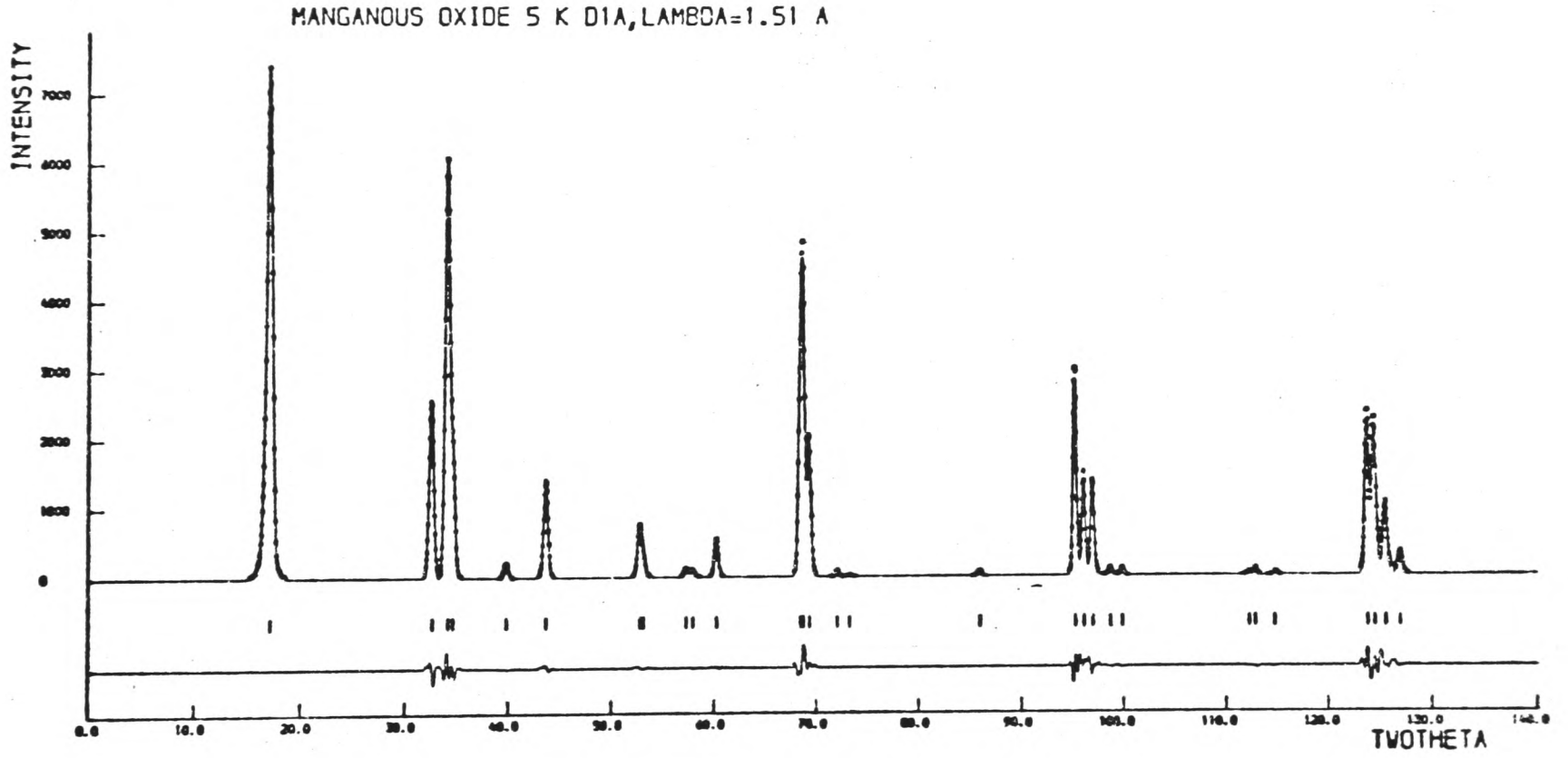
## RIETVELD REFINEMENT RESULTS

Observed data are plotted as crosses, and the calculated profile appears as a full line. Below are the reflection positions and the difference between observed and calculated profiles. Only observed data are plotted for the peak at lowest angle (magnetic (111)), since this was not included in refinements.

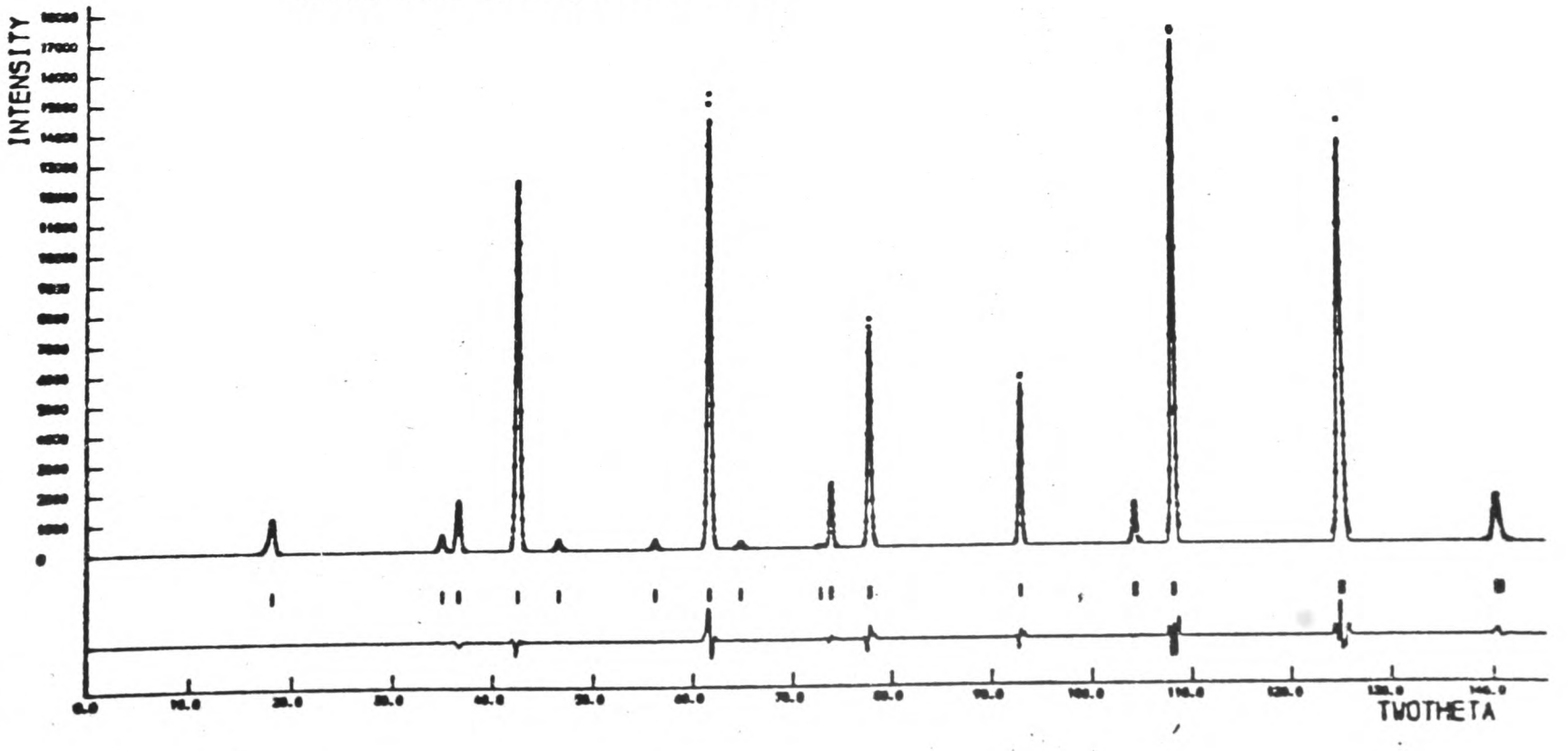
COBALTOUS OXIDE 5K D1A,LAMBDA=1.904 A



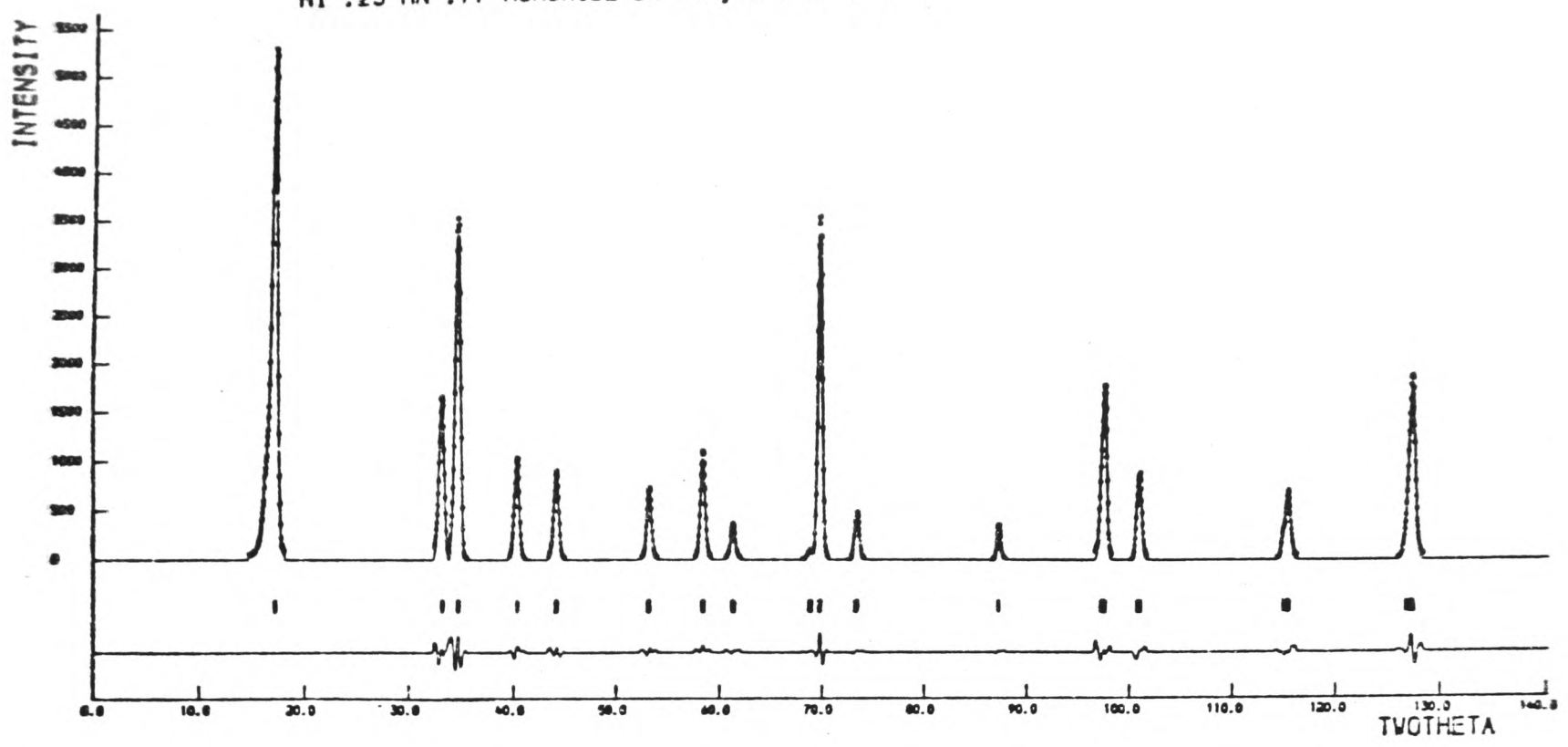

MANGANOUS OXIDE 5 K D1A,LAMBDA=1.51 A



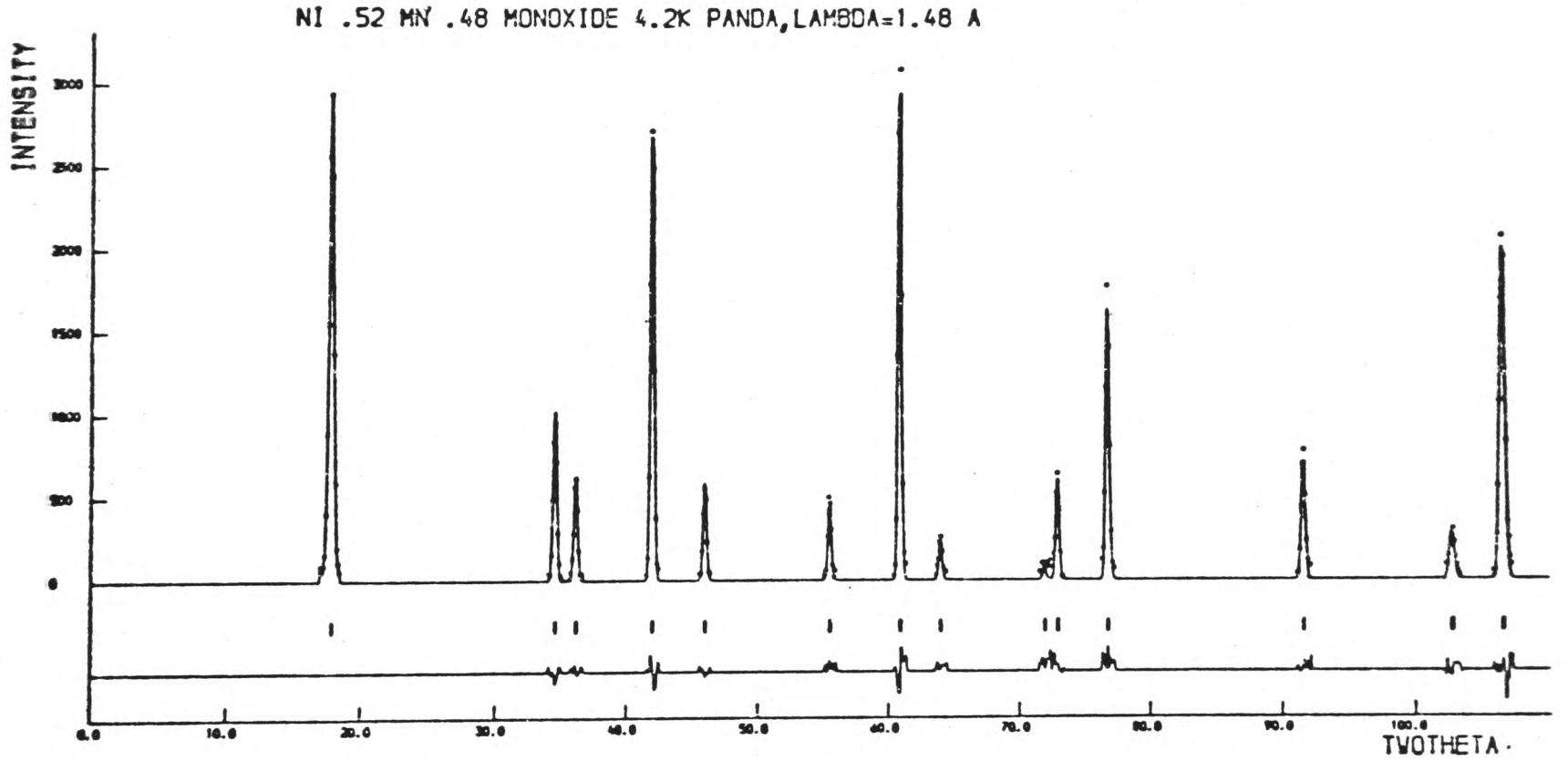

NICKEL OXIDE 5K D1A,LAMBDA=1.51 A



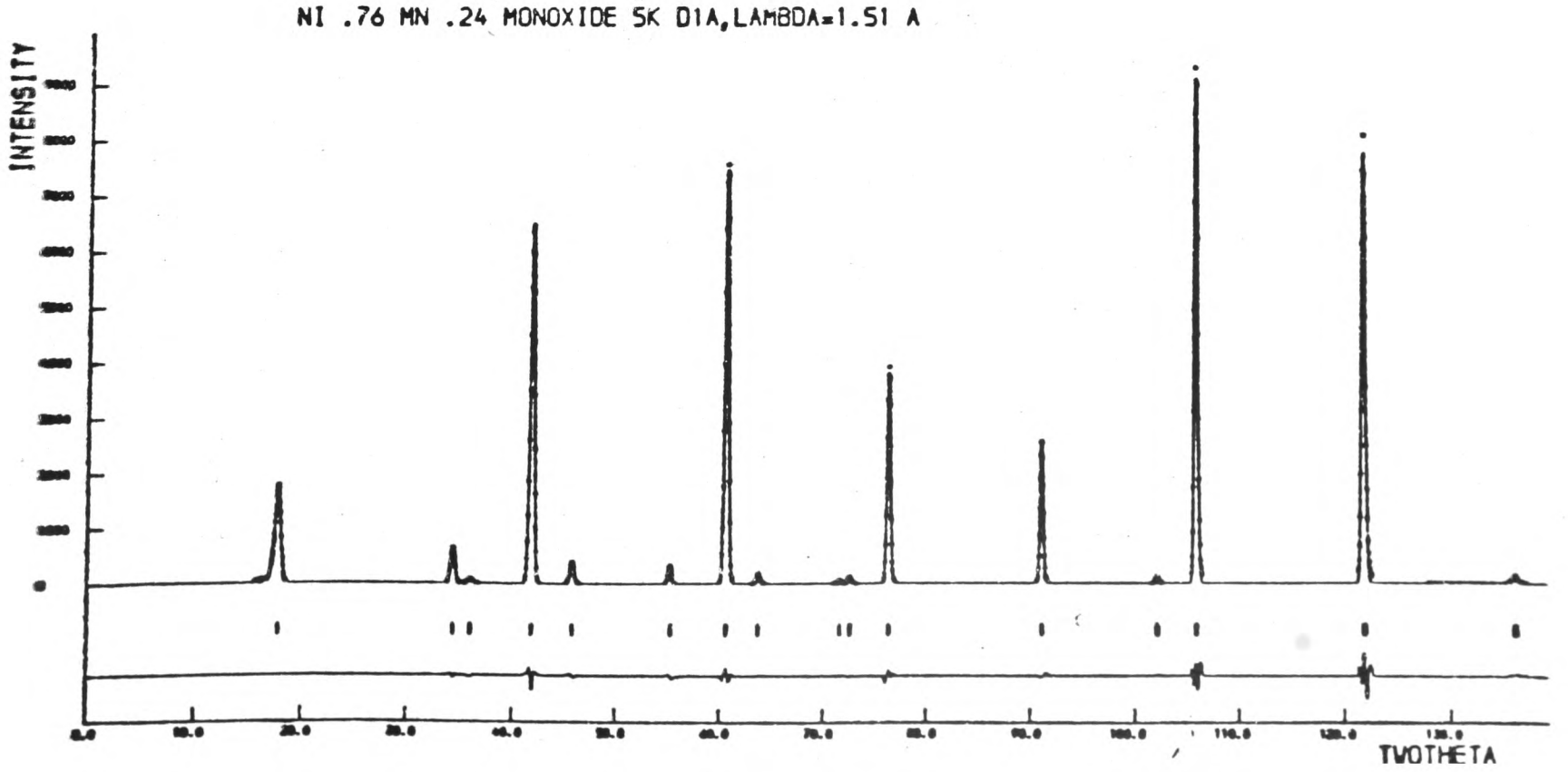
NI .23 MN .77 MONOXIDE 5K D1A,LAMBDA=1.51 A

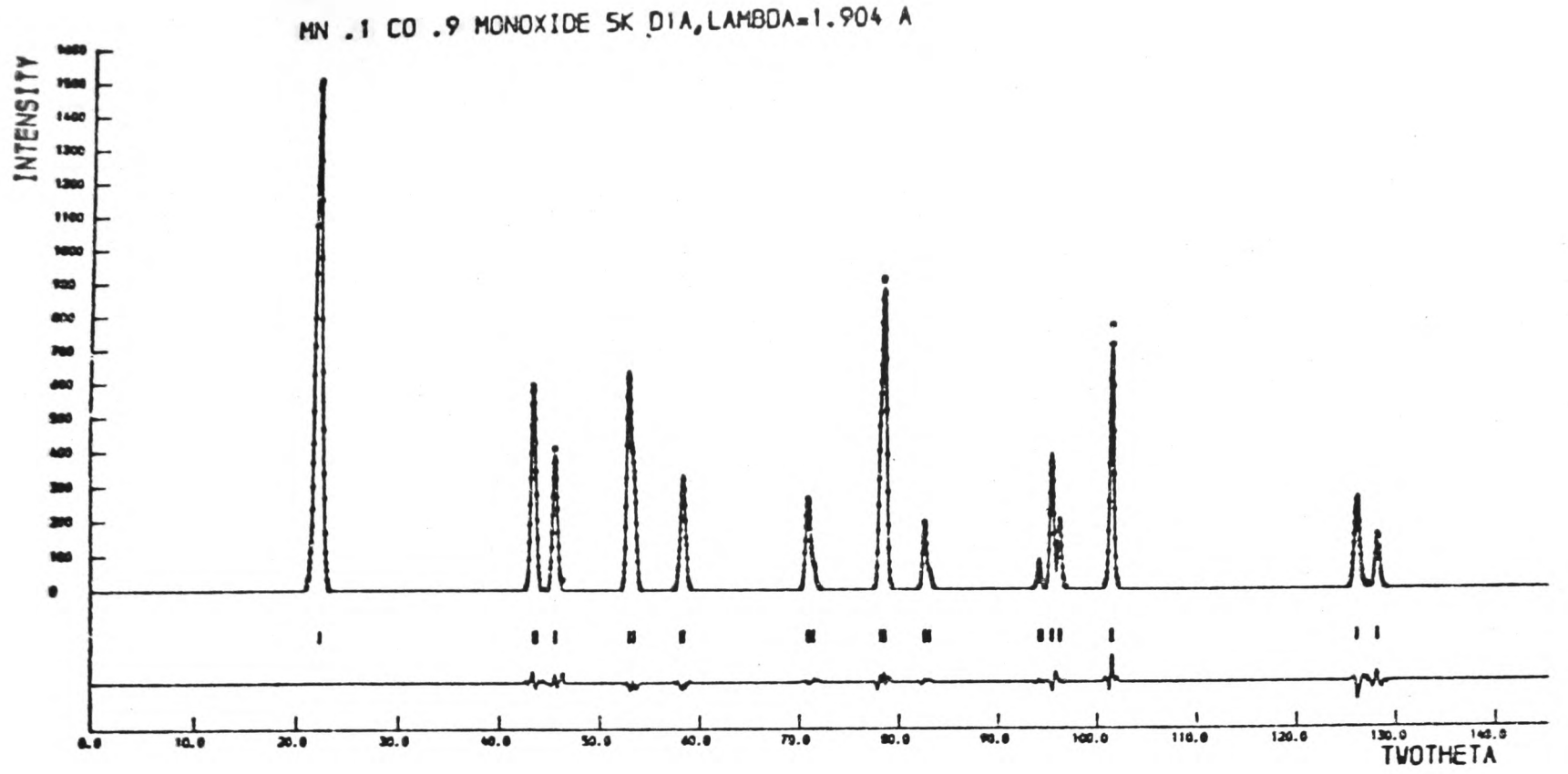


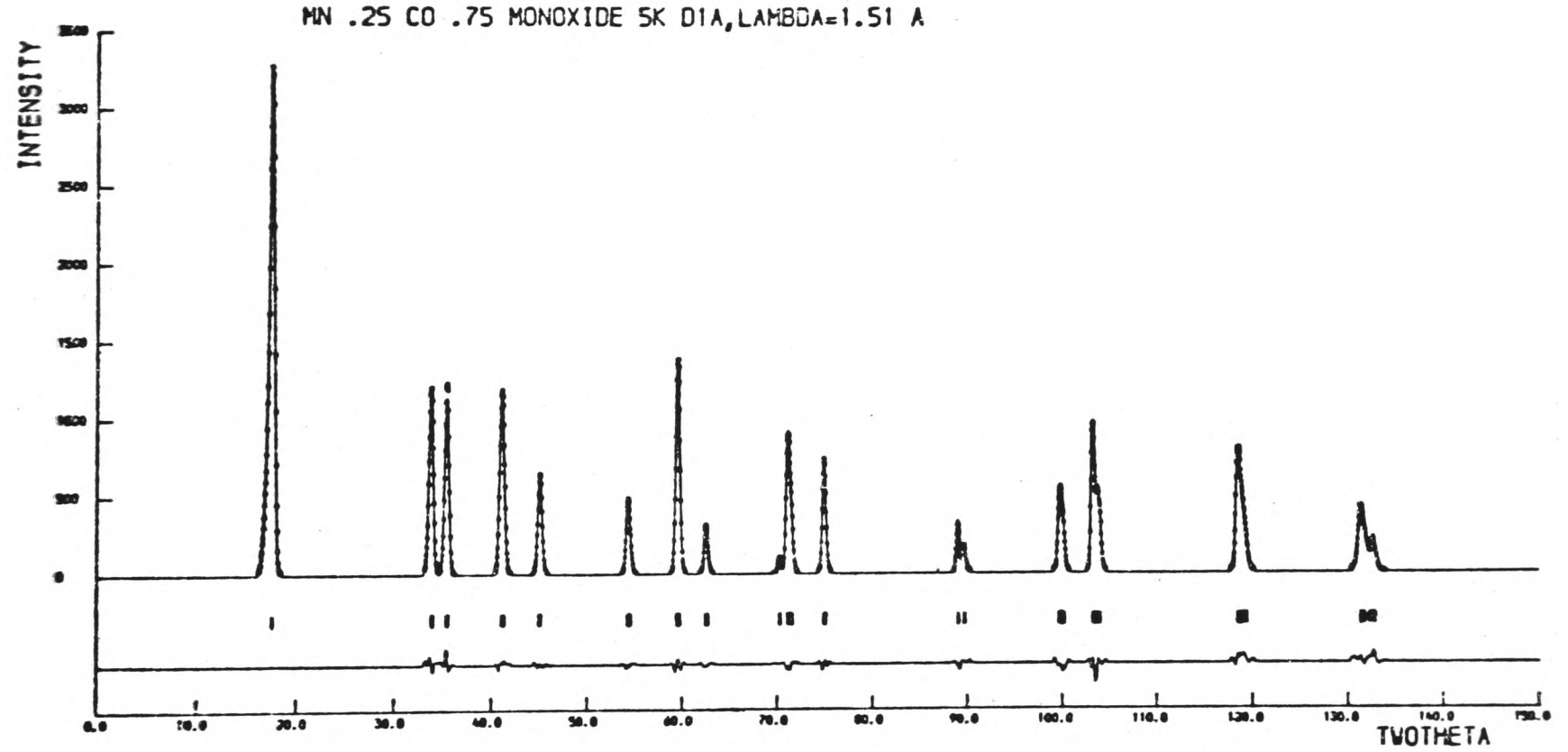

NI .52 MN .48 MONOXIDE 4.2K PANDA,LAMBDA=1.48 A

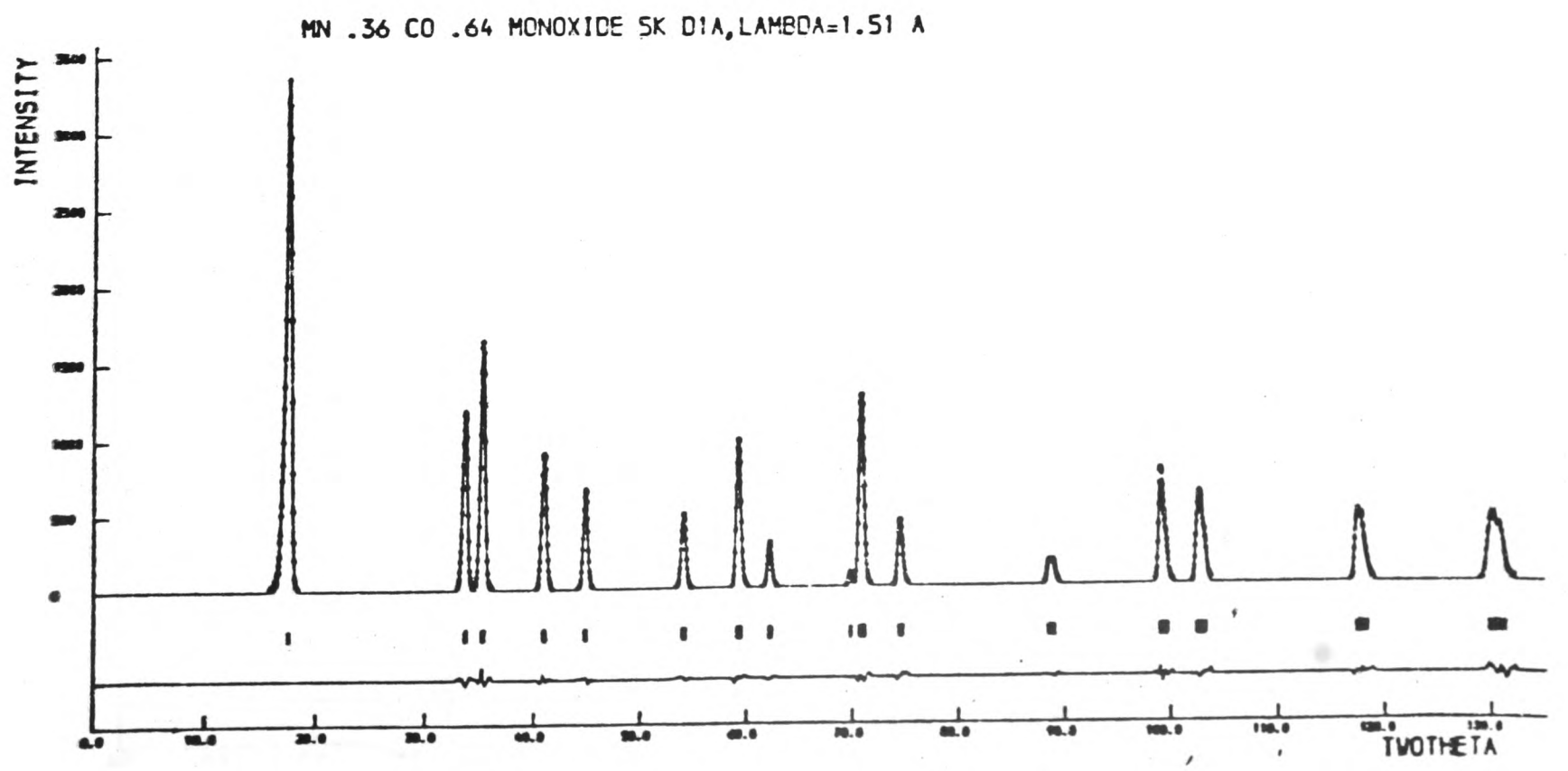


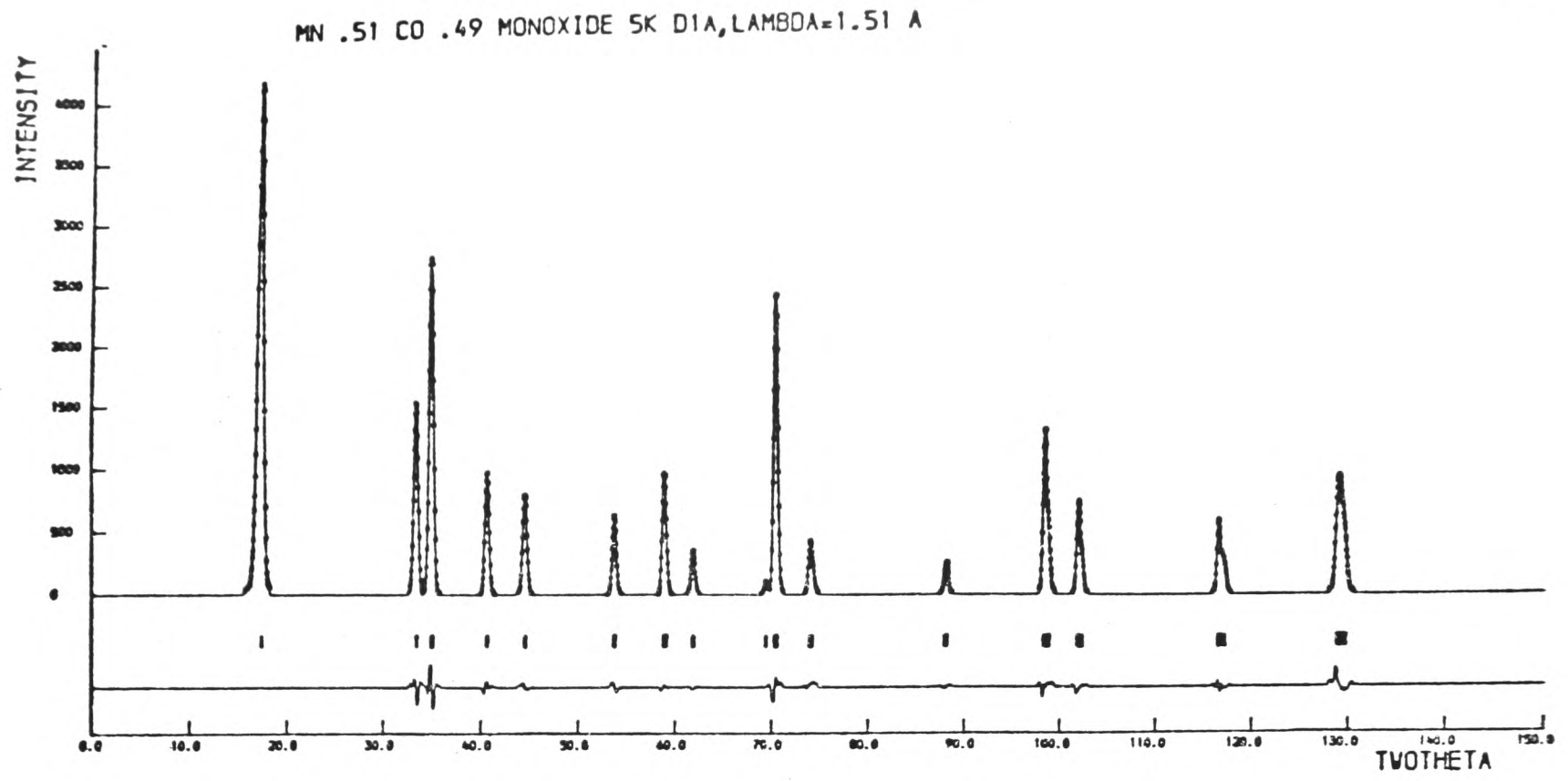

NI .76 MN .24 MONOXIDE 5K D1A,LAMBDA=1.51 A

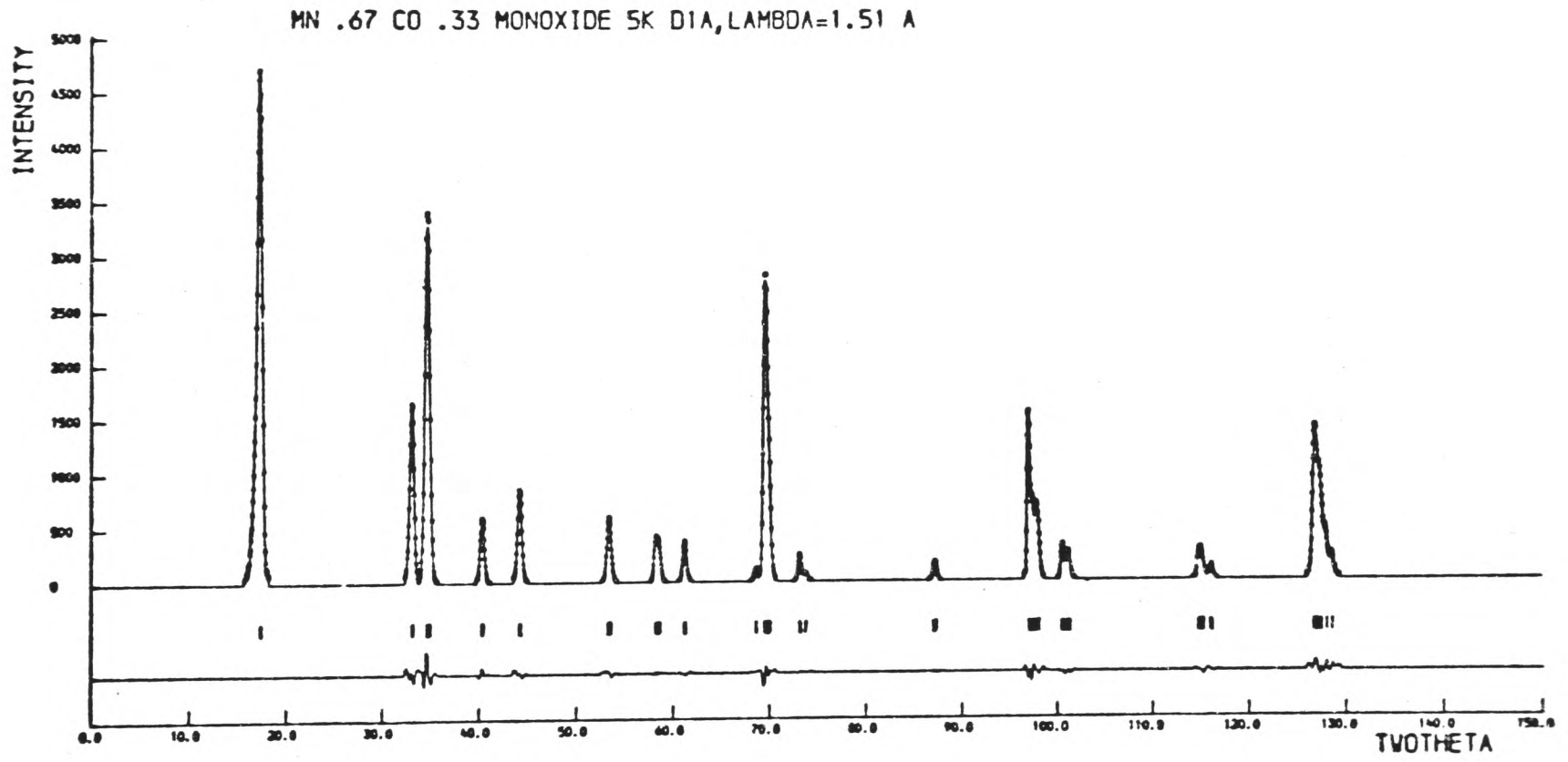


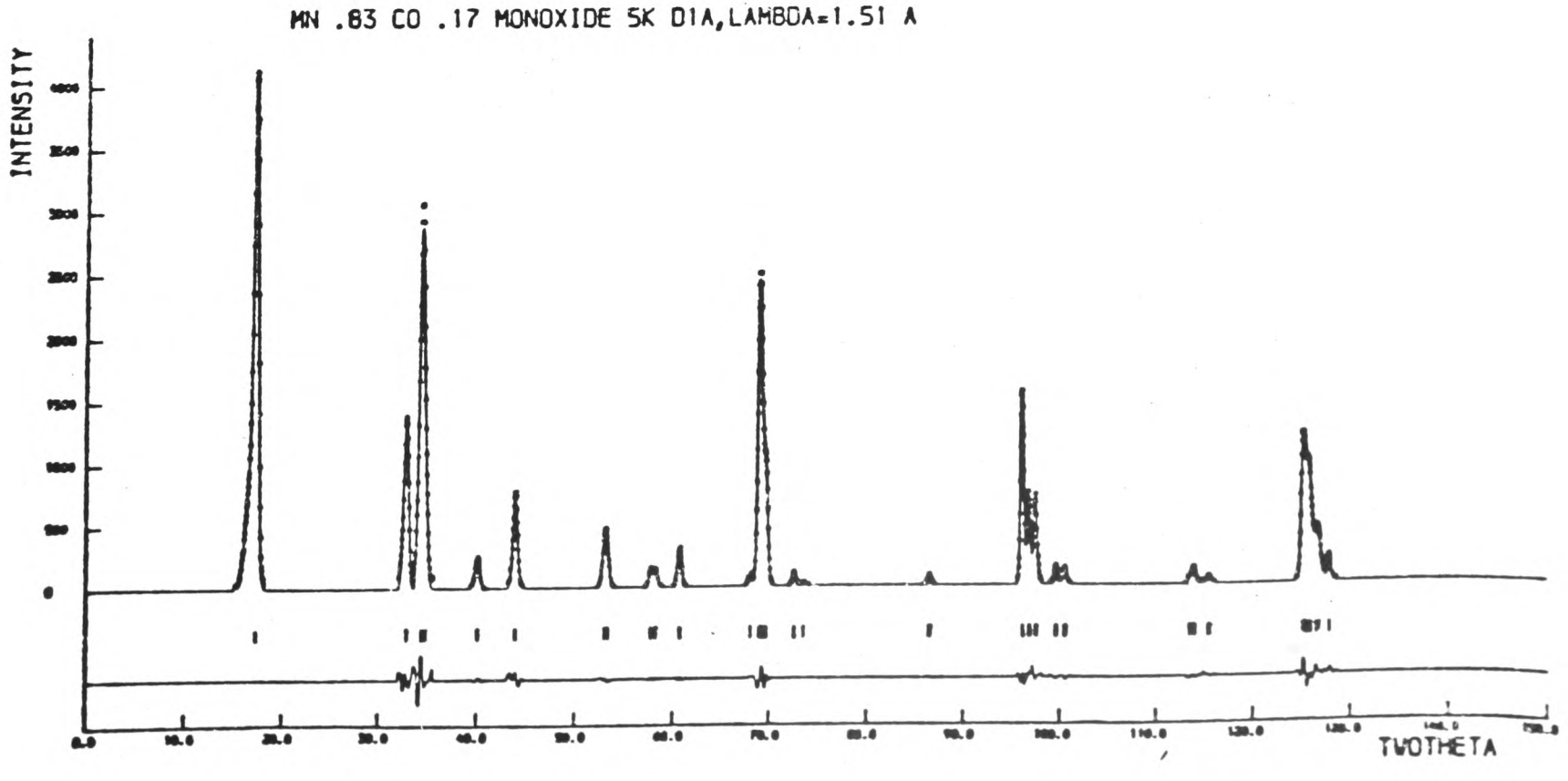

MN .1 CO .9 MONOXIDE 5K D1A, LAMBDA=1.904 A
INTENSITY
TWOTHETA


MN .25 CO .75 MONOXIDE 5K D1A, LAMBDA=1.51 A
INTENSITY
TWOTHETA

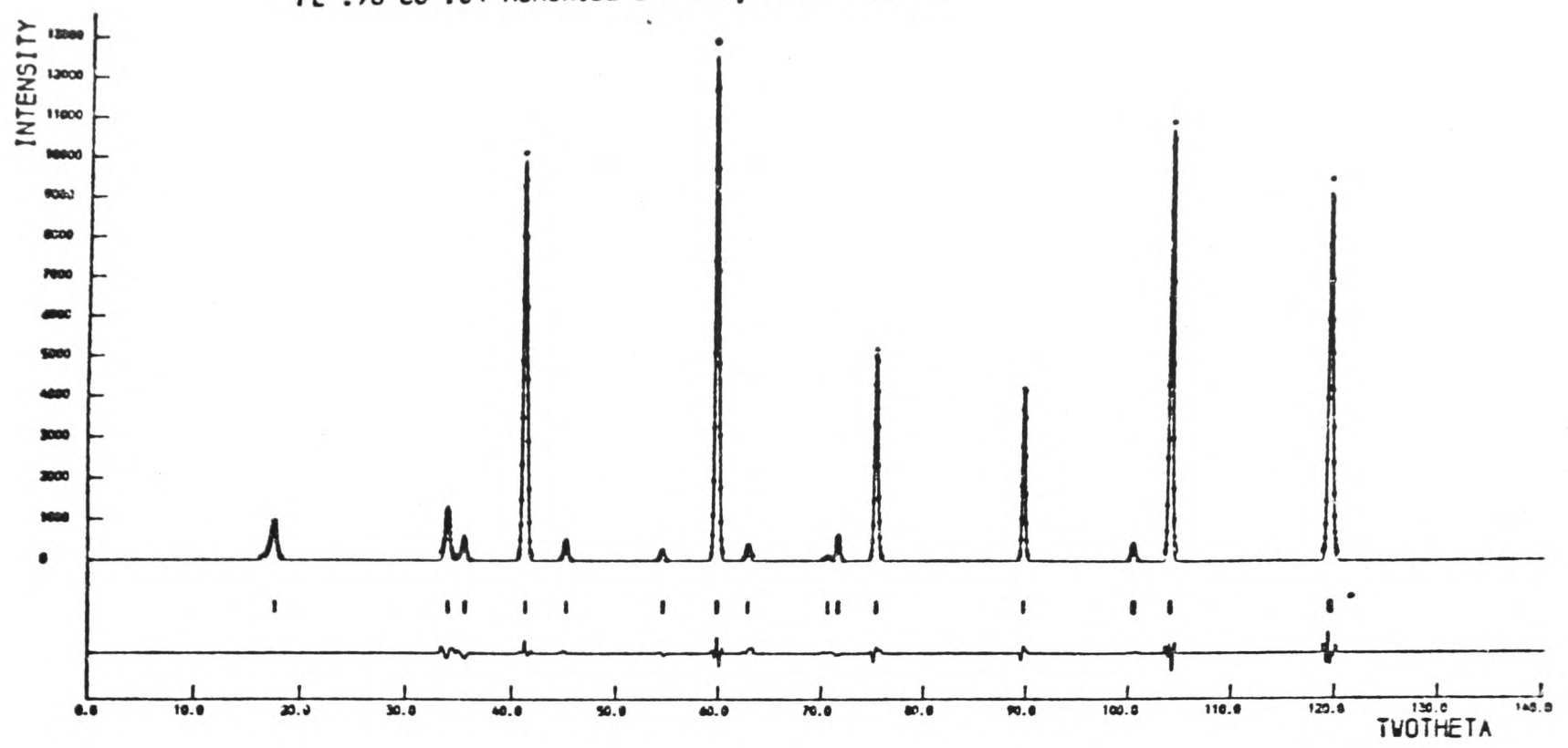

MN .36 CO .64 MONOXIDE 5K D1A, LAMBDA=1.51 A
INTENSITY
TWOTHETA


MN .51 CO .49 MONOXIDE 5K D1A,LAMBDA=1.51 A
INTENSITY
TWOTHETA

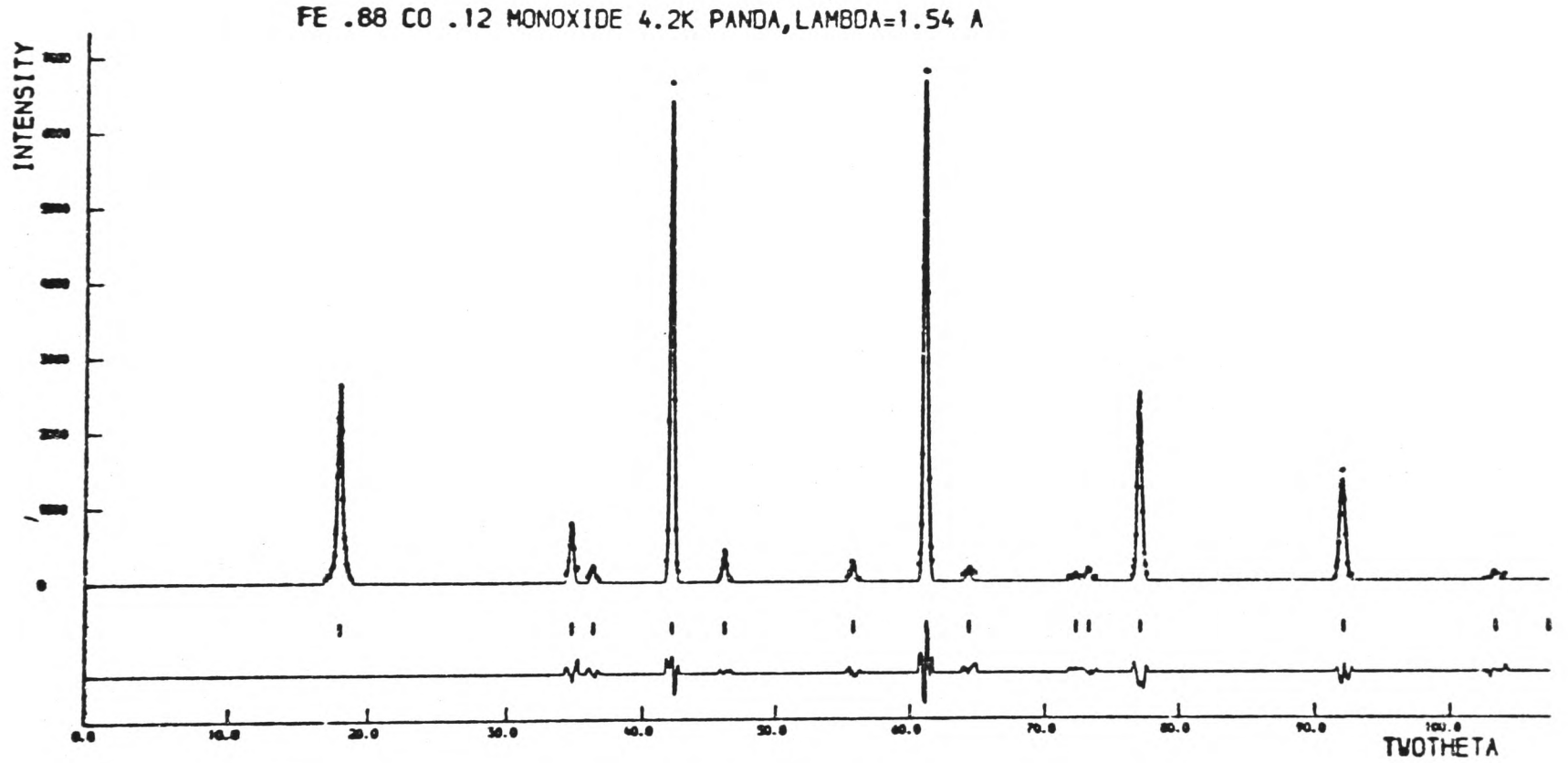

MN .67 CO .33 MONOXIDE 5K D1A,LAMBDA=1.51 A
INTENSITY
TWOTHETA


MN .83 CO .17 MONOXIDE 5K D1A,LAMBDA=1.51 A
INTENSITY
TWOTHETA

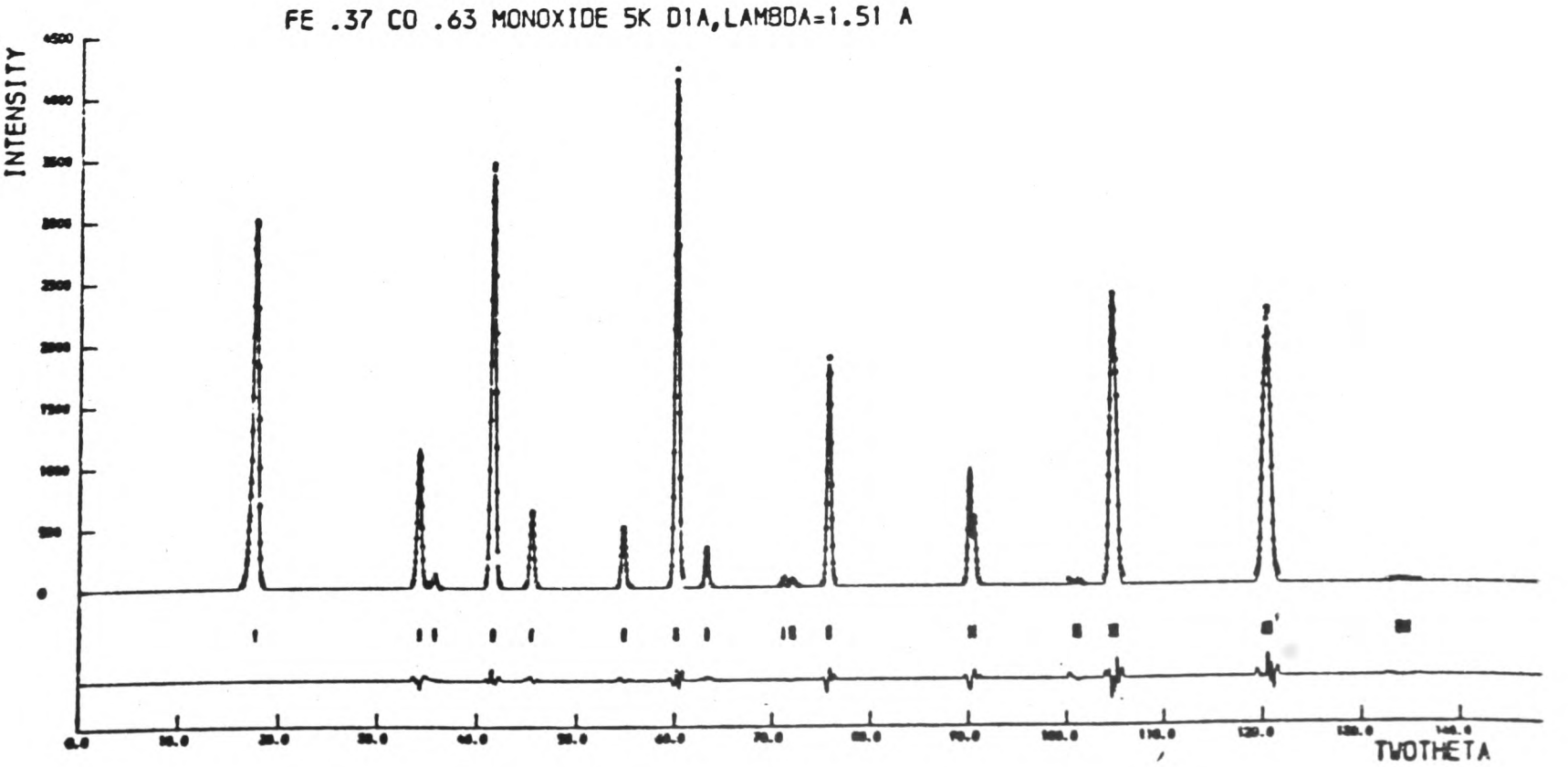
FE .96 CO .04 MONOXIDE 5 K D1A, LAMBDA=1.51 A



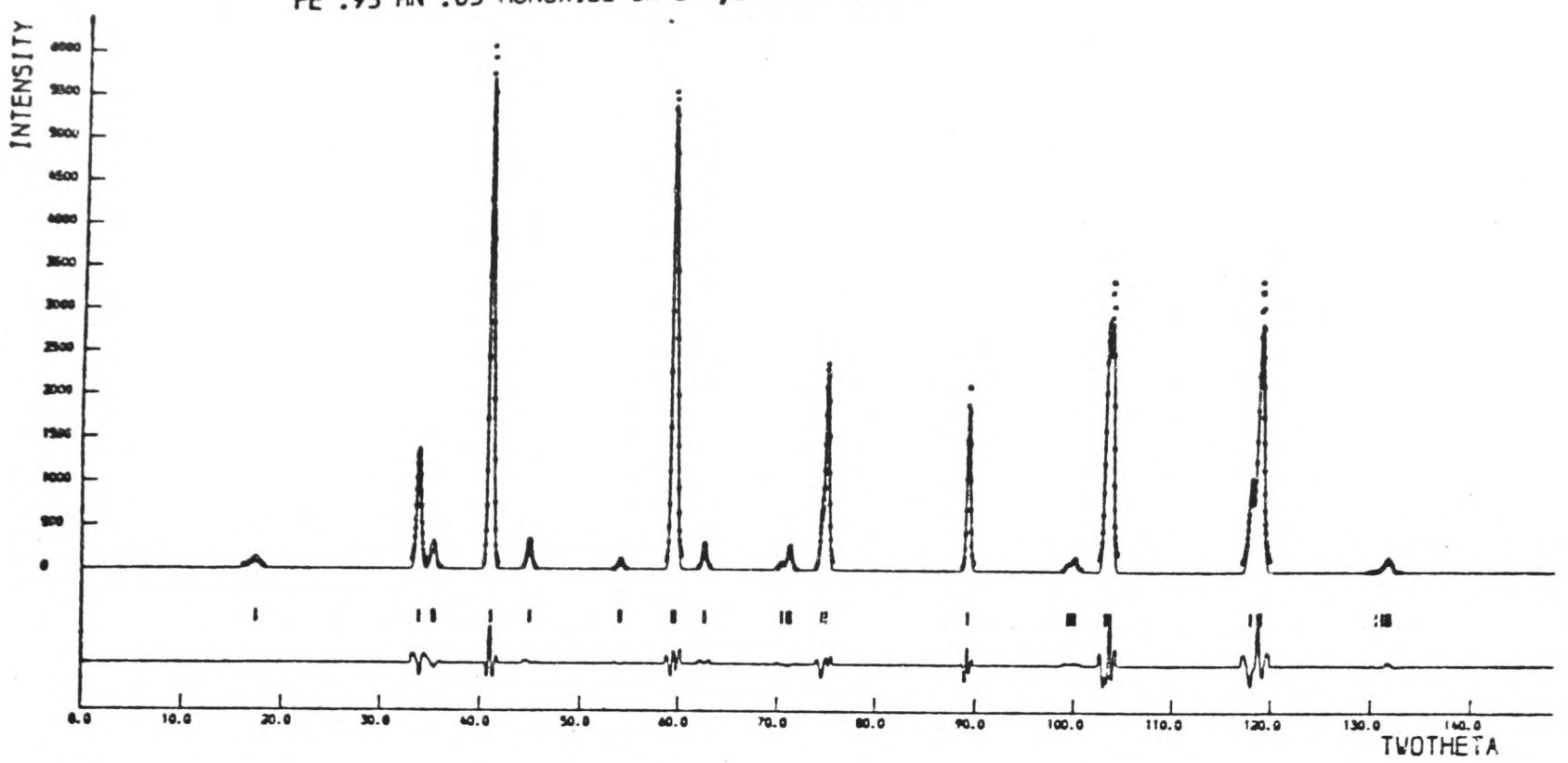

FE .88 CO .12 MONOXIDE 4.2K PANDA, LAMBDA=1.54 A



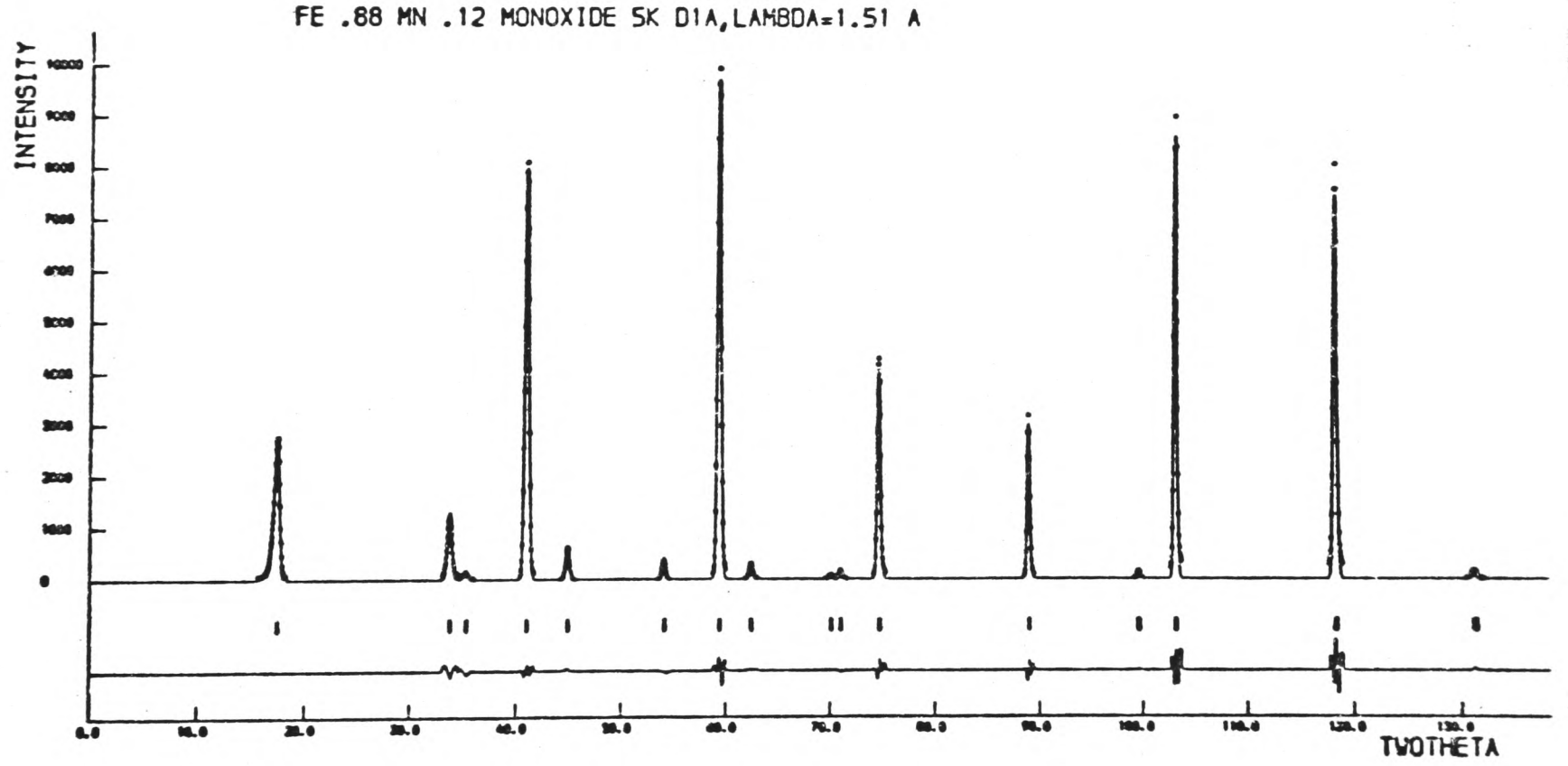

FE .37 CO .63 MONOXIDE 5K D1A, LAMBDA=1.51 A



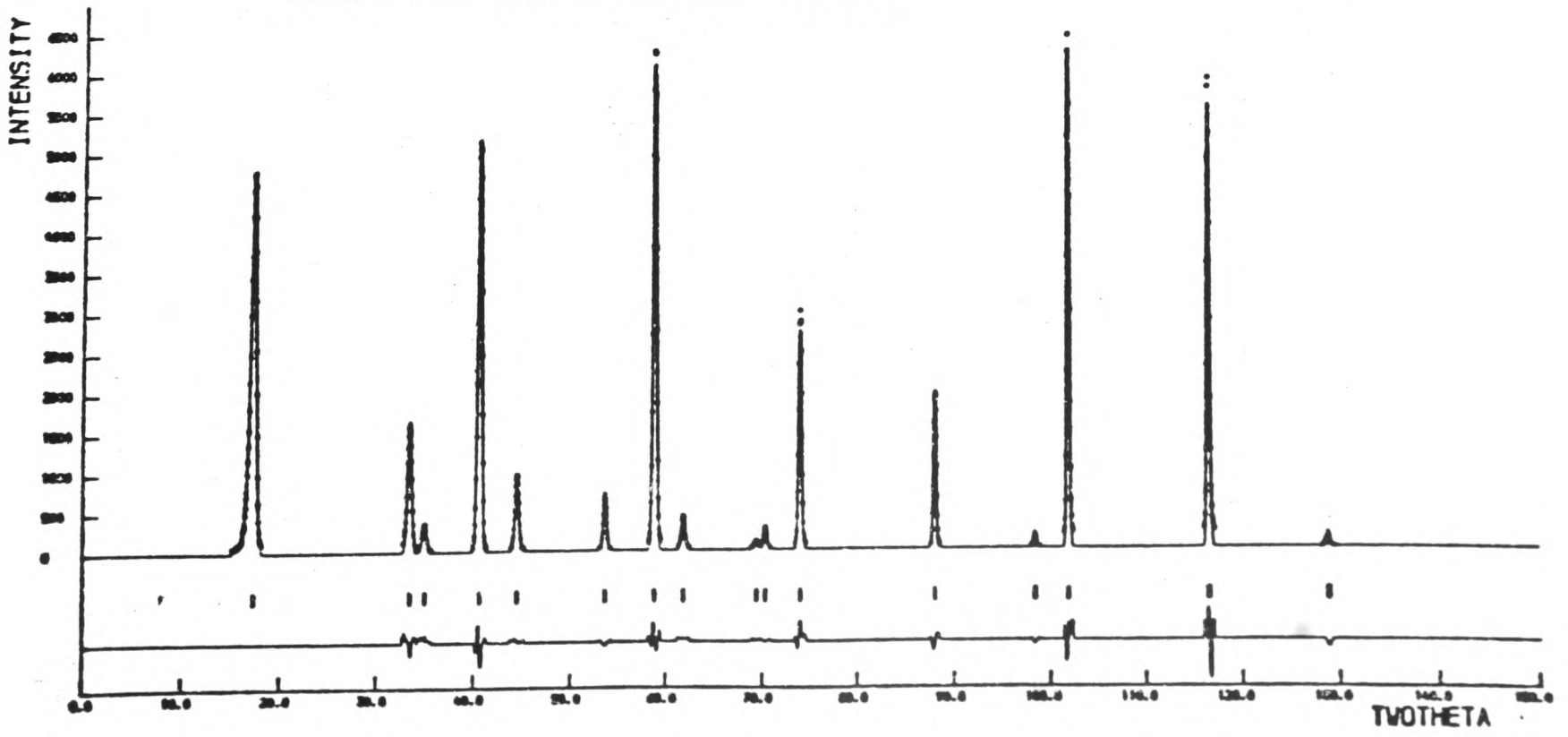
FE .95 MN .05 MONOXIDE SK D1A, LAMBDA=1.51 A

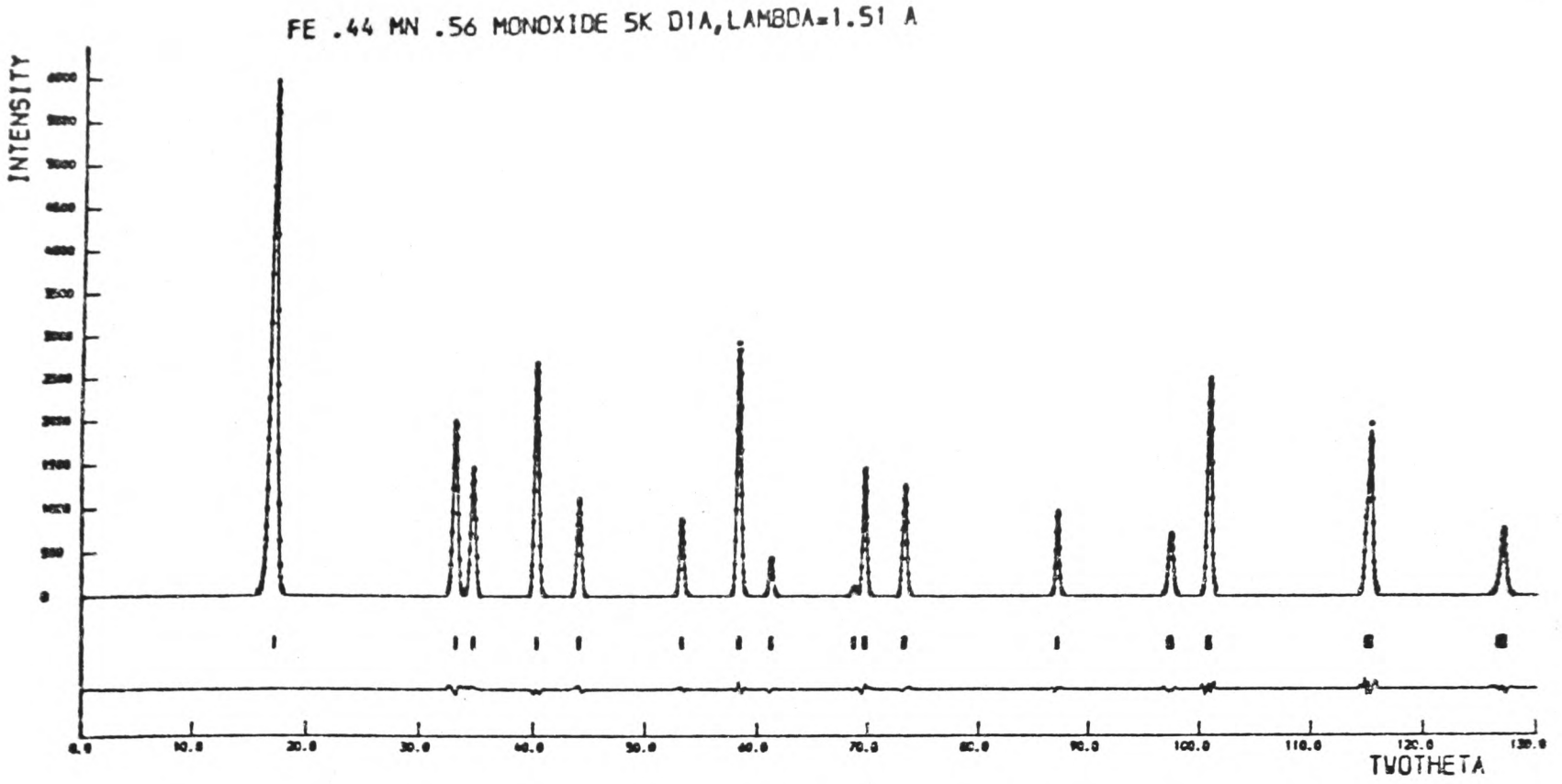


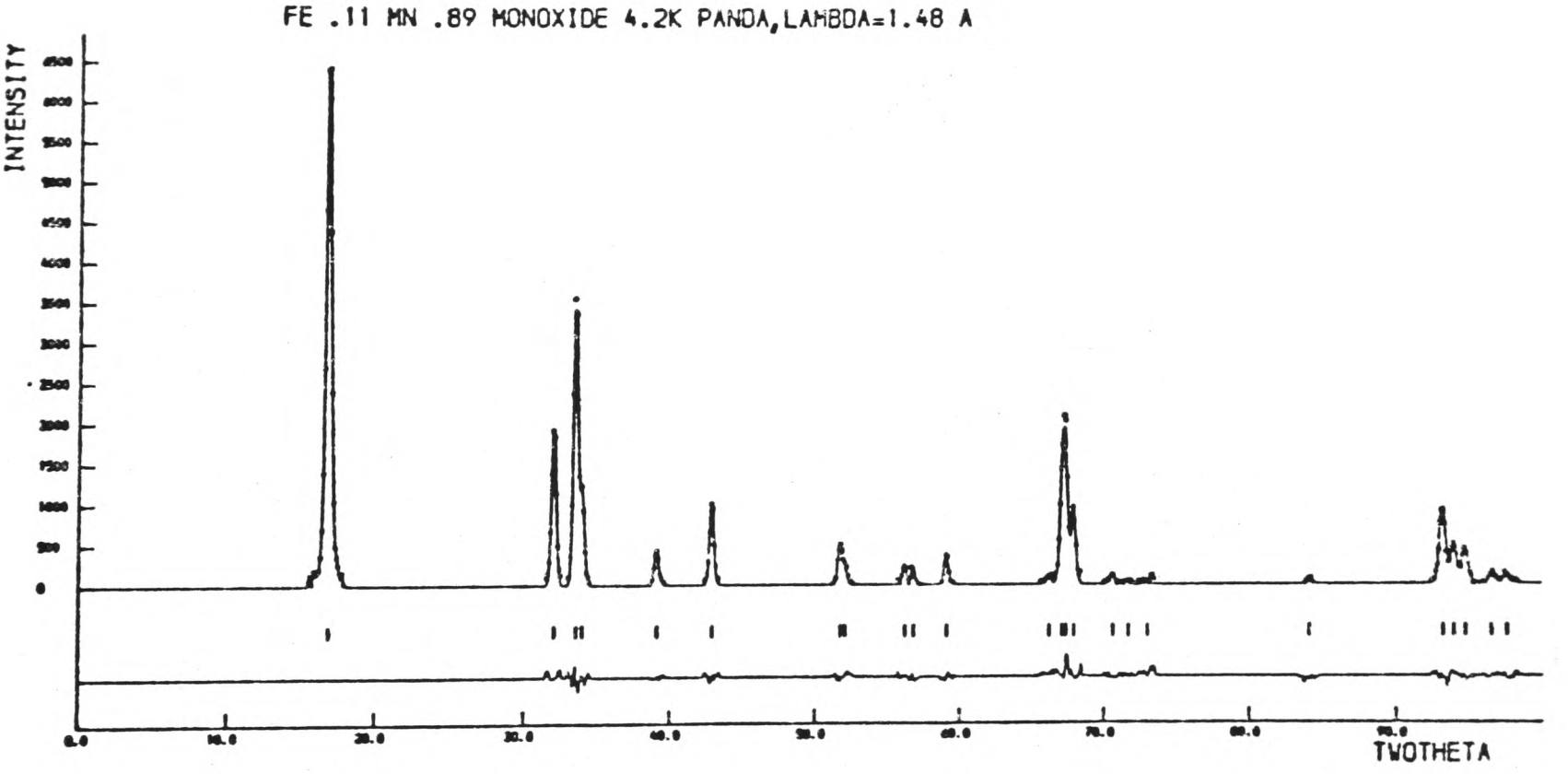

FE .88 MN .12 MONOXIDE SK D1A, LAMBDA=1.51 A




FE .64 MN .36 MONOXIDE SK D1A, LAMBDA=1.51 A




FE .44 MN .56 MONOXIDE 5K D1A, LAMBDA=1.51 A
INTENSITY
TWOTHETA


FE .11 MN .89 MONOXIDE 4.2K PANDA, LAMBDA=1.48 A
INTENSITY
TWOTHETA

# APPENDIX II

## MAGNETIC SUSCEPTIBILITY DATA FOR $(Mn_xFe_{1-x})_zO$

(Corrected molar magnetic susceptibility values are in c.g.s. units x $10^{-2}$)

$(Mn_{0.10}Fe_{0.90})_{0.931}O$

| T(K) | $\chi_m$, APPLIED FIELD (KG) | | | | | | | | |
|---|---|---|---|---|---|---|---|---|---|
| | 1 | 2 | 3 | 4 | 5 | 6 | 7 | 8 | 9 |
| 48.9 | 0.931 | 0.810 | 0.810 | 0.784 | 0.788 | 0.773 | 0.774 | 0.807 | 0.784 |
| 57.0 | 0.971 | 0.821 | 0.831 | 0.807 | 0.794 | 0.786 | 0.790 | 0.801 | 0.797 |
| 67.1 | 1.012 | 0.888 | 0.846 | 0.823 | 0.810 | 0.805 | 0.806 | 0.819 | 0.816 |
| 77.7 | 1.012 | 0.888 | 0.862 | 0.838 | 0.833 | 0.825 | 0.823 | 0.832 | 0.855 |
| 91.8 | 0.971 | 0.899 | 0.878 | 0.855 | 0.846 | 0.840 | 0.842 | 0.855 | 0.861 |
| 105.7 | 1.012 | 0.899 | 0.899 | 0.868 | 0.864 | 0.859 | 0.861 | 0.879 | 0.880 |
| 116.2 | 1.012 | 0.921 | 0.913 | 0.891 | 0.886 | 0.876 | 0.874 | 0.911 | 0.887 |
| 128.5 | 1.012 | 0.921 | 0.925 | 0.909 | 0.900 | 0.895 | 0.896 | 0.913 | 0.909 |
| 141.6 | 1.051 | 0.954 | 0.947 | 0.926 | 0.921 | 0.915 | 0.915 | 0.947 | 0.931 |
| 153.1 | 1.052 | 0.976 | 0.972 | 0.952 | 0.945 | 0.939 | 0.944 | 0.980 | 0.956 |
| 164.8 | 1.091 | 1.021 | 1.012 | 0.993 | 0.980 | 0.971 | 0.972 | 1.004 | 0.976 |
| 176.5 | 1.133 | 1.042 | 1.045 | 1.027 | 1.016 | 1.009 | 1.007 | 1.033 | 0.989 |
| 182.5 | 1.163 | 1.098 | 1.091 | 1.065 | 1.048 | 1.041 | 1.040 | 1.057 | 1.034 |
| 187.2 | 1.163 | 1.109 | 1.091 | 1.068 | 1.053 | 1.043 | 1.045 | 1.077 | 1.034 |
| 191.4 | 1.173 | 1.087 | 1.096 | 1.068 | 1.053 | 1.044 | 1.049 | 1.061 | 1.040 |
| 195.4 | 1.173 | 1.098 | 1.090 | 1.059 | 1.047 | 1.038 | 1.039 | 1.065 | 1.046 |
| 198.8 | 1.173 | 1.109 | 1.085 | 1.059 | 1.047 | 1.034 | 1.034 | 1.065 | 1.034 |
| 201.9 | 1.173 | 1.087 | 1.077 | 1.053 | 1.042 | 1.029 | 1.032 | 1.060 | 1.031 |
| 202.3 | 1.213 | 1.109 | 1.080 | 1.059 | 1.045 | 1.031 | 1.033 | 1.056 | 1.027 |
| 221.0 | 1.172 | 1.076 | 1.059 | 1.035 | 1.020 | 1.013 | 1.009 | 1.037 | 1.008 |
| 236.3 | 1.092 | 1.042 | 1.034 | 1.005 | 0.997 | 0.981 | 0.981 | 1.001 | 0.976 |
| 246.7 | 1.092 | 1.020 | 1.012 | 0.987 | 0.970 | 0.961 | 0.962 | 0.988 | 0.982 |
| 269.7 | 1.091 | 0.987 | 0.986 | 0.958 | 0.939 | 0.931 | 0.926 | 0.956 | 0.935 |
| 280.5 | 1.052 | 0.965 | 0.960 | 0.934 | 0.919 | 0.908 | 0.908 | 0.935 | 0.915 |
| 289.5 | 1.011 | 0.954 | 0.944 | 0.915 | 0.903 | 0.895 | 0.892 | 0.919 | 0.984 |
| 296.6 | 1.052 | 0.943 | 0.929 | 0.912 | 0.894 | 0.884 | 0.882 | 0.915 | 0.878 |
| 313.7 | 0.971 | 0.921 | 0.913 | 0.885 | 0.868 | 0.855 | 0.853 | 0.860 | 0.855 |

$(Mn_{0.23}Fe_{0.77})_{0.929}O$

| T(K) | $\chi_m$, APPLIED FIELD (KG) | | | | | | | | |
|---|---|---|---|---|---|---|---|---|---|
| | 1 | 2 | 3 | 4 | 5 | 6 | 7 | 8 | 9 |
| 47.3 | 0.794 | 0.724 | 0.733 | 0.726 | 0.722 | 0.720 | 0.720 | 0.720 | 0.724 |
| 55.8 | 0.761 | 0.733 | 0.724 | 0.722 | 0.718 | 0.714 | 0.713 | 0.715 | 0.716 |
| 77.2 | 0.794 | 0.733 | 0.729 | 0.722 | 0.717 | 0.715 | 0.716 | 0.715 | 0.721 |
| 77.5 | 0.782 | 0.713 | 0.722 | 0.716 | 0.714 | 0.709 | 0.709 | 0.708 | 0.711 |
| 82.8 | 0.782 | 0.714 | 0.726 | 0.725 | 0.718 | 0.716 | 0.714 | 0.716 | 0.718 |
| 97.4 | 0.782 | 0.714 | 0.738 | 0.735 | 0.732 | 0.729 | 0.727 | 0.728 | 0.732 |
| 110.8 | 0.814 | 0.758 | 0.766 | 0.753 | 0.749 | 0.745 | 0.743 | 0.743 | 0.749 |
| 123.6 | 0.847 | 0.766 | 0.770 | 0.768 | 0.758 | 0.756 | 0.758 | 0.757 | 0.765 |
| 135.6 | 0.847 | 0.793 | 0.791 | 0.779 | 0.777 | 0.773 | 0.772 | 0.771 | 0.781 |
| 149.0 | 0.880 | 0.819 | 0.812 | 0.803 | 0.796 | 0.796 | 0.796 | 0.794 | 0.807 |
| 161.7 | 0.880 | 0.828 | 0.836 | 0.829 | 0.825 | 0.820 | 0.819 | 0.820 | 0.847 |
| 167.8 | 0.912 | 0.863 | 0.869 | 0.856 | 0.852 | 0.846 | 0.847 | 0.846 | 0.871 |
| 173.8 | 0.944 | 0.890 | 0.889 | 0.883 | 0.875 | 0.871 | 0.870 | 0.870 | 0.895 |
| 178.7 | 1.009 | 0.942 | 0.938 | 0.929 | 0.913 | 0.907 | 0.904 | 0.906 | 0.924 |
| 184.3 | 1.009 | 0.942 | 0.934 | 0.920 | 0.910 | 0.904 | 0.904 | 0.903 | 0.921 |
| 186.1 | 1.009 | 0.933 | 0.934 | 0.918 | 0.908 | 0.903 | 0.898 | 0.900 | 0.917 |
| 191.3 | 0.977 | 0.925 | 0.913 | 0.904 | 0.899 | 0.890 | 0.888 | 0.888 | 0.909 |
| 202.5 | 0.944 | 0.863 | 0.889 | 0.878 | 0.870 | 0.860 | 0.860 | 0.860 | 0.879 |
| 214.4 | 0.944 | 0.863 | 0.869 | 0.856 | 0.848 | 0.844 | 0.841 | 0.839 | 0.859 |
| 225.8 | 0.912 | 0.845 | 0.848 | 0.838 | 0.827 | 0.822 | 0.818 | 0.817 | 0.836 |
| 234.8 | 0.879 | 0.819 | 0.827 | 0.819 | 0.811 | 0.805 | 0.800 | 0.802 | 0.809 |
| 254.9 | 0.847 | 0.784 | 0.787 | 0.776 | 0.769 | 0.765 | 0.763 | 0.761 | 0.764 |
| 265.5 | 0.850 | 0.770 | 0.774 | 0.764 | 0.755 | 0.753 | 0.747 | 0.745 | 0.750 |
| 275.1 | 0.814 | 0.749 | 0.754 | 0.746 | 0.740 | 0.733 | 0.731 | 0.729 | 0.732 |
| 285.0 | 0.782 | 0.749 | 0.750 | 0.737 | 0.730 | 0.725 | 0.724 | 0.722 | 0.724 |
| 291.6 | 0.782 | 0.740 | 0.742 | 0.732 | 0.726 | 0.722 | 0.718 | 0.714 | 0.720 |

$(Mn_{0.36}Fe_{0.64})_{0.954}O$

| T(K) | $\chi_m$, APPLIED FIELD, KG | | | | | | | | |
|---|---|---|---|---|---|---|---|---|---|
| | 1 | 2 | 3 | 4 | 5 | 6 | 7 | 8 | 9 |
| 48.0 | 0.736 | 0.676 | 0.689 | 0.689 | 0.688 | 0.687 | 0.690 | 0.689 | 0.693 |
| 57.0 | 0.736 | 0.665 | 0.679 | 0.679 | 0.682 | 0.583 | 0.683 | 0.685 | 0.688 |
| 67.5 | 0.676 | 0.689 | 0.685 | 0.690 | 0.692 | 0.692 | 0.692 | 0.696 | 0.695 |
| 80.0 | 0.687 | 0.700 | 0.703 | 0.702 | 0.702 | 0.705 | 0.707 | 0.709 | 0.709 |
| 105.6 | 0.736 | 0.709 | 0.730 | 0.729 | 0.731 | 0.730 | 0.731 | 0.732 | 0.736 |
| 125.7 | 0.736 | 0.741 | 0.751 | 0.756 | 0.754 | 0.755 | 0.758 | 0.760 | 0.762 |
| 143.1 | 0.817 | 0.774 | 0.786 | 0.788 | 0.790 | 0.790 | 0.790 | 0.793 | 0.799 |
| 158.1 | 0.839 | 0.857 | 0.856 | 0.857 | 0.857 | 0.859 | 0.861 | 0.870 | 0.870 |
| 161.7 | 0.861 | 0.878 | 0.879 | 0.879 | 0.878 | 0.882 | 0.884 | 0.895 | 0.894 |
| 165.7 | 0.850 | 0.868 | 0.868 | 0.869 | 0.868 | 0.871 | 0.876 | 0.885 | 0.883 |
| 169.7 | 0.839 | 0.857 | 0.859 | 0.861 | 0.859 | 0.862 | 0.866 | 0.874 | 0.874 |
| 173.5 | 0.828 | 0.852 | 0.850 | 0.852 | 0.851 | 0.852 | 0.855 | 0.862 | 0.863 |
| 177.2 | 0.839 | 0.847 | 0.850 | 0.850 | 0.851 | 0.852 | 0.853 | 0.859 | 0.858 |
| 189.2 | 0.807 | 0.827 | 0.826 | 0.825 | 0.823 | 0.825 | 0.827 | 0.833 | 0.831 |
| 200.2 | 0.817 | 0.785 | 0.801 | 0.803 | 0.800 | 0.801 | 0.803 | 0.805 | 0.809 |
| 220.2 | 0.776 | 0.752 | 0.766 | 0.767 | 0.765 | 0.764 | 0.765 | 0.765 | 0.769 |
| 237.0 | 0.736 | 0.720 | 0.740 | 0.738 | 0.740 | 0.740 | 0.742 | 0.743 | 0.745 |
| 257.6 | 0.736 | 0.739 | 0.705 | 0.706 | 0.705 | 0.706 | 0.706 | 0.707 | 0.709 |
| 274.9 | 0.695 | 0.665 | 0.689 | 0.685 | 0.687 | 0.685 | 0.685 | 0.685 | 0.688 |
| 284.9 | 0.695 | 0.665 | 0.674 | 0.673 | 0.673 | 0.673 | 0.675 | 0.675 | 0.677 |
| 296.6 | 0.695 | 0.564 | 0.664 | 0.662 | 0.658 | 0.656 | 0.657 | 0.658 | 0.660 |

$(Mn_{0.5}Fe_{0.5})_{0.971}O$

| T(K) | $\chi_m$, APPLIED FIELD (KG) | | | | | | | | |
|---|---|---|---|---|---|---|---|---|---|
| | 1 | 2 | 3 | 4 | 5 | 6 | 7 | 8 | 9 |
| 47.4 | 2.218 | 2.187 | 2.264 | 2.271 | 2.279 | 2.288 | 2.334 | 2.364 | 2.396 |
| 56.7 | 1.972 | 1.924 | 2.010 | 1.992 | 2.009 | 1.994 | 1.996 | 2.004 | 1.997 |
| 65.6 | 1.479 | 1.119 | 1.048 | 1.074 | 1.050 | 1.045 | 1.038 | 1.029 | 1.029 |
| 77.6 | 0.679 | 0.659 | 0.672 | 0.671 | 0.670 | 0.671 | 0.674 | 0.673 | 0.674 |
| 90.1 | 0.741 | 0.659 | 0.695 | 0.684 | 0.688 | 0.683 | 0.689 | 0.686 | 0.688 |
| 108.7 | 0.741 | 0.659 | 0.702 | 0.702 | 0.702 | 0.711 | 0.711 | 0.711 | 0.712 |
| 128.9 | 0.741 | 0.709 | 0.733 | 0.737 | 0.739 | 0.736 | 0.735 | 0.743 | 0.744 |
| 145.9 | 0.802 | 0.757 | 0.787 | 0.782 | 0.783 | 0.790 | 0.785 | 0.786 | 0.790 |
| 154.1 | 0.864 | 0.807 | 0.818 | 0.817 | 0.815 | 0.816 | 0.818 | 0.822 | 0.822 |
| 161.8 | 0.864 | 0.840 | 0.848 | 0.844 | 0.841 | 0.838 | 0.842 | 0.838 | 0.841 |
| 173.0 | 0.864 | 0.823 | 0.825 | 0.826 | 0.818 | 0.822 | 0.820 | 0.817 | 0.823 |
| 193.4 | 0.802 | 0.757 | 0.771 | 0.764 | 0.771 | 0.771 | 0.773 | 0.777 | 0.789 |
| 212.2 | 0.802 | 0.708 | 0.741 | 0.737 | 0.743 | 0.740 | 0.743 | 0.744 | 0.744 |
| 230.1 | 0.741 | 0.676 | 0.702 | 0.702 | 0.708 | 0.709 | 0.711 | 0.712 | 0.713 |
| 250.1 | 0.741 | 0.759 | 0.701 | 0.680 | 0.681 | 0.681 | 0.681 | 0.683 | 0.684 |
| 268.7 | 0.741 | 0.701 | 0.648 | 0.649 | 0.653 | 0.656 | 0.657 | 0.656 | 0.659 |
| 286.9 | 0.679 | 0.626 | 0.625 | 0.627 | 0.629 | 0.634 | 0.634 | 0.634 | 0.636 |
| 297.3 | 0.679 | 0.593 | 0.618 | 0.618 | 0.620 | 0.622 | 0.622 | 0.622 | 0.624 |

$(Mn_{0.66}Fe_{0.34})_{0.954}O$

| T(K) | $\chi_m$, APPLIED FIELD (KG) | | | | | | | | |
|---|---|---|---|---|---|---|---|---|---|
| | 1 | 2 | 3 | 4 | 5 | 6 | 7 | 8 | 9 |
| 47.5 | 0.964 | 0.849 | 0.828 | 0.800 | 0.784 | 0.765 | 0.754 | 0.750 | - |
| 51.2 | 1.018 | 0.856 | 0.831 | 0.802 | 0.783 | 0.767 | 0.756 | 0.751 | - |
| 56.4 | 0.964 | 0.804 | 0.766 | 0.717 | 0.727 | 0.708 | 0.700 | 0.693 | - |
| 61.5 | 0.937 | 0.790 | 0.763 | 0.738 | 0.716 | 0.704 | 0.693 | 0.688 | - |
| 67.2 | 0.937 | 0.790 | 0.763 | 0.735 | 0.717 | 0.700 | 0.694 | 0.685 | - |
| 77.5 | 0.909 | 0.790 | 0.763 | 0.731 | 0.712 | 0.697 | 0.689 | 0.681 | 0.686 |
| 87.2 | 0.994 | 0.827 | 0.783 | 0.751 | 0.729 | 0.714 | 0.705 | 0.699 | 0.710 |
| 103.9 | 0.991 | 0.842 | 0.800 | 0.766 | 0.745 | 0.730 | 0.721 | 0.718 | 0.724 |
| 122.0 | 0.991 | 0.856 | 0.831 | 0.796 | 0.776 | 0.761 | 0.751 | 0.749 | 0.750 |
| 135.7 | 1.018 | 0.886 | 0.859 | 0.830 | 0.810 | 0.793 | 0.787 | 0.803 | 0.790 |
| 140.0 | 1.046 | 0.916 | 0.890 | 0.860 | 0.837 | 0.826 | 0.819 | 0.828 | 0.821 |
| 141.7 | 1.046 | 0.916 | 0.894 | 0.860 | 0.840 | 0.827 | 0.818 | 0.832 | 0.834 |
| 148.3 | 1.046 | 0.908 | 0.869 | 0.846 | 0.826 | 0.810 | 0.804 | 0.822 | 0.815 |
| 154.5 | 0.991 | 0.879 | 0.856 | 0.826 | 0.807 | 0.792 | 0.786 | 0.802 | 0.796 |
| 158.7 | 0.991 | 0.879 | 0.842 | 0.814 | 0.798 | 0.782 | 0.775 | 0.776 | 0.779 |
| 165.7 | 0.991 | 0.864 | 0.842 | 0.812 | 0.794 | 0.781 | 0.774 | 0.772 | 0.778 |
| 177.5 | 0.964 | 0.849 | 0.814 | 0.788 | 0.770 | 0.753 | 0.747 | 0.746 | 0.752 |
| 189.2 | 0.936 | 0.827 | 0.793 | 0.766 | 0.746 | 0.734 | 0.727 | 0.723 | 0.735 |
| 200.5 | 0.909 | 0.811 | 0.776 | 0.750 | 0.732 | 0.717 | 0.710 | 0.706 | 0.720 |
| 210.0 | 0.881 | 0.790 | 0.759 | 0.735 | 0.717 | 0.706 | 0.699 | 0.695 | 0.707 |
| 223.7 | 0.854 | 0.760 | 0.738 | 0.717 | 0.697 | 0.685 | 0.675 | 0.672 | 0.680 |
| 234.8 | 0.881 | 0.745 | 0.728 | 0.701 | 0.684 | 0.670 | 0.662 | 0.659 | 0.672 |
| 241.2 | 0.854 | 0.752 | 0.717 | 0.693 | 0.678 | 0.666 | 0.658 | 0.654 | 0.669 |
| 251.5 | 0.854 | 0.738 | 0.711 | 0.683 | 0.668 | 0.654 | 0.647 | 0.643 | 0.656 |
| 261.9 | 0.826 | 0.738 | 0.697 | 0.671 | 0.653 | 0.642 | 0.634 | 0.630 | 0.629 |
| 274.8 | 0.799 | 0.708 | 0.683 | 0.655 | 0.638 | 0.626 | 0.618 | 0.614 | 0.621 |
| 286.1 | 0.799 | 0.693 | 0.662 | 0.645 | 0.627 | 0.614 | 0.607 | 0.602 | 0.614 |
| 296.0 | 0.772 | 0.686 | 0.655 | 0.637 | 0.618 | 0.604 | 0.598 | 0.593 | 0.605 |